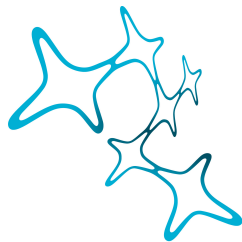


FLORIAN RICHTER

SPATIOTEMPORAL FILTERING
OF THE INPUT ELEMENTS TO
THE *DROSOPHILA* MOTION
DETECTOR



Graduate School of
Systemic Neurosciences

LMU Munich

Dissertation der Graduate School of Systemic Neurosciences der
Ludwig-Maximilians-Universität München

30th of November, 2021

Florian Richter

Spatiotemporal filtering of the input elements to the Drosophila motion detector

Dissertation der Graduate School of Systemic Neurosciences der
Ludwig-Maximilians-Universität München.

E-MAIL:

frichter@neuro.mpg.de

30th of November, 2021

First reviewer and supervisor
Prof. Dr. Alexander Borst

Second reviewer
Prof. Dr. Ruben Portugues

Date of submission
30th of November, 2021

Date of Defense
3rd of May, 2022

DEDICATION

To my parents.

SUMMARY

Extracting the direction of visual motion is a critical task for the survival of every animal that relies on vision. Although the anatomy of visual circuits was cartographed in mammals and flies alike over a century ago, the physiology of these cells remained speculative for long. Behavioral experiments with the snout weevil *Chlorophanus viridis* served as the basis for the proposal of an algorithmic model for elementary motion detection. In essence, two spatially separated inputs, one of which is delayed in time, are integrated in a non-linear operation. Since the first stage of the visual transduction cascade – photoreceptors – do not distinguish the direction of motion, the computation must occur in the circuitry downstream. In the fruit fly *Drosophila melanogaster* dense electron microscopic reconstruction, cell-type-specific driver lines, and genetically encoded indicators have led to significant progress over the past decade. We now know that: (1) motion information is split into parallel ON and OFF pathways, (2) T4 and T5 cells are the first direction-selective neurons in the fly motion vision pathway, (3) and two complementary mechanisms create direction-selectivity on T4 and T5 cells dendrites. One is responsible for enhancing signals when cells are stimulated in their preferred direction and the other for suppressing motion signals that are presented in the opposite direction.

Since the beginning of my doctoral work, the functional roles of the inputs to T4 and T5 cells are under debate. In the first manuscript, we used 2-photon calcium imaging in combination with white noise stimuli to identify the spatio-temporal response properties of all columnar input elements to the elementary motion detectors. After reverse correlating the signals with the stimulus, we found that input elements exhibit a range of temporal properties that can be grouped into two classes: low-pass filter and band-pass filter. Placing the cells onto the model in different spatial configurations and looking for those arrangements which would recapitulate T4 & T5 responses most faithfully, we were able to make suggestions about the anatomical wiring of the presynaptic partners to the T4 and T5 cells dendrites. This finding was later confirmed by an EM reconstruction data set. We also showed that the filter characteristics of the input elements are not fixed but instead can be influenced by neuromodulation.

In this study, we exclusively used the genetically encoded calcium indicator GCaMP. The relationship between the calcium signal of any given cell with its transmitter output can however, be complex. In the second study, we, therefore, set out to measure the transmitter release of all glutamatergic neurons in the motion vision pathway. We were able to show that spatial aspects of the receptive fields, measured with the recently developed glutamate sensor iGluSnFR, and GCaMP, are preserved. In the temporal domain, however, we find that these responses are substantially sped up in the glutamate signal. The results give a more realistic picture of the dynamics of

the glutamatergic input, which the motion-sensitive T₄ cell receives from a presynaptic partner (Mi9).

Flies reliably track the direction of motion over a large range of velocities and contrasts. Correlation-type motion detector models, however, are vulnerable to contrast changes when estimating the velocity in natural environments. In the last study, we set out to close this gap. Using 2-photon calcium imaging, we demonstrated that neurons presynaptic to T₄ and T₅ cells implement an adaptive non-linear gain control mechanism. By blocking the output of medullary neurons, we were able to show that this adaptive gain reduction, at least partially, arises from feedback rather than feedforward inhibition. Lastly, integrating a divisive normalization step into the model dramatically increased its motion vision robustness.

The three studies included in this thesis are presented chronologically and were published in peer-reviewed journals.

CONTENTS

1	INTRODUCTION	1
1.1	From anatomy to physiology	2
1.1.1	Basics of neural transmission	3
1.1.2	Measuring neural activity	4
1.1.3	Manipulating neural activity	7
1.1.4	Receptive fields	9
1.1.5	Optomotor response	11
1.2	The fly visual system	11
1.2.1	Lamina	14
1.2.2	Medulla	16
1.2.3	Lobula complex	18
1.3	Models of motion detection	23
1.4	Concluding remarks	26
2	PUBLICATIONS	29
2.1	The temporal tuning of the <i>Drosophila</i> motion detectors is determined by the dynamics of their input elements	29
2.2	Glutamate signaling in the fly visual system	67
2.3	Dynamic signal compression for robust motion vision in flies	89
3	DISCUSSION	127
3.1	The visual system of flies and mammals - Commonalities and differences	128
3.1.1	Anatomy and functional structure	128
3.1.2	Parallel pathways	131
3.1.3	Motion vision circuitry	133
3.1.4	Biophysical implementation of filtering	136
3.2	Fly motion vision	140
3.3	Concluding remarks	145
	Bibliography	147

LIST OF FIGURES

Figure 1	Synaptic transmission at chemical synapses.	5
Figure 2	The fly retina.	12
Figure 3	The <i>Drosophila</i> lamina neurons.	15
Figure 4	Anatomy of columnar neurons the fly optic lobe.	17
Figure 5	T4 and T5 cells.	18
Figure 6	Lobula plate tangential cells.	20
Figure 7	Lobula plate intrinsic neurons.	21
Figure 8	Schematic of the "center for optic motion perception".	23
Figure 9	Classical correlation type models for motion detection.	24

Figure 10	Hybrid detector.	25
Figure 11	Comparison of vertebrate and invertebrate anatomy.	129
Figure 12	Convergence and divergence in the visual system.	130
Figure 13	Space and time in retinal bipolar cells.	134
Figure 14	Temporal delay mechanisms.	135
Figure 15	Distribution of input synapses and receptors on T ₄ and T ₅ cells.	141

In honor of the famous German physicist and physiologist Hermann von Helmholtz, Siegmund Exner wrote for Helmholtz's 70th birthday an entire book about the facette eye of crustaceans and insects on the occasion. In the preface, he described how he, "[...] despite being a physiologist, was distracted with considerable force from his actual work by the immense diversity of facet eyes. Everyone who would know the abundant wealth of invertebrate eyes would be bored by studying the vertebrate eye. Why would nature pursue two so substantially different ways to come to the same result of equipping a living creature with an eye? A topic which I consider to be of indubitable scientific appeal and which demands anatomical, biological, physical, and physiological thinking." (freely translated from German) (Exner, 1891).¹

Whoever observed an insect under a microscope will immediately realize that they are diving into an otherwise hidden world of almost alien-like creatures with strange grimaces. Maybe most prominently one will see the arrays of facets staring back that seem fundamentally different from what one usually defined as "eye". It is therefore hard to deny Siegmund Exner's fascination. But why of all species should one study the visual system of *Drosophila melanogaster*? The answer lies in the fruit fly's history as a classical model for genetics ranging back more than one century (Morgan, 1910). This history provides neuroscientists with an unparalleled wealth of tools that are perfectly tailored to investigating fundamental questions that arise in visual systems such as: How does the brain extract behaviorally relevant information from complex visual cues, such as luminance, contrast, motion, color, the recognition of conspecifics and objects?

Motion vision is an especially appealing topic to study in *Drosophila* for various reasons. First, flies exhibit a stereotyped motion-guided behavior which serves as a read-out. Algorithmic models proposing how the computation of motion vision can take place, have existed for long. Second, the entire visual circuitry has recently been mapped via high-resolution electron microscopy studies. Third, there is an armory of a genetic toolbox that grants access to the circuit.

¹ "Die vorliegende Studie ist das Resultat mehrjähriger Arbeiten, welche mich stärker, als man es von einem Physiologen erwarten mag, fesselten. Das Facettenauge liegt abseits von den viel begangenen Wegen unserer Wissenschaft. Einerseits aber hat es einen unzweifelhaften wissenschaftlichen Reiz, nachzuforschen, wie und warum die Natur zwei so grundverschiedene Mittel benutzt, um anscheinend zu demselben Ziele zu gelangen, ein Lebewesen mit Augen auszustatten; andererseits zeigte sich mir, einmal dem Gegenstande nähergetreten, eine solche Fülle von Formen und Erscheinungen, dass dieselben von Frage zu Frage drängend, Antwort auf Antwort verlangten, und in ihrer Mannigfaltigkeit, indem sie anatomisches, biologisches, physikalisches und physiologisches Denken erforderten, das Interesse immer wieder wachriefen. Das Auge der Wirbellosen ist ein Proteus im Vergleiche zum Auge der Wirbeltiere, ja letzteres könnte Jeden langweilen, der den Reichthum des ersteren kennen gelernt hat" (Exner, 1891).

Throughout my Ph.D., I placed a particular focus on the question of how circuit elements prior to the first motion-sensitive neurons filter visual signals and how this aids the computation of direction selectivity. In the following, I will first explain the state-of-the-art techniques that I used for this endeavor. I will then introduce the visual system of the fly and give insights into purely theoretical approaches that tackle the question of how the direction of motion can be computed. This will lay the groundwork for understanding the main part of my dissertation.

1.1 FROM ANATOMY TO PHYSIOLOGY

In 1873, Camillo Golgi discovered that when applying potassium dichromate and silver nitrate to the tissue of the nervous system, only some cells were stained black while others remained transparent (Golgi, 1873). Why this is the case is still not fully understood. Conventional stainings during that time always labelled all cells, which rendered an inspection of a single cell impossible due to the densely interconnected networks of the nervous tissue upon which the nervous tissue is built. From this newly developed staining method, one could finally see the elementary units building the basis for the brain: neurons. The technique was later adopted and improved by another neuroscientist from Petilla de Aragón in northeastern Spain: Santiago Ramón y Cajal. He used this method to observe the various cell types that emerged in stark black against the yellow background and studied the fine arborizations of the cells under a microscope. To be able to preserve his observations and show them to other people, Ramón y Cajal produced nearly three thousand drawings over the course of five decades. Because of the unprecedented detail of his work, his paintings, until today, are considered an invaluable contribution not only to science but also to art. Although these stainings and drawings marked a breakthrough in neuroscience, scientists had to infer the function of the abundantly diverse cell types purely from their anatomy. Looking at the same pictures, Golgi and Ramón y Cajal, advocated different theories on:

- 1) How the brain is structured.
- 2) How information flows within one neuron.

Concerning the first question, Golgi advocated the idea that the neurites of different cells are fused to form a single continuous network of nerve fibers, a so-called reticulum. His theory was hence termed *reticular theory*. On the other hand, Cajal brought forward the idea that neurons communicate by contact and not by continuity and that neurons obey the rule of cell theory, which says that all living tissue consists of individual elementary units. Following this logic, Ramón y Cajal thought of the brain as yet another organ that is built from countless individual cells, in this case, neurons. This way of interpreting the results was termed the *neuron doctrine*. Half a century later, in the 1950s, Ramón y Cajal's theory was proven right by electron microscopic images showing that there is a cleft between the end of each axon of one cell and the dendrite of another. In this cleft, chemical substances are

released from the first cell and are taken up by the second, allowing for the flow of information. This cleft is what we today call a synapse.

The second disagreement arose from the structure of neurons themselves. Both scientists observed that there are two different types of extensions from the cell body. One usually branches out into numerous ramifications (dendrite), whereas the other consists of only one thin branch that thickens at the end (axon). Camillo Golgi was a proponent of the idea that the dendrites of neurons only serve as nutrient deliverants and that communication between cells happens from axon to axon. Ramón y Cajal, on the other hand, envisioned that electrical signals would follow the rule of dynamic polarization, meaning that information flows from the dendrites and cell body towards the axon terminal (Newman et al., 2017).

Although both of Cajal's theories were superior to the ones that were developed by Camillo Golgi, the two scientists were awarded the Nobel prize in physiology and medicine in 1906 "in recognition of their work on the structure of the nervous system". (<https://www.nobelprize.org/prizes/medicine/1906/summary/>)

Ever since, scientists have made big efforts to understand cell-to-cell communication. In neurons, this communication takes place at a specialized site: the *synapse*.

1.1.1 Basics of neural transmission

At the core of anything carried out within the CNS, from reflexes to cognition, lies cell-to-cell communication. In the nervous system, this communication has to happen fast and precisely. How signals propagate *within* a cell is a topic of substantial complexity. I will focus on explaining the basics of communication *between* cells as we primarily studied networks of neurons instead of isolated units. On average, a mammalian neuron receives signals from over a thousand synaptic connections, some cells in the cerebellum (Purkinje cells) even exceeding as much as 100.000. Despite the vast number and specialization of synapses, two basic types of synaptic transmission can be extracted:

1) *Electrical synapse*

Stereotyped electrical signals are rapidly passed onto connected cells via specialized bridging channels called *gap junctions* (on average 4nm) that allow a direct flux of ions. The postsynaptic potential change is therefore inseparably related to the presynaptic one in terms of size and shape (exception: rectifying synapses, e.g. in the crayfish giant motor synapse). Such speedy transmission can be advantageous for escape responses described in many animal species, including tail-flip responses of goldfish via Mauthner cells or fast take-off jumps in *Drosophila* via the giant fiber neuron (Eaton et al., 1981; Ache et al., 2019; Fayyazuddin et al., 2006; Allen and Murphey, 2007; Thomas and Wyman, 1984; Von Reyn et al., 2014).

2) *Chemical synapse*

At first, an electrical signal has to be produced and then propagated from its origin (usually dendrite) towards the end of the cell (axon terminal). When the changes in membrane voltage travelling along the cell, reach the axon, an intricate mechanism is triggered. Opening of voltage-gated calcium channels leads to an increase in cell-internal calcium levels as seen in Figure 1 a. At a chemical synapse, there is no direct contact between the cells; in fact, there is a cleft of about 20-40 nm. The transmission of chemical signals depends on the diffusion of neurotransmitters, molecules that are released from the presynaptic terminal (Figure 1 b) and, after diffusion, bind to specific receptors in the postsynaptic cell. Two major groups of receptors exist: Ionotropic receptors are ion channels that open directly when a transmitter is bound, while metabotropic receptors act indirectly on ion channels through activation of a biochemical second-messenger cascade. In both cases, the flow of ions changes the conductance and voltage of the postsynaptic cell's membrane (Figure 1 c). This operation is more time-consuming than the pure electrical transmission of signals but offers the opportunity for more interesting computations. At chemical synapses, signals can be potentiated (amplified) or depressed (diminished) and can be very fast (ms) or rather sluggish (minutes)(reviewed in (Cowan and Kandel, 2001; Eccles, 1976).

Within the visual system of the fly, chemical synapses are thought to play the critical role in computation. As a consequence, in the following sections, I will focus on such synapses. For all three steps in chemical synaptic transmission (summarized in Figure 1), various tools exist to measure the cell's voltage, calcium level, or transmitter release. In the following sections, I will present a selection of tools to measure and manipulate neural activity, highlight their advantages and disadvantages, and elucidate how behavior can serve as a read-out for circuit function.

1.1.2 Measuring neural activity

ELECTROPHYSIOLOGY As mentioned before, neurons use electrical potentials to transmit information. Electrophysiology allows for the direct observation of voltage or current changes along the membrane at extremely high temporal resolution. Many variations of this method are still being used in modern neuroscience. Placing an electrode directly in the vicinity of the cell of interest allows for extracellular recordings, making it possible to record large-amplitude deflections in the cell's voltage (i.e. action potentials). Insect neurons however often do not fire action potentials but rather use graded potentials for the transmission of information (Haag and Borst, 1998). With an often better-suited variant of this method, one can use a sharp micropipette to poke a hole into the membrane of the cell of interest, granting access to the internal solution of the neuron. By comparing the difference in electric potential of the intracellular solution and the solution in the pipette, changes in intracellular currents can be inferred. Recordings like these were used to

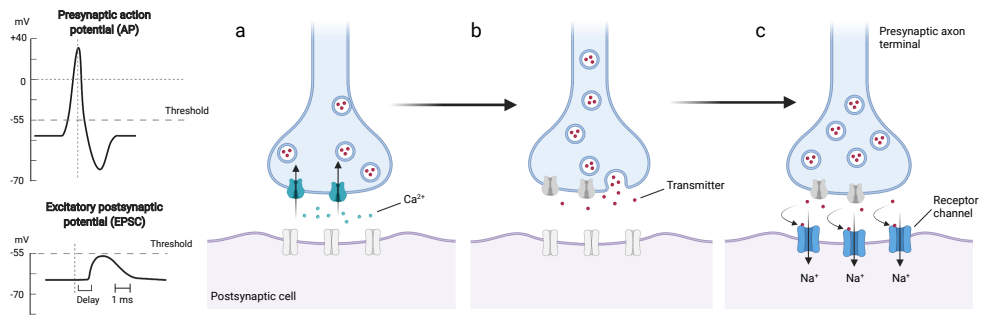


Figure 1: Synaptic transmission at chemical synapses. Depicted is the intricate process from voltage changes in the presynapse to a change in postsynaptic potential. The top row shows presynaptic release sites with vesicles and calcium channels. The bottom row shows postsynaptic sites with receptors. **a.** An increase in membrane voltage in the presynaptic terminal leads to the opening of voltage-gated calcium channels. **b.** The increase in intracellular calcium levels results in the fusion of the vesicle membrane with the outer membrane. The transmitter is released into the synaptic cleft. **c.** Neurotransmitter molecules diffuse towards specific receptors in the postsynaptic cell. Transmitters bind to receptors and cause ion channels to open/close, thereby changing membrane conductance and potential.

characterize large lobula plate tangential cells (see Section 1.2) of the blowfly *Calliphora erythrocephala* (Hausen, 1976; Krapp et al., 1998).

Due to the small size of *Drosophila* neurons, sharp electrode recordings are hard to achieve. A third option, which proved to be better suited, is whole-cell patch-clamp recording, a method that was first used in Hamill et al. (1981). Placing a glass pipette in close vicinity of the cells membrane and applying some pressure forms a small bulge in the membrane. Releasing the pressure optimally results in a sealed surface between pipette and membrane. As a consequence, the resistance rises immensely until a so-called gigaseal is reached. Afterwards, suction is applied to remove the piece of membrane that is engulfed by the pipette. When the seal is stable, the experimenter has electrical access to the cell's interior. *In vivo* patch-clamp recordings in *Drosophila* have been established in many brain areas including the visual (Joesch et al., 2008; Behnia et al., 2014) and the olfactory system (Wilson et al., 2004).

FUNCTIONAL IMAGING Despite the efforts that have already been made, for many *Drosophila* neurons, the small size rendered electrophysiological recordings very difficult. Furthermore, cell bodies are often separated from the dendrites and axons by long neurites, such that recorded signals might be attenuated before they reach the recording site.

Therefore the invention of 2-photon microscopy made functional imaging especially tempting for visual neuroscience (Denk et al., 1990; Helmchen and Denk, 2005). This method uses a highly pulsed laser that squeezes light into tiny intervals so that many photons are shot onto a fluorophore in femtoseconds. By absorbing a photon, an electron of a fluorescent molecule is lifted to a higher energy state. This can be achieved by either absorbing

one photon of a shorter wavelength or by absorbing two photons that have twice the wavelength of the shorter one (Göppert-Mayer, 1931). In other words, the electron in the fluorescent molecule can achieve a higher energy state either by taking up a violet-blue photon from 450 nm light or by taking up two photons at the same time from light that has the wavelength 900 nm. This doubling of the wavelength has various advantages.

First, it reduces light scattering. The frequency of the light is directly proportional to the scattering of the light. In other words, violet light at 400 nm wavelength has twice the frequency of red light at 800 nm but will provoke 16 times as much light scattering.

The second advantage, compared to conventional one-photon imaging, is decreased bleaching. At high energy light exposure, fluorophores lose their brightness. Light of longer wavelengths has a lower frequency and therefore carries less energy. This allows for a longer time span, in which signals can be obtained. Additionally focusing the light beam in only one spot prevents the tissue above, and below from bleaching. Therefore, 2-photon imaging reduces bleaching to a minimum.

Third, if one wants to study the neuronal signals in a visual circuit, it is best for the light source that creates the fluorescent image to not overlap with the light that is being used to create the stimuli, since this can cause artifacts. Light above 900 nm can be seen neither by the human nor by the fly's eye and therefore lends itself well to visual neuroscience (reviewed in (Svoboda and Yasuda, 2006)).

Because of these convenient properties, I used 2-photon imaging as the main technique throughout my Ph.D. In order to take advantage the technological innovations, however, genetical tools needed to be developed.

GENETICS *Drosophila* has been used as a model organism for studying genetics for more than a century (Morgan, 1910; Bellen et al., 2010). Ever since, the knowledge from genetics has advanced many fields in science, including neuroscience.

The basis of gene expression is always a two-component expression system where a driver-line, which defines the neurons of interest, is combined with an effector line, which defines the gene that should be expressed (Brand and Perrimon, 1993). For this purpose the Gal4/UAS and *lexA/lexAop* system have been developed for *Drosophila* (Venken et al., 2011).

The Gal4/UAS-system is a binary expression system that is derived from yeast, where the transcription factor Gal4 binds, under the control of an endogenous promoter, to the Upstream Activation sequence (UAS), ultimately leading to protein expression (Brand and Perrimon, 1993). Loosely speaking, the Gal4 therefore determines the 'where' and the UAS the 'what' of expression. Crossing a fly with the Gal4 driver line with a fly that possesses the UAS effector line (F_0 generation) results in offspring (F_1 Generation) that possesses a combination of both. Only then the gene of interest will be expressed.

A complementary system, which is based on the bacterial DNA-binding protein-operator Lex-A-op, is controlled by the expression of LexA (Lai and Lee, 2006). Combining the two expression systems allows the experimenter to target two different populations of cells with two different effectors.

Classically, Gal4 fly lines have been created by injecting randomly integrating transposable P-elements into *Drosophila* embryos (Hayashi et al., 2002). Missing control over specific insertion sites, however, often results in broad expression patterns, which render them unsuitable for circuit manipulations. Nowadays efficacy is increased by directly cloning DNA fragments with presumed enhancer activity, and specificity is increased by intersectional strategies, such as the split-Gal4 system (Pfeiffer et al., 2008; Jenett et al., 2012). Here, the Gal4 is split into two functional subunit, the transcription activating domain (AD) and the DNA binding domain (DBD). Both subunits are under the control of different specific enhancers. One domain alone is not sufficient to initiate Gal4 transcription alone, therefore only in cells containing both subunits, transcription is started (Luan et al., 2006).

The result of this work, can be seen in large libraries containing thousands of fly lines, where most cell-types of the fly brain can be targeted with high specificity (Pfeiffer et al., 2010). Combining precise genetic expression with functional imaging together with genetically expressed indicators has been a predominant method for measuring voltage (genetically encoded voltage indicators = GEVI, (Bando et al., 2019)), calcium (genetically encoded calcium indicators = GECI, (Chen et al., 2013)) and transmitter release (reviewed in (Sabatini and Tian, 2020)) in *Drosophila* neuroscience.

1.1.3 Manipulating neural activity

For the sole purpose of describing the physiological characteristics of a pre- or postsynaptic cell, the above-mentioned methods are well suited. However, in circuit neuroscience, one strives to identify the role of individual cells in the broader perspective of an entire circuit. Manipulating the activity of individual cell types or even single cells is therefore extremely useful.

TOOLS FOR ACTIVATING NEURONS One of the ways to learn about the circuit function of individual cell types is through activation. This, for instance, allows to determine, whether the activity of one neuron is sufficient to drive certain reflexes or behaviors. The heat-sensitive cation channel *dTrpA1* has been developed for reversible activation of cells (Rosenzweig et al., 2005; Parisky et al., 2008). By increasing the temperature of the tissue, the experimenter can control the activation of a certain cell with moderate temporal resolution.

Optogenetic tools offer a solution with high temporal precision. The development and diversification of optogenetic techniques have enormously boosted neuroscience in general and are being used nowadays in virtually all genetic animal models and even for therapeutic treatment of neurodegenerative eye disease (*retinitis pigmentosa*) in humans (Sahel et al., 2021). The first light-gated cation called *Channelrhodopsin-2*, abbreviated as *ChR2*, has been successfully extracted from the green alga *Chlamydomonas reinhardtii* (Harz and Hegemann, 1991; Nagel et al., 2003) and expressed in the nematode *Caenorhabditis elegans* and hippocampal neurons of mammals (Nagel et al., 2005; Boyden et al., 2005). By shining blue light onto cells that genetically express these light-sensitive cation pores, it is possible to deliver

optical, non-invasive, reliable excitation with millisecond precision (for review see (Deisseroth, 2015)).

TOOLS FOR BLOCKING NEURAL ACTIVITY Combined with a functional read-out — e.g., the recording of downstream neural activity in motion-sensitive elements — silencing individual neurons in a circuit can help to reverse engineer the roles of specific units. The basics in neural transmission, depicted in Figure 1, show three major attack points to disentangle cell-to-cell communication:

1. Abolishing the electrical signal such that the subsequent cascade of calcium influx and transmitter release is not triggered.
2. Interfering with the cascade that sets off vesicle release.
3. Getting rid of the postsynaptic receptors.

Classically, pharmacology was the go-to option for this pursuit, however, applying substances onto the neural tissue often sets limits when interpreting the results. Even when substances are applied locally via, for instance, a pipette, diffusion to surrounding tissue often cannot be prevented, thereby interfering with up- or downstream circuits. Additionally, most drugs, with some exceptions (e.g. tetrodotoxin binding to voltage-gated sodium channels), bind unspecifically to receptors, therefore leading to off-target effects (Trevor et al., 2010).

Nowadays, researchers can make use of the rich neurogenetic toolbox of *Drosophila*, allowing cell-type-specific manipulations. For instance, the presynaptic electrical signal can be silenced by genetically overexpressing the inwardly rectifying potassium channel *Kir2.1* and therefore constantly hyperpolarizing the cell (Baines et al., 2001; Johns et al., 1999). Ultimately, this leaves the cell's membrane less excitable and the subsequent machinery is not triggered.

Although this intervention is permanent and potentially interferes with circuits during development, there is a reversible option. The light-gated anion channel *GtACR* has been extracted from the cryptophyte algae *Guillardia theta* (Govorunova et al., 2015). Genetically expressing the channel in the neurons of interest and simply applying light of the right wavelength, this channel opens, allowing the influx of negatively charged Cl^- ions, ultimately causing the cell to hyperpolarize. This combination is a highly sensitive, precisely timed, reversible method for steering the neural activity (for review of optogenetic tools see (Fenno et al., 2011)).

Instead of interfering with the electrical signal of the presynaptic cell, it is also possible to disrupt the mechanism that leads to transmitter release. The neurotoxin *tetanus toxin light chain* (TNT) irreversibly cleaves the synaptic protein synaptobrevin, which is essential for transmitter release (Sweeney et al., 1995).

A less permanent approach is expressing the dominant-negative version of the gene *shibire^{ts}*, a temperature-sensitive allele of the dynamin protein (Kosaka and Ikeda, 1983; Henley et al., 1999). At room temperature ($\approx 25^\circ \text{C}$) the dynamin protein is involved in the reuptake of neurotransmitters from the synaptic cleft into to the presynaptic cell (endocytosis). Here, the GTPase

dynamins assemble around the shaft of endocytic vesicles, which intrude at the presynaptic membrane. The dynamin protein constricts the vesicle membrane, which ultimately leads to the scission of the vesicle membrane from the membrane of the presynaptic cell. Increasing the temperature to around 29° Celsius, the conformation of dynamin is changed, rendering it dysfunctional. This effect is reversible by bringing the specimen back to room temperature (Kitamoto, 2001).

As the third possible point of intervention, numerous genetic tools have been invented to either knockdown or knock out neurotransmitter receptors. At the level of the DNA, CRISPR/Cas9 has emerged as a prime tool for gene ablation (Port et al., 2014, 2020). With this method, virtually any targeted genetic modification in almost any organism or cell type is feasible today. One of the problems, though, is that this can be very time-consuming to achieve (reviewed in (Heidenreich and Zhang, 2016)).

Historically, RNA interference was one of the first ways to tackle proteins. Here, short pieces of mostly double-stranded RNA, together with an enzymatic protein complex (RNA-induced silencing complex, RISC), interfere with target mRNA transcripts. In the first step, with the help of ribonuclease-enzymes (e.g. Dicer or Drosha), large double-stranded RNA molecules are cut into smaller double-stranded pieces. The fragments are then separated into single strands and integrated into the RISC complex. This activates the enzymatic complex that now can cleave or block mRNA that is complementary to the uptaken RNA strand. As a result, translation of the protein is blocked. Today, large libraries of RNAi lines exist with manifold lines that allow cell-type-specific gene inactivation (Dietzl et al., 2007). Unfortunately, this method is prone to off-target effects and often low efficacy (Perkins et al., 2015).

Lastly, proteins can be directly affected by targeted proteolysis, a method that circumvents the processes of transcription and translation. Here, the target protein can be marked directly for proteasomal degradation (reviewed in (Röth et al., 2019)).

1.1.4 Receptive fields

Whether a response in a sensory neuron is elicited under natural conditions depends on whether it matches with the *receptive field* of the neuron. The concept was first introduced to describe the area on a dog's body surface where a scratch reflex can be elicited (Sherrington, 1906). Later, it became more popular when Hartline (1938) used the term to describe the firing of a bullfrog retinal ganglion cell (RGC) in dependence of the position of the light stimulus. Generally, *spatial receptive fields* are described as the area in sensory space where a neuron's activity can be modulated. In visual neuroscience, for instance, this would be the pixels on the stimulation screen where changes in luminance or contrast can elicit a response in a certain neuron. This receptive field definition can be extended to the temporal domain. Here, the *temporal receptive field* describes the time window in the past, in which the presentation of a visual stimulus in the spatial receptive field had an impact on the neuron's response.

A receptive field is termed *linear* when the output of a system is proportional to its input. The output of a linear system can therefore be predicted as a weighted sum of the inputs. Mathematically this can be described with the equations:

$$R(x + y) = R(x) + R(y) \quad (1)$$

which implies

$$R(n \cdot x) = n \cdot R(x) \quad (2)$$

If these conditions are not met, the system is non-linear (Cruse, 1996). Non-linearity occurs, for instance, when two channels are multiplied. Biological systems are most often of non-linear nature, however, for understanding the system it is useful to identify the underlying linear operations first.

In visual neuroscience, one will often encounter center-surround receptive fields, where the preference of the center subregion is antagonistic to the preference of the surround. A subregion is termed *ON*, when illumination increments, and *OFF* when light decrements lead to an increase in neural activity. In a receptive field where the center and surround are equally balanced, this operation corresponds to spatially band-pass filtering the image. In the literature such a type of spatial filter is often called *difference-of-gaussians* (*DOG*) or *Mexican hat*. In this receptive field configuration, uniform illumination would yield a net-zero response, whereas differences in stimulus intensity between the center and the surround would lead to strong responses. An antagonistic receptive field configuration is thus well-suited for the discrimination of local rather than global contrast changes (Bonin et al., 2005; DeAngelis et al., 1995). For the identification of the receptive field of a neuron, classically, parameterized stimuli were used, such as spots of light, bars, or edges. A moving edge, for instance, represents a spatial step function. Here, the input value abruptly increases and is then kept at the new value. The output of the system - or in our case a neuron - is called the step response or transient function. Another input function is the impulse function $x(t) = \Delta(t)$, or pulse function. It describes a brief pulse that immediately drops back to its original value. The response to an impulse function is called the impulse response or weighting function $g(t)$. According to system theory, knowing the impulse response of a filter, everything that is to know about the linear filter can be deduced. For visual systems, such an impulse function would be an infinite short and infinite strong pulse of light. Per definition, such a stimulus does not exist and can only be approximated, with concomitant inaccuracies (Cruse, 1996).

This problem can be circumvented by the use of *white noise* stimuli that allow, together with reverse-correlation, access to the impulse response of a filter. This technique has first been used in the auditory system (Eggermont et al., 1983), and was later broadly applied to describe the spatio-temporal receptive fields of macaque primary visual cortex neurons (Cottaris and De Valois, 1998; Ringach et al., 1997; Ringach, 2002).

For primary sensory neurons, a linear receptive field often yields a reasonably good approximation to the "true" receptive field, however higher-order neuronal receptive fields can rarely be described by pure linear means.

Non-linear operations are included, for instance, in motion vision (Borst and Helmstaedter, 2015) or divisive normalization (Carandini and Heeger, 2012). Therefore an alternative definition of a receptive field is more applicable here: the receptive field of a neuron is its optimal stimulus.

1.1.5 Optomotor response

Given that the assumed purpose of neural circuits is to control an animal's actions, behavior serves as a critical read-out to test hypotheses derived from physiological experiments. This is particularly true when we assign function to particular components of a circuit; only if it affects behavior in a predictable way can we assume a causal relationship. *Drosophila* possesses a rich repertoire of visually guided, stereotyped behaviors such as mating, escaping and landing responses, fixation responses, and the optomotor response (Borst, 2014; Muijres et al., 2014; Tammero and Dickinson, 2002; Land and Collett, 1974).

The *optomotor response* describes a compensatory reflex to external visual perturbations. For instance, when a fly is placed in a striped paper drum and the pattern is moved clockwise, the fly will also move clockwise because it mistakes the surrounding visual motion for a counterclockwise turn of the body (Götz, 1964; Borst et al., 2010). The optomotor response was classically observed in tethered walking or tethered flying flies where the head and the thorax of the fly are glued to a metal holder whereas the rest of the body can move freely. In tethered walking experiments, for example, the fly walks on an air-suspended styrofoam ball while visual stimuli are delivered. The turning response is then read out as the rotation of the styrofoam ball (Buchner, 1976). In tethered flight, differences in wingbeat amplitude (Götz, 1987) or torque (Fermi and Reichardt, 1963; Götz, 1964) can be analyzed as a readout for the compensatory responses of the fly to visual stimulation.

In freely behaving animals, these experiments are more difficult to perform because ego-motion produces not only visual feedback but also proprioceptive cues, conveyed by club-shaped appendices, called halteres, that are originally derived from the hind wings. With modern high-speed cameras, however, it is possible to present visual stimuli and track the fly's behavior simultaneously (Mronz and Lehmann, 2008; Strauss et al., 1997; Leonte et al., 2021).

1.2 THE FLY VISUAL SYSTEM

The nervous system of an adult *Drosophila melanogaster* consists of around 200,000 neurons (199,380 +- 3400) (Raji and Potter, 2021). It is subdivided into the ventral nerve cord, located in the thorax, as well as the abdomen, and the central brain and optic lobes in the head of the fly. More than half of all neurons (107,270 +- 2,720) are dedicated to the optic lobe, the part of the brain that extracts visual cues such as luminance, contrast, color, motion, and position of an object.

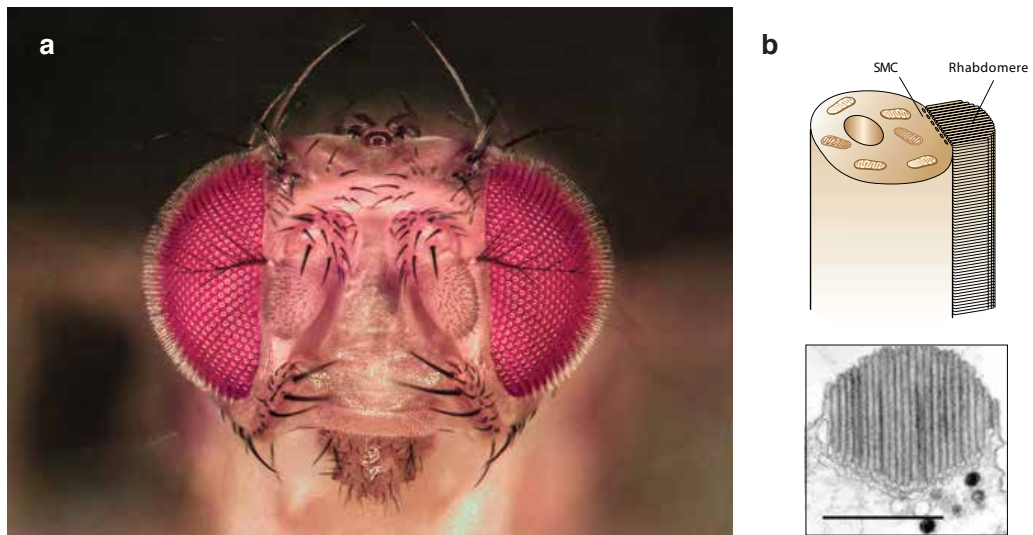


Figure 2: The fly retina. **a** Focused stack of the *Drosophila* head. 22 images were acquired with a camera on top of a binocular microscope. Images were aligned and stacked using Adobe Photoshop. **b** Top: Schematic of a *Drosophila* photoreceptor structure. To maximize absorption, the photoreceptive membrane is organized in tightly packed tubular microvilli, forming the rhabdomere. Bottom: Electron microscopic image of a rhabdomere. Scale bar = 1 μm . Pictures in **b** are taken with permission from [Hardie and Raghu \(2001\)](#).

The optic lobe consists of the neural structures called lamina, medulla, lobula, and lobula plate consist of a web of repetitive columns, maintaining retinotopy. That is, neighboring points in visual space are processed by neighboring ommatidia and within neighboring columns in each of the four layers. Two optic chiasmata can be found in the optic lobe, the outer one between the lamina and medulla, and the inner one between the medulla and lobula complex ([Fischbach and Dittrich, 1989](#)). This leads to a double inversion of the visual image along the anteroposterior axis. Neurons in *Drosophila* can be put into two anatomically distinct categories. Unicolumnar cells strictly adhere to retinotopic structure, meaning that a neuron is found once within one column and its arborizations do not ramify into neighboring columns. Accordingly, the second type of neurons span more than one column and are therefore termed multi-columnar.

As a dipteran species, *Drosophila* has facet eyes that are fundamentally different from mammalian eyes. Whereas our eyes use only one lens to focus light onto the retina, each of the fly's eyes consists of a hexagonal lattice of about 800 ommatidia, each individually equipped with a spherically curved lens that has an acceptance angle ρ of about 5° (which matches the angle between ommatidia $\Delta\phi$), resulting in a rather poor spatial resolution and acuity ([Götz, 1965](#); [Land, 1997](#)). Interestingly, there is a trend in dipteran species that the smaller the insect, the greater is the receptor's acceptance angle. While this angle for larger blowflies amounts to 1° , the much smaller *Drosophila*'s ommatidia have an acceptance angle of $\approx 5^\circ$ (for comparison: human spatial resolution in the fovea is better than 0.001°). If *Drosophila* had as many ommatidia as the larger blowfly *Calliphora* (roughly 5000), this would lead to a reduction in lens diameter and result in the loss of sensitivity,

ultimately leaving the receptors in photon noise. As a consequence, lenses are not scaled to the size of the eye but rather the number of ommatidia is reduced.

Each ommatidium houses 8 different photoreceptors (R1-R8). R1-R6 are organized in a circular manner enclosing R7 and R8, which are stacked upon each other. R1-R6 expresses the rhodopsin 1 (Rh1), which is sensitive to a wide range of light wavelengths. It reaches peak sensitivity at two distant locations in the light spectrum: one in at approximately 480nm (e.g. green light) and one in the ultraviolet area. In the absence of this pigment, motion detection is impaired (Heisenberg and Buchner, 1977; Rister et al., 2007). R7 and R8 express different types of rhodopsins, with more distinct absorption peaks, suited for their role in color vision and the detection of polarized light vectors (Yamaguchi et al., 2008; Wernet and Desplan, 2004; Wernet et al., 2003).

The photoreceptors in flies are extraordinarily sensitive, such that when electrophysiologically recording from a photoreceptor, a discrete inward current (quantum bump) can be observed in reaction to the absorption of even a single photon (Yeandle and Spiegler, 1973; Baylor et al., 1979). Through adaptation, the photoreceptors can cope with brightness changes from dusk till dawn, where the number of photons arriving at the retina can easily change by orders of magnitude, from as little as one photon up to a million per second. Mammalian rods instead saturate quickly at increasing light intensity, making a less sensitive set of photoreceptors, the cones, necessary (Hardie and Raghu, 2001).

NEURAL SUPERPOSITION Due to the circular arrangement of R1-R6 in each ommatidium, each photoreceptor collects light from a slightly offset visual angle. Because the eye of the fly is curved, however, photoreceptors in adjacent columns possess the same optical axis. According to the hexagonal structure of the fly's eye this means that seven photoreceptors from seven different ommatidia receive light from the same position in visual space. This concept is called *neural superposition* (Kirschfeld, 1967). The inputs of the seven photoreceptors converge downstream in one lamina cartridge, thereby increasing the sensitivity of the visual system, without losing spatial resolution.

Depending on the ecological niche of the species, evolution makes trade-offs in favor of one or the other. *Drosophila*, a "true fly" (dipterian), is roaming around early in the morning or late in the evening, therefore, sensitivity might be more crucial for the animal's survival than having the environment sharply resolved.

PHOTOTRANSDUCTION The fruit fly's lack of spatial vision is compensated for not only by the extraordinary sensitivity but also by speed. Through a process called phototransduction, light signals are converted into electrochemical signals. Phototransduction in flies is highly optimized and incorporates the fastest G-protein-signalling cascade known, allowing for a flicker fusion rate of about 200 Hz whereas, for comparison, the human flicker fusion rate lies at around 60-90 Hz (Hecht and Wald, 1934; Heisenberg and Wolf, 1984; Hardie and Juusola, 2015). The fly's photoreceptor cell surface

is largely covered by a subcellular structure that functions as a light guide, called rhabdomere (Figure 2 b). The rhabdomeres in turn consist of ≈ 30.000 tightly packed light-absorbing compartments, called microvilli. In the microvilli, photo-active molecules, rhodopsins (Rh), absorb light and kick off a cascade of chemical reactions.

The chromophore 3-hydroxy-11-cis-retinal is bound to the rhodopsin. After absorbing a photon it changes its conformation to the all-trans configuration, thereby converting the rhodopsin into an activated state (metarhodopsin or M-state). Strikingly, in invertebrates, metarhodopsin can be directly re-isomerized to rhodopsin simply by the absorption of longer wavelength light. This constitutes a temporal advantage over the vertebrate phototransduction where all-trans-retinal must be re-isomerized through a slow enzymatically driven process. This rapid back and forth between the two states is enabled by the fact that the screening pigment is permeable for long-wavelength light. This way, the light of longer wavelengths is trapped and can continuously reset the transduction cascade (Hardie and Raghu, 2001). Due to this, the fly's eyes appear red to the human observer. After the M-state is reached, a G-protein coupled cascade activates phospholipase C (PLC), which hydrolyzes PIP₂ to DAG, IP₃ and a proton. Two light-sensitive channels (TRP and TRPL) are subsequently activated, which allows sodium and calcium to enter the cell and depolarize the membrane, ultimately leading to the release of the inhibitory neurotransmitter histamine (reviewed in (Hardie, 1989; Hardie and Raghu, 2001; Hardie and Juusola, 2015)).

1.2.1 Lamina

Primary visual information from the photoreceptors is further processed in the subsequent neuropil, called the lamina. Here, around 6000 cells are organized to approximately 750 repetitive, retinotopic lamina cartridges (Braitenberg, 1967; Kirschfeld, 1967). Extensive Golgi stainings performed by Ramón y Cajal and Sánchez (1915), that go back as far as to the beginning of the 20th century, provided an almost complete overview of the general repertoire of neurons in the insect optic lobe. Next to the photoreceptors R₁-R₆, at least 12 different classes of lamina affiliated neurons were found in house flies (Strausfeld, 1976), as well as in *Drosophila* (Fischbach and Dittrich, 1989). These 12 neurons can be subdivided into groups, according to the direction of information flow and anatomical arrangement. One group contains five feedforward lamina output neurons, L₁-L₅, another one is built up from 6 putative feedback neurons (T₁, Lat, Law₁, Law₂, C₂, C₃), and lastly, there is one lamina intrinsic cell (Lai). For the latter two groups, the anatomical layout is strikingly different from the first one. Here, cell bodies reside in the second optic ganglion, sending their projections upwards, and hence appear 'flipped' by 180° compared to L₁-L₅, suggesting a feedback role instead of feedforward (Tuthill et al., 2013). Some but not all neurons in this group span multiple columns and are thought to provide feedback from the subsequent optic ganglia. Although the anatomical details were laid out in exquisite detail by Fischbach and Dittrich (1989), only electron microscopy could shed light onto the intricate connectivity maps that form the lamina

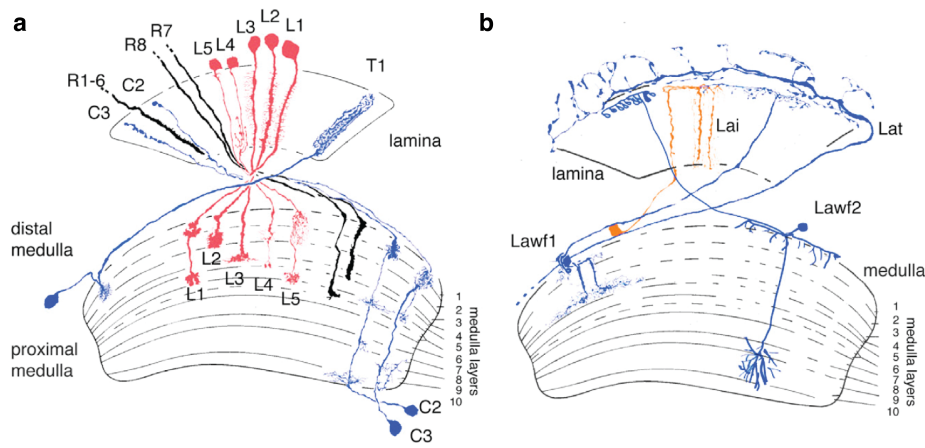


Figure 3: The *Drosophila* lamina neurons. **a** All columnar neurons with connections within the lamina. Photoreceptors R₁-R₆ are providing input from the retina. R₇+R₈ surpassing the lamina and projecting into the medulla. Putative feedforward neurons (L₁-L₅) are shown in red. Putative feedback neurons (C₂, C₃, T₁) are shown in blue. Each neuron exists once per column. **b**. Multicolumnar neurons that possess projections in the lamina are depicted. Multicolumnar neurons exist less than once per column, but the population of neurons of each cell type covers the entire visual field. Orange colored Lai (Lamina intrinsic neuron) is confined only within the lamina, whereas blue neurons (Lat, Lawf₁, Lawf₂) project from the medulla towards the lamina, likely providing feedback. The figure is taken with permission from Tuthill et al. (2013).

circuit. This made the fly lamina one of the anatomically best studied circuits (Takemura et al., 2017; Meinertzhagen and O’Neil, 1991; Rivera-Alba et al., 2011).

Physiologically, L₁ and L₂ are the most thoroughly characterized neurons in the lamina circuit. Sharp electrode recordings in larger flies (e.g. the blowfly *Calliphora vicina*, *Calliphora stygia*, or the dragonfly *Hemicordulia tau*) (Laughlin and Hardie, 1978; Laughlin and Osorio, 1989) and calcium imaging in *Drosophila* (Clark et al., 2011; Reiff et al., 2010) surprisingly revealed identical response properties of both neuron types. The fact that both cells react in such a similar pattern becomes more intuitive when considering the tight electrical coupling of the two cell types (Joesch et al., 2010). Both cells hyperpolarize to flashes of light (ON) and depolarize to the offset (OFF) of such a stimulus. This response, opposite to that of the photoreceptors, can be readily explained by the presence of the histamine-gated chloride channel *ort*, which effectively leads to a sign inversion of the respective photoreceptor response (Hardie, 1989). Importantly, lamina cells are not selective for the direction of visual motion. An additional difference between photoreceptors and L₁+L₂ signal becomes apparent when comparing their temporal filter properties. In a high luminance regime, for instance, L₁ and L₂ cells keep responding maximally, when stimulated with light modulating sinusoidally at 60-80 Hz, while photoreceptor responses already drop to \approx 50 % of their initial response amplitude (Straka and Ammermüller, 1991). When recorded with a sharp electrode at the soma, all lamina monopolar cells exhibit graded potentials (Laughlin and Hardie, 1978; Laughlin, 1981;

Laughlin and Osorio, 1989), but spikes have been recorded in the first optic chiasm of the blowfly *Calliphora vicina* between lamina and medulla, without knowing the identity of individual cells (Jansonius and Van Hateren, 1991, 1993a,b). Furthermore, L2 receptive fields possess an inhibitory antagonistic surround, thereby altering the spatial response properties of the cell (Freifeld et al., 2013). Although electrically the two cells react indistinguishably, something striking is happening at the axon terminals of L1 and L2 cells. Here, the motion vision pathway is split into two separate channels, one for the motion of luminance increments (ON) and the other for the motion of luminance decrements (OFF) (Joesch et al., 2010; Eichner et al., 2011; Strother et al., 2014; Behnia et al., 2014). While L2 releases acetylcholine, an excitatory neurotransmitter, L1 releases glutamate which in invertebrates, can act as an inhibitory neurotransmitter (Cully et al., 1996; Liu and Wilson, 2013; Mauss et al., 2014).

Genetically blocking the output of L1 neurons renders motion-sensitive lobula plate tangential cells (LPTC, see Section 1.2.3) unresponsive to ON motion. Blocking L2 cells abolishes the responses of LPTCs to OFF motion (Joesch et al., 2010). This result was confirmed by behavioral experiments, where the ability of walking flies to follow either ON or OFF motion was impaired when blocking either L1 or L2, respectively (Clark et al., 2011; Maisak et al., 2013). Permanently hyperpolarizing (via *Kir2.1*) L1 and L2 together renders the flies completely motion blind (Tuthill et al., 2013; Bahl et al., 2013). Hence, both cells are required for motion vision.

Recently developed genetically encoded calcium indicators have provided access to other *Drosophila* lamina monopolar cells. In contrast to L1 and L2, L3 and L4 do not receive direct photoreceptor input. Instead, input is provided by other lamina cells and downstream medulla neurons. Whereas L3 reacts with a much more sustained response, L4 possesses temporal characteristics similar to L1 and L2 (Meier et al., 2014; Silies et al., 2013).

Permanently hyperpolarizing L2 and L4 reduces the fly's ability to follow progressive motion. Additionally to the neurons in the repetitive lamina cartridges, the lamina also receives input from downstream partners (C2, C3, T1) that are thought to provide feedback from subsequent downstream circuits in the medulla. Silencing these neurons drastically impairs the fly's reaction to regressive motion (Tuthill et al., 2013). Lastly, lamina wide-field neurons respond to slow luminance changes, suggesting a neuromodulatory role (Tuthill et al., 2014).

1.2.2 Medulla

The medulla consists of 10 layers, M1 to M10. Cell types increase in variety, such that one single column houses more than 60 different cell types (compared to 12 cell types in one lamina cartridge). Based on their anatomical structure, the columnar medulla neurons can be grouped into medulla intrinsic (Mi), transmedulla (Tm), and transmedulla Y (TmY) cells. While Mi cells connect different layers within the medulla, Tm cells arborize in the medulla layers of various layers as well as in the lobula. Lastly, TmY cells bifurcate, connecting the medulla to the subsequent optic ganglia, the lobula, and the

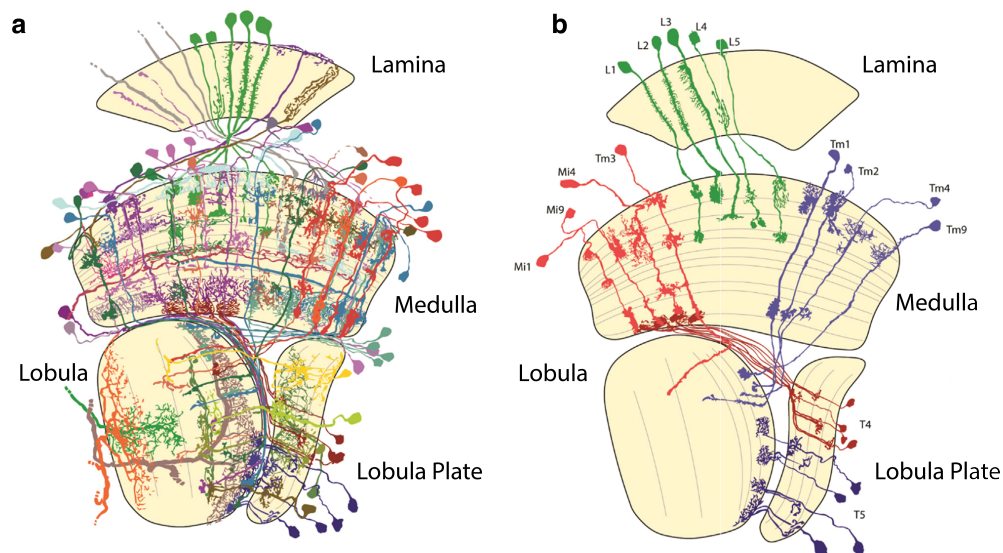


Figure 4: Anatomy of columnar neurons in the fly optic lobe. **a** Morphology of abundant cell types, reproduced from [Fischbach and Dittrich \(1989\)](#). **b** Columnar cell types in the motion vision circuit. Used with permission from [Borst et al. \(2020a\)](#).

lobula plate. Via staining, it is possible to extract valuable information about the anatomical structure of individual cell types. How these neurons are connected, however, has long remained a matter of speculation. Over the past decade, electron microscopy has resolved medulla circuitry completely ([Takemura et al., 2008, 2011, 2013, 2017](#)). However, none of the connectomic studies report the connections of multicolumnar neurons (such as Dm cells).

Using serial-section transmission EM (ssTEM), [Takemura et al. \(2013\)](#) found a spatial offset of about 1° between Mi1 and Tm3 cells when aligning the receptive field centers of both cell types along the preferred direction of the postsynaptic T4 cell. Around the same time [Behnia et al. \(2014\)](#) accomplished, to date, the only patch-clamp electrophysiology recordings in columnar medulla neurons. Importantly, none of the medulla cells were found to be direction-selective. The authors found a temporal offset between the two main inputs to T4 cells (Mi1 & Tm3) of 18 ms. Since any model for motion detection (see Section 1.3) requires a spatial and a temporal offset between the inputs the authors suggested that Mi1 & Tm3 are the neural substrates of the inputs to the *Drosophila* ON motion detector ([Behnia et al., 2014; Takemura et al., 2013](#)). Both, the spatial as well as the temporal offset, however, seem surprisingly small considering the high degree of direction selectivity measured in T4 cells ([Maisak et al., 2013](#)).

By constantly hyperpolarizing either of the two cell types individually (via *Kir2.1*) and simultaneously recording from large motion-sensitive lobula plate tangential cells (LPTC), [Ammer et al. \(2015\)](#) found that only Mi1 is required for ON motion along the preferred direction across all stimulus regimes. Importantly, blocking Tm3 only affects LPTC responses to higher stimulus velocities but leaves responses to lower velocities unaltered. This result was confirmed by behavioral experiments in the same study. This led to the conclusion, that Mi1 and Tm3 cannot be the only inputs to the ON

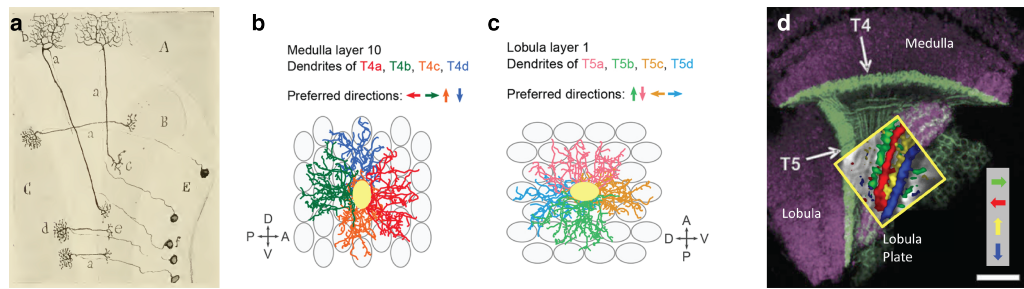


Figure 5: T4 and T5 cells. **a** First drawing of the *curiosos elementos* (T4 and T5 cells). Drawings of Golgi stainings made in the optic lobe of the horsefly. Taken from [Ramón y Cajal and Sánchez \(1915\)](#) **b** Schematic of T4 cell dendrite orientation. Frontal view of medulla layer 10. Four T4 subtype dendrites enter a single medulla column, extending along four distinct directions. **c** Same as in **b** only for T5 cells. Pictures in **b** and **c** taken with permission from [Hoermann et al. \(2020\)](#) **d** Confocal image of T4/T5 cells expressing GFP (green). In the inset, the four layers in the lobula plate are colored according to the preferred direction of the different subtypes, revealed by 2-photon calcium imaging. Scale bar = 20 μm . Picture adapted with permission from [Borst and Helmstaedter \(2015\)](#).

elementary motion detector, since taking out only one alone was not enough to result in ON motion blindness.

In the OFF pathway [Meier et al. \(2014\)](#) published first reliable recordings of identified medulla interneurons in *Drosophila*. [Meier et al. \(2014\)](#) used genetically encoded calcium indicators to characterize the response properties of the transmedulla neuron Tm2 (additionally to L4). By blocking the synaptic output (via *shibire^{ts}*), they proved this neuron to be an essential component in the OFF motion vision pathway.

In light of new connectomic data for both ON ([Takemura, 2015](#)) and OFF ([Shinomiya et al., 2014](#)) pathways, it is an interesting subject to complete the physiological roles of newly discovered neurons in the circuit (e.g. Mi4 and Mi9).

1.2.3 Lobula complex

The lobula complex consists of two neuropils: the lobula and the lobula plate. The lobula consists of 6 and the lobula plate of four layers. In the OFF motion vision pathway, the Tm cells (Tm1, Tm2, Tm4, Tm9) ramify in a layer-specific manner. While Tm cells differ anatomically, all four neurons share a connection to T5 dendrites in the first layer of the lobula ([Shinomiya et al., 2014](#)).

T4T5 CELLS In the most proximal layer of the medulla, M10, and the first layer of the lobula, two interesting cell types reside; the bushy T cells T4 & T5. Their first anatomical descriptions were already made by [Ramón y Cajal and Sánchez \(1915\)](#) (Figure 5 a). There are four subtypes of T4 and T5 cells (T4a-T4d, T5a-Td) that connect the medulla (T4) and the lobula (T5) to the lobula plate. Each subtype's dendrite is anatomically oriented in one of the four cardinal directions (See Figure 5 b,c) ([Fischbach and Dit-](#)

trich, 1989; Ramón y Cajal and Sánchez, 1915; Strausfeld, 1976). Each T4 and T5 subtype arborizes specifically in one of the four layers of the lobula plate (Figure 5 d) (Fischbach and Dittrich, 1989). T4 and T5 cells are the first cells in the circuit that respond in a direction-selective manner (Maisak et al., 2013). This had been a subject of speculation for long based on deoxy-glucose experiments, where flies were presented with patterns moving in only one particular direction. Deoxy-glucose would only label cells that were active during the stimulus presentation. Depending on the direction in which the stimulus was presented, different subtypes of T4 and T5 cells were marked, making them top candidates for being the elementary motion detectors (Buchner et al., 1984; Bausenwein and Fischbach, 1992; Bausenwein et al., 1992). The final proof that these cells are direction-selective was found by *in vivo* 2-photon calcium imaging experiments. It could be shown that each subtype of T4 and T5 cells respond preferentially to one of the four cardinal directions, which are front-to-back (T4T5a), back-to-front (T4T5b), upward (T4T5c), and downward (T4T5d) motion. Furthermore, when presented with stimuli where the motion contains only one contrast polarity, T4 cells respond only to ON motion and T5 cells only to OFF motion (Figure 5 d) (Maisak et al., 2013). Blocking both T4 and T5 cells abolishes responses to motion in subsequent motion-sensitive lobula plate tangential cells (Schnell et al., 2012), impairs the optomotor response of tethered flies walking on a styrofoam ball (Bahl et al., 2013), cancels the tethered flight escape behavior when confronted with a looming stimulus (Schilling and Borst, 2015), and, finally, reduces the fly's ability to maintain a straight flight path (Leonte et al., 2021). Taken together, these experiments suggest that T4 and T5 cells are the key players in conveying motion information to the downstream circuits that drive behavior.

LPTC In the lobula plate, T4 and T5 provide excitatory input onto large lobula plate tangential cells (LPTC) and lobula plate intrinsic neurons (LPi). LPTC dendritic trees span large areas of the lobula plate, sometimes over the range of the entire layer. Consequently, their receptive fields cover a large part of the visual field. More than 60 different types of neurons can be attributed to that group, together forming a heavily intertwined network of electrical and chemical synaptic connections (for review see (Borst et al., 2010)). LPTCs were anatomically and physiologically described in detail in larger flies like *Calliphora vicina* (Hausen, 1976, 1982a,b; Hengstenberg, 1982) but also to a smaller extent in *Drosophila* (Fischbach and Dittrich, 1989; Hopp et al., 2014; Haikala et al., 2013; Fujiwara et al., 2017; Maimon et al., 2010).

LPTCs can be grouped:

- according to anatomical ramification, i.e. whether the cells project within the same brain hemisphere (ipsilateral) or whether the axons are sent over to the contralateral side;
- based on whether they respond to stimulation with graded potentials, or an increase in spike rate, or both;
- based on their visual response characteristics, i.e. whether they primarily respond to motion in the horizontal or the vertical plane;

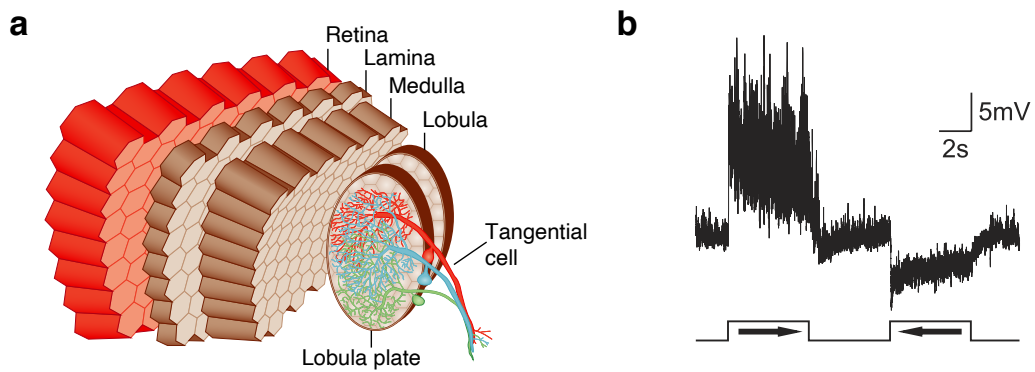


Figure 6: Lobula plate tangential cells. **a** Schematic of the fly visual system. Retina, lamina, medulla, and lobula complex are arranged in a hexagonal grid structure. In the lobula plate, the anatomy of 3 different HS cells is depicted. Schematic from [Borst \(2014\)](#) **b** Electrophysiological recording of an HS-N cell. The cell depolarizes to a vertical sine grating moving from front to back and hyperpolarizes to motion in the opposite direction. The cell is therefore direction-selective and motion-opponent. Arrows denote the direction towards which the grating was moving. Insets show stimulus onset and offset. Recording from [Schnell et al. \(2010\)](#).

- or if they process local or global motion cues (for an extensive review see ([Borst and Haag, 2002](#))).

Regarding their response characteristics, *Drosophila's* LPTCs can be divided into two major groups. Horizontal system (HS) and the vertical system (VS) cells. At least three different HS cells (tiling the layer into "south", "equatorial" and "north": HS-N, HS-E, HS-S) and 6 VS (VS1-6) cell types (plus 3 VS like cells), as well as dorsal and the ventral centrifugal horizontal (dCH and vCH) cells were identified in the fruit fly. Their large dendritic stratifications in the lobula plate, some sampling from over 100 columns, are layer-specific. HS cells, for instance, mainly receive input from layer 1, therefore processing visual motion information in the horizontal plane. VS cells, on the other hand, mainly ramify in layer 4 (but some also additionally stratify to other layers) and process vertical motion information ([Boergens et al., 2018](#); [Joesch et al., 2008](#); [Schnell et al., 2010](#); [Wei et al., 2020](#)).

Lobula plate tangential cells depolarize when presented with motion along their preferred direction (PD) and hyperpolarize when presented with motion in the null direction (ND), thus exhibiting motion opponency (Figure 6 b) (for review see ([Borst and Haag, 2002](#))). This is a result of integrating excitatory input from T4 and T5 cells from one layer in the lobula plate and subtracting the input from the adjacent layer. The preferred direction is dependent on the location of the dendrites. Combining all preferred directions onto the dendritic tree, a complex vector pattern arises, so-called flow-fields ([Gibson, 1950](#)) that describe the optimal pattern of motion that results from ego-motion, such as walking or flight. Thus, LPTCs can be seen as specialized filters for the detection of optic flow patterns that emerge from ego-motion ([Krapp and Hengstenberg, 1996](#)).

LPT1 Blocking the output T4 and T5 cells not only abolishes depolarization of LPTCs when stimulated with motion along their preferred direction (PD)

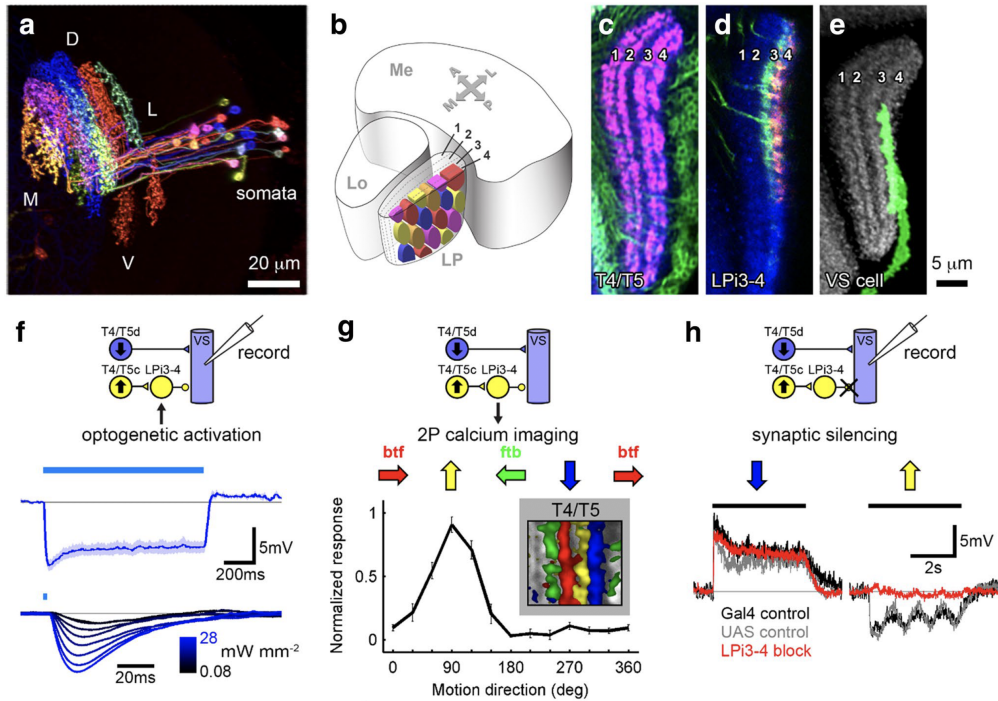


Figure 7: Lobula plate intrinsic neurons (LPi). **a** Multi-color flip-out of LPi₃₋₄ cells. Each color represents one cell covering one part of the visual field. For orientation: D = dorsal, V = ventral, L = lateral, M = medial. **b** Schematic of a cross-section through the optic lobe. Note that cells only cover layers 3+4. **c** Horizontal cross-section of the lobula plate showing T4 and T5 cells expressing GFP (green) and a presynaptic marker in violet (synaptotagmin-HA). Axon terminals in violet reveal the layered structure of the lobula plate. **d** Expression of GFP (green) and synaptotagmin-HA (red) in LPi₃₋₄ cells. Note that these cells exclusively have presynaptic terminals in layer 4. **e** GFP staining of a VS cell dendrite in layer 4 of the lobula plate. **f** Top: schematic of the putative circuit wiring diagram between T4/T5c+d cells, LPi₃₋₄, and VS cells. The electrode in VS cells stands for patch-clamp recordings at the cell body. Middle: While constant optogenetic activation (1 s) of LPi₃₋₄ cells VS cells hyperpolarize in a sustained manner. Bottom: Differently strong brief pulses (2 ms) of light are delivered. With increasing light intensity (from black to blue, in mW/mm²) the amplitude and latency of the response increases. **g** LPi cells are direction-selective. Calcium activity of LPi₃₋₄ neurons after presentation with moving gratings in different directions. Normalized responses show a clear preference for upward motion. Note that this is the same preference that T4/T5c cells do in the same layer (Inset). **h** Silencing LPi₃₋₄ cells abolishes electrical null direction responses in VS cells recorded in patch-clamp. Figure taken with permission from [Borst et al. \(2020b\)](#).

response) but also affect the hyperpolarization when stimulated with motion along their null direction (ND response, see Figure 6 b) the same way (Schnell et al., 2012). Furthermore, when T₄ and T₅ are optogenetically activated, LPTCs respond with a fast excitation followed by inhibition (Figure 7 f, (Mauss et al., 2014)). Both of these findings suggest that T₄ and T₅ cells not only provide excitation but also indirect inhibition from the adjacent lobula plate layer onto LPTCs. Lobula plate intrinsic neurons (LPi) are prime candidates for this task since they bi-stratify in a layer-specific manner, such that dendrites from one subtype exclusively reside in one and axons in the neighboring layer. Equivalent to the T₄/T₅ cells, at least two subtypes of LPis exist: LPi₃₋₄, and LPi₄₋₃, each receiving excitation from T₄/T₅ cells in one layer and providing feedforward glutamatergic inhibitory input via the glutamate-gated chloride channel *GluCl α* to LPTC dendrites in the adjacent layer. As 2-photon calcium imaging experiments revealed, LPis are direction-selective (Figure 7 g, (Mauss et al., 2015)) and have the same preferred direction as the T₄T₅ cells from which they receive input. Taken together, lobula plate tangential cells thus integrate local direction-selective information twice. One could ask: why twice? As mentioned above, LPTCs are selective for flow-fields that emerge when maneuvering through the world (Krapp and Hengstenberg, 1996; Krapp et al., 2001). VS cells, for instance, are mainly selective for uniformly downward moving flow fields that arise when the fly is lifting itself upward during flight. The retinal image will consequently move downward. Moving straight forward, however, produces an expanding flow field. Here, the VS cell will receive opposite directional information in different parts of its receptive field that will lead to a cancellation of the response since one is excitatory (T₄/T₅) and the other inhibitory (LPi). Blocking LPis strongly reduces the flow-field selectivity of VS cells. By subtracting motion-opponent signals, LPis are thus essential for increasing flow-field selectivity (Mauss et al., 2015).

1.3 MODELS OF MOTION DETECTION

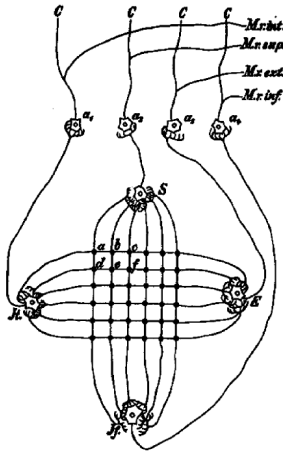


Figure 8: Schematic of the "center for optic motion perception". Retinal fibers feed into the summation points S, E, J_t , and J_t that are connected via differently long retinal fibers. The different lengths of the cables illustrate different lengths of time needed for the signal to travel. The first delay and compare mechanism for motion detection. With permission from Exner (1894).

same for both directions.

The Hassenstein-Reichardt correlator

One such elementary motion detector was proposed in 1956 by Bernhard Hassenstein and Werner Reichardt (Hassenstein, 1951; Hassenstein and Reichardt, 1956). From behavioral experiments with the snout weevil *Chlorophanus viridis* they concluded that the non-linear interaction must be multiplicative. This model is now referred to as the *Hassenstein-Reichardt (HR) correlator*, *Reichardt detector*, or *elementary motion detector*. For the sake of simplicity, I will only use the abbreviated term *HR correlator*.

Several computational models in the literature are dealing with the question: how does one single unit compute the direction of motion? The earliest example goes back to the late 19th century from Exner (1894) seen in Figure 8. Many ideas have been brought forward in the past decades. Purely algorithmic approaches have been made and tested experimentally on the behavioral level or at the level of single neurons.

Elementary motion detectors must fulfill three major requirements (Borst and Egelhaaf, 1989):

1) Spatial offset

At least two input units are required that must be spatially separated. One needs two points in space that can be compared. A single point cannot give information about the direction of motion.

2) Temporal asymmetry

At least one of the inputs must be delayed in time compared to the other one. Otherwise, the input signals arrive to the subsequent stage at the same time, independent of the direction of the stimulus.

3) Non-linear interaction

Inputs signals must be nonlinearly integrated at the subsequent stage. If this were not the case, the output of the detector would, on average, be the

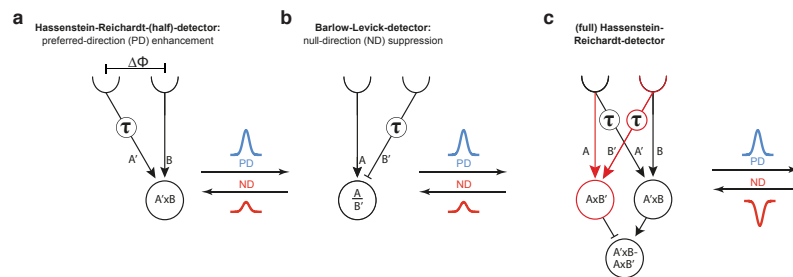


Figure 9: Classical correlation type models for motion detection. Input units are separated by an angle $\Delta\Phi$. One input signal is delayed in time by τ . Signals are non-linearly integrated in the subsequent stage. **a** Multiplicative half detector unit after [Hassenstein and Reichardt \(1956\)](#). **b** Divisive half detector unit by [Barlow and Levick \(1965\)](#). Note that both detectors result in the same directionally selective output signal (i.e. large positive signal in PD = blue curve and smaller response in ND = red curve). **c** Full HR-correlator: Two mirror-symmetric subunits of the HR-correlator are combined. After the multiplication stages, the two subunit output signals are subtracted from each other, resulting in a motion opponent detector, which responds positively when stimulated in PD (blue curve) and negatively when stimulated in ND (red curve). Modified and used with permission from [Arenz et al. \(2017\)](#).

In this model two spatially offset input signals, one of which is delayed in time compared to the other one, are subsequently integrated in a multiplicative manner. Stimulating the detector in one direction (the so-called preferred direction = PD) leads to a greater signal than when stimulated in the other direction (null direction = ND) ([Hassenstein and Reichardt, 1956](#)). This is simply because the overlap of the input signals is greater for one case compared to the other. A subsequent multiplication of those signals, therefore, leads to an enhanced response (preferred direction enhancement). Stimulation in the other direction results in a smaller response since the two incoming input signals are offset from each other. A multiplication of those two signals will lead to a smaller response (Figure 9 a). Combining two HR-subunits in a mirror-symmetric fashion and subtracting the output signals from each other, as depicted in Figure 9 c, results in a so-called *Full HR detector*. As a consequence, responses are motion-opponent, meaning that the detector produces positive output for PD stimuli and negative output for ND stimuli. Such an arrangement was necessary for a good match of behavioral ([Fermi and Reichardt, 1963](#); [Hassenstein and Reichardt, 1956](#); [Götz, 1964](#)) and electrophysiological ([Joesch et al., 2008](#); [Borst et al., 2010](#); [Haag et al., 2004](#)) responses in invertebrates.

Barlow-Levick correlator

A similar approach for achieving direction selectivity is taken by the Barlow-Lewick (BL) detector. Two input signals are separated in space and one input is temporally filtered, while the other one passes on a 'direct' unfiltered signal. Instead of multiplying the two signals, as in the HR-correlator, the Barlow-Levick detector uses division as the non-linear operation ([Barlow and Levick, 1965](#)). Here, the signal on the other side of the detector

(null side) is delayed. Therefore, when stimulated in the preferred direction, the overlap of the signal at the non-linear stage is small and leads to a large response. Stimulation in the other direction results in greater overlap. Dividing these signals, therefore, suppresses the null-direction response (Figure 9 b).

Both detector types can be discriminated experimentally with a clever stimulus design called apparent motion (Schuling et al., 1989; Egelhaaf et al., 1992; Eichner et al., 2011; Fisher et al., 2015a; Haag et al., 2016). Instead of constant movement, stimuli are presented in discrete consecutive steps. When the response is larger to a stimulus moving in the preferred direction, compared to the added responses when stimuli are presented in isolation, a preferred direction enhancement is in place. This speaks in favor of an HR-correlator. If, on the other hand, the response of a given cell is smaller when stimulated along the null direction, compared to isolated stimulation, then a null direction suppression mechanism is present (Barlow-Levick correlator).

Hybrid detectors

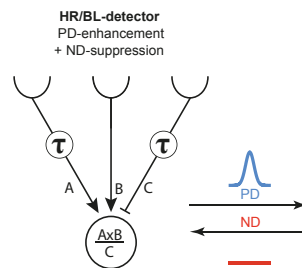


Figure 10: Hybrid detector consisting of one HR and one BL unit. Signals are sampled at three different points in space. The outer two arms of the detector are delayed in time (τ = Delay). In the subsequent stage input signals from the detector arms A and B are multiplied, and divided by the signal from C. Stimulation of the detector along the preferred direction results in a positive response (blue curve); stimulation in the null direction leads to zero response. Modified and used with permission from (Arenz et al., 2017).

In *Drosophila*, such apparent motion experiments were performed in T4 and T5 cells (Haag et al., 2016, 2017; Fisher et al., 2015a). By genetically expressing calcium indicators and precisely delivering visual stimuli to individual lamina cartridges via a telescopic aperture, Haag et al. (2016) found both mechanisms in place in T4 and T5 cells. Both mechanisms create direction selectivity, although at different locations in the receptive field (Haag et al., 2016, 2017; Leong et al., 2016). Sequences of apparent motion moving in the preferred direction of the cell amplify the signal from the first to the second position, i.e. on the preferred side of the receptive field. Conversely, the signal is only suppressed on the null side (i.e. from position C->B) of the receptive field when the stimulus moves along the null direction. Consequently, a new model was proposed, combining both an HR-correlator and a BL-correlator subunit to create direction selectivity in T4 and T5 cells (Figure 10). This detector has three instead of only two input lines, two instead of one of which are filtered in time and, lastly, at the non-linear stage,

the signals are multiplied and divided. This ensures a higher degree of direction selectivity, which better matches physiological data from 2-photon calcium imaging (Haag et al., 2016). For instance, whereas the original two-arm model of Hassenstein and Reichardt needed two subunits and an additional subtraction stage to completely shut down null direction responses, the three-arm detector achieves that one stage earlier (Figure 10).

1.4 CONCLUDING REMARKS

At the start of my Ph.D. in 2016, physiological evidence for T4 and T5 cells being the elementary motion detectors in the fly visual system was already provided. Despite a rather extensive physiological characterization of T4 and T5, the upstream input elements remained poorly understood. While the visual response properties of Mi1 & Tm3, for the ON-pathway, and Tm1 & Tm2, for the OFF, had been electrophysiologically described, it became clear that at least for the ON pathway Mi1 and Tm3 could not be the sole ‘two arms’ of the motion detector. Furthermore, a more complete set of EM connectomic data supported the hypothesis that there are more than two inputs to the *Drosophila* motion detectors. Additional 2-photon calcium imaging experiments revealed that, in fact, two complementary mechanisms create direction selectivity by precisely applying apparent motion stimuli onto individual visual units. A new model was proposed that requires at least three different inputs. But how do the inputs map onto the newly proposed model? In the first Manuscript 2.1, we combined white noise stimulation, 2-photon calcium imaging, and reverse correlation to characterize the spatial and temporal receptive fields of all putative input elements to T4 and T5 cells, two of which (Mi4, Mi9) have not been described before.

Since all cells were measured with the same stimulus, we now had a good filter bank at hand, to simulate the optimal positioning of each input filter in a model for the best fit to the T4 and T5 data. Intriguingly, the proposed positioning later matched the anatomical arrangement of input synapses on the dendrites of T4 cells (for T5 cells, results were less clear).

Knowing the response properties of the inputs and the anatomical arrangement of the synapses, it was time to zoom in from the cellular level onto the level of the T4 cell membrane. More questions arose: what neurotransmitters are being used by the inputs? What receptors are being expressed? How does this orchestrate direction selectivity at the biophysical level?

One input on the dendritic tips of T4 cells, Mi9, was particularly interesting, since it had an OFF-center receptive field despite being located in the ON pathway. In the Manuscript 2.2, we were able to confirm the glutamatergic transmitter phenotype of this cell and with the help of new tools to directly measure its transmitter output with high temporal precision. This work has to be seen as a mosaic piece in understanding the biophysical mechanism that creates direction selectivity.

Finally in the last Manuscript 2.3, we dealt with the question of why the behavior of the fly stays robust despite the variability of visual parameters in naturalistic environments, where the motion detector model is the same, but

its input signals become normalized. Our findings led to three publications in peer-reviewed journals.

2 | PUBLICATIONS

2.1 THE TEMPORAL TUNING OF THE DROSOPHILA MOTION DETECTORS IS DETERMINED BY THE DYNAMICS OF THEIR INPUT ELEMENTS

SUMMARY Detecting the direction of motion contained in the visual scene is crucial for many behaviors. However, because single photoreceptors only signal local luminance changes, motion detection requires a comparison of signals from neighboring photoreceptors across time in downstream neuronal circuits. For signals to coincide on readout neurons that thus become motion and direction selective, different input lines need to be delayed with respect to each other. Classical models of motion detection rely on non-linear interactions between two inputs after different temporal filtering. However, recent studies have suggested the requirement for at least three, not only two, input signals. Here, we comprehensively characterize the spatiotemporal response properties of all columnar input elements to the elementary motion detectors in the fruit fly, T4 and T5 cells, via two-photon calcium imaging. Between these input neurons, we find large differences in temporal dynamics. Based on this, computer simulations show that only a small subset of possible arrangements of these input elements maps onto a recently proposed algorithmic three-input model in a way that generates a highly direction-selective motion detector, suggesting plausible network architectures. Moreover, modulating the motion detection system by octopamine-receptor activation, we find the temporal tuning of T4 and T5 cells to be shifted toward higher frequencies, and this shift can be fully explained by the concomitant speeding of the input elements.

AUTHORS Alexander Arenz, Michael S. Drews (co-first-author), **Florian G. Richter**, Georg Ammer and Alexander Borst

CONTRIBUTIONS A.A., M.S.D., and A.B. conceived the study and designed the experiments. A.A. conducted and analyzed the measurements of T4/T5 cell responses. M.S.D. designed the projector-based stimulation arena and performed and analyzed the measurements of the OFF-pathway elements. **F.G.R.** performed and analyzed the experiments describing the ON-pathway neurons. G.A. performed and analyzed the patch-clamp recordings from lobula plate tangential cells. M.S.D. performed the computer simulations. A.A. wrote the manuscript with the help of all authors.

The Temporal Tuning of the *Drosophila* Motion Detectors Is Determined by the Dynamics of Their Input Elements

Highlights

- Input neurons to the fly motion detectors show diverse temporal filter properties
- Octopamine activation accelerates detector velocity tuning and input cell dynamics
- Dynamics of input neurons correctly predict velocity tuning of motion detectors

Authors

Alexander Arenz, Michael S. Drews, Florian G. Richter, Georg Ammer, Alexander Borst

Correspondence

arenz@neuro.mpg.de

In Brief

Recent algorithmic models of visual motion detection in the fly rely on processing of three input channels. By characterizing the spatiotemporal response properties of the neurons presynaptic to fly motion-sensing cells across two tuning states, Arenz, Drews, et al. predict functional roles for these neurons in computing the direction of motion.



CrossMark

Arenz et al., 2017, Current Biology 27, 929–944
April 3, 2017 © 2017 Elsevier Ltd.
<http://dx.doi.org/10.1016/j.cub.2017.01.051>

CellPress

The Temporal Tuning of the *Drosophila* Motion Detectors Is Determined by the Dynamics of Their Input Elements

Alexander Arenz,^{1,2,3,*} Michael S. Drews,^{1,2} Florian G. Richter,¹ Georg Ammer,¹ and Alexander Borst¹¹Department of Circuits—Computation—Models, Max Planck Institute of Neurobiology, Am Klopferspitz 18, 82152 Martinsried, Germany²Co-first author³Lead Contact*Correspondence: arenz@neuro.mpg.de<http://dx.doi.org/10.1016/j.cub.2017.01.051>

SUMMARY

Detecting the direction of motion contained in the visual scene is crucial for many behaviors. However, because single photoreceptors only signal local luminance changes, motion detection requires a comparison of signals from neighboring photoreceptors across time in downstream neuronal circuits. For signals to coincide on readout neurons that thus become motion and direction selective, different input lines need to be delayed with respect to each other. Classical models of motion detection rely on non-linear interactions between two inputs after different temporal filtering. However, recent studies have suggested the requirement for at least three, not only two, input signals. Here, we comprehensively characterize the spatiotemporal response properties of all columnar input elements to the elementary motion detectors in the fruit fly, T4 and T5 cells, via two-photon calcium imaging. Between these input neurons, we find large differences in temporal dynamics. Based on this, computer simulations show that only a small subset of possible arrangements of these input elements maps onto a recently proposed algorithmic three-input model in a way that generates a highly direction-selective motion detector, suggesting plausible network architectures. Moreover, modulating the motion detection system by octopamine-receptor activation, we find the temporal tuning of T4 and T5 cells to be shifted toward higher frequencies, and this shift can be fully explained by the concomitant speeding of the input elements.

INTRODUCTION

The detection of visual motion arising from ego-motion is crucial for course stabilization in flies [1]. Sets of large tangential cells in the lobula plate of the fly optic lobe respond selectively to the optic flow resulting from whole-body rotation around different axes. As single photoreceptors respond to local luminance

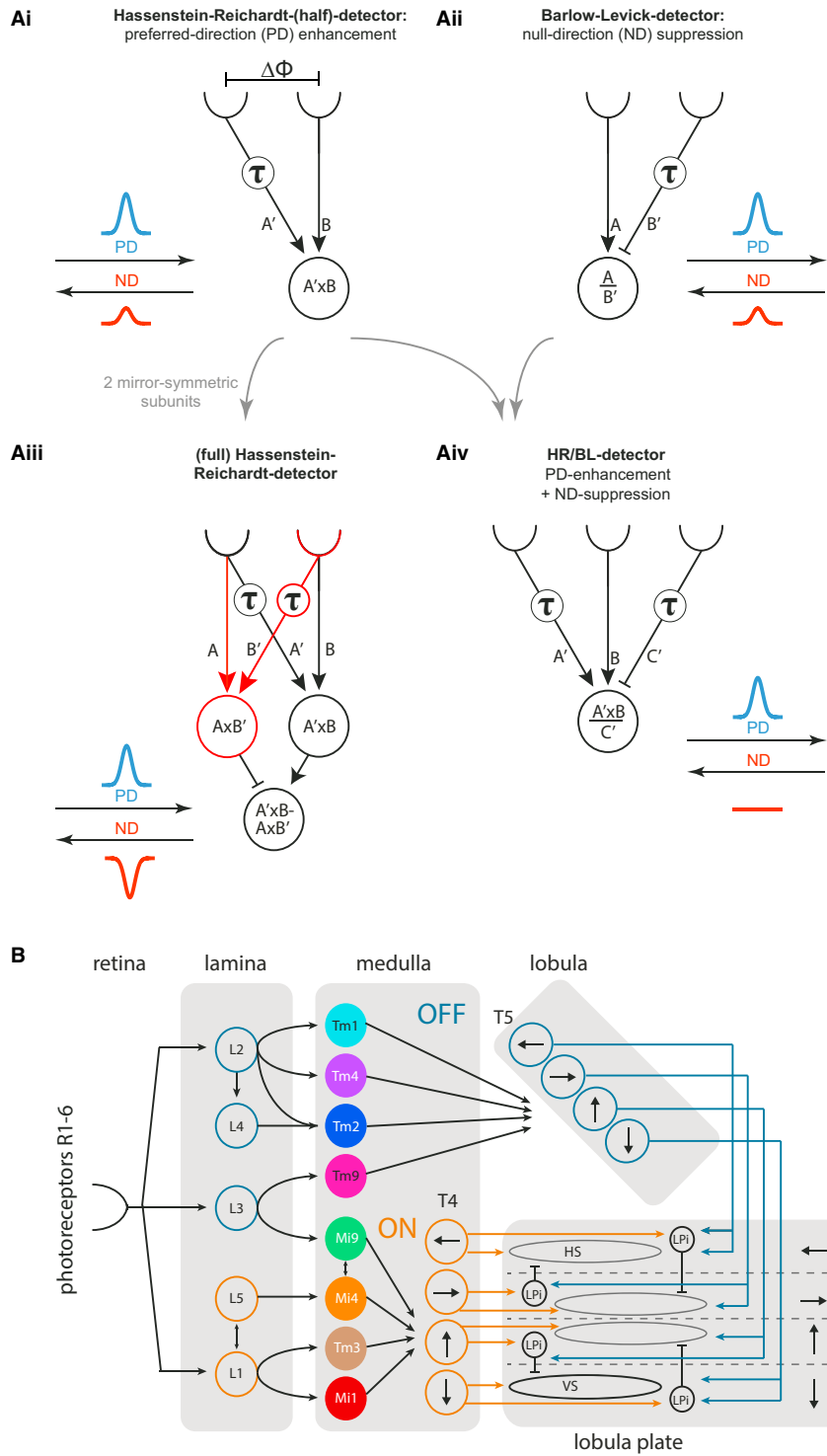
changes in a non-direction-selective way, the intervening circuitry of the optic lobe [2–5] (Figure 1) must serve to extract the feature of visual motion by spatiotemporal comparison of the responses of neighboring photoreceptors.

Two competing algorithmic models of motion detectors have been proposed (Figure 1A). Both models rely on asymmetric temporal filtering of two input signals that are then fed into a non-linearity. They differ by the type of non-linearity employed and the location of the delay filter. In the Barlow-Levick (BL) detector (Figure 1Aii) [6], the delay is located on the preferred side and the non-linearity is inhibitory, leading to a suppression of signals moving in the null direction (ND). In the Hassenstein-Reichardt (HR) detector (Figure 1Ai) [7], the delay is located on the null side and the non-linearity is excitatory, leading to an enhancement of signals moving in the preferred direction (PD). In the full HR detector (Figure 1Aiii), two of those subunits, or half-detectors, are arranged in a mirror-symmetric fashion and subtracted from each other to yield a fully opponent detector (for review, see [8]).

How do the proposed elements of these algorithmic models map onto the neural circuits of the fly, and how does direction selectivity arise? The fly optic lobe consists of four neuropils downstream of the retina: the lamina, medulla, lobula, and lobula plate (Figure 1B). Photoreceptors synapse onto lamina monopolar cells. These lamina cells feed into two separate pathways encoding for different contrast polarities [9–11]: the ON pathway encodes brightness increments, and the OFF pathway encodes brightness decrements. In each pathway, the direction of visual motion is computed separately [12, 13]. In both pathways, lamina neurons connect onto a distinct set of medulla neurons. In the ON pathway, these medulla neurons have axon terminals in layer 10 of the medulla, where they overlap with the dendrites of T4 neurons [4]. In the OFF pathway, transmedulla neurons project to the lobula, where they synapse onto the dendrites of T5 neurons [5]. T4 and T5 neurons each fall into four subclasses, which respond selectively to visual motion in one of the four cardinal directions (front-to-back, back-to-front, up, and down) and project their axons according to this preference to one of the four layers of the lobula plate [14]. There, T4 and T5 cells converge and provide direct excitatory cholinergic input onto wide-field lobula plate tangential cells [15]. In addition, T4 and T5 cells synapse onto lobula plate intrinsic (LPI) neurons, which in turn inhibit tangential cells in the adjacent, oppositely tuned layer [16], making tangential cells fully motion opponent. Hence, T4 and T5



CrossMark



(legend on next page)

neurons would represent the half-detector units of the fully opponent motion detector model just before the subtraction stage. Although the HR detector describes the responses of lobula plate tangential cells well, the responses of T4 and T5 neurons are more directionally selective than would be expected for the half-detectors of the HR model [14, 17].

In the ON pathway, medulla intrinsic neuron 1 (Mi1) and transmedullary neuron 3 (Tm3) were originally suggested as the main inputs onto T4 neurons from electron-microscopic reconstructions [4]. These data showed a small spatial offset of about a fifth of a column, about 1° in visual space, between Mi1 and Tm3 synapsing onto the same T4 neuron, with Tm3 located toward the null side of the T4 neuron. Based on this spatial offset, two possible implementations of the motion detector were suggested: a HR correlator with Tm3, or a BL detector with Mi1, as the delayed arm. Subsequent patch-clamp recordings showed a small temporal delay of ~ 20 ms for Mi1 with regard to Tm3, as well as a similar temporal offset of Tm1 with respect to Tm2 in the OFF pathway [18]. This led to the suggestion of HR correlator implementations with Mi1 and Tm1 as the delayed and Tm3 and Tm2 as the direct arms in the ON and the OFF pathway, respectively [18, 19].

However, new findings from several recent studies question this model. First, new electron-microscopic circuit reconstructions show additional synaptic input from Mi4 and Mi9 cells onto T4 cells (Lou Scheffer, personal communication; https://web.archive.org/web/20150218101857/http://emanalysis.janelia.org/flyem_tables.php), and from the transmedulla neurons Tm4 and Tm9 onto T5 cells [5]. Second, when all four input cell types in the OFF pathway were considered, large differences in their temporal response kinetics to flashes of dark bars were revealed [20]. Whereas Tm1, Tm2, and Tm4 respond like band-pass filters with different time constants, Tm9 has the response characteristic of a pure low-pass filter, together forming a filter bank that lends itself well to the construction of motion detectors. Third, whereas blocking the synaptic output of Mi1 severely reduces responses of tangential cells to moving ON edges, blocking Tm3 output only affects responses to edges moving at higher angular velocities but leaves responses to lower velocities unchanged [21]. This again argues against Tm3 being one of the two arms of the motion detector under all conditions. Similarly, in the OFF pathway, all four cell types were shown to contribute to the detection of moving OFF edges. Blocking their synaptic output decreased the responses of downstream tangential cells and

reduced the optomotor response to OFF edges [20]. However, no blocks of single cell types or of two types in combination fully abolished the responses to dark edges, suggesting either redundancy or a more complicated implementation than previously suggested. Fourth, recent experiments based on the sequential stimulation of individual laminar cartridges revealed that the elementary motion detectors in the ON pathway, T4 neurons, implement ND suppression [17] in addition to PD enhancement [22] (Figure 1Aiv). Spatiotemporal receptive fields of T5 neurons are consistent with a similar model in the OFF pathway [23]. This more elaborate motion detector implementation could explain the high direction selectivity. However, in contrast to both HR and BL detectors, it relies on at least three input elements.

Taken together, in both pathways, evidence mounts for a neural implementation that is more complicated than either the BL or the HR model alone, and there is a multitude of combinations possible to place the known columnar input elements into the proposed algorithmic three-arm model of the *Drosophila* motion detectors.

In order to dissect the roles and contributions of individual cell types, it would be helpful to modify their temporal response dynamics and observe the effect on the downstream motion detectors. One remarkable property of tangential cells is that their velocity tuning is not fixed but dependent on the behavioral state of the fly, as has been observed in *Drosophila* and *Lucilia*. In walking [24] as well as in tethered flying flies [25, 26], the temporal-frequency tuning shifts toward higher frequencies, corresponding to higher velocities, potentially matching the expected change of the stimulus statistics from resting to active locomotion. The behavioral effect can be mimicked in resting flies by pharmacological activation of octopamine receptors with octopamine [26] or the octopamine agonist chlordimeform (CDM) [25, 27]. The physiological source of this neuromodulation is octopaminergic neurons that project to the medulla, lobula, and lobula plate [28, 29]. They become activated during flight and are both necessary and sufficient for the increase in responses to higher temporal frequencies [26]. Importantly, this change in the temporal tuning could be reproduced in computer simulations by decreasing the low-pass filter time constant in the HR detector [25], indicating that identifying the input elements that change their kinetics under octopamine activation might help to pinpoint their functional roles in the detector.

Figure 1. Theoretical Models for Visual Motion Detection and the Underlying Neuronal Circuitry

(A) Algorithmic models of motion detectors based on variations of a common theme of spatiotemporal correlations of local luminance changes detected by photoreceptors. (Ai) In the Hassenstein-Reichardt (HR) correlator (of which a half-detector is shown here), a delay (τ) on the first of two arms activated by motion in the preferred direction (PD) causes coincidence of the two signals from neighboring photoreceptors (separated by an angle, $\Delta\phi$). A multiplicative non-linearity results in a PD enhancement. (Aii) In the Barlow-Levick (BL) detector the delay is located on the opposite arm, and the non-linearity is suppressive/inhibitory, causing a null-direction (ND) suppression. (Aiii) In the full HR correlator, two mirror symmetric subunits from (Ai) are subtracted, resulting in a fully opponent detector, which not only depolarizes in PD but also hyperpolarizes in ND. (Aiv) A recently proposed model, based on the responses of T4 neurons to apparent motion stimuli, combines PD enhancement and ND suppression along the PD axis.

(B) Schematic of the circuitry of the *Drosophila* optic lobe showing neuron classes suggested to be involved in visual motion detection. Local luminance changes are detected by photoreceptors in the retina and relayed via lamina monopolar neurons (classes L1–L5) and medulla neurons (Mi1, Tm3, Mi4, Mi9, Tm1, Tm2, Tm4, and Tm9) to T4 and T5 neurons. The latter are the first neurons in the visual pathway that respond selectively to motion. Both T4 and T5 form four subtypes that respond to one of the cardinal directions and project accordingly to the four layers of the lobula plate, thus forming a map of visual motion directions. In the lobula plate, they synapse onto large-field tangential cells (horizontal system [HS] and vertical system [VS] cells), as well as onto lobula plate intrinsic (LPi) cells that in turn form inhibitory synapses onto tangential cells in the adjacent layer of opposite PD. This inhibition corresponds to the subtraction stage in the full HR correlator (Aiii) and endows lobula plate tangential cells with full motion opponency.

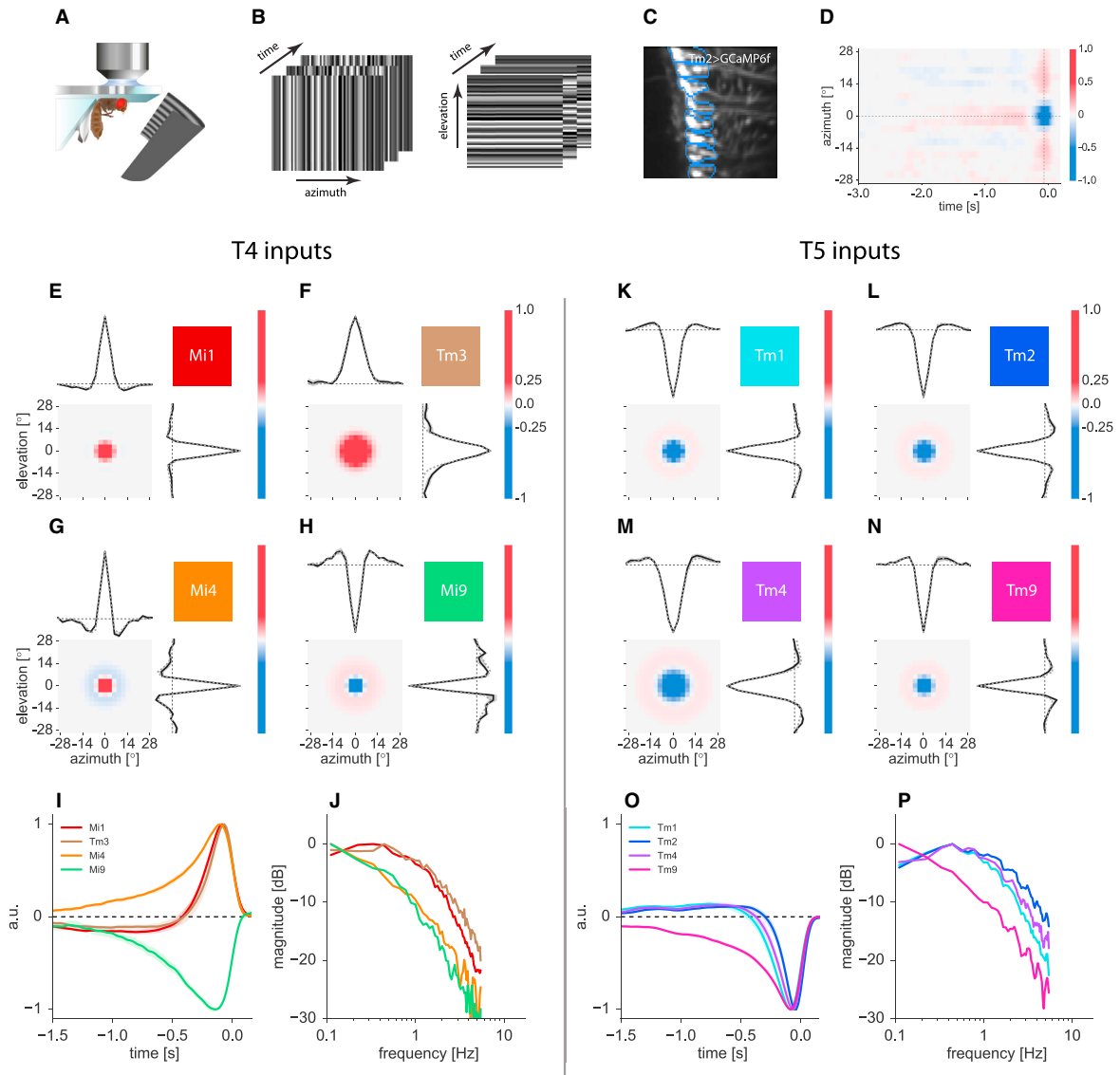


Figure 2. Response Properties of the ON- and OFF-Pathway Medulla Columnar Elements

(A) Two-photon calcium imaging of immobilized flies.

(B) Schematic of vertical (left) and horizontal (right) white-noise stimulus illustrated by three frames.

(C) Terminals of Tm2 neurons expressing the genetically encoded calcium indicator GCaMP6f. Regions of interest (ROIs) for the analysis of calcium indicator fluorescence changes encompass single terminals.

(D) Average aligned spatiotemporal receptive field of all Tm2 cells from (C) for a white-noise stimulus consisting of vertical bars. Along the vertical axis, the center-surround structure of the OFF-center receptive field is visible in the heat color code (vertical dashed line at the time of the peak of the response). The section along the time axis through the receptive field center reveals the temporal response kernel.

(E–H) Receptive fields of Mi1 (E), Tm3 (F), Mi4 (G), and Mi9 (H) for vertical (upper left) and horizontal (lower right) white-noise bar stimulation. From these, the two-dimensional receptive fields were constructed as a two-dimensional difference of Gaussians (Supplemental Experimental Procedures).

(I) Temporal kernels resulting from the reverse correlation of the calcium response with the white-noise stimulus for Mi1, Tm3, Mi4, and Mi9.

(J) Temporal kernels in frequency-space (constructed from the temporal kernels in (I)) revealing Mi1 and Tm3 as band-pass filters and Mi4 and Mi9 as low-pass filters. (For the measurements of the spatial receptive fields: Mi1: N = 5 flies, n = 35 cells; Tm3: N = 6, n = 37; Mi4: N = 5, n = 33; Mi9: N = 7, n = 29. For the determination of the temporal kernels twice as many measurements, from the horizontal and vertical one-dimensional noise stimulus, could be used.)

(legend continued on next page)

In this study, we comprehensively characterize the spatiotemporal response profiles of all known columnar input elements of both the ON and OFF motion detectors in the fruit fly *Drosophila melanogaster* and take advantage of the motion detectors' state-dependent tuning characteristics. Using computer simulations, we test which combinations of input elements result in the observed properties of T4 and T5 neurons and thereby narrow down their possible cellular implementation. In particular, we address the question of whether the response dynamics of the input elements are sufficient to yield realistic motion detectors, or whether additional mechanisms on the synaptic or dendritic level are required to further modify the dynamics of the input signals.

RESULTS

Characterization of the Columnar Input Neurons to T4 Cells

The functional role of the input neurons to the elementary motion detectors and their correspondence to elements of any detector model depend crucially on their spatiotemporal response characteristics. For this reason, we characterized the spatial extent of the receptive fields as well as the response dynamics of all putative input elements to the T4 and T5 cells: Mi1, Tm3, Mi4, and Mi9 in the ON pathway, and Tm1, Tm2, Tm4, and Tm9 in the OFF pathway. Expressing the genetically encoded calcium indicator GCaMP6f [30] with cell-type-specific Gal4-driver lines, we imaged calcium signals in single terminals in layer 10 of the medulla or the proximal lobula for the ON- and OFF-pathway elements, respectively.

To precisely map the receptive fields of the input elements, we used a one-dimensional white-noise stimulus consisting of 2.8° wide horizontal or vertical bars covering the full extent of the arena (Figures 2A–2D; Figure S1; Supplemental Experimental Procedures). The spatiotemporal receptive fields were then determined from the neuron's calcium response by reverse correlation. The spatial components of these are the one-dimensional horizontal and vertical projections of the underlying two-dimensional spatial receptive field of the cell. In all cases, they strongly resembled a difference of Gaussians (DOG; also called a “Mexican hat”). Because they were similar for both the horizontal and vertical dimensions, we fitted a two-dimensional DOG to reconstruct two-dimensional spatial receptive fields (Figures 2E–2H and 2K–2N). The temporal component of the spatiotemporal receptive field reflects the temporal filtering properties of the neuron (impulse response). The extracted temporal filters were validated by predicting held-out test sequences of neuronal responses from the stimulus for two example neuron types (Mi1 and Tm9) (Figure S2; see Supplemental Experimental Procedures).

All four cell types in the ON pathway, Mi1, Tm3, Mi4, and Mi9, showed locally confined receptive fields that appeared isotropic in the horizontal and vertical dimensions (Figures 2E–2H). Mi1, Mi4, and Mi9 cells revealed a receptive field center with a half-

width diameter of approximately 6°–7°, corresponding to about one optical column. In contrast, the receptive field center of Tm3 was substantially larger, with a half-width diameter of about 12°. Mi4 and Mi9, and to a lesser degree Mi1, also revealed a significant antagonistic surround, giving them spatial band-pass characteristics. This antagonistic surround had a half-width diameter of approximately 20° for both Mi4 and Mi9 (Table S1). Because the area and thus the volume under the curve are proportional to the square of the radius, the amplitude ratio of surround to center should equal the inverse of the ratio of the squares of their half-widths for the center and the antagonistic surround to cancel perfectly. Notably, this relation is fulfilled for both low-pass elements, and the integrals of their surrounds perfectly match their respective centers, thus predicting no responses to wide-field flicker stimuli. At the same time, the spatial band-pass filter enhances responses to edges within the visual scene. In the case of Mi1, the integral of the surround reached about 50% of the one of the center. For Tm3, surround inhibition was completely absent, such that those cells have a pure low-pass characteristic in the spatial domain.

The temporal component of the spatiotemporal receptive field centers yielded the impulse responses, which reflect the temporal filtering properties of the respective cell type. Mi1 and Tm3 showed band-pass filter characteristics, as can be seen in their biphasic impulse responses (Figure 2I) and in their response spectra (Figure 2J). In contrast, Mi4 and Mi9 appeared as pure low-pass filters (Figures 2I and 2J). Surprisingly, and in contrast to the other elements of the ON pathway, Mi9 showed the inverse contrast preference, with an increased calcium response to darkening in its receptive field center (OFF response). However, apart from the polarity, the time course and filter characteristics of Mi9 were very similar to those of Mi4 (Figures 2I and 2J). Thus, the four ON-pathway elements can essentially be grouped into two classes: two fast-transient cells (Mi1 and Tm3) and two slow-sustained cells (Mi4 and Mi9). Within each class, the cells' impulse responses revealed only small differences.

Characterization of the Columnar Input Neurons to T5 Cells

We next performed analogous experiments on the OFF-pathway elements Tm1, Tm2, Tm4, and Tm9. Mirroring the situation in the ON pathway, all four neurons of the OFF pathway had locally confined isotropic receptive fields (Figures 2K–2N). In agreement with previous reports [18, 20], they were all excited by luminance decrements. Accordingly, they revealed an OFF receptive field center. The receptive fields of all four cells also had an antagonistic surround component, giving them a spatial band-pass characteristic. In contrast to Mi4 and Mi9, however, the surround inhibition, with respect to the center, was weaker, which should render them more responsive to wide-field flicker. As a parallel to the ON-pathway elements, three of the neurons, Tm1, Tm2, and Tm9, showed a receptive field center with a half-width diameter of about 7°, whereas one element, Tm4, had a larger receptive field center, with a half-width diameter of approximately 10°.

(K–P) Characterization of the inputs to T5 cells in the OFF pathway. Spatial receptive fields of Tm1 (K), Tm2 (L), Tm4 (M), and Tm9 (N). Temporal kernels in the time (O) and frequency domain (P) for the four input elements in the OFF pathway. (Tm1: N = 8 flies, n = 71 cells; Tm2: N = 9, n = 93; Tm4: N = 5, n = 35; Tm9: N = 5, n = 32.)

Graphs depict the mean. Shaded areas around the line, where displayed, represent \pm SEM. See also Figures S1 and S2 and Tables S1 and S2.

The half-width of the antagonistic surround amounted to about 25° for Tm1, Tm2, and Tm9 and to 35° for Tm4 (Table S2). As for Mi1, and in contrast to Mi4 and Mi9, the antagonistic surround strength for all OFF input elements reached about 50% of the center, as calculated above on the basis of the amplitude and half-width ratios.

As for the ON-pathway elements, we assessed the temporal filter dynamics by measuring the impulse responses within the receptive field centers (Figures 2O and 2P). This revealed a clear band-pass characteristic for Tm1, Tm2, and Tm4 with rather short low-pass time constants of about 100–270 ms. In contrast, the impulse response of Tm9 reflected a pure low-pass filter with a much longer time constant of about 500 ms. Within the group of band-pass filters, Tm1, Tm2, and Tm4 responses have different time courses (Figure 2O) and response spectra (Figure 2P), corroborating a previous study [20]. Thus, as a striking difference from the ON-pathway elements, where two fast and two slow cells are found, the OFF pathway comprises three fast and only one slow cell.

Application of the Octopamine Agonist CDM Changes the Temporal Frequency Tuning of T4 and T5 Cells

It has previously been shown that activation of the octopamine system modulates the temporal-frequency tuning of lobula plate tangential cells [25, 26]. This effect could be implemented directly at the level of the tangential cells, or indirectly, by modifying the temporal tuning properties of its presynaptic input neurons, i.e., the T4/T5 cells. The latter case would give a handle to manipulate the elementary motion detectors and potentially allow narrowing down of their cellular implementation.

We first confirmed that the activation of the octopamine system with the octopamine agonist CDM [31] at a concentration of $20 \mu\text{M}$ [25] shifts the temporal tuning of tangential cells in the lobula plate of immobilized *Drosophila* to higher frequencies (Figure S3), corroborating earlier findings using octopamine [26].

Next we focused on T4 and T5 neurons. We performed two-photon Ca^{2+} imaging in *Drosophila* expressing the genetically encoded calcium indicator GCaMP6m in the subset of T4/T5 neurons that are upward motion selective and project their axons to layer 3 of the lobula plate (T4c/T5c) (Figure 3A). Visual stimulation was presented on a semi-cylindrical LED arena and consisted of full-contrast square-wave gratings with a spatial wavelength of 24° , moving at 12 different velocities ranging from $1.2^\circ/\text{s}$ to $480^\circ/\text{s}$, corresponding to temporal frequencies from 0.05 to 20 Hz, in PD and ND. Responses of T4 and T5 neurons were quantified as relative change of fluorescence (DF/F) amplitudes within small regions of interest in lobula plate layer 3 (example traces in Figure 3B). We found a temporal-frequency optimum of 1 Hz for motion in PD (Figure 3C, black traces). Application of CDM shifted the temporal-frequency optimum from 1 Hz in control to about 2.5 Hz (Figure 3C, magenta traces). Recording Ca^{2+} signals from the dendrites of either T4 or T5 cells, we found that T4 and T5 cells, considered separately, exhibited a similar temporal-frequency tuning, under control conditions as well as after application of CDM, and a similar shift in their tuning with CDM (Figures 3D and 3E).

In order to distinguish changes in the response to isolated motion stimuli from changes in the temporal integration of periodic signals, we also tested the velocity tuning of T4 and T5 neu-

rons to moving edges. For this, we presented bright and dark edges of full contrast moving at different speeds ranging from $3^\circ/\text{s}$ to $300^\circ/\text{s}$ in PD (Figures 3F and 3G). Corroborating previous results [14], T4 neurons responded selectively to bright edges, whereas T5 neurons were found to be selective for motion of dark edges. Measuring the calcium responses in the axon terminals in the lobula plate, we found that under control conditions the responses were highest to edges moving at the slowest velocity of $3^\circ/\text{s}$ for both ON and OFF edges, i.e., T4 and T5 neurons, respectively (Figures 3F and 3G, black traces). As was seen for the grating stimuli above, application of CDM shifted the optimal stimulus condition to higher velocities of $12^\circ/\text{s}$ (Figures 3F and 3G, magenta traces).

Therefore, the shift of the temporal tuning properties of lobula plate tangential cells during flight or mimicked by the application of octopamine-receptor agonists (Figure S3 [25, 26]) is already present at the level of the T4 and T5 cells, thus affecting the tuning of the elementary motion detectors.

Octopamine-Receptor Activation Speeds the Input Elements of T4 and T5 Cells

Different possible mechanisms could explain this shift of temporal tuning in T4/T5 cells. On the one hand, octopamine signaling could affect the synaptic inputs onto T4 and T5 neurons by changing the kinetics of neurotransmitter receptors or the dendritic integration of those signals in T4/T5 neurons. Different input elements with different response kinetics could differentially contribute to the postsynaptic signals in different states through changes in their response amplitude or via their synaptic weight. On the other hand, the kinetics of some or all input elements could speed up. We set out to test the latter hypothesis, i.e., that the response characteristics and tuning of the elementary motion detectors result directly from the temporal dynamics of the respective input elements.

For this, we characterized the spatiotemporal receptive fields of all input elements in both the ON and OFF pathways after activation of the octopamine system with CDM and compared them to control conditions. Application of CDM left the spatial receptive fields of all four input neurons in the ON pathway unaffected (Figure 4A). However, it accelerated the response kinetics of all four cell types to different degrees, with much stronger effects on the fast band-pass elements Mi1 and Tm3 than on the slow low-pass filters Mi4 and Mi9 (Figures 4B and 4C, magenta traces; Figures S4A, S5Ai, and S5Bi). As for control conditions, response kinetics of Mi1 and Tm3, as well as of Mi4 and Mi9, remained similar to each other after addition of CDM. In the OFF pathway, the results were very similar. The spatial receptive fields appeared unchanged by CDM for any of the columnar input neurons (Figure 4D). However, in the temporal domain, addition of CDM to the bath sped up the impulse responses significantly (Figures 4E and 4F, magenta traces; Figures S4B, S6Ai, and S6Bi), as was seen in the ON-pathway band-pass elements.

Computer Simulations Based on the Input Elements' Temporal Filters Suggest Candidate Motion Detectors

The input elements to the motion-detecting neurons T4 and T5 can be roughly grouped into two classes: temporal low-pass filters with large time constants, and band-pass filters with

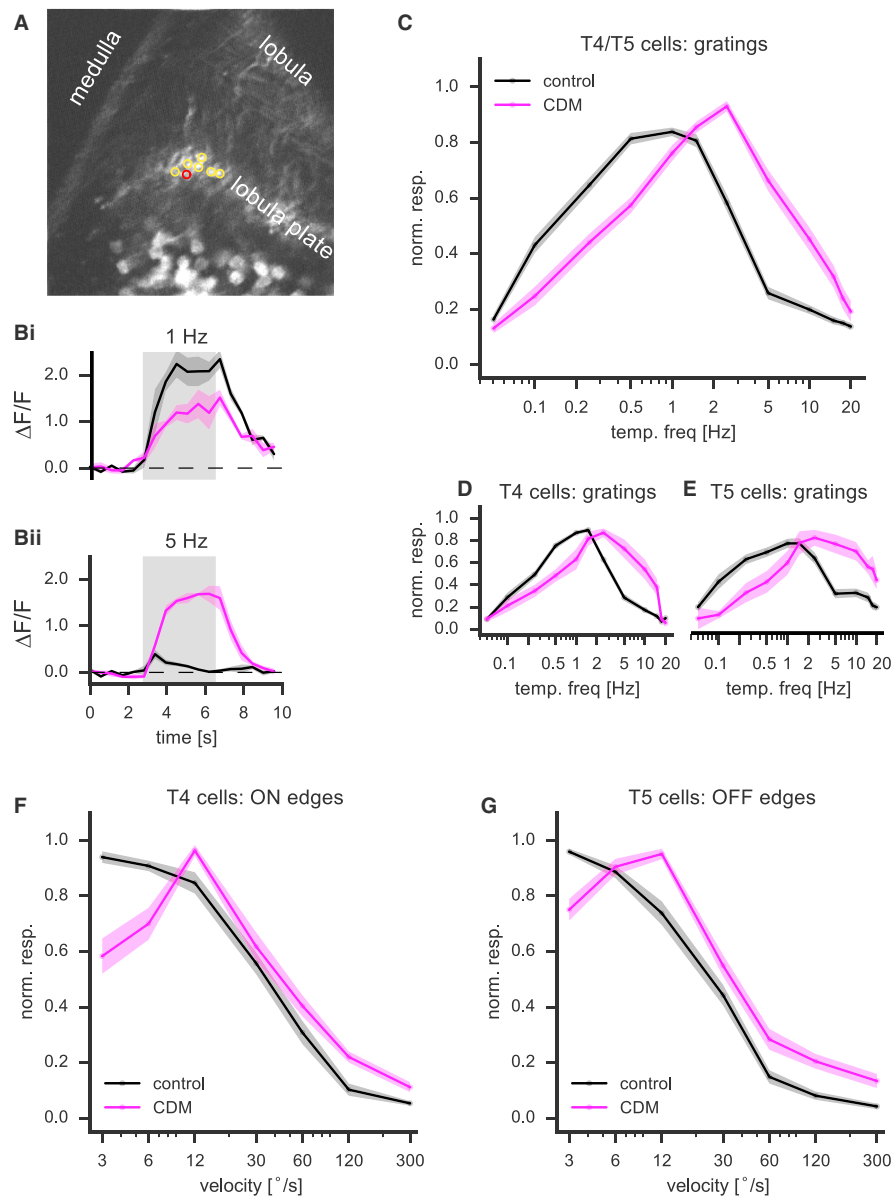


Figure 3. Application of CDM Shifts the Temporal-Frequency and Velocity Tunings of T4/T5 Cells to Higher Velocities

(A) T4/T5 neurons of the upward motion-selective subtype “c” projecting their axons to layer 3 of the lobula plate, expressing the genetically encoded calcium indicator GCaMP6m. The circles mark ROIs in the lobula plate; the red circle corresponds to the example calcium traces in (B).

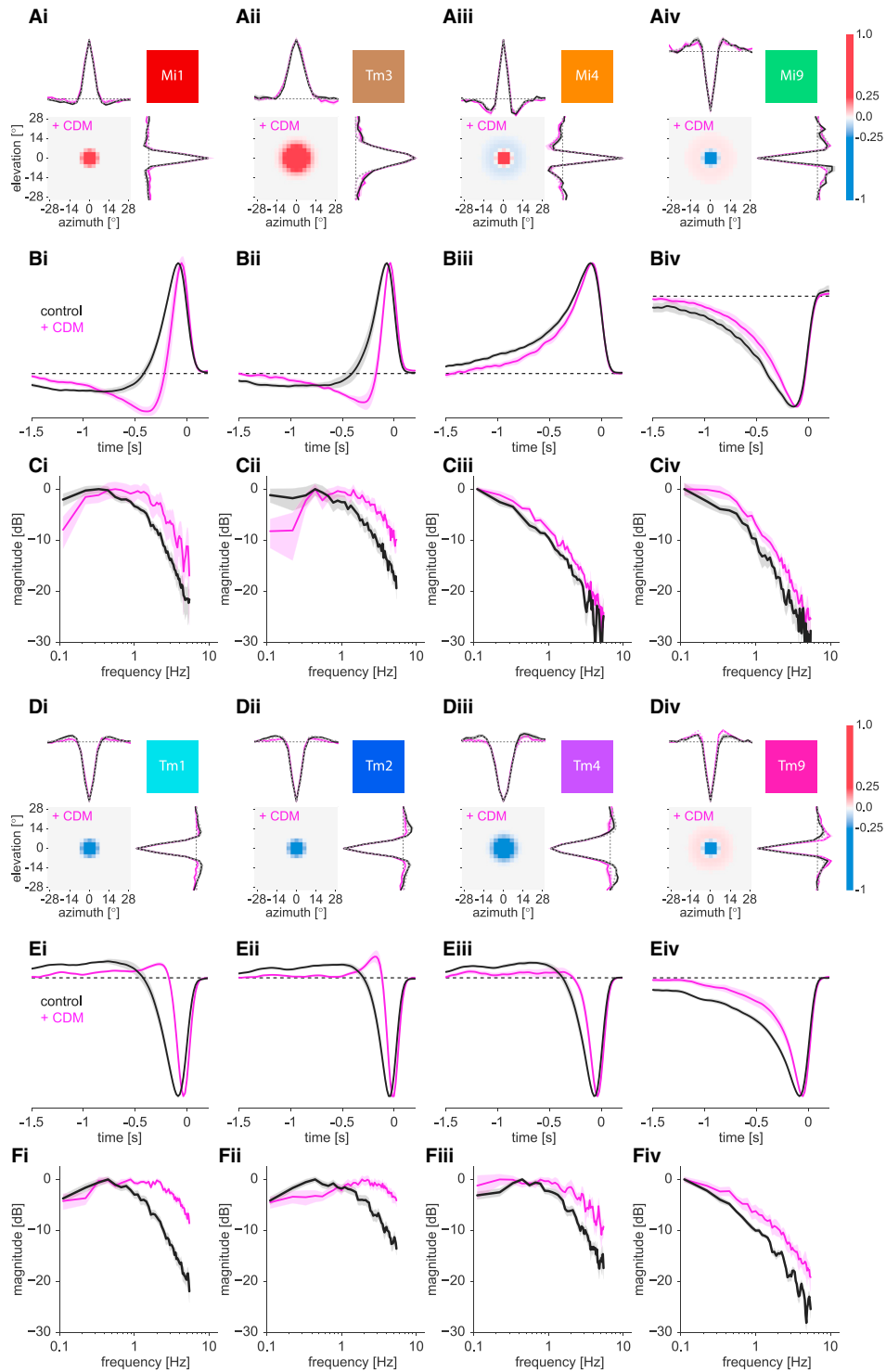
(B) Example of calcium responses (fluorescence changes) in the axon terminals of T4/T5 cells in response to square-wave gratings moving at temporal frequencies of 1 Hz (Bi) and 5 Hz (Bii) in control (black) and after application of CDM (magenta).

(C) Population average of responses of T4/T5 axon terminals to square-wave gratings moving in the PD (up). Application of CDM leads to a shift of the temporal tuning optimum ($N_{\text{cont}} = 36$ flies, $n_{\text{cont}} = 80$ ROIs; $N/n_{\text{CDM}} = 15/39$).

(D and E) Characterization of the temporal-frequency tuning in T4 (D) and T5 dendrites (E). As observed for the axon terminals, application of CDM (magenta) shifts the temporal-frequency tunings of both T4 and T5 cells to higher frequencies, as compared to control (black) (T4: $N_{\text{cont}} = 27$ flies, $n_{\text{cont}} = 52$ ROIs, $N/n_{\text{CDM}} = 9/14$; T5: $N/n_{\text{cont}} = 18/27$, $N/n_{\text{CDM}} = 7/9$).

(F and G) Population average of responses of T4 and T5 axon terminals in the lobula plate to bright (F; T4) and dark edges (G; T5), moving at different velocities, in control (black) and after application of CDM (magenta) ($N_{\text{cont}} = 9$ flies, $n_{\text{cont}_T4} = 21$, $n_{\text{cont}_T5} = 37$ ROIs; $N_{\text{CDM}} = 6$, $n_{\text{CDM}_T4} = 16$, $n_{\text{CDM}_T5} = 17$).

Graphs depict the mean. Shaded areas around the line represent \pm SEM. See also [Figure S3](#).



(legend on next page)

significantly shorter time constants. We used the above-determined spatial receptive fields and response kinetics of the input elements and asked whether these could predict the responses of their postsynaptic targets, the elementary motion detector T4/T5 cells, without the necessity of additional filters or delays implemented either at the level of the synapses between the inputs and the T4/T5 cells or within the dendrites of the T4/T5 cells itself. In addition, we asked whether the observed shift in the temporal tuning in T4/T5 cells after application of the octopamine agonist CDM could be fully explained by the change of filter properties of the respective input neurons.

Although GCaMP6f has relatively fast kinetics when compared with other calcium indicators, it still possesses a decay time constant on the order of hundreds of milliseconds [30, 32]—long enough to significantly prolong the calcium signals of cells that have temporal dynamics on the same order of magnitude. In order to correct for this temporal filtering by the calcium indicator itself, we deconvolved the impulse responses in the frequency domain with a GCaMP6f low-pass filter (Figures S5 and S6). These corrected spectra were used as an approximation of the underlying filter properties of the input cells by fitting first-order filters to the average corrected frequency responses (Tables S1 and S2). We then used these values as well as the spatial filter characteristics in our computer simulations of a motion detector. Because the synaptic transmitters and postsynaptic receptors, and therefore the sign of the synaptic inputs, are not known, we decided not to make any assumptions about the sign of the synapses and ignored the response polarities of the determined receptive fields in our simulations.

Our simulations were based on a motion detector that combines PD enhancement and ND suppression, resembling a hybrid of a HR half-detector and a BL detector, as described in Haag et al. [17] (Figure 1Aiv). In this detector, three inputs with receptive fields offset by 5° each along the PD axis are processed such that an enhancing input A on the null side (left) forms a multiplicative non-linearity with the central, direct input (B), whereas a suppressing input (C) on the preferred side (right) implements a divisive non-linearity. The response of this detector equals the product of the input signals on the enhancing and the direct arm, divided by the signal from the suppressing arm (see the Supplemental Experimental Procedures).

There are 24 possible permutations that map the four input elements of each pathway onto the three positions of this detector, each one resulting in a detector with different tuning properties. Without making any further assumptions, we asked whether some of these combinations would yield more direction-selective

motion detectors than others. Each simulated detector was tested with moving square-wave gratings, and the responses were quantified in three ways (Figure 5A): (1) To assess how well the particular detector model discriminates between motion along PD and ND across velocities, we simulated square-wave gratings moving in PD and ND at different speeds covering more than three orders of magnitude. From the simulated responses, we calculated a direction selectivity index (DSI) as the relative difference between PD and ND responses, averaged over all grating velocities/temporal frequencies. (2) To judge the frequency tuning, we determined the temporal frequency evoking the maximum response in PD (temporal-frequency optimum, f_{opt}). (3) To characterize the direction tuning beyond PD and ND, emphasizing tuning sharpness, we simulated gratings moving in 12 equally spaced directions at the f_{opt} of each detector, as determined above. From those simulated responses, the normalized length of the tuning vector (L_{dir}) was calculated [33]. This tuning vector length of the hybrid detector was furthermore compared with the ones of the constituting HR and BL modules (Figures 1Ai and 1Aii, respectively).

In general, detectors with the low-pass filters Mi4 and Mi9 on both the outer enhancing and suppressing arms, flanking one of the band-pass elements Mi1 or Tm3, performed extremely well: they showed a rather high degree of direction selectivity and tuning sharpness (Figure 5B), in good agreement with the experimental data from T4 cells (compare with [14]), and their temporal-frequency optimum matched that of T4 cells as well (Figure 5B, right; compare with Figures 3C and 3D).

In addition, most combinations with one central low-pass neuron, Mi4, or, particularly, Mi9, flanked by the two band-pass elements Mi1 and Tm3, also achieved high direction-selectivity values. The PD (see arrows in Figure 5B, left) of these detectors is inverted as a consequence of the position of the delay in the HR and BL sub-modules. However, when considering both sub-modules separately (blue and red bars, respectively, in Figure 5B, right), the BL alone showed very low tuning sharpness (L_{dir}) and thus contributed little to the hybrid detector. This affects the tuning specificity of the hybrid detector, as can be seen when comparing, for example, Tm3xMi9/Mi1 with Mi9xTm3/Mi4. Both detectors are built on the same HR detector (using the same cells), but the one that employs Mi4 for the BL part of the model has a higher tuning sharpness. The same is true for all other pairs of this kind: given one pair of cells for the HR module, the implementation that places two low-pass filters on the outer arms of the detector always has the sharper tuning.

Figure 4. Activation of Octopamine Receptors Accelerates the Temporal Filters of the ON- and OFF-Pathway Medulla Columnar Elements

(A) Spatial receptive fields of Mi1 (Ai), Tm3 (Aii), Mi4 (Aiii), and Mi9 (Aiv) for vertical (upper left) and horizontal (lower right) white-noise bar stimulation under control conditions (black traces) and after application of CDM (magenta traces and two-dimensional receptive fields).

(B) Temporal kernels for Mi1 (Bi), Tm3 (Bii), Mi4 (Biii), and Mi9 (Biv) revealing the faster time course after application of CDM (magenta) as compared to control (black).

(C) Temporal kernels in frequency-space, constructed from the temporal kernels in (B). Application of CDM (magenta) leads to a shift of the center frequency of the band-pass filters as compared to control (black). (For the measurements of the spatial receptive fields [controls are as in Figure 2]: Mi1: $N/n_{CDM} = 5$, $n_{CDM} = 31$; Tm3: $N/n_{CDM} = 6/34$; Mi4: $N/n_{CDM} = 5/38$; Mi9: $N/n_{CDM} = 7/37$. Again, the temporal kernel results determined from the horizontal and vertical one-dimensional noise stimuli were pooled, resulting in twice as many measurements.)

(D–F) Analogous to (A)–(C), the spatial receptive fields (Di–Div), temporal kernels (Ei–Eiv), and frequency spectra (Fi–Fiv) of the OFF-pathway elements Tm1, Tm2, Tm4, and Tm9. (Controls are as in Figure 2; Tm1: CDM: $N_{CDM} = 8$, $n_{CDM} = 67$; Tm2: $N/n_{CDM} = 9/93$; Tm4: $N/n_{CDM} = 5/28$; Tm9: $N/n_{CDM} = 5/42$.)

Graphs depict the mean. Shaded areas around the line represent \pm SEM. See also Figure S4 and Tables S1 and S2.

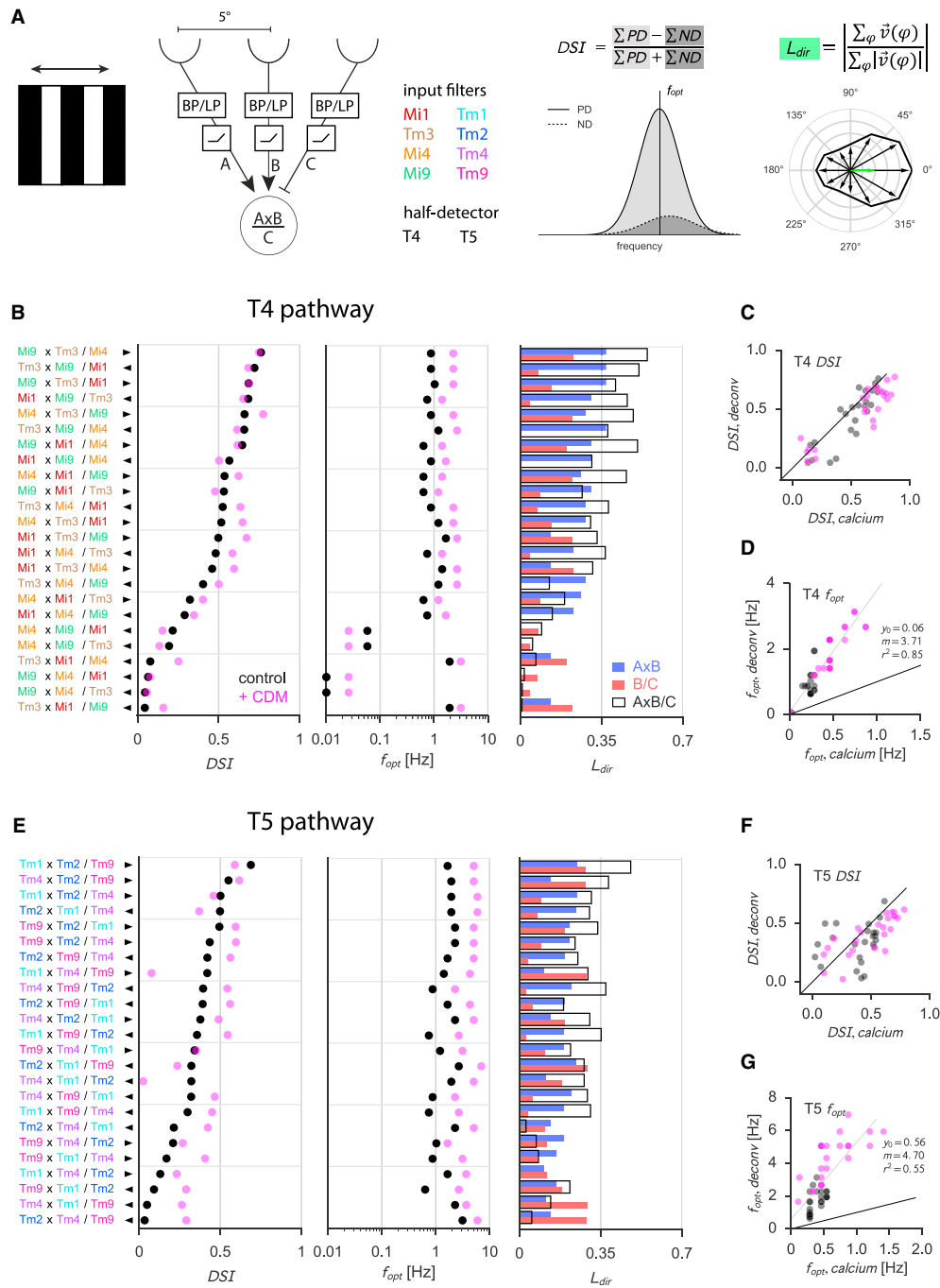


Figure 5. Computer Simulations of Elementary Motion Detectors

(A) Left: schematic of a three-arm detector combining a multiplicative PD enhancement and a divisive ND suppression. The positions of the enhancing (“A”), central (“B”), and suppressing (“C”) input can be occupied by any but different input elements. Those input elements are described by their temporal filtering characteristics, implemented as a band-pass (BP) and low-pass filter (LP) with subsequent rectification. The receptive fields of the three inputs are offset by 5° each. The simulated detectors are stimulated with square-wave gratings moving at different temporal frequencies in PD and ND. Middle: the direction selectivity (*legend continued on next page*)

Similarly, detectors that incorporated two elements with similar temporal response properties (such as Mi1 and Tm3) on two adjacent positions tended to perform worse, especially with respect to the L_{dir} value, indicating poor tuning sharpness. This can be easily explained by the fact that both the HR and BL modules of the hybrid detector rely on temporal differences in their respective two input arms. Inputs with more similar kinetics thus render the corresponding module less effective in creating direction selectivity. In fact, the best detectors were those where both halves showed high direction selectivities on their own (Figure 5B, right), provided the PDs of both modules were aligned.

Interestingly, almost all combinations showed a shift in their tuning toward higher temporal-frequency optima by about a factor of 2 when the filter properties after application of the octopamine agonist CDM were used, matching the experimental data. As a control that the direction selectivities in our simulations were not dependent on the used deconvolution filter, we repeated the simulations with the raw temporal kernels derived from the calcium responses. The same arrangements of input elements led to the motion detectors with the highest direction-selectivity values (Figure 5C), consistent with the notion that it is the relative filter properties that are crucial. Deconvolution merely changes the temporal frequency of the visual stimulus that leads to the maximum response (Figure 5D).

In the above simulations, we followed an unbiased approach with all inputs separated by 5° , thus having receptive fields arising from neighboring neuro-ommatidia. However, electron-microscopic reconstructions have shown a spatial offset between Tm3 and Mi1 cells projecting to the same T4 cell of about 1° in this order along the PD of the postsynaptic T4 cell [4]. The smaller spatial offset could counterbalance the small differences in temporal kinetics between these cells. Repeating the above simulations of the three-arm detector under these constraints still resulted in poorly direction-selective detectors for these combinations, with L_{dir} values of 0.38 (for Mi9xTm3/Mi1, as compared to 0.41 for a 5° offset) or less. In fact, when considering only a simple two-arm detector (HR or BL type), any detector that consisted of Tm3 and Mi1 with a spatial offset of 1° resulted in L_{dir} values of less than 0.06 for both types of detectors (in comparison to 0.13 for a 5° offset).

Although the evidence is weaker for the structure of the motion detector implementation in T5, we constructed analogous motion detectors for the OFF pathway with the measured receptive fields and response kinetics of the columnar inputs onto T5 neurons (Figure 5E). In contrast to the ON pathway, only one out of

the four input elements, Tm9, constitutes a low-pass filter, whereas the other three, Tm1, Tm2, and Tm4, exhibit band-pass characteristics. Most input element combinations resulted in motion detectors with low direction selectivity. Notably, the highest direction selectivity resulted from detectors with the low-pass filter Tm9 on the suppressing arm. Naturally, detectors with the fastest input (principally Tm2) in the central position flanked by two slower elements achieved higher direction selectivities, as with this arrangement the PDs of the HR and BL sub-units are aligned. Arrangements with the sole low-pass filter, Tm9, in the central position resulted in detectors with poor directional tuning, both measured as DSI across all frequencies and L_{dir} , resulting from a virtually ineffective BL half (Figure 5E, right). Interestingly, combinations with the band-pass filters Tm1 and Tm4 constituting either half of the detector tended to perform comparatively poorly—and sometimes even showed a complete breakdown of direction selectivity—in at least one of the simulated physiological states. This can be explained by the fact that the small differences in the temporal response kinetics of these neurons were not stable between control and under CDM (Figure S6). As was seen for the ON pathway, using the spatiotemporal filters extracted under CDM in the simulations led to an increase of the temporal-frequency optimum by about a factor of 2 across all detectors (Figure 5E, middle, magenta dots). Again, the simulations were robust to the deconvolution applied to account for the filtering by the calcium indicator (Figure 5F). The best arrangements were the same irrespective of whether the raw or deconvolved filters were used, and only the temporal-frequency optimum was affected (Figure 5G).

Taken together, we find distinctly different response kinetics of the input elements in both the ON and the OFF pathway, from band-pass filters to pure low-pass filters. These map naturally onto hybrid elementary motion detectors implementing PD enhancement and ND suppression. The best-performing detectors arise when the fastest element occupies the central arm, flanked by slower inputs on the enhancing and suppressing arms. In the ON pathway, two low-pass inputs, Mi4 and Mi9, are found to fill this role. In the OFF pathway, the single low-pass element, Tm9, appears to be best positioned on the suppressing arm to achieve the highest direction selectivity.

DISCUSSION

To understand how motion detection is implemented on the dendrites of T4 and T5 cells, we describe in this study the response

of the detector is assessed across all temporal frequencies based on the area under the temporal-frequency tuning curves in PD and ND as the direction selectivity index: $DSI = (\Sigma PD - \Sigma ND) / (\Sigma PD + \Sigma ND)$. The dotted line indicates the temporal-frequency optimum (f_{opt}) for responses in PD. Right: illustration of the normalized tuning vector length (L_{dir}) as a measure for direction selectivity and tuning sharpness. L_{dir} is calculated as the vector sum of all responses according to the direction of stimulus motion, normalized to the sum of all response vector lengths.

(B–D) Characterization of the simulated motion detectors for the ON pathway.

(B) Direction selectivity (left), temporal-frequency optimum (middle), and normalized tuning vector length (right) for all possible permutations of the four ON-pathway input elements on the three positions of the simulated detector. The magenta dots indicate the effect of CDM application on direction selectivity and temporal-frequency tuning resulting from the accelerated temporal filters of the input elements. Arrows indicate the PD with respect to the corresponding cell arrangements. For the tuning vector length, the hybrid detectors (black open bars) were compared to their constituting HR (“AxB”; blue) and BL modules (“B/C”; red).

(C and D) Direction-selectivity indices (C) and temporal-frequency optima (D) of all detectors based on the deconvolved filter kernels as shown in (B) plotted against the detectors based on the raw calcium kernels.

(E–G) Same as (B)–(D) but for the OFF pathway.

See also Figures S5 and S6.

properties of the elementary motion detectors in *Drosophila*, the T4 and T5 neurons, as well as all of their known columnar synaptic input neurons, under two different tuning regimes. With this comprehensive characterization, we are able to narrow down the cellular implementation of the motion detectors and suggest probable wiring diagrams.

All of these input elements possess spatially restricted receptive fields with centers spanning one to two ommatidia. All, with the exception of the ON-pathway band-pass neuron Tm3, have pronounced antagonistic surrounds. Particularly for the low-pass filter elements Mi4 and Mi9, the strong antagonistic surround fully counterbalances the excitatory center. This should not only eliminate sensitivity to large-field flicker stimuli but more importantly curtail the otherwise tonic responses of pure low-pass filters to moving edges, and thus strongly improve direction selectivity. The locally confined receptive fields are in agreement with previous studies [18, 20, 34] but in contradiction to [35], which described Tm9 as a wide-field neuron. In both pathways, one neuron shows a larger receptive field (Tm3 in the ON pathway, and Tm4 in the OFF pathway). The larger receptive field sizes of Tm3 [18] and Tm4 neurons are consistent with the multi-columnar input these neurons receive based on electron-microscopic reconstructions [4, 5].

All elements of the OFF pathway respond to light OFF in the center of their receptive fields, consistent with [20]. In the ON pathway, Mi1, Tm3 [18], and Mi4 analogously show an ON-center response. Mi9, however, despite being an element in the ON pathway, responds positively to OFF stimuli. This could suggest a sign reversal through an inhibitory synapse onto T4. However, it is not known what neurotransmitter is released by Mi9, and thus whether it excites or inhibits T4 neurons.

Within each of the two pathways, we find a diversity of temporal filter characteristics from fast band-pass filters to pure low-pass filters with slow-sustained responses. These differences in temporal dynamics make them ideal components for motion detection without the need of postulating further processing by slow synaptic signaling or electrotonic filtering within the dendrites of T4 and T5 cells. Where the response kinetics of these cells have been previously described, our data are consistent. In particular, Mi1, Tm3, Tm1, Tm2, and Tm4 have previously been shown to respond transiently to sustained stimuli, i.e., to possess band-pass characteristics [18, 20, 34]. Tm3 appears faster than Mi1 [18] (but see [36]), and Tm2 faster than Tm1 [18, 20, 36]. However, these temporal differences are often very small. On the other hand, Tm9 in the OFF pathway has been described as a low-pass filter [20, 35], which matches our results. In the ON pathway, we find that the previously uncharacterized cell types Mi4 and Mi9 also show pure temporal low-pass response characteristics. Thus, in both pathways, input elements with slow-sustained and fast-transient responses are found, which then converge onto the dendrites of T4 and T5 cells, respectively. Yet the relative distribution differs. In the ON pathway, two input elements show pure low-pass characteristics (Mi4 and Mi9), whereas in the OFF pathway, Tm9 constitutes the only pure low-pass filter. Two of the three input elements that constitute pure low-pass filters, namely Mi9 in the ON and Tm9 in the OFF pathway, receive their lamina input primarily from the lamina monopolar neuron L3 [37]. As L3 has been shown to respond in a slower and more sustained fashion [38] than,

e.g., the transient L2 [10, 11], this could explain the low-pass characteristics of Mi9 and Tm9. L3, like all lamina neurons, responds positively to light decrements, and it releases the excitatory neurotransmitter acetylcholine, explaining the OFF response of Tm9 and Mi9. The response dynamics of Mi4 are likely to be heavily shaped by the strong reciprocal connections with Mi9 [37]. These reciprocal connections, and thus likely the cells themselves, would have to be inhibitory, as these cells show opposite response polarities.

Based on the spatial receptive fields and response kinetics, we could ask which input neurons could play which role in the motion detector. Previous computer simulations based on the measured dynamics of Tm cells in the OFF pathway have shown that most combinations of two elements result in classical (full) HR detectors with similar temporal tuning optima roughly matching the tuning of tangential cells [20]. In that study, only the combination of Tm2 and Tm4 could be excluded, as their filter time constants were too similar to each other to result in a functioning detector. However, subtraction of oppositely tuned half-detectors not only leads to motion opponency but increases direction selectivity of otherwise poorly tuned half-detectors. Consequently, the tuning of lobula plate tangential cells represents a rather indirect readout. By comparing simulations of the half-detector stage with recordings from T4 and T5 neurons, we can exclude the majority of possible combinations of input elements based on their temporal-frequency optimum or directional selectivity (see below).

Based on visual stimulation of single individual columns, T4 neurons have recently been shown to implement both PD enhancement and ND suppression [17]. The receptive fields of these interactions are spatially offset along the PD axis in this order. The corresponding hybrid of an HR half-detector and a BL detector requires a minimum of three columnar inputs: a fast central input, flanked by two outer inputs providing signals that are delayed relative to the central one.

In our computer simulations for the ON pathway (Figure 5), the majority of detectors with the highest direction selectivity fall into two groups: (1) the two low-pass filter elements Mi4 and Mi9 on the outer enhancing and suppressing arms, and either of the fast band-pass elements Mi1 and Tm3 on the central arm, matching the above layout, and (2) the inverted arrangement, with one central low-pass filter, flanked by the band-pass filter elements Mi1 and Tm3. This also resulted in an inverted PD.

In the latter case, however, the BL subunit considered alone contributed very little to the directional tuning (Figure 5B, right), as the low-pass-filtered central excitatory input tends to outlast the corresponding suppression from the band-pass outer arm. This reduces the tuning sharpness of these detectors. Furthermore, this implementation does not match the arrangement of PD-enhancement and ND-suppression receptive fields along the PD in this order found for T4 cells [17]. Additionally, this arrangement would require Mi1 and Tm3 on the outer arms of the model, which is in stark contrast to their reported 1° spatial offset [4].

Among the more direction-selective detectors was also one combination with Tm3 on the central and Mi1 on the suppressing arm. However, the resulting BL subunit considered alone shows very poor directional tuning, and the direction selectivity arises

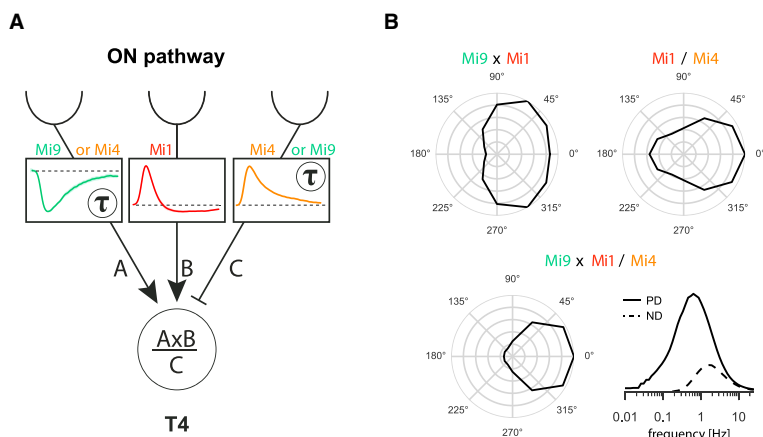


Figure 6. Proposed Implementation of the Elementary Motion Detectors in the ON Pathway

(A) T4 neurons implement both PD enhancement and ND suppression with receptive fields offset in this order along the PD axis. This requires one central fast arm being flanked by two delayed or stronger low-pass-filtered inputs. The relatively fast kinetics of Mi1 or Tm3 would suggest either or both for the central input. Mi4 and Mi9, on the other hand, show pure low-pass characteristics in their temporal kernels fitting the requirements of the two outer arms. The signs of both outer-arm synapses depend on the arrangement of Mi4 and Mi9 to accommodate their respective response polarity and match them to the required enhancing and suppressive inputs.

(B) Simulated detector responses for gratings moving across the visual field in 12 different directions, separated from each other by 30°. Top: directional tuning for the two sub-modules of this

detector. Top left: the pure HR (half) detector Mi9xMi1 shows some direction selectivity but has a low tuning sharpness. Top right: the pure BL detector Mi1/Mi4 shows a substantial response in the ND direction (180°). Bottom: directional tuning for the hybrid detector Mi9xMi1/Mi4. This hybrid detector is very sharply tuned to rightward motion (left), whereas its direction selectivity remains high across stimulus frequencies (right).

virtually exclusively from the HR subunit. Even taking the reported small anatomical offset of about 1° between these cells into account [4] did not compensate for the small temporal differences but actually resulted in even worse directional tuning. This indicates that sizable differences not only in the temporal but also in the spatial domain are a prerequisite for direction selectivity. Similar considerations are true for all combinations that place neurons with similar response kinetics on neighboring arms. In general, the most effective hybrid detectors result from combinations of cells that are arranged such that the respective HR and BL sub-detectors are as direction selective as possible and aligned in their PD.

For detectors where two low-pass filters flank a central band-pass filter element, both Mi1 and Tm3 seem feasible to fill the role of the latter. However, a previous study blocking the synaptic output of Tm3 found an effect on the response of tangential cells to moving ON edges only at high but not at low to moderate velocities [21]. Hence, although we do not exclude a functional role for Tm3 in ON motion detection, this finding argues against Tm3 as the (sole) central arm of the detector in the ON pathway, as the interference especially with the central arm should fully abolish the detection of motion.

Taken together, an implementation of the ON elementary motion detector as depicted in Figure 6 seems most likely: Mi1 as the fast central input, flanked by the low-pass elements Mi4 and Mi9 constituting the suppressing and enhancing arm in either order. Depending on the location, these neurons need to be either both excitatory or both inhibitory to accommodate their respective response polarity and fulfill the required role of enhancing and suppressing input. Considering their opposite polarity and reciprocal connection, it is more likely that both neurons are inhibitory. This would place Mi9 on the enhancing arm (“A” in Figure 6A), and Mi4 on the suppressing arm (“C” in Figure 6A). Importantly, with the observed range of temporal response characteristics in the input elements, it is not necessary to postulate further delays at the synaptic or dendritic level.

In the OFF pathway, the algorithmic structure of motion detection is less clear. On the one hand, spatiotemporal receptive field measurements of T5 neurons reveal excitatory and inhibitory sub-fields that are offset along the PD axis and appropriately tilted in space and time to support PD enhancement and ND suppression [23]. This would suggest a similar architecture as for T4. On the other hand, other studies have only reported PD enhancement for T5 [22, 39]. Nevertheless, we performed analogous simulations based on the measured T5 input kinetics and receptive fields assuming a similar detector architecture. The two detectors with the highest direction selectivity incorporated the low-pass filter, Tm9, into their suppressing arm (Figure 5E). Lacking a second pure low-pass filter input in the OFF pathway, the central and enhancing arms were occupied with band-pass filters. Because the PDs of PD enhancement and ND suppression need to be aligned, the fastest element of the combination, principally Tm2, must be located in the central position. This is also illustrated by the two worst combinations (Figure 5E, right), where even though the BL module on its own performs quite well, the oppositely oriented HR module destroys the direction selectivity of the hybrid detector. As above, hybrid detectors with the low-pass filter, Tm9, on the central arm perform poorly, as the constituting BL half contributes little to direction selectivity in those combinations (Figure 5E, right; e.g., Tm2xTm9/Tm4).

According to our simulations, and if the structure for T5 resembles the hybrid detector proposed for T4, the arrangement of a central Tm2, flanked on the null side by an enhancing Tm1 and on the preferred side by a suppressing Tm9 input, achieves by far the best direction selectivity. This implementation would predict inhibitory/suppressing input from Tm9 onto T5, which could be experimentally tested. Consistent with this arrangement, out of all four T5 columnar inputs, blocking the synaptic output from Tm4 cells results in the lowest reduction in OFF-edge responses in tangential cells [20]. Nevertheless, those blocking experiments indicate that Tm4 plays a role in the detector that awaits resolving.

In this study, we have shown that the activation of the octopamine system by CDM shifts the temporal-frequency and velocity tuning of T4 and T5 neurons to higher temporal frequencies/velocities, mirroring the temporal tuning shift in tangential cells of the lobula plate observed under active locomotion or octopaminergic activation [24–27]. At the level of T4 and T5 neurons, we find a temporal-frequency optimum of about 1–1.5 Hz for moving gratings under control conditions, corroborating previous studies [14, 17, 22]. Application of CDM shifts the temporal-frequency optimum to 2.5 Hz. T4 and T5 cells show a velocity optimum for moving edges at 3°/s or lower under control conditions, which shifts to about 12°/s under CDM. The much higher velocity optimum observed in tangential cells [40] results from the summation of synaptic inputs from the larger number of T4 and T5 neurons swept by the edge during the same time interval at higher velocities.

In parallel to the temporal-frequency tuning shift in T4 and T5 neurons, the temporal response properties of the input elements, in particular of the band-pass filter elements, accelerate. Indeed, the shift in the tuning of T4 and T5 neurons (Figure 3) can be fully accounted for by the speeding of their input elements (Figures 4 and 5). This further supports the hypothesis that the temporal kinetics of the input elements alone, without any further filtering at the synaptic or T4/T5 dendritic levels, represent the delay stage of the elementary motion detectors.

Interestingly, we observe that whereas the order of input elements with respect to their filter characteristics generally remained the same under CDM, Tm1 became faster than Tm4 (Figure S6). As a consequence, simulated motion detectors using combinations that relied on temporal differences between these two cell types suffered a strong reduction or complete breakdown of direction selectivity under CDM (Figure 5). Considering cell-to-cell variability and such changes under different physiological conditions, detectors relying on small differences in the dynamics of their input elements [18, 39] will not be robust.

Octopaminergic neurons broadly innervate the optic lobes, specifically the medulla, lobula, and lobula plate [26, 28, 29]. They activate during flight and are necessary and sufficient for the observed change in the temporal tuning profile of tangential cells [26]. Although the molecular and cellular mechanisms of action on the medulla neurons and T4/T5 cells, as well as the precise physiological activation of the octopamine system, are beyond the scope of this study, a few points are worth noting. Four different types of octopamine receptors exist in *Drosophila* that are all G protein-coupled receptors but act via different pathways and thus will have different effects [41, 42]. Of those four types, only the octopamine receptors Oamb and to a lesser degree Oct1 β R appear to be expressed in the optic lobes [42]. The expression pattern of these octopamine receptors is not known at the cellular level. Considering that all input elements in both the ON and the OFF pathway are accelerated in their responses, albeit to different degrees, it is entirely possible that those changes are indirect and inherited from neurons in the lamina or even the retina. For example, an accelerated response in L1 and L2, and to a smaller degree in L3, could explain the observed response changes in the medulla neurons described here. So far, octopaminergic neurons have not been shown to innervate the retina and lamina directly [26, 28, 29], yet octopamine might nevertheless directly or indirectly affect

photoreceptors or lamina neurons. For example, lamina wide-field neurons, projecting from the medulla back into the lamina and forming synaptic inputs to lamina neurons [43], are modulated by the behavioral state and octopamine signaling [44]. Although it cannot be excluded that octopamine acts at multiple levels, including on T4/T5 neurons directly, we have shown that the observed tuning shift in T4/T5 neurons can be fully accounted for by the changes in the temporal dynamics of their input elements.

Pharmacological activation, like any optogenetic or other exogenous activation of the octopamine system, is unlikely to capture all subtleties of the physiological changes during active locomotion, yet it can serve as a tool to manipulate the tuning of the visual motion detection system. At the same time, considering the match between pharmacological manipulation and physiological state changes observed at the level of lobula plate tangential cells [24–26], it is highly likely that the speeding of the filter characteristics in the medulla neurons described here is relevant under physiological conditions.

We have shown that it is possible to construct a hybrid HR/BL detector (as proposed in [17]) with the measured filters for the cellular elements for both the ON and the OFF pathway across different network states. From these, we can predict anatomical arrangements that would give rise to the observed response characteristics of the elementary motion detectors. Although we cannot rule out additional synaptic or dendritic filter mechanisms, we show that the temporal dynamics of the input elements alone are sufficient to explain the response properties of the elementary motion detectors across different tuning regimes. Future studies using the genetic toolbox of *Drosophila* to activate or block individual input neurons and studying the effects on visual responses in the T4 and T5 cells, as well as neurotransmitter and receptor expression pattern analyses and electron-microscopic reconstructions of the wiring, will be required to verify and further confine the proposed circuitry.

EXPERIMENTAL PROCEDURES

Experimental procedures are described in detail in the [Supplemental Experimental Procedures](#).

SUPPLEMENTAL INFORMATION

Supplemental Information includes Supplemental Experimental Procedures, six figures, and two tables and can be found with this article online at <http://dx.doi.org/10.1016/j.cub.2017.01.051>.

AUTHOR CONTRIBUTIONS

A.A., M.S.D., and A.B. conceived the study and designed the experiments. A.A. conducted and analyzed the measurements of T4/T5 cell responses. M.S.D. designed the projector-based stimulation arena and performed and analyzed the measurements of the OFF-pathway elements. F.G.R. performed and analyzed the experiments describing the ON-pathway neurons. G.A. performed and analyzed the patch-clamp recordings from lobula plate tangential cells. M.S.D. performed the computer simulations. A.A. wrote the manuscript with the help of all authors.

ACKNOWLEDGMENTS

We thank Stefan Prech for help in designing the projector-based stimulus arena, Jürgen Haag for sharing his expertise in two-photon microscopy, and

Wolfgang Essbauer and Michael Sauter for fly husbandry. We are very grateful to Michael Reiser, Gerry Rubin, and Aljoscha Leonhardt for sharing unpublished fly lines. We would also like to thank Aljoscha Leonhardt for many helpful discussions, and Alex Mauss for critically reading the manuscript. This work was supported by an EMBO Long-Term Fellowship (A.A.), the Deutsche Forschungsgemeinschaft (SFB 870), and the Max Planck Society.

Received: October 28, 2016
 Revised: December 19, 2016
 Accepted: January 25, 2017
 Published: March 23, 2017

REFERENCES

- Borst, A. (2014). Fly visual course control: behaviour, algorithms and circuits. *Nat. Rev. Neurosci.* *15*, 590–599.
- Fischbach, K.F., and Dittrich, A.P.M. (1989). The optic lobe of *Drosophila melanogaster*. I. A Golgi analysis of wild-type structure. *Cell Tissue Res.* *258*, 441–475.
- Bausenwein, B., Dittrich, A.P., and Fischbach, K.F. (1992). The optic lobe of *Drosophila melanogaster*. II. Sorting of retinotopic pathways in the medulla. *Cell Tissue Res.* *267*, 17–28.
- Takemura, S.-Y., Bharioke, A., Lu, Z., Nern, A., Vitaladevuni, S., Rivlin, P.K., Katz, W.T., Olbris, D.J., Plaza, S.M., Winston, P., et al. (2013). A visual motion detection circuit suggested by *Drosophila* connectomics. *Nature* *500*, 175–181.
- Shinomiya, K., Karuppudurai, T., Lin, T.-Y., Lu, Z., Lee, C.-H., and Meinertzhagen, I.A. (2014). Candidate neural substrates for off-edge motion detection in *Drosophila*. *Curr. Biol.* *24*, 1062–1070.
- Barlow, H.B., and Levick, W.R. (1965). The mechanism of directionally selective units in rabbit's retina. *J. Physiol.* *178*, 477–504.
- Hassenstein, B., and Reichardt, W. (1956). Systemtheoretische Analyse der Zeit-, Reihenfolgen- und Vorzeichenbewertung bei der Bewegungspertzeption des Rüsselkäfers *Chlorophanus*. *Z. Naturforsch. B* *11*, 513–524.
- Borst, A., and Helmstaedter, M. (2015). Common circuit design in fly and mammalian motion vision. *Nat. Neurosci.* *18*, 1067–1076.
- Joesch, M., Schnell, B., Raghu, S.V., Reiff, D.F., and Borst, A. (2010). ON and OFF pathways in *Drosophila* motion vision. *Nature* *468*, 300–304.
- Strother, J.A., Nern, A., and Reiser, M.B. (2014). Direct observation of ON and OFF pathways in the *Drosophila* visual system. *Curr. Biol.* *24*, 976–983.
- Clark, D.A., Bursztyn, L., Horowitz, M.A., Schnitzer, M.J., and Clandinin, T.R. (2011). Defining the computational structure of the motion detector in *Drosophila*. *Neuron* *70*, 1165–1177.
- Eichner, H., Joesch, M., Schnell, B., Reiff, D.F., and Borst, A. (2011). Internal structure of the fly elementary motion detector. *Neuron* *70*, 1155–1164.
- Joesch, M., Weber, F., Eichner, H., and Borst, A. (2013). Functional specialization of parallel motion detection circuits in the fly. *J. Neurosci.* *33*, 902–905.
- Maisak, M.S., Haag, J., Ammer, G., Serbe, E., Meier, M., Leonhardt, A., Schilling, T., Bahl, A., Rubin, G.M., Nern, A., et al. (2013). A directional tuning map of *Drosophila* elementary motion detectors. *Nature* *500*, 212–216.
- Mauss, A.S., Meier, M., Serbe, E., and Borst, A. (2014). Optogenetic and pharmacologic dissection of feedforward inhibition in *Drosophila* motion vision. *J. Neurosci.* *34*, 2254–2263.
- Mauss, A.S., Pankova, K., Arenz, A., Nern, A., Rubin, G.M., and Borst, A. (2015). Neural circuit to integrate opposing motions in the visual field. *Cell* *162*, 351–362.
- Haag, J., Arenz, A., Serbe, E., Gabbiani, F., and Borst, A. (2016). Complementary mechanisms create direction selectivity in the fly. *eLife* *5*, e17421.
- Behnia, R., Clark, D.A., Carter, A.G., Clandinin, T.R., and Desplan, C. (2014). Processing properties of ON and OFF pathways for *Drosophila* motion detection. *Nature* *512*, 427–430.
- Behnia, R., and Desplan, C. (2015). Visual circuits in flies: beginning to see the whole picture. *Curr. Opin. Neurobiol.* *34*, 125–132.
- Serbe, E., Meier, M., Leonhardt, A., and Borst, A. (2016). Comprehensive characterization of the major presynaptic elements to the *Drosophila* OFF motion detector. *Neuron* *89*, 829–841.
- Ammer, G., Leonhardt, A., Bahl, A., Dickson, B.J., and Borst, A. (2015). Functional specialization of neural input elements to the *Drosophila* ON motion detector. *Curr. Biol.* *25*, 2247–2253.
- Fisher, Y.E., Silies, M., and Clandinin, T.R. (2015). Orientation selectivity sharpens motion detection in *Drosophila*. *Neuron* *88*, 390–402.
- Leong, J.C.S., Esch, J.J., Poole, B., Ganguli, S., and Clandinin, T.R. (2016). Direction selectivity in *Drosophila* emerges from preferred-direction enhancement and null-direction suppression. *J. Neurosci.* *36*, 8078–8092.
- Chiappe, M.E., Seelig, J.D., Reiser, M.B., and Jayaraman, V. (2010). Walking modulates speed sensitivity in *Drosophila* motion vision. *Curr. Biol.* *20*, 1470–1475.
- Jung, S.N., Borst, A., and Haag, J. (2011). Flight activity alters velocity tuning of fly motion-sensitive neurons. *J. Neurosci.* *31*, 9231–9237.
- Suver, M.P., Mamiya, A., and Dickinson, M.H. (2012). Octopamine neurons mediate flight-induced modulation of visual processing in *Drosophila*. *Curr. Biol.* *22*, 2294–2302.
- Longden, K.D., and Krapp, H.G. (2010). Octopaminergic modulation of temporal frequency coding in an identified optic flow-processing interneuron. *Front. Syst. Neurosci.* *4*, 153.
- Sinakevitch, I., and Strausfeld, N.J. (2006). Comparison of octopamine-like immunoreactivity in the brains of the fruit fly and blow fly. *J. Comp. Neurol.* *494*, 460–475.
- Busch, S., Selcho, M., Ito, K., and Tanimoto, H. (2009). A map of octopaminergic neurons in the *Drosophila* brain. *J. Comp. Neurol.* *513*, 643–667.
- Chen, T.-W., Wardill, T.J., Sun, Y., Pulver, S.R., Renninger, S.L., Baohan, A., Schreiner, E.R., Kerr, R.A., Orger, M.B., Jayaraman, V., et al. (2013). Ultrasensitive fluorescent proteins for imaging neuronal activity. *Nature* *499*, 295–300.
- Roeder, T. (1995). Pharmacology of the octopamine receptor from locust central nervous tissue (OAR3). *Br. J. Pharmacol.* *114*, 210–216.
- Schnell, B., Weir, P.T., Roth, E., Fairhall, A.L., and Dickinson, M.H. (2014). Cellular mechanisms for integral feedback in visually guided behavior. *Proc. Natl. Acad. Sci. USA* *111*, 5700–5705.
- Mazurek, M., Kager, M., and Van Hooser, S.D. (2014). Robust quantification of orientation selectivity and direction selectivity. *Front. Neural Circuits* *8*, 92.
- Meier, M., Serbe, E., Maisak, M.S., Haag, J., Dickson, B.J., and Borst, A. (2014). Neural circuit components of the *Drosophila* OFF motion vision pathway. *Curr. Biol.* *24*, 385–392.
- Fisher, Y.E., Leong, J.C.S., Sporar, K., Ketkar, M.D., Gohl, D.M., Clandinin, T.R., and Silies, M. (2015). A class of visual neurons with wide-field properties is required for local motion detection. *Curr. Biol.* *25*, 3178–3189.
- Yang, H.H., St-Pierre, F., Sun, X., Ding, X., Lin, M.Z., and Clandinin, T.R. (2016). Subcellular imaging of voltage and calcium signals reveals neural processing in vivo. *Cell* *166*, 245–257.
- Takemura, S.-Y., Xu, C.S., Lu, Z., Rivlin, P.K., Parag, T., Olbris, D.J., Plaza, S., Zhao, T., Katz, W.T., Umayam, L., et al. (2015). Synaptic circuits and their variations within different columns in the visual system of *Drosophila*. *Proc. Natl. Acad. Sci. USA* *112*, 13711–13716.
- Silies, M., Gohl, D.M., Fisher, Y.E., Freifeld, L., Clark, D.A., and Clandinin, T.R. (2013). Modular use of peripheral input channels tunes motion-detecting circuitry. *Neuron* *79*, 111–127.

39. Salazar-Gatzimas, E., Chen, J., Creamer, M.S., Mano, O., Mandel, H.B., Matulis, C.A., Pottackal, J., and Clark, D.A. (2016). Direct measurement of correlation responses in *Drosophila* elementary motion detectors reveals fast timescale tuning. *Neuron* *92*, 227–239.
40. Leonhardt, A., Ammer, G., Meier, M., Serbe, E., Bahl, A., and Borst, A. (2016). Asymmetry of *Drosophila* ON and OFF motion detectors enhances real-world velocity estimation. *Nat. Neurosci.* *19*, 706–715.
41. Farooqui, T. (2007). Octopamine-mediated neuromodulation of insect senses. *Neurochem. Res.* *32*, 1511–1529.
42. El-Kholy, S., Stephano, F., Li, Y., Bhandari, A., Fink, C., and Roeder, T. (2015). Expression analysis of octopamine and tyramine receptors in *Drosophila*. *Cell Tissue Res.* *361*, 669–684.
43. Rivera-Alba, M., Vitaladevuni, S.N., Mishchenko, Y., Lu, Z., Takemura, S.Y., Scheffer, L., Meinertzhagen, I.A., Chklovskii, D.B., and de Polavieja, G.G. (2011). Wiring economy and volume exclusion determine neuronal placement in the *Drosophila* brain. *Curr. Biol.* *21*, 2000–2005.
44. Tuthill, J.C., Nern, A., Rubin, G.M., and Reiser, M.B. (2014). Wide-field feedback neurons dynamically tune early visual processing. *Neuron* *82*, 887–895.

Current Biology, Volume 27

Supplemental Information

The Temporal Tuning of the *Drosophila*

Motion Detectors Is Determined

by the Dynamics of Their Input Elements

Alexander Arenz, Michael S. Drews, Florian G. Richter, Georg Ammer, and Alexander Borst

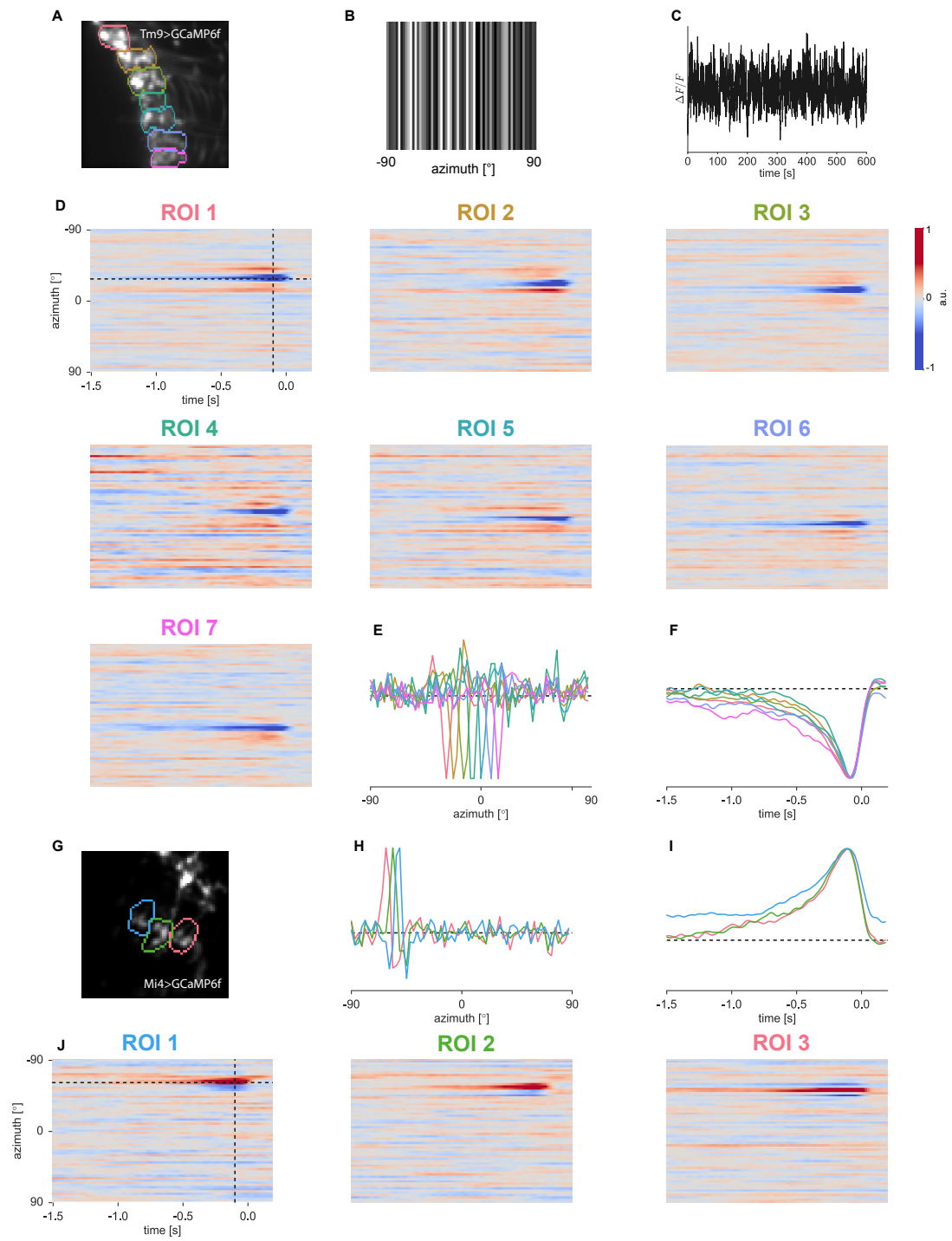


Figure S1. Related to Figure 2. Example acquisition of spatiotemporal receptive fields via stochastic stimulation and reverse correlation of calcium signals for the neurons Tm9 and Mi4.

(A) 2-photon image from a fly expressing GCaMP6f in Tm9 axon terminals in the lobula. Highlighted in color are seven manually drawn regions of interest (ROIs) around individual terminals from neighboring columns.

(B) Snapshot of one frame of the one-dimensional horizontal noise stimulus.

(C) Calcium trace from a single ROI in response to 10 minutes of white noise stimulation.

(D) Spatiotemporal receptive fields obtained by reverse correlation of the calcium signals in each ROI with the stimulus.

(E) Cross-sections through the receptive fields along the space axis reflecting the retinotopic organisation of the lobula.

(F) Cross-sections through the receptive fields along the temporal axis revealing the low-pass characteristics of Tm9.

(G-J) Same for Mi4.

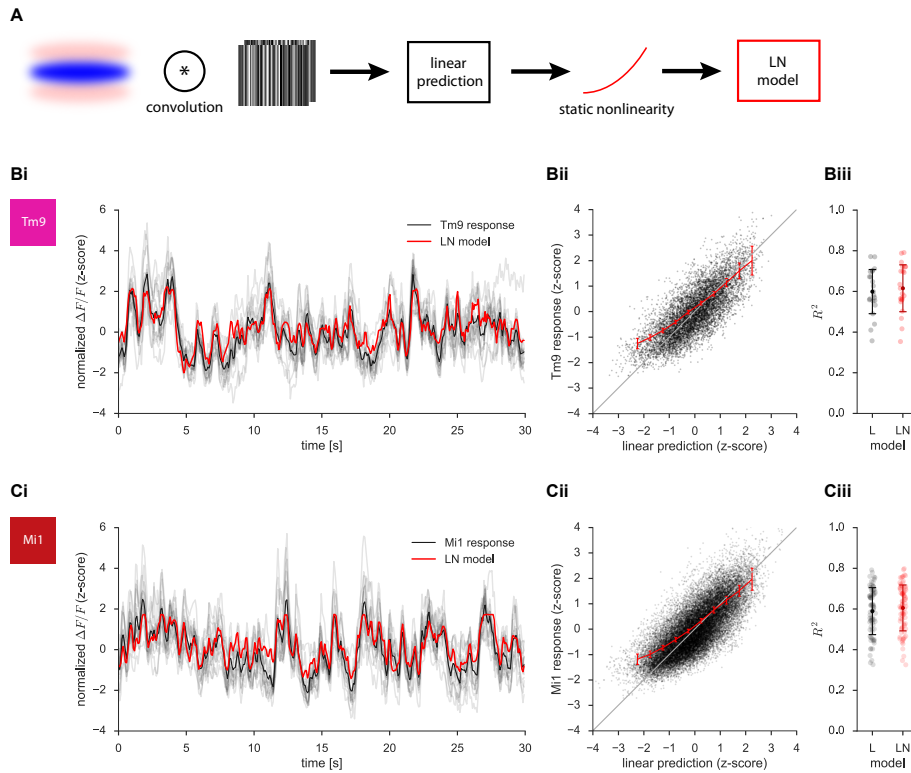


Figure S2. Related to Figure 2. Prediction of calcium responses in Tm9 and Mi1 terminals from the linear spatiotemporal receptive fields.

(A) Schematic of the model. The linear prediction of individual axon terminal responses (of Tm9 or Mi1) to a white noise stimulus is given by the convolution of the stimulus with the respective spatio-temporal receptive field of the cell. A linear-nonlinear model (LN) is built by remapping the output of the linear prediction with a static nonlinearity.

(Bi) Actual response of an exemplary Tm9 axon terminal (black) and the prediction of the LN model (red). (Bii) Scatter plot of the linear prediction against the actual response for all cells recorded. The static nonlinearity (red) is obtained by averaging the point cloud within discrete bins along the x-axis for each axon terminal. (Biii) Coefficient of determination for the linear model (L, black) and the linear-nonlinear model (LN, red). The linear model prediction alone accounted for 60% and the LN model for 62% of the response variance. Circles represent measurements of individual terminals, the bar shows the standard deviation and the mean among all cells measured ($N = 4$, $n = 22$).

(C) Same as in (B), but for Mi1 ($N = 4$, $n = 78$). The L model alone accounted for 59% and the LN model for 61% of the response variance.

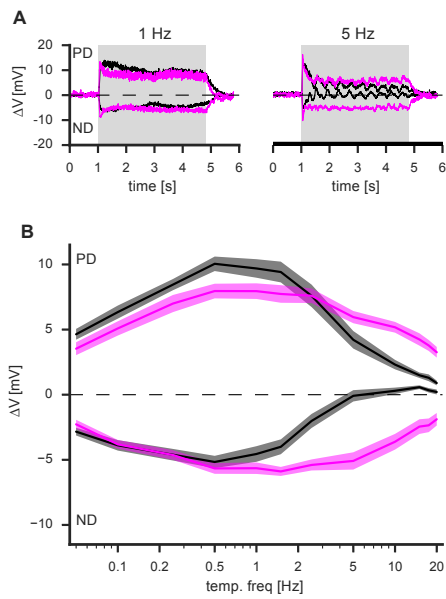
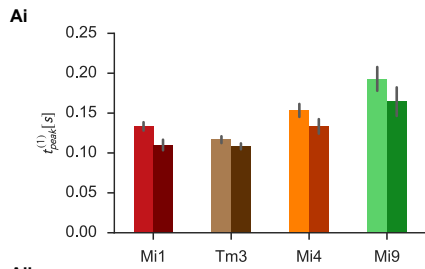


Figure S3. Related to Figure 3. Temporal frequency tunings of lobula plate tangential cells change with the application of the octopamine agonist CDM.

(A) Voltage responses of HS and VS tangential cells in the lobula plate (population average, $N = 15$ flies, $n=15$ cells) to square-wave gratings moving in the preferred or null direction in control (black) and after application of CDM (magenta) for gratings moving at a temporal frequency of 1 Hz (left) or 5 Hz (right). The period of motion of the grating is indicated by the grey-shaded region.

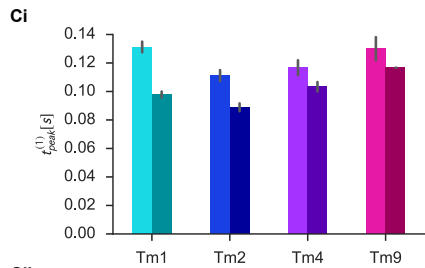
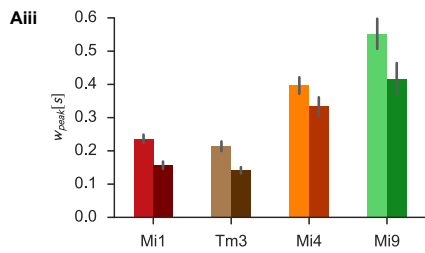
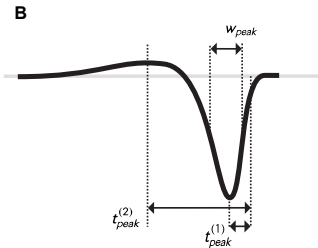
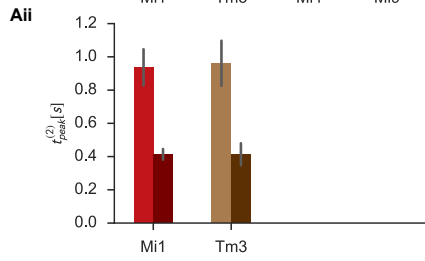
(B) Average voltage responses over the stimulation period for square-wave gratings at different temporal frequencies. Responses, measured as average voltage deflections over the whole stimulus period, peaked at 0.5 Hz in both the preferred (as maximum average depolarization) and null (as maximum average hyperpolarization) direction. Application of the octopamine agonist chlordimeform (CDM; magenta) at a final concentration of 20 μM resulted in increased responses to higher temporal frequencies from 2-20 Hz.



Aiv

	$t_{peak}^{(1)}$	$t_{peak}^{(2)}$	W_{peak}
Mi1	0.108	0.013	0.014
Tm3	0.076	0.004	< 0.001
Mi4	0.033	n.a	0.041
Mi9	0.259	n.a	0.037

control vs CDM



Civ

	$t_{peak}^{(1)}$	$t_{peak}^{(2)}$	W_{peak} [s]
Tm1	< 0.001	0.004	< 0.001
Tm2	< 0.001	0.005	< 0.001
Tm4	0.016	0.564	0.003
Tm9	0.178	n.a	0.015

control vs CDM

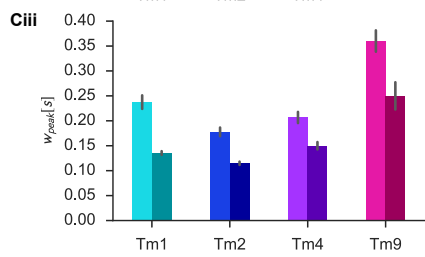
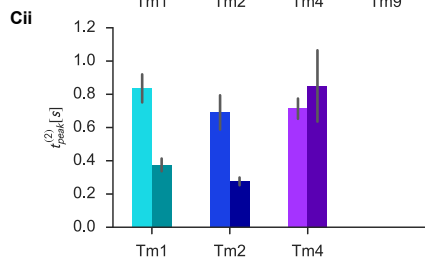


Figure S4. Related to Figure 2 and 4. Analysis of the temporal filters of the inputs to T4 and T5.

(A) T4 inputs. We quantified the shape of the temporal filters, as well as their change after application of CDM, by three measures (B): the time-to-peak for the first peak ($t_{\text{peak}}^{(1)}$, (Ai)) and, for the biphasic filter kernels of band-pass filters, to the second peak ($t_{\text{peak}}^{(2)}$, (Aii)), as well as the full-width at half-maximum for the first peak (w_{peak} , (Aiii)) of the temporal kernel. Measurements after application of CDM are presented in a darker color shade (right bars) than for the control condition (left bars) of the respective cell. Statistical comparisons between control and CDM condition (based on a paired t-test) are shown in (Aiv), highlighted in red color when statistical significance is observed (with a gradient in the red nuance from light to dark red indicating p values of $p < 0.05$, $p < 0.01$ and $p < 0.001$).
(C) Same, for T5 inputs.

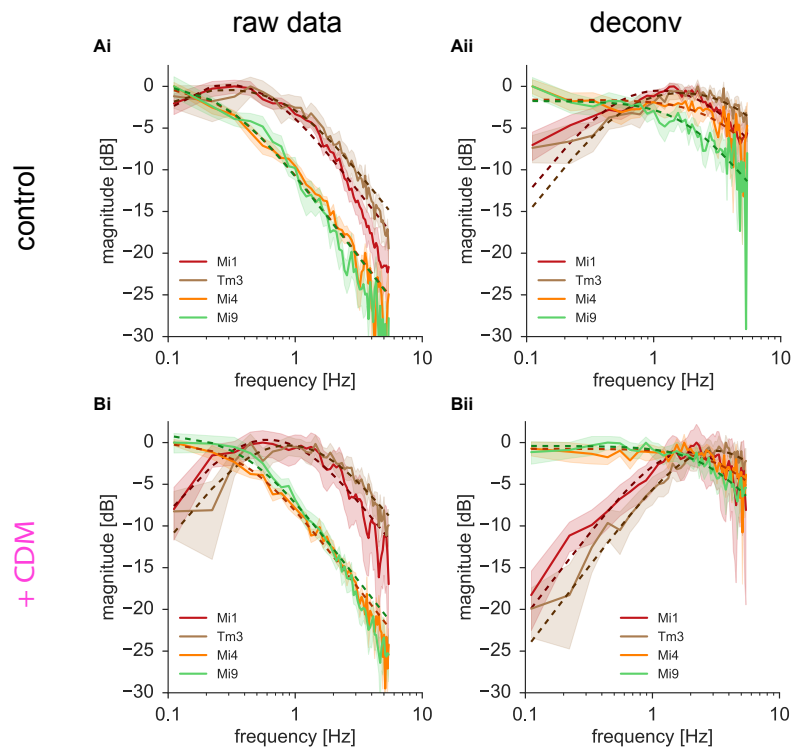


Figure S5. Related to Figure 5. Model fitting on the frequency spectra of the ON pathway elements.

(Ai) Frequency spectrum derived from calcium imaging experiments for the ON pathway columnar neurons Mi1, Tm3, Mi4, Mi9. (Aii) Frequency spectrum after deconvolution with a low-pass filter representing the dynamics of the calcium indicator GCaMP6f. Dashed lines represent the fitted frequency responses of 1st order band-pass or low-pass filters.

(Bi, Bii) Like (Ai, Aii), for the spectra determined from the recordings after application of CDM.

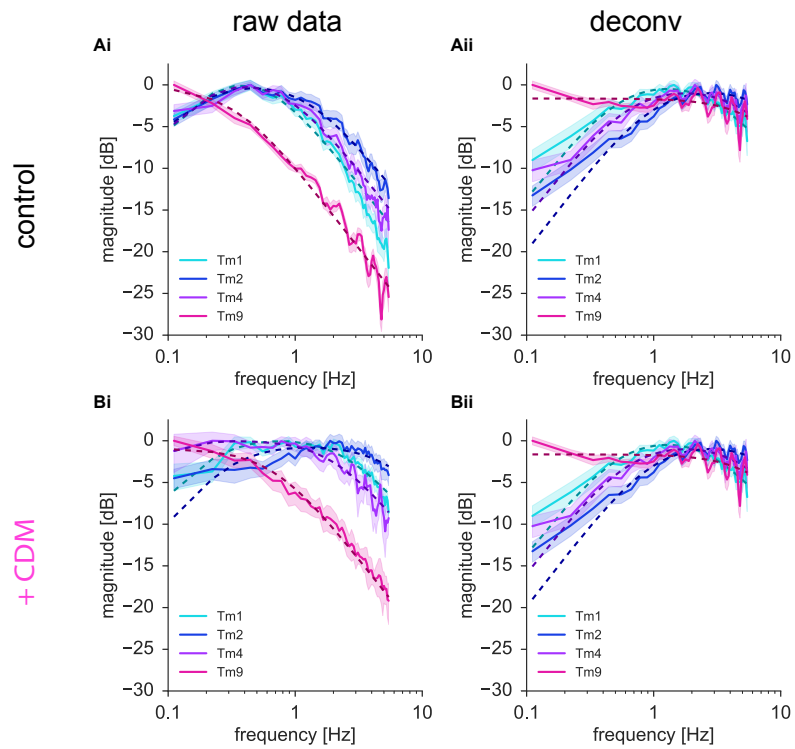


Figure S6. Related to Figure 5. Model fitting on the temporal filter frequency spectra of the OFF pathway elements.

(Ai) Measured frequency spectra based on calcium imaging experiments for the OFF pathway elements Tm1, Tm2, Tm4 and Tm9. (Aii) Frequency spectra after deconvolution with a filter describing the dynamics of the calcium indicator. Dashed lines represent the fitted frequency responses of 1st order band-pass or low-pass filters.

(Bi, Bii) Same as (Ai, Aii), after application of CDM.

	Mi1		Tm3		Mi4		Mi9	
	control	+ CDM						
A_{sur}	1.271	1.314	0.996	1.204	1.007	1.000	0.982	1.060
$t_{\text{HP, rise}}$	1.078 s	0.445 s	1.769 s	0.340 s				
$t_{\text{LP, rise}}$	0.266 s	0.143 s	0.158 s	0.086 s	0.519 s	0.370 s	0.546 s	0.373 s
$R^2_{\text{LP, rise}}$	0.975	0.942	0.971	0.925	0.984	0.990	0.982	0.987
A_{deconv}	1.146	1.643	1.035	2.034	0.831	0.906	0.789	0.940
$t_{\text{HP, deconv}}$	0.318 s	0.075 s	0.260 s	0.044 s				
$t_{\text{LP, deconv}}$	0.054 s	0.075 s	0.027 s	0.044 s	0.038 s	0.028 s	0.077 s	0.043 s
$R^2_{\text{LP, deconv}}$	0.872	0.851	0.768	0.955	0.666	0.643	0.832	0.906
$A_{\text{sur}} / A_{\text{con}}$	0.022	0.028	0.000	0.000	0.132	0.093	0.063	0.043
FWHM_{con}	6.81 °	7.09 °	11.91 °	12.40 °	6.47 °	6.49 °	6.37 °	6.37 °
FWHM_{sur}	28.81 °	19.86 °	-	-	16.14 °	20.02 °	23.98 °	28.08 °
R^2_{LP}	0.995	0.990	0.985	0.984	0.987	0.989	0.980	0.992

Table S1. Related to Figure 2 and 4. Spatio-temporal response properties of T4 input cells.
Numerical parameters derived from the model fits to the temporal and the spatial components of the spatio-temporal receptive fields obtained from reverse correlation for the ON-pathway neurons.

	Tm1		Tm2		Tm4		Tm9	
	control	+ CDM						
A_{raw}	1.419	1.072	1.068	0.933	1.218	0.990	0.961	0.890
$t_{ISI,raw}$	0.632 s	0.754 s	0.962 s	0.558 s	0.788 s	2.210 s		
$t_{LP,raw}$	0.271 s	0.051 s	0.113 s	0.020 s	0.186 s	0.070 s	0.462 s	0.220 s
$R^2_{LP,raw}$	0.978	0.901	0.979	0.564	0.972	0.930	0.985	0.981
A_{deconv}	1.117	2.217	1.038	2.657	1.018	1.002	0.827	0.836
$t_{ISI,deconv}$	0.296 s	0.032 s	0.153 s	0.018 s	0.249 s	0.086 s		
$t_{LP,deconv}$	0.044 s	0.032 s	0.014 s	0.018 s	0.024 s	0.015 s	0.017 s	0.008 s
$R^2_{LP,deconv}$	0.895	0.974	0.893	0.990	0.807	0.880	0.273	0.226
A_{str} / A_{cen}	0.040	0.029	0.035	0.026	0.054	0.005	0.046	0.071
$FWHM_{cen}$	8,12 °	7,34 °	7,93 °	7,23 °	11,45 °	10,10 °	6,92 °	6,53 °
$FWHM_{str}$	27,14 °	20,46 °	30,52 °	23,01 °	34,62 °	72,03 °	23,78 °	21,74 °
R^2_s	0.997	0.995	0.994	0.991	0.992	0.988	0.995	0.995

Table S2. Related to Figure 2 and 4. Spatio-temporal response properties of T5 input cells.

Numerical parameters derived from the model fits to the temporal and the spatial components of the spatio-temporal receptive fields obtained from reverse correlation for the OFF-pathway neurons.

Supplemental Experimental Procedures

Flies/preparation

Flies were raised and kept on standard cornmeal-agar medium on a 12 hour light/12 hour dark cycle at 25°C and 60% humidity. For patch-clamp recordings from tangential cells, Canton S flies were used. For calcium imaging experiments, the genetically-encoded calcium indicators GCaMP6f or GCaMP6m [S1] were expressed using the Gal4/UAS- or LexA/lexAop-system in cell-type specific driver lines, resulting in the following genotypes:

Short name	Genotype
Mi1>GC6f	<i>w-; R19F01-AD/UAS-GCaMP6f; R71D01-DBD/UAS-GCaMP6f</i>
Tm3>GC6f	<i>w-; UAS-GCaMP6f; R13E12-Gal4</i>
Mi4>GC6f	<i>w-; R48A07-AD/UAS-GCaMP6f; R13F11-DBD/UAS-GCaMP6f</i>
Mi9>GC6f	<i>w-; R48A07-AD/UAS-GCaMP6f; VT046779-DBD/UAS-GCaMP6f</i>
Tm1>GC6f	<i>w-; UAS-GCaMP6f; VT12717-Gal4</i>
Tm2>GC6f	<i>w-; UAS-GCaMP6f; VT12282-Gal4</i>
Tm4>GC6f	<i>w-; UAS-GCaMP6f; R35H01-Gal4</i>
Tm9>GC6f	<i>w-; UAS-GCaMP6f; VT65303-Gal4</i>
T4/T5>GC6m	<i>w-; Sp/CyO ; VT50384-lexA, lexAop-GCaMP6m/TM6b</i>

The transgenic fly lines driving split-Gal4 expression in the medulla neurons Mi1, Mi4 and Mi9, respectively, were generated and will be described in [S2] (with the Mi1 driver line corresponding to their transgenic fly line SS00809, Mi4 to SS01019, and Mi9 to SS02432).

For electrophysiological and calcium imaging experiments, flies were prepared as previously described [S3, S4]. Briefly, flies were anaesthetized on ice or with CO₂, fixed with their backs, legs and wings to a Plexiglas holder with the back of the head exposed to a recording chamber filled with fly external solution. The cuticula at the back of the head on one side was cut away with a fine hypodermic needle and removed together with muscles and air sacs covering the underlying optic lobe. To gain access to tangential cells for electrophysiological recordings, the neurolemma covering the brain was partially digested by applying 0.5mg/ml collagenase IV (Gibco) with a glass electrode to the brain until the tangential cell somata were exposed. Where indicated, the octopamine agonist chlordimeform (CDM, Sigma Aldrich) was added as a 2mM stock solution (in external solution) directly to the bath to yield a final concentration of 20 μM. Diffusion was allowed for 15 min before recordings recommenced.

Patch-clamp recordings from vertical and horizontal system tangential cells were performed as previously described [S4].

2-Photon calcium imaging

Calcium imaging was performed on custom-built 2-photon microscopes as previously described [S3] controlled with the ScanImage software in Matlab [S5]. Acquisition rates were between 3.8 and 15 Hz, image resolution between 64x64 and 128x128 pixels. Before starting the acquisition, we verified that the receptive fields of the cells were located on the stimulus arena by showing a search stimulus consisting of moving gratings.

Visual stimulation

For the study of visual responses of lobula plate tangential cells and T4/T5 neurons, visual stimuli were presented on an **LED arena**, based on a design by [S6], covering approximately 180° in azimuth and 90° in elevation. Stimuli covered the whole extent of the arena and were presented at full contrast. Square-wave gratings had a spatial wavelength of 24°, and moved with velocities of 1.2-480°/s in the preferred and null direction, corresponding to temporal frequencies ranging from 0.05 to 20°/s. Single stimulation periods of moving gratings lasted for 3.8 s, separated by periods of 5 s where the grating remained stationary. For the edge velocity tuning, bright or dark edges of full contrast were presented, moving at velocities of 3 to 300 °/s in the preferred (up) and null direction (down) of T4c/T5c neurons, separated by 6 s. All stimuli were presented in a pseudo-random order with 3-5 repetitions per stimulus.

The spatio-temporal response properties of the Mi and Tm columnar input elements were determined on a custom-built **projector-based arena** that allowed for greater stimulus flexibility. Stimuli were projected with 2 commercial micro-projectors (TI DLP Lightcrafter 3000) onto the back of an opaque cylindrical screen covering 180° in azimuth and 105° in elevation of the fly's visual field. The projectors were programmed to use only the green LED (OSRAM L CG H9RN) which emits light between 500nm to 600nm wavelength. This increased the refresh rate from 60 to 180 Hz (at 8 bit color depth). To prevent overlap between the spectra of the GCaMP signal and the arena light, we placed two long-pass filters (Thorlabs FEL0550 and FGL550) in front of each projector restricting the stimulus light to wavelengths above 550nm. A band-pass filter in front of the photomultiplier (Brightline 520/35) allowed only the portion of the light within the GCaMP emission spectrum to be detected. Additional shielding of stray light from the arena with black foil effectively suppressed any leak of the arena light into the photomultiplier signal. The maximum luminance achieved by our stimulation system is 276 ± 48 cd/m². For all stimuli used here, we set the medium brightness to a 8-bit grayscale value of 50, which corresponds to a medium luminance of 55 ± 11 cd/m².

Stimuli were rendered using a custom written software in Python 2.7. To account for the curvature of the arena screen, our software pre-distorts the generated images such that the projected image appears as a regular grating on the screen. For that, the software takes advantage of functions from Panda3D, a framework for 3D rendering for Python.

Gaussian noise stimulus

To generate the horizontal white noise stimulus, we partitioned the cylindrical screen into 64 bars, so that each bar covered an angle of approximately 2.8° in azimuth. For each bar, samples were drawn at a frame rate of 60 Hz from a Gaussian distribution, so that the standard deviation was at 25% contrast around a mean intensity value of 50 on the 8-bit grayscale of the display devices. We then filtered the random samples for each bar with a Gaussian filter with a standard deviation of 5 Hz in the frequency domain which leads to a stimulus auto-correlation function that is a Gaussian with approximately 45ms standard deviation. Since the calcium indicator dynamics of GCaMP and the data acquisition frame rate (12 Hz in this case) place a lower bound on the temporal precision of the signal we can extract from calcium imaging experiments, we restricted the frequency content of the stimulus in this way to the relevant domain. The whole stimulus sequence was 10 minutes long and was exported as a video file in H.264 format with lossless compression. For the vertical noise the same stimulus was rotated by 90° and scaled such that 54 bars covered the height of the screen, accounting for the aspect ratio of the screen being approximately 1.2.

Data acquisition and analysis

Data analysis was performed offline using custom-written routines in Matlab and Python 2.7 (with the SciPy and OpenCV-Python Libraries).

For the **electrophysiological experiments**, baseline-subtracted voltage responses of tangential cells were averaged across trials, and the response to gratings was quantified as the average voltage over the whole period of the respective stimulus presentation. Preferred direction was front-to-back for HS and down for VS cells, null direction the corresponding opposite direction. For Suppl. Figure S3 voltage responses over the individual stimuli were averaged across all cells.

Calcium imaging: Images were automatically registered using vertical and horizontal translations to correct for the movement of the brain. Fluorescence changes ($\Delta F/F$ values) were then calculated by dividing every registered frame by the average of the registered first 5 images of the recording. Regions of interest (ROIs) were selected on the average raw image by hand: in layer 10 of the medulla for the ON, in the lobula for the OFF pathway elements, outlining single terminals. For T4 and T5 neurons, ROIs were routinely chosen in the lobula plate, encompassing small regions with single to few axon terminals, or selected to cover single neurites between medulla or lobula and lobula plate. For Figure 3D&E, ROIs were drawn in the medulla for T4 and in the lobula for T5 neurons to separate those 2 cell types. Averaging the fluorescence change over this ROI in space resulted in a $\Delta F/F$ time course. Neuronal responses were quantified as the maximum $\Delta F/F$ value over the stimulation period plus the subsequent 0.5 s, subtracted by the average of the baseline period covering the 2 frames before the respective stimulus onset. To average across cells/ROIs, responses were first normalized to the maximum response of each ROI to the corresponding stimulus set. For edges, normalization was performed separately to ON and OFF stimuli to take any selection bias for T4 or T5 cells within the ROI into account.

White noise reverse-correlation

For the input elements, spatio-temporal receptive fields were calculated following standard reverse-correlation methods (Figure S1) [S7, S8]. First, the mean value was subtracted from the raw signals of single ROIs by using a low-pass filtered version of the signal (Gaussian filter with 120 seconds standard deviation) as a baseline for a $\Delta F/F$ -like representation of the signal. This effectively removed slow baseline fluctuations caused by bleaching and very slow changes in the average calcium level from the signals.

We then calculated the stimulus-response reverse correlation function

$$K(x, \tau) = \int_0^T dt S(x, t - \tau) \cdot R(t)$$

where S denotes the stimulus and R the response of the neuron.

The resulting spatiotemporal fields were normalized in z-score and as a quality control only receptive fields with peak amplitudes above 10 standard deviations from the mean were taken for further analysis (for Mi9 the threshold was lowered to 7). Cross-sections through the receptive fields along the space axis were fit with a Gaussian function to determine the position of the peak.

Since one imaging frame is built up continuously over one sample time, ROIs lying at different y-coordinates in the image will in fact be imaged at slightly different times. Since the stimulus is presented at a higher frame rate of 60 Hz, this leads to a notable peak shift between the impulse responses of different ROIs. We corrected for this by translating the spatiotemporal receptive field of each ROI by a) the time difference between the start of a frame and the effective sampling point estimated by the y-coordinate of the center of mass of the respective ROI and b) the start time of the white noise stimulus within the very first frame acquired during stimulation.

Spatio-temporal receptive fields resulting from different ROIs (that were retinotopically shifted) were then centered about each other to generate a mean receptive field. To ensure receptive fields of input elements were fully covered, cells with a receptive field center less than 10 pixels (28°) from the edge of the arena were excluded.

Frozen noise

Filter kernels were validated by testing their ability to predict the neuronal responses from the stimulus. For this, neurons were again stimulated with a white-noise stimulus, only this time part of the stimulus consisted of 15 repetitions (each 30 seconds long) of a white-noise sequence ('frozen noise') to eliminate noise in the neuronal responses. As above, spatio-temporal filter kernels were then reconstructed from responses to single repetition stimulus sequences (20 minutes long). Analogously to above, only receptive fields with a peak higher than 20 standard deviations were included for further analysis. Subsequently the averaged response during the held-out test portion of the stimulus was predicted for each recorded cell individually. Linear predictions were obtained by convolution of the spatio-temporal filter kernels with the frozen noise stimulus along the time axis. Filter kernels were thresholded versions of the spatio-temporal receptive fields (all values below 5% of the peak amplitude as well as regions further away than 15° from the receptive field center were set to zero). Both, the predicted response trace and the actual mean response to the frozen noise stimulus, were normalized in z-score in order to make different cells with varying calcium indicator expression levels and therefore different absolute signal values comparable. The static nonlinearity for the LN model was estimated for each cell by averaging all values from the actual mean response corresponding to values of the predicted response within bins of size 0.5 from -2.5 to +2.5 z-score (see scatter plots Bii and Cii in Suppl. Figure S2). Prediction accuracy of the linear filter was assessed through the correlation of the predicted versus actual response of the neuron [S9].

Spatial receptive field model

The one-dimensional spatial receptive fields (Figure 2 E-H and K-N, top and right) are cross-sections through the peak of the spatiotemporal receptive fields along the space axis and are averaged over the 12 samples (200ms) around the peak. For almost all columnar neurons measured we found a small-field, antagonistic center-surround organization of the spatial receptive field using both the horizontal and the vertical white noise stimulus.

Mathematically, receptive fields of this kind can be described as a difference of Gaussians

$$RF_{1D}(\varphi) = e^{-\frac{\varphi^2}{2\sigma_{cen}^2}} - A_{rel} \cdot e^{-\frac{\varphi^2}{2\sigma_{sur}^2}}$$

without loss of generality for the horizontal one-dimensional receptive field along the azimuth φ . Here, σ_{cen} and σ_{sur} are the standard deviations of center and surround, respectively, and $A_{rel} = A_{sur}/A_{cen}$ denotes the relative strength of the surround in relation to the amplitude of the center Gaussian (which is normalized to 1).

To reconstruct a two-dimensional receptive field from the measured one-dimensional projections, we chose the same mathematical approach as above, only in 2D:

$$RF_{2D}(\varphi, \vartheta) = e^{-\frac{(\varphi^2 + \vartheta^2)}{2\sigma_{cen}^2}} - A_{rel} \cdot e^{-\frac{(\varphi^2 + \vartheta^2)}{2\sigma_{sur}^2}}$$

For simplicity, throughout the analysis we used the small-angle approximation $\tan \vartheta \approx \vartheta$ for the vertical axis or the elevation ϑ even if receptive fields span angles larger than 5° . Thus, we neglected perspective distortions induced by the arena screen not being spherical, but cylindrical. Accounting for additional distortions induced by the relative displacement of the fly's body in relation to the elevation of the receptive field on the arena would require even more detailed mathematical description, yet we did not observe any severe irregularities in the spatial receptive fields.

It is important to note that receptive field estimation via a one-dimensional stimulus as performed here yields in fact a projection of the underlying two-dimensional spatial receptive field:

$$RF_{1D}(\varphi) = \int_{-\infty}^{\infty} RF_{2D}(\varphi, \vartheta) d\vartheta$$

Hence, we fitted the above function $RF_{2D}(\varphi, \vartheta)$ such that its projections along the horizontal and vertical axis would agree with the given one-dimensional receptive field projections measured via reverse correlation. The fitting procedure was implemented using standard least-square algorithms (SciPy 0.16.1). The resulting values for A_{rel} , σ_{cen} and σ_{sur} and the corresponding coefficients of the fit are given in Table S1 and S2 for each neuron type.

Temporal filter model

The time-reversed impulse responses shown in Figure 2&4 are cross-sections through the center of the spatiotemporal receptive fields along the time axis and are averaged over the three center pixels. For the frequency domain representations in Figure 2&4, impulse responses were Fourier-transformed, averaged, and the resulting amplitude spectrum (absolute value) was divided by the power spectrum of the stimulus for frequencies below 5.5 Hz (below the Nyquist frequency). This is equivalent to deconvolving the impulse response with the stimulus auto-correlation and thereby correcting for non-white input signals [S7]. All frequency-space-representations are plotted on a double logarithmic scale expressing all signal gains in decibel according to convention in filter theory.

The complicated relationships between calcium, calcium indicator, voltage and neurotransmitter release of a cell render it impossible to precisely characterize each of these aspects having access to only the calcium indicator fluorescence as a read-out. However, we can assume under certain conditions that the calcium indicator itself essentially acts as a simple low-pass filter on the calcium signal [S10], which is a kind of distortion that we are able to correct for by applying deconvolution.

GCaMP6f is designed to have especially fast kinetics. However, we can find decay constants in the order of several hundreds milliseconds that vary depending on the system under observation [S1]. As an approximation we chose a time constant of 350 ms for a plausible low-pass filter that distorted the calcium signals in our system, which lies in the range of reported decay constants for GCaMP6f [S1, S11].

We corrected the frequency domain representations of the temporal filters of all cells by dividing the spectra with the frequency response of a 1st order low-pass filter with this time constant. Since this was restricted to frequencies below the Nyquist frequency, we did not have to apply additional techniques to avoid the impact of poor signal-to-noise ratios at higher frequencies.

For quantitative description and further simulations, we sought to describe the response characteristic of each cell under each condition with a simplified model that catches the main properties. For that, we fitted simple 1st order filters to the corrected frequency responses of all cells. We did this separately for each condition, i.e. for control and CDM condition and for the raw filters (corrected by the stimulus power spectrum only) and the deconvolved filters (corrected by the GCaMP filter) respectively.

In particular, we approximated Mi1, Tm3, Tm1, Tm2 and Tm4 as band-pass filters and fitted a band-pass model consisting of a 1st order high-pass and a 1st order low-pass filter to the frequency responses (Figures S5, S6). The band-pass model was parametrized by a multiplicative amplitude and the two time constants of the filters. Parameters were optimized using a standard implementation of the Levenberg-Marquardt algorithm (SciPy). Similarly, Mi4, Mi9 and Tm9 frequency responses were fit using a 1st order low-pass filter model.

Computational modeling

Neural simulations (Figure 5 and 6) were based on a motion detector that combines preferred-direction enhancement and null-direction suppression, resembling a hybrid of a Hassenstein-Reichardt half-detector and a Barlow-Levick detector, as suggested in [S12].

Stimuli were simulated in a 2-dimensional space covering 90° in both azimuth and elevation with 1° resolution. Each hypothetical motion (half-)detector had three neighboring input lines (termed A, B and C) which were offset by 5° from each other along the horizontal axis (for simplicity). Each input line consisted of a spatial and a temporal filter that was applied to the stimulus before further processing. The spatial filter was modeled as a 2D convolution with a Mexican hat filter kernel using the above definition (see “Spatial receptive field model”) and the fitted parameters from table S1 and S2. The temporal filter consisted of either a 1st order band-pass or as a 1st order low-pass filter with the time constants from the table correspondingly. Subsequent rectification simulated the polarity selectivity of the input lines to the downstream motion detector. To implement the nonlinear interaction between the three input lines in the most simplified, we modelled the nonlinear action as $A \cdot B / (C + 0.1)$ involving only one free parameter to avoid division by zero. 270 of these elementary motion detectors were arranged on a 2-dimensional grid, separated by 5° from each other.

To evaluate the performance and tuning of the simulated detectors across stimulus frequencies, we measured the mean response of the simulated (half-)detectors to moving gratings at different speeds. Vertically oriented square wave gratings of 24° wavelength were swept over the detector array with 50 different velocities corresponding to 50 different contrast frequencies

logarithmically spaced between 0.01 Hz and 20 Hz. The gratings moved for 5s to the right followed by a pause of 0.5s and 5s of motion in the opposite direction. The time step for all simulations was 10 ms. The direction of the stimulus that elicited the strongest response across all frequencies was termed the preferred direction (PD) of the respective motion detector. Consequently, the other direction was the null direction (ND).

The direction selectivity of the resulting tuning curve was evaluated by defining a direction selectivity index (DSI)

$$DSI = \frac{\sum PD - \sum ND}{\sum PD + \sum ND}$$

where the sum goes over all frequencies simulated. This definition produces DSI values between 0 and 1, where 1 means perfect, and 0 means no direction selectivity. Secondly, the optimal frequency f_{opt} was defined as the stimulus frequency that elicited the strongest response in PD direction.

The above measure only quantifies the response difference between the two opposing directions of motion along the main axis of the detector. However, it cannot distinguish between detectors that differ in their response properties to intermediate directions of motion. Hence, we additionally assessed the directional tuning specificity of each detector by measuring its response to differently oriented moving gratings. We stimulated the model with square wave gratings of 24° wavelength, rotated by different angles from 0° to 360° in steps of 30° , and measured the mean response of the detector array at the optimal frequency f_{opt} , as determined above. From the corresponding simulated responses, the direction selectivity was quantified as the length of the normalized response vector:

$$L_{dir} = \frac{\left| \sum_{\varphi} \vec{v}(\varphi) \right|}{\sum_{\varphi} |\vec{v}(\varphi)|}$$

where $\vec{v}(\varphi)$ is a vector proportionally scaled with the mean detector response and pointing in the corresponding stimulus direction of motion given by the rotation angle φ of the stimulus. This quantity L_{dir} has been suggested as a robust measure of direction selectivity that includes both relative response magnitude and tuning width of a direction selective neuron [S13].

For the bar plots in Figure 5B&E (right column) the simulations were repeated also for all possible implementations of a two-arm detector whose nonlinear interaction was either modelled as $A \cdot B$ for a classical Hassenstein-Reichardt-(half-)detector or as $B/(C + 0.1)$ for a Barlow-Levick-detector.

All simulations were performed using Python 2.7.

Statistics

Throughout this article, values are reported as mean \pm standard error (SEM). In order to quantify the significance of the effect of CDM application on the temporal response characteristics of the medulla cells, we defined three different measures for the impulse responses: a) the time to the first peak $t_{peak}^{(1)}$ is the time between the onset of the impulse response (defined as the time when it has reached 15% of its maximum value) and the time when it has reached its maximum value; b) the time to the second peak $t_{peak}^{(2)}$ is similarly defined as the time between the onset of the impulse response and the peak of the subsequent undershoot or overshoot, which is defined only for the band-pass filters; c) lastly, we defined a peak width w_{peak} as the width of the first

peak at half maximum. We quantified these values for each fly and tested the change between control and CDM condition for significance using a paired t-test.

Supplemental References

- S1. Chen, T.-W., Wardill, T. J., Sun, Y., Pulver, S. R., Renninger, S. L., Baohan, A., Schreiter, E. R., Kerr, R. A., Orger, M. B., Jayaraman, V., et al. (2013). Ultrasensitive fluorescent proteins for imaging neuronal activity. *Nature* 499, 295–300.
- S2. Strother, J. A., Wu, S.-T., Wong, A. M., Nern, A., Rogers, E. M., Le, J. Q., Rubin, G. M., and Reiser, M. B. The emergence of directional selectivity in the visual motion pathway of *Drosophila*. *Neuron* *in press*.
- S3. Maisak, M. S., Haag, J., Ammer, G., Serbe, E., Meier, M., Leonhardt, A., Schilling, T., Bahl, A., Rubin, G. M., Nern, A., et al. (2013). A directional tuning map of *Drosophila* elementary motion detectors. *Nature* 500, 212–216.
- S4. Ammer, G., Leonhardt, A., Bahl, A., Dickson, B. J., and Borst, A. (2015). Functional specialization of neural input elements to the *Drosophila* ON motion detector. *Curr Biol* 25, 2247–2253.
- S5. Pologruto, T. A., Sabatini, B. L., and Svoboda, K. (2003). ScanImage: flexible software for operating laser scanning microscopes. *BioMed Eng OnLine* 2, 13.
- S6. Reiser, M. B., and Dickinson, M. H. (2008). A modular display system for insect behavioral neuroscience. *J Neurosci Methods* 167, 127–139.
- S7. French, A. S. (1976). Practical nonlinear system analysis by Wiener kernel estimation in the frequency domain. *Biol Cybern* 24, 111–119.
- S8. Dayan, P., and Abbott, L. F. (2005). *Theoretical Neuroscience*. MIT Press.
- S9. Clark, D. A., Bursztyn, L., Horowitz, M. A., Schnitzer, M. J., and Clandinin, T. R. (2011). Defining the computational structure of the motion detector in *Drosophila*. *Neuron* 70, 1165–1177.
- S10. Borst, A., and Abarbanel, H. D. I. (2007). Relating a calcium indicator signal to the unperturbed calcium concentration time-course. *Theor Biol Med Model* 4, 7.
- S11. Schnell, B., Weir, P. T., Roth, E., Fairhall, A. L., and Dickinson, M. H. (2014). Cellular mechanisms for integral feedback in visually guided behavior. *Proc Natl Acad Sci USA* 111, 5700–5705.
- S12. Haag, J., Arenz, A., Serbe, E., Gabbiani, F., and Borst, A. (2016). Complementary mechanisms create direction selectivity in the fly. *eLife* 5:e17421.
- S13. Mazurek, M., Kager, M., and Van Hooser, S. D. (2014). Robust quantification of orientation selectivity and direction selectivity. *Front Neural Circuits* 8, 92.

2.2 GLUTAMATE SIGNALING IN THE FLY VISUAL SYSTEM

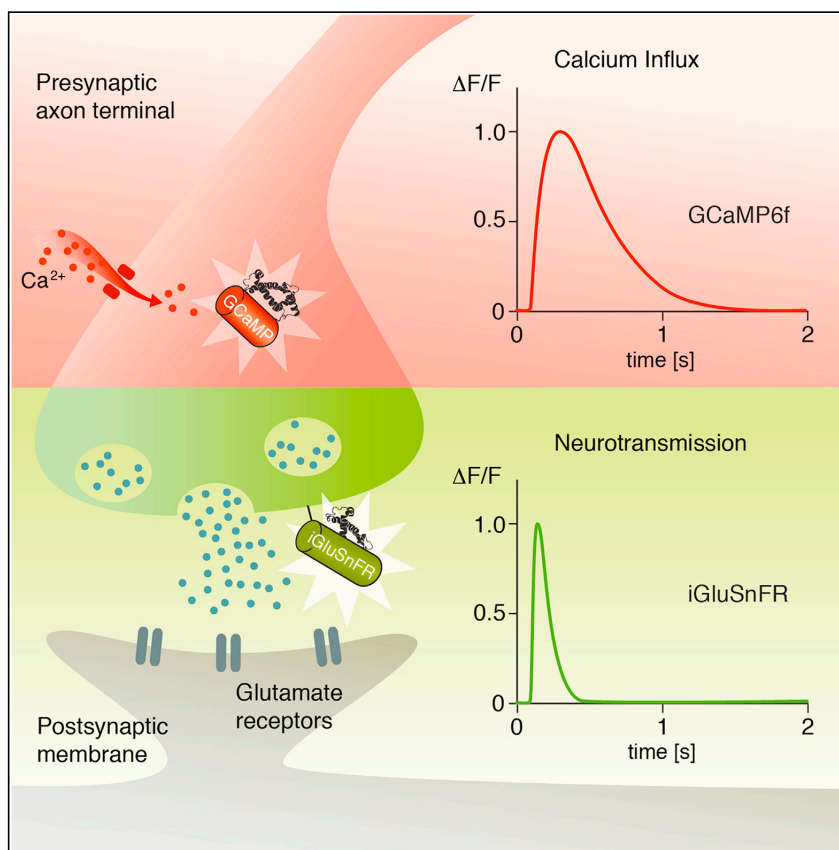
SUMMARY For a proper understanding of neural circuit function, it is important to know which signals neurons relay to their downstream partners. Calcium imaging with genetically encoded calcium sensors like GCaMP has become the default approach for mapping these responses. How well such measurements represent the true neurotransmitter output of any given cell, however, remains unclear. Here, we demonstrate the viability of the glutamate sensor iGluSnFR for 2-photon *in vivo* imaging in *Drosophila melanogaster* and prove its usefulness for estimating spatiotemporal receptive fields in the visual system. We compare the results obtained with iGluSnFR with the ones obtained with GCaMP6f and find that the spatial aspects of the receptive fields are preserved between indicators. In the temporal domain, however, measurements obtained with iGluSnFR reveal the underlying response properties to be much faster than those acquired with GCaMP6f. Our approach thus offers a more accurate description of glutamatergic neurons in the fruit fly.

AUTHORS Florian Richter, Sandra Fendl (co-first author), Jürgen Haag, Michael Drews, and Alexander Borst.

CONTRIBUTIONS F.G.R., S.F., and A.B. conceived the study and designed the experiments. F.G.R. conducted and analyzed the imaging experiments for Mi9 and L1. S.F. performed and analyzed all stainings. J.H. performed and analyzed the LPi experiments. M.S.D. performed data analysis and model fitting of the receptive fields. F.G.R. wrote the manuscript with the help of all authors.

Article

Glutamate Signaling in the Fly Visual System



Florian G. Richter,
Sandra Fendl,
Jürgen Haag,
Michael S. Drews,
Alexander Borst

frichter@neuro.mpg.de
(F.G.R.)
aborst@neuro.mpg.de (A.B.)

HIGHLIGHTS

The glutamate sensor iGluSnFR is suitable for 2-photon imaging in the fruit fly

Response properties obtained with iGluSnFR are much faster than those with GCaMP6f

Spatial aspects of receptive fields are preserved between indicators

Richter et al., iScience 7, 85–95
September 28, 2018 © 2018
The Author(s).
<https://doi.org/10.1016/j.isci.2018.08.019>



Article

Glutamate Signaling
in the Fly Visual SystemFlorian G. Richter,^{1,2,*} Sandra Fendl,^{1,2} Jürgen Haag,¹ Michael S. Drews,¹ and Alexander Borst^{1,3,*}

SUMMARY

For a proper understanding of neural circuit function, it is important to know which signals neurons relay to their downstream partners. Calcium imaging with genetically encoded calcium sensors like GCaMP has become the default approach for mapping these responses. How well such measurements represent the true neurotransmitter output of any given cell, however, remains unclear. Here, we demonstrate the viability of the glutamate sensor iGluSnFR for 2-photon *in vivo* imaging in *Drosophila melanogaster* and prove its usefulness for estimating spatiotemporal receptive fields in the visual system. We compare the results obtained with iGluSnFR with the ones obtained with GCaMP6f and find that the spatial aspects of the receptive fields are preserved between indicators. In the temporal domain, however, measurements obtained with iGluSnFR reveal the underlying response properties to be much faster than those acquired with GCaMP6f. Our approach thus offers a more accurate description of glutamatergic neurons in the fruit fly.

INTRODUCTION

To understand how neural circuits operate and carry out certain computations, it is essential to observe the signals that are transmitted from cell to cell. Synaptic transmission via chemical synapses proceeds in four major stages: (1) Depolarization in the presynapse opens voltage-gated calcium channels. (2) The resulting calcium influx leads to the fusion of transmitter-filled vesicles and the presynaptic membrane. (3) Transmitter molecules are released into the synaptic cleft where they diffuse and bind receptors in the postsynaptic membrane. (4) The subsequent activation of these receptors leads to opening or closing of ion channels, either directly or indirectly, with the resulting ion flux ultimately changing the postsynaptic membrane conductance and potential (reviewed in [Di Maio, 2008]). This fundamental signaling cascade, from electric potential to calcium to transmitter release to postsynaptic electric potential, orchestrates computation within any neuronal circuit.

For monitoring voltage changes, electrophysiology is the default approach. Here, direct observations of both de- and hyperpolarization in pre- or postsynaptic cells are possible. Due to the position or size of many neurons, however, direct single-cell recordings are often not feasible and have to be replaced by indirect extracellular recordings or optical imaging. Only recently genetically encoded voltage indicators (GEVIs) have emerged as powerful tools for recording neuronal activity (Cao et al., 2013; Jin et al., 2012; St-Pierre et al., 2014; Tsutsui et al., 2013; Yang et al., 2016). Experiments with optical voltage indicators such as ASAP2f that are compatible with 2-photon imaging, however, remain challenging due to weak signal-to-noise ratio (Yang et al., 2016). The fluorescence level of genetically encoded calcium indicators (GECIs) is thought to correlate with transmitter release and is therefore suitable for identifying the crucial signal to the postsynaptic cell (Zucker, 1993). Although GECIs are being improved continuously and some variants were designed to have especially fast kinetics (e.g., GCaMP6f [Chen et al., 2013]), temporal resolution is still limited due to calcium buffering (Borst and Abarbanel, 2007). This usually leads to decay constants in the order of several hundreds of milliseconds that vary depending on the system under observation (Arenz et al., 2017; Chen et al., 2013). For glutamatergic neurons, a tool to potentially overcome these limitations is the recently developed fast glutamate sensor iGluSnFR (Marvin et al., 2013).

Visual motion detection is a canonical example for computation in neural microcircuits. Prevalent models posit that, in both mammalian retina and fly visual system, local direction selectivity emerges from the nonlinear interaction between precisely tuned spatiotemporal filters (Barlow and Levick, 1965; Von Hassenstein and Reichardt, 1956). Recent work in connectomics on the visual system of *Drosophila melanogaster* has revealed this computation to be implemented by a circuit that consists of only a few dozen individual cells (Takemura et al., 2017). The optic lobe is the largest neuropil in the fruit fly's brain and consists of the

¹Max-Planck-Institute of Neurobiology, 82152 Martinsried, Germany

²These authors contributed equally

³Lead Contact

*Correspondence: frichter@neuro.mpg.de (F.G.R.), aborst@neuro.mpg.de (A.B.)
<https://doi.org/10.1016/j.isci.2018.08.019>



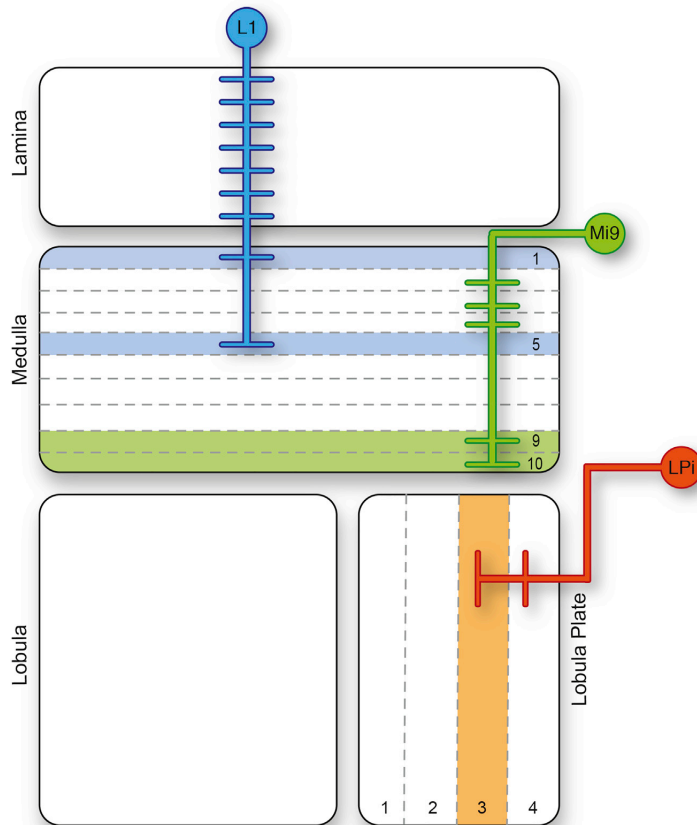


Figure 1. Schematic of the *Drosophila* Optic Lobe

Schematic of the *Drosophila* optic lobe with glutamatergic cell types in the motion vision pathway. The three cell types are not directly connected to each other but play an important role in the circuit. For the sake of simplicity, postsynaptic partners of the glutamatergic neurons are not displayed but can be reviewed in [Mauss et al. \(2015\)](#) and [Takemura et al. \(2011, 2017\)](#). Colored layers indicate area where we imaged glutamate release of the respective cell type.

four consecutive neuropils: lamina, medulla, lobula, and lobula plate (Figure 1). Lamina monopolar cells L1 and L2, among others, receive direct photoreceptor input and feed into two parallel pathways ([Bausenwein et al., 1992](#); [Bausenwein and Fischbach, 1992](#); [Borst, 2014](#); [Clark et al., 2011](#); [Joesch et al., 2010](#); [Rister et al., 2007](#); [Shinomiya et al., 2014](#); [Silies et al., 2013](#); [Takemura et al., 2017](#); [Tuthill et al., 2013](#)). The ON pathway processes the motion of light increments, whereas the OFF pathway processes the motion of light decrements only ([Eichner et al., 2011](#); [Joesch et al., 2013, 2010](#)). Among the medulla interneurons that connect the lamina cells to direction-selective T4 and T5 neurons ([Maisak et al., 2013](#); [Takemura et al., 2017](#)), we find the glutamatergic cell Mi9 that has been characterized with a receptive field responsive to OFF in the center and an antagonistic ON surround ([Arenz et al., 2017](#); [Strother et al., 2017](#)). T4 and T5 neurons each come in four subtypes, tuned to one of the four cardinal directions, and project, according to their preferred direction, to one of the four layers in the lobula plate. Here, T4 and T5 cells make excitatory cholinergic connections onto the dendrites of large tangential cells as well as onto inhibitory lobula plate interneurons (LPis). These neurons in turn inhibit large field tangential cells in the adjacent layer during null direction motion and thus increase their flow-field selectivity ([Hausen et al., 1980](#); [Hopp et al., 2014](#); [Schnell et al., 2010](#); [Scott et al., 2002](#); [Wasserman et al., 2015](#)). To provide this inhibition, LPis release glutamate onto the glutamate

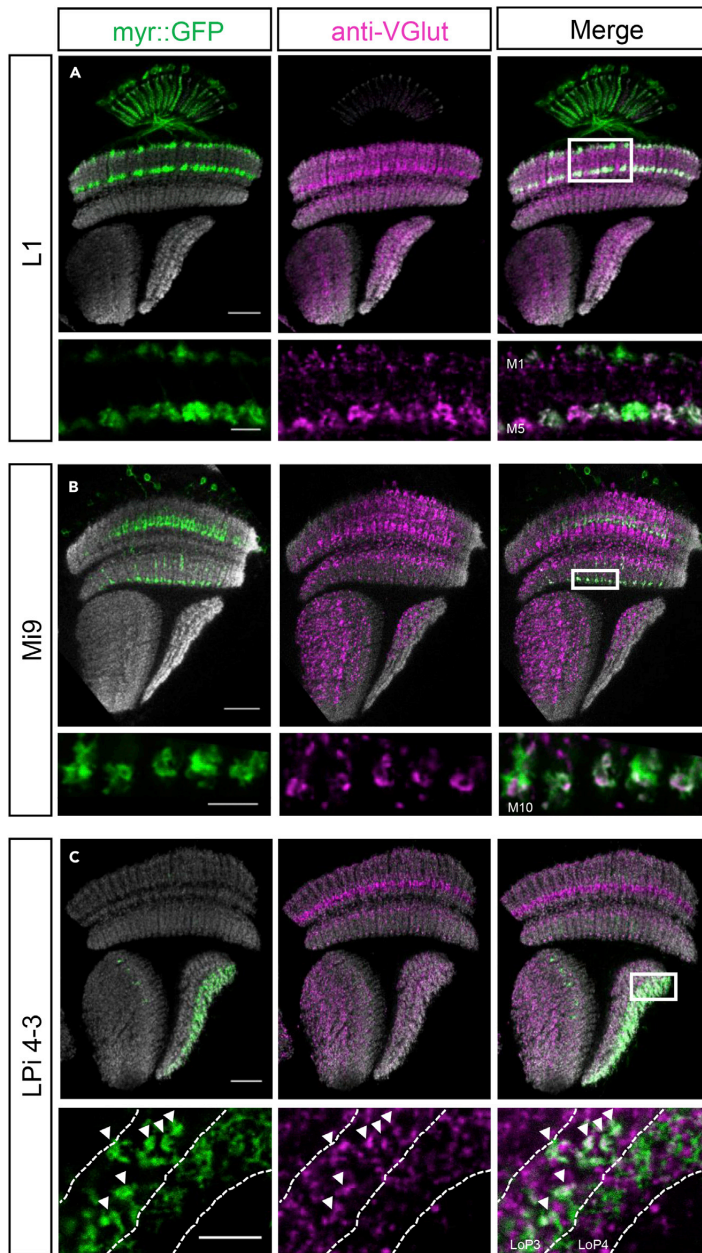


Figure 2. Vesicular Glutamate Transporter VGlut Localizes to Axon Terminals of L1, Mi9, and LPI4-3 Neurons Indicating their Glutamatergic Phenotype

(A–C) Upper rows show overviews of optic lobes with L1 (A), Mi9 (B), and LPI4-3 (C) labeled with myr::GFP (green), background staining against bruchpilot brp (gray), and anti-VGlut staining (magenta). In the lower rows higher magnifications of axon terminals of L1, Mi9, and LPI4-3 neurons are depicted (sections marked with white boxes in overview images).

Figure 2. Continued

(A) L1 axon terminals in medulla layers 1 and 5 show overlapping signal with anti-VGlu staining.
 (B) VGlu protein co-localizes with Mi9 axons in layer 10 of the medulla.
 (C) Lobula plate intrinsic neurons LPi4-3 have their dendrites in layer 4 and project their terminals to layer 3. Labeled with arrowheads are LPi boutons in layer 3 showing overlapping signal with anti-VGlu staining. Shown here are single planes of confocal stacks. Scale bar for overview of optic lobes is 20 μm . For higher magnification close-ups the scale is 5 μm . White dashed lines in the lower panel are manually drawn and indicate layers of the lobula plate.

receptor $\text{GluCl}\alpha$, which is an inhibitory glutamate receptor only found in invertebrates (Liu and Wilson, 2013; Mauss et al., 2015, 2014).

The exact biophysical mechanisms by which T4 and T5 become direction selective remain unclear. To understand on a cell-by-cell level how direction selectivity is achieved, precise measurements of the signals transmitted between neurons are crucial. In this study, we focus on the final stage of the synaptic signaling cascade, i.e., transmitter release. First, we confirm the neurotransmitter phenotype of all known glutamatergic cell types (L1, Mi9, LPi) in the *Drosophila* motion vision pathway. Second, using the recently developed fast glutamate sensor iGluSnFR (Marvin et al., 2013), we comprehensively characterize their spatiotemporal response profiles and compare them with the ones obtained expressing the genetically encoded calcium indicator GCaMP6f (Chen et al., 2013).

RESULTS**The Vesicular Glutamate Transporter VGlu Localizes to Axon Terminals of L1, Mi9, and LPi4-3 Neurons**

VGlu or DVGLUT (CG9887) is the only vesicular glutamate transporter known in *Drosophila*. VGlu is located in the vesicle membrane of glutamatergic neurons where it fills the synaptic vesicles with glutamate. The protein localizes to presynaptic terminals of all known glutamatergic neuromuscular junctions (NMJs) as well as to synapses throughout the CNS neuropil in *Drosophila* (Daniels, 2004). Hence, VGlu is the most commonly used marker for glutamatergic neurons. Several antibodies have been raised against VGlu to identify glutamatergic neurons in the nervous system of the fruit fly (Daniels, 2004; Mahr and Aberle, 2006).

Recent studies revealed the glutamatergic phenotype of L1, Mi9, and LPi neurons—each of them a crucial element of the motion vision pathway of the fruit fly (Joesch et al., 2010; Kolodziejczyk et al., 2008; Mauss et al., 2015; Takemura et al., 2017, 2011). The somata of these cell types showed positive immunoreactivity against the VGlu antibody, which was raised against a C-terminal peptide—CQMPSYDPOGYQQQ (Daniels, 2004). Interestingly, this antibody labeled mainly cell bodies of designated neurons. Since it is known that the vesicular glutamate transporter VGlu is localized to axon terminals, we investigated the glutamatergic transmitter phenotype of L1, Mi9, and LPi4-3 in more detail. We used a different anti-VGlu antibody (Mahr and Aberle, 2006), which only labels neuronal arborizations in the optic lobe neuropil and no somata. In general, the VGlu protein is highly abundant throughout all four neuropils of the optic lobe (Figure 2).

The axon terminals of L1 neurons show clear overlap with the anti-VGlu signal in layer M1 and M5 of the medulla (Figure 2A). The vesicular glutamate transporter VGlu resides at the presynaptic sites of L1 neurons, which indicates their glutamatergic phenotype. In layer M10 of the medulla, the same is found for Mi9 neurons: VGlu staining in this layer is co-localized with GFP-labeled Mi9 axon terminals (Figure 2B). This suggests that Mi9 neurons are glutamatergic and that they are the only source of glutamate in layer M10 of the medulla. Furthermore, we found an overlapping signal of LPi4-3 terminals in layer 3 of the lobula plate and anti-VGlu staining (Figure 2C). This confirms recent findings (Mauss et al., 2015) that described LPi neurons as glutamatergic, being presynaptic only in one of the two layers where it arborizes.

In summary, we could show that the protein VGlu localizes to axon terminals of the glutamatergic neurons L1, Mi9, and LPi4-3.

Faster Sensor Kinetics Enable More Precise Characterization of Visual Interneurons

One commonly used approach to characterize a sensory neuron is to find its preferred stimulus. This can be achieved by using a white noise input and cross-correlating the resulting output with the input (Dayan and

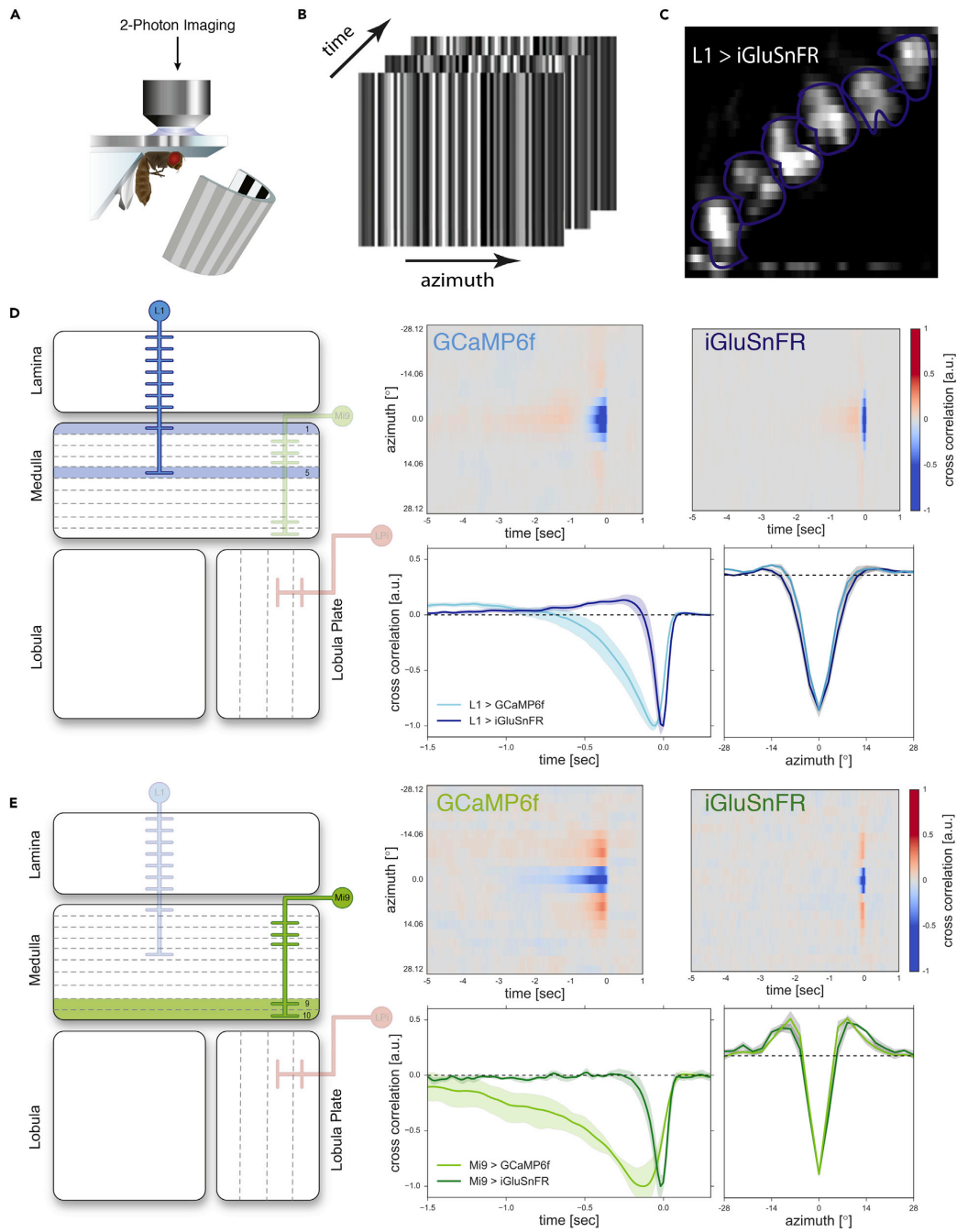


Figure 3. Response Properties of the ON Pathway Columnar Elements L1 and Mi9

(A) Experimental setup: Fly tethered to a plastic holder under the 2-photon microscope looking onto the stimulus arena (see also [Transparent Methods](#)).
 (B) Schematic of three frames of the white noise stimulus consisting of 64 horizontal bars.
 (C) Example of 2-photon image of L1 expressing iGluSnFR. In purple are manually drawn region of interest ROIs.
 (D) Left: Schematic of the *Drosophila* optic lobe. The cell type related to the right panel is highlighted. Right upper panel: Averaged aligned spatiotemporal receptive fields after reverse correlation of L1 expressing either the glutamate indicator iGluSnFR (5 flies and 66 cells) or GCaMP6f (5 flies and 60 cells). Cross sections along space and time axes result in receptive fields in right lower panel. Spatial receptive fields do not differ significantly for both indicators. Temporal kernels differ substantially. Impulse responses are shorter for iGluSnFR than for GCaMP6f. Shaded areas indicate a confidence interval of 95%.
 (E) Same as (D) only for Mi9 (with iGluSnFR: 5 flies, 26 cells; with GCaMP6f: 5 flies, 50 cells).

[Abbott, 2013](#); [French, 1976](#); [Ringach and Shapley, 2004](#)), which yields the linear spatiotemporal receptive field as a result (e.g., [Figures 3D and 3E](#), upper panel). The receptive field of a neuron is defined as the location of a stimulus in space and the time relative to its occurrence in which the neuron's response is modulated by the stimulus. The receptive field also describes the specific filtering properties of a system, in space as well as in time. Here, we use simple first-order low-pass, high-pass, or band-pass filters to quantify these filtering properties using the measured receptive fields. A low-pass filter only allows low frequencies to pass and attenuates high frequencies. Conversely, a high-pass filter attenuates low frequencies and allows high frequencies to pass. A band-pass filter is a combination of a high-pass and a low-pass filter in series, allowing signals within a certain frequency band to pass and attenuating all others ([Cruse, 1996](#)). In a linear system, the filters characterized this way are equivalent to the neurons' impulse responses. The temporal impulse response reveals critical aspects of the cellular response kinetics ([Dayan and Abbott, 2013](#); [Ringach and Shapley, 2004](#)).

For this reason, we characterized the spatial extent of the receptive fields as well as the response dynamics of all known glutamatergic cells in the motion vision circuit of *Drosophila* L1, Mi9, and LPi4-3. Expressing either the fast version of the genetically encoded calcium indicator GCaMP6f ([Chen et al., 2013](#)) or the fast glutamate-sensing reporter iGluSnFR ([Marvin et al., 2013](#)) with cell-type-specific Gal4 driver lines, we imaged glutamate and calcium signals in single axon terminals ([Figure 3C](#)). To precisely map the receptive fields of these cells, we used a one-dimensional white noise stimulus consisting of 2.8° wide vertical bars covering the full extent of the arena (180°, [Figure 3B](#), see also [Methods](#)). The spatiotemporal receptive fields were then determined from the neuron's calcium or glutamate response by reverse correlation. Cross sections through the peak of the spatiotemporal receptive fields along the space axis therefore yield the one-dimensional spatial receptive fields depicted in [Figures 3D and 3E](#). Cross sections along the time axis yield the temporal filtering properties of the neuron ([Chichilnisky, 2001](#); [Dayan and Abbott, 2013](#); [French, 1976](#); [Ringach, 2004](#)).

To calculate the spatial extent of the cells' receptive field, we fitted a Mexican hat function (also called difference of Gaussians) that best resembled the center-surround structure of the estimated spatial receptive fields. Both neurons show a small confined center of ~7° for Mi9 and 9–11° for L1. The full width at half maximum of the surround is about 40–50° for L1 and 20–30° for Mi9. Considering the uncertainty of the fitted model parameters, these values are similar and lie in the same order of magnitude when comparing results from imaging with both sensors. In addition, testing the raw data of both conditions against each other we find no significant difference (see [Figures S2A and S2B](#), p value > 0.5, Welch's t test) of spatial receptive fields neither for L1 nor for Mi9. Both neurons show a small confined center of ~7° for Mi9 and 9–11° for L1. The size of the surround has the same order of magnitude for both sensors, 40–50° for L1 and 20–30° for Mi9. This is within the range of uncertainty that the fit is subject to. Testing the raw data of both conditions against each other for the two cell types, however, does not yield a significant difference (see [Figures S2A and S2B](#), right panel).

For a reliable estimation of the time constants of the temporal responses, we transferred the impulse responses of L1 and Mi9 into frequency space and fitted either a first-order low-pass or a first-order band-pass filter to the neurons' responses (see [Figures S1C and S1D](#)). For L1, we find that the data are best represented by a band-pass filter. The filter derived from the iGluSnFR signal has a low-pass time constant of 70 ms and a high-pass time constant of about 400 ms (see [Figure S1A](#)). The time constants derived from the GCaMP6f signal are significantly larger with low-pass and high-pass time constants of 350 and about 1,180 ms, respectively. For Mi9, we find that the temporal properties are best described by a low-pass filter. The estimated time constant of the Mi9 temporal kernel ([Figure 3D](#), lower

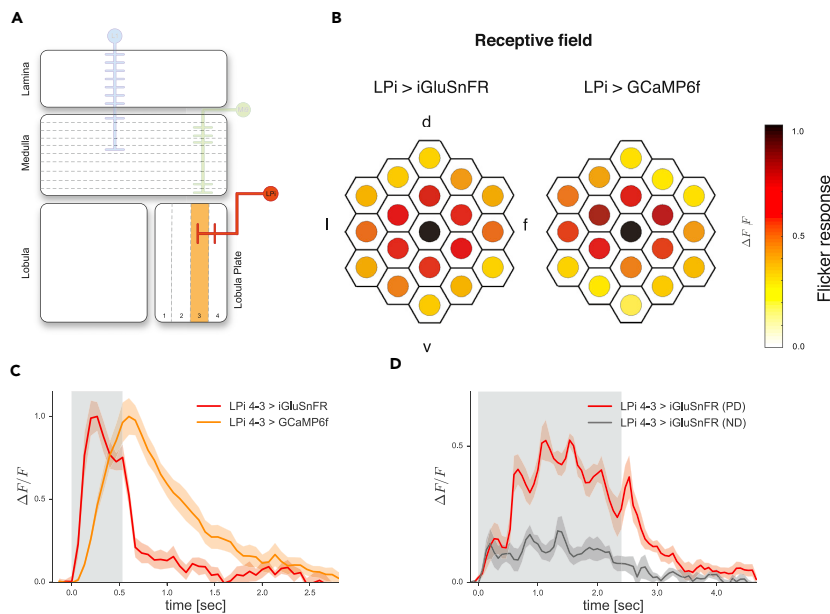


Figure 4. Response Properties of the Direction Selective Lobula Plate Interneuron LPI4-3

(A) Schematic of the *Drosophila* optic lobe with LPI4-3 highlighted.

(B) Comparison of spatial receptive field size of LPI4-3 cells recorded with iGluSnFR (left, $n = 24$ cells from 7 flies) or GCaMP6f (right, $n = 14$ cells from 5 flies). The responses of individual cells to flicker stimuli presented at 19 different columnar positions were averaged after alignment to the maximum (in black) and normalization. d, Dorsal; v, ventral; l, lateral; f, frontal.

(C) Time course of LPI4-3 response upon local flicker stimulation. The decay of the signal is faster for iGluSnFR response. (D) LPI4-3 expressing iGluSnFR show glutamatergic direction selective responses ($n = 8$ cells from 5 flies). Five consecutive flicker stimuli were shown along the preferred (downward) or null (upward) direction of the neuron, acting as apparent motion. Shaded areas indicate mean \pm SEM.

left) is 75 ms when measured with iGluSnFR compared with about 610 ms when measured with GCaMP6f (see Figure S1B).

For both cell types, the temporal kernel of the calcium response can be derived by low-pass filtering the faster glutamate signal. This is because the kinetics of the calcium sensor can be approximated by a low-pass filter when the intracellular calcium concentration is small compared to the KD value of the indicator (Borst and Abarbanel, 2007). For both cells, i.e., L1 and Mi9, we can fit the glutamatergic signal to the calcium signal by filtering it with a low-pass filter with a time constant of 360 ms (see Figures S2A and S2B, left panel). LPis, as motion-selective neurons, are not suitable for white noise analysis. To characterize the response properties of the LPI4-3 (Figure 4A), we first stimulated single ommatidia with local flicker stimuli that were placed precisely onto the lattice of the fly's eye via a custom-built telescopic device (see Transparent Methods and [Haag et al., 2017, 2016]). LPI4-3 cells responded to the individual pulses with different amplitudes, depending on the position of the stimulus (Figure 4C). The maximum response (Figure 4B, black center) of a recorded neuron was then set as the receptive field's center. All other responses to adjacent stimulation are normalized accordingly. Single flicker stimulations in the center of the receptive field show different time courses (Figure 4C) when using the two different indicators. The onset of the calcium response is much slower when compared with the glutamate response. In fact, whereas the glutamate signal shows a short transient peak response and then plateaus after ~ 500 ms, the calcium signal does not resolve any similar details in the time course of the response. The calcium signal decays back to zero in approximately 2 s after stimulus offset, whereas the glutamatergic signals are back at the baseline level in less than 200 ms. This loss-of-response features can be explained by the characteristics of the

calcium indicator, which acts as a low-pass filter (Borst and Abarbanel, 2007). Low-pass filtering the glutamate response ($\tau = 446$ ms, Figure S2C) results in a similar slope and decay as the calcium response. We also asked if the glutamatergic signal of the LPis is indeed direction selective as expected from Mauss et al. (2015). To assess this question we tested LPi4-3 cells with five light pulses of 472 ms duration positioned along the dorsoventral axis of the eye. When stimulated sequentially from dorsal to ventral (Figure 4D), the cell responded more strongly (PD, red line) than when we showed the same stimulus in the opposite direction (ND, black line, paired sample t test, p value < 0.01). We therefore conclude that the sensor is indeed also suitable for resolving glutamatergic direction-selective signals.

DISCUSSION

In this study we showed that all three investigated cell types (L1, Mi9, LPi4-3) express the vesicular transporter for glutamate, VGLut, in their axon terminals (Figure 2). To our knowledge, L1, Mi9, and LPi are the only glutamatergic cells in the *Drosophila* motion vision circuit. Two studies using either antibody stainings (Kolodziejczyk et al., 2008) or a Flp-out analysis of the *dvGluT*CNSIII-Gal4 driver line (heat-shock inducible flipase excises stop-cassette upstream of *mCD8-GFP* to label only a few cells) (Raghu and Borst, 2011) found L2 cells to be glutamatergic. However, a recent RNA sequencing study that characterized gene expression patterns of more than 60 different cell types of the optic lobe could not confirm the expression of VGLut in L2 (Davis et al., 2018). Although they could identify other cell types like Dm cells, Lai, PB_1, Tm29, and TmY5a as glutamatergic due to their expression of VGLut, none of the other cells in the motion vision circuit (besides L1, Mi9, and LPi) seem to express VGLut. The role of Dm, Lai, PB, Tm29, and TmY5a cells in general and their potential contribution to motion vision in the fly brain are not known to date.

We also demonstrated that the spatial receptive fields measured with the glutamate sensor iGluSnFR are almost identical to the ones measured with the calcium sensor GCaMP6f (Figures 3 and 4). Both neurons possess a local OFF center receptive field with a differently strong antagonistic ON surround. Surround inhibition is a phenomenon frequently found in the early processing stages in visual systems: Bipolar and ganglion cells of the mammalian retina possess receptive fields with an antagonistic center-surround structure (reviewed in Shapley and Lennie, 1985), and first-order interneurons of the insect compound eye share this feature as well (Srinivasan et al., 1982). Functionally, a neuron with a center-surround antagonism acts as a spatial band-pass filter, enhancing the neuron's responses to edges over full field illuminations. Such band-pass filtering reduces redundancy in natural images (Srinivasan et al., 1982). We find such spatial band-pass characteristics for both cell types, L1 and Mi9. Based on their spatial receptive fields, we predict, for instance, no response of Mi9 to wide field dark flashes since the integral of the spatial receptive field is close to zero.

In the time domain, however, the glutamate signal turned out to be much faster than the calcium signal derived from the same cells. Due to their small size, many visual interneurons in the fly brain are inaccessible to electrophysiological recordings, so only a few direct recordings have been reported (Behnia et al., 2014; Gruntman et al., 2018; Juusola et al., 2016). Since data from voltage recordings from L1, Mi9, and LPi are not available so far, a direct comparison with the time constant estimated here is not possible. Simulation studies predicted time constants between 50 and 100 ms for the delayed input to the fly motion-detecting neurons (Eichner et al., 2011; Leonhardt et al., 2016). Since Mi9 is thought to provide this signal to T4 cells, the elementary motion-sensing neurons in the ON pathway, the low-pass time constant of 75 ms estimated here matches this prediction well. In addition, a previous study determined the low-pass time constant for Mi9 to be around 550 ms from calcium imaging experiments. A deconvolution of the filter with an estimated GCaMP kernel led to a resulting time constant of 63 ms (Arenz et al., 2017). This result again is in line with the time constants of the Mi9-iGluSnFR of 75 ms reported here.

In the mammalian CNS, glutamate is the most abundant and major excitatory transmitter (Meldrum, 2000; Traynelis et al., 2010). Glutamate binds to two types of receptors: metabotropic (mGluRs) and ionotropic glutamate receptors (iGluRs). iGluRs can be divided into N-methyl-D-aspartate (NMDA) and non-NMDA receptors (α -amino-3-hydroxy-5-methyl-4-isoxazolepropionic acid [AMPA] and kainate receptors) according to their response to agonist molecules NMDA and AMPA (Mosbacher et al., 1994). Analysis of the *Drosophila* genome annotated 14 iGluRs genes, which show sequence similarities with vertebrate AMPA, kainate, and NMDA receptors (Littleton and Ganetzky, 2000). However, the kainate receptor DKaiR1D and the AMPA receptor DGluR1A have different agonist/antagonist selectivity from the vertebrate's pharmacology-based classification (Li et al., 2016). Furthermore, invertebrates like *Drosophila melanogaster* possess a third type of iGluR, the so-called glutamate-gated chloride channel GluCl α , which



is inhibitory (Cully et al., 1996; Liu and Wilson, 2013). Glutamate can also act on metabotropic glutamate receptors, which signal via slower G-protein-coupled pathways. In mammals, eight mGluRs have been described (Conn and Pin, 1997). In contrast, the *Drosophila* genome encodes only one functional mGluR (DmGluRA), which is expressed at the glutamatergic NMJ localized in the presynaptic boutons (Bogdanik et al., 2004). Regarding the broad range of glutamate receptors in *Drosophila*, glutamate can act as a fast, slow, excitatory, or inhibitory transmitter (Li et al., 2016; Liu and Wilson, 2013; Mauss et al., 2015).

This gives rise to interesting speculations about the respective role of glutamate for each of the cell types investigated. In the case of the LPis, glutamate binds to the inhibitory glutamate receptor GluCl α on the dendrites of large-field tangential cells, inhibiting them during null direction motion and, thus, enhancing their flow-field selectivity (Mauss et al., 2015). In the case of L1, the glutamatergic output signal seems to be key for the sign inversion of L1's OFF response in the ON pathway. This is because all *Drosophila* photoreceptors (R1-R8) depolarize upon illumination and release histamine onto lamina neurons, which results in the opening of chloride channels (Hardie, 1989; Hardie and Raghu, 2001). Therefore, lamina monopolar cells transiently hyperpolarize upon illumination onset and respond with a rebound excitation at illumination offset (Laughlin et al., 1987). L1 and L2 neurons respond in an identical way (Joesch et al., 2010). L1 possess an OFF receptive field center (Figure 3D) and therefore depolarizes to OFF stimuli, in contrast to its described downstream synaptic partners, which depolarize to ON stimuli (Arenz et al., 2017; Behnia et al., 2014; Strother et al., 2017; Yang et al., 2016). Hence, an inversion of the sign must occur at the synapse of L1 and its downstream partners. Since L1 is glutamatergic and GluCl α is the only inhibitory receptor described in *Drosophila*, the glutamatergic signal is likely to be responsible for this sign inversion. Whether the downstream partners of L1 indeed express GluCl α , however, is beyond the scope of this study and awaits further investigation. The hypothesis outlined above suggests that the mechanism by which a common photoreceptor input signal is split into an ON and an OFF pathway in invertebrates is different from the one in the mammalian retina where glutamatergic photoreceptors hyperpolarize in response to light. This signal is directly transmitted, i.e., without sign inversion, by ionotropic glutamate receptors expressed on the dendrites of OFF bipolar cells (Euler et al., 2014) and sign inverted by metabotropic glutamate receptors expressed on the dendrites of ON bipolar cells (Masu et al., 1995). In case of Mi9, the functional interpretation of an inhibitory glutamatergic signal is less intuitive. Mi9 directly contacts the dendrites of T4 cells, the first direction-selective neurons in the ON pathway (Takemura et al., 2017). Given the OFF response of Mi9 cells (Figure 3D), T4 cells are expected to be inhibited in darkness via the Mi9-T4 synapse. A moving ON edge would inhibit Mi9 followed by a closure of chloride channels and, thus, an increased input resistance in postsynaptic T4 cells, resulting in an amplification of a subsequently delivered excitatory input signal. Computer simulations have shown that such a two-fold signal inversion can indeed form the biophysical basis of preferred direction enhancement underlying direction selectivity in T4 cells (Borst, 2018).

Taken together our results could demonstrate the functionality of the fast glutamate reporter iGluSnFR in glutamatergic neurons of the fruit fly *Drosophila melanogaster*. It allowed for a more faithful description of important elements of the motion vision pathway, in particular with respect to their temporal response properties.

Limitations of the Study

Since iGluSnFR is anchored to the outer side of the plasma membrane, it senses extracellular glutamate that is present in the synaptic cleft. In addition, the iGluSnFR signal is affected by spillover and diffusion to iGluSnFR molecules outside the cleft. Thus, the iGluSnFR signal should present an upper limit to the "real" time course, i.e., the one of glutamate in the synaptic cleft as seen by the postsynaptic receptors. For the same reason, one might record an iGluSnFR signal even if the indicator is expressed on a neuron that is not glutamatergic or does not receive glutamatergic input, but ramifies within the same volume where glutamate is being released from other cells.

METHODS

All methods can be found in the accompanying [Transparent Methods supplemental file](#).

SUPPLEMENTAL INFORMATION

Supplemental Information includes Transparent Methods and two figures and can be found with this article online at <https://doi.org/10.1016/j.isci.2018.08.019>.

ACKNOWLEDGMENTS

We thank Aljoscha Leonhardt for careful proofreading of the manuscript. We would also like to acknowledge Hermann Aberle for sharing the VGluT antibody with us and Julia Kuhl for designing the graphical abstract. We thank Wolfgang Essbauer and Michael Sauter for fly husbandry. This work was supported by the Deutsche Forschungsgemeinschaft (SFB 870) and the Max Planck Society. F.G.R., M.S.D., S.F., and A.B. are members of the Graduate School of Systemic Neurosciences (GSN) Munich.

AUTHOR CONTRIBUTIONS

F.G.R., S.F., and A.B. conceived the study and designed the experiments. F.G.R. conducted and analyzed the imaging experiments for Mi9 and L1. S.F. performed and analyzed all stainings. J.H. performed and analyzed the LPi experiments. M.S.D. performed data analysis and model fitting of the receptive fields. F.G.R. wrote the manuscript with the help of all authors.

DECLARATION OF INTERESTS

The authors declare no competing interests.

Received: July 5, 2018

Revised: August 13, 2018

Accepted: August 23, 2018

Published: September 28, 2018

REFERENCES

- Arenz, A., Drews, M.S., Richter, F.G., Ammer, G., and Borst, A. (2017). The temporal tuning of the *Drosophila* motion detectors is determined by the dynamics of their input elements. *Curr. Biol.* *27*, 929–944.
- Barlow, H.B., and Levick, W.R. (1965). The mechanism of directionally selective units in rabbit's retina. *J. Physiol.* *178*, 477–504.
- Bausenwein, B., Dittrich, A.P.M., and Fischbach, K.F. (1992). The optic lobe of *Drosophila melanogaster* - II. Sorting of retinotopic pathways in the medulla. *Cell Tissue Res.* *267*, 17–28.
- Bausenwein, B., and Fischbach, K.F. (1992). Activity labeling patterns in the medulla of *Drosophila melanogaster* caused by motion stimuli. *Cell Tissue Res.* *270*, 25–35.
- Behnia, R., Clark, D.A., Carter, A.G., Clandinin, T.R., and Desplan, C. (2014). Processing properties of ON and OFF pathways for *Drosophila* motion detection. *Nature* *512*, 427–430.
- Bogdanik, L., Mohrmann, R., Ramaekers, A., Bockaert, J., Grau, Y., Broadie, K., and Parmentier, M.L. (2004). The *Drosophila* metabotropic glutamate receptor DmGluRA regulates activity-dependent synaptic facilitation and fine synaptic morphology. *J. Neurosci.* *24*, 9105–9116.
- Borst, A. (2018). A biophysical mechanism for preferred direction enhancement in fly motion vision. *PLoS Comput. Biol.* *14* (6), e1006240.
- Borst, A. (2014). In search of the holy grail of fly motion vision. *Eur. J. Neurosci.* *40*, 3285–3293.
- Borst, A., and Abarbanel, H.D. (2007). Relating a calcium indicator signal to the unperturbed calcium concentration time-course. *Theor. Biol. Med. Model.* *4*, 7.
- Cao, G., Platisa, J., Pieribone, V.A., Raccuglia, D., Kunst, M., and Nitabach, M.N. (2013). Genetically targeted optical electrophysiology in intact neural circuits. *Cell* *154*, 904–913.
- Chen, T.-W., Wardill, T.J., Sun, Y., Pulver, S.R., Renninger, S.L., Baohan, A., Schreier, E.R., Kerr, R.A., Orger, M.B., Jayaraman, V., et al. (2013). Ultrasensitive fluorescent proteins for imaging neuronal activity. *Nature* *499*, 295–300.
- Chichilnisky, E.J. (2001). A simple white noise analysis of neuronal light responses. *Network* *12*, 199–213.
- Clark, D.A., Bursztyn, L., Horowitz, M.A., Schnitzer, M.J., and Clandinin, T.R. (2011). Defining the computational structure of the motion detector in *Drosophila*. *Neuron* *70*, 1165–1177.
- Conn, P.J., and Pin, J.-P. (1997). Pharmacology and function of metabotropic glutamate receptors. *Annu. Rev. Pharmacol. Toxicol.* *37*, 205–237.
- Cruse, H. (1996). *Neural Networks as Cybernetics Systems*.
- Cully, D.F., Parese, P.S., Liu, K.K., Schaeffer, J.M., and Arena, J.P. (1996). Identification of a *Drosophila melanogaster* glutamate-gated chloride channel sensitive to the antiparasitic agent avermectin. *J. Biol. Chem.* *271*, 20187–20191.
- Daniels, R.W. (2004). Increased expression of the *Drosophila* vesicular glutamate transporter leads to excess glutamate release and a compensatory decrease in quantal content. *J. Neurosci.* *24*, 10466–10474.
- Davis, F.P., Nern, A., Picard, S., Reiser, M.B., Rubin, G.M., Eddy, S.R., and Henry, G.L. (2018). A genetic, genomic, and computational resource for exploring neural circuit function. *bioRxiv*. <https://doi.org/10.1101/385476>.
- Dayan, P., and Abbott, L.F. (2013). *Theoretical neuroscience: computational and mathematical modeling of neural systems*. *J. Chem. Inf. Model.* *53*, 1689–1699.
- Di Maio, V. (2008). Regulation of information passing by synaptic transmission: a short review. *Brain Res.* *1225*, 26–38.
- Eichner, H., Joesch, M., Schnell, B., Reiff, D.F., and Borst, A. (2011). Internal structure of the fly elementary motion detector. *Neuron* *70*, 1155–1164.
- Euler, T., Haverkamp, S., Schubert, T., and Baden, T. (2014). Retinal bipolar cells: elementary building blocks of vision. *Nat. Rev. Neurosci.* *15*, 507–519.
- French, A.S. (1976). Practical nonlinear system analysis by Wiener kernel estimation in the frequency domain. *Biol. Cybern.* *24*, 111–119.
- Gruntman, E., Romani, S., and Reiser, M.B. (2018). Simple integration of fast excitation and offset, delayed inhibition computes directional selectivity in *Drosophila*. *Nat. Neurosci.* *21*, 250–257.
- Haag, J., Arenz, A., Serbe, E., Gabbiani, F., and Borst, A. (2016). Complementary mechanisms create direction selectivity in the fly. *Elife* *5*, <https://doi.org/10.7554/eLife.17421e>.
- Haag, J., Mishra, A., and Borst, A. (2017). A common directional tuning mechanism of *Drosophila* motion-sensing neurons in the ON and in the OFF pathway. *Elife* *6*, 1–15.
- Hardie, R.C. (1989). A histamine-activated chloride channel involved in neurotransmission at a photoreceptor synapse. *Nature* *339*, 704–706.

- Hardie, R.C., and Raghu, P. (2001). Visual transduction in *Drosophila*. *Nature* 413, 186–193.
- Hausen, K., Wolburg-Buchholz, K., and Ribi, W.A. (1980). The synaptic organization of visual interneurons in the lobula complex of flies - a light and electron microscopical study using silver-intensified cobalt-impregnations. *Cell Tissue Res.* 208, 371–387.
- Hopp, E., Borst, A., and Haag, J. (2014). Subcellular mapping of dendritic activity in optic flow processing neurons. *J. Comp. Physiol. A Neuroethol. Sens. Neural Behav. Physiol.* 200, 359–370.
- Jin, L., Han, Z., Platisa, J., Wooltorton, J.R.A., Cohen, L.B., and Pieribone, V.A. (2012). Single action potentials and subthreshold electrical events imaged in neurons with a fluorescent protein voltage probe. *Neuron* 75, 779–785.
- Joesch, M., Schnell, B., Raghu, S.V., Reiff, D.F., and Borst, A. (2010). ON and OFF pathways in *Drosophila* motion vision. *Nature* 468, 300–304.
- Joesch, M., Weber, F., Eichner, H., and Borst, A. (2013). Functional specialization of parallel motion detection circuits in the fly. *J. Neurosci.* 33, 902–905.
- Juusola, M., Dau, A., Zheng, L., and Rien, D. (2016). Electrophysiological method for recording intracellular voltage responses of *Drosophila* photoreceptors and interneurons to light stimuli in vivo. *J. Vis. Exp.* 112, 1–16.
- Kolodziejczyk, A., Sun, X., Meinertzhagen, I.A., and Nässel, D.R. (2008). Glutamate, GABA and acetylcholine signaling components in the lamina of the *Drosophila* visual system. *PLoS One* 3, e2110.
- Laughlin, S.B., Howard, J., and Blakeslee, B. (1987). Synaptic limitations to contrast coding in the retina of the blowfly *Calliphora*. *Proc. R. Soc. Lond. B Biol. Sci.* 231, 437–467.
- Leonhardt, A., Ammer, G., Meier, M., Serpe, E., Bahl, A., and Borst, A. (2016). Asymmetry of *Drosophila* ON and OFF motion detectors enhances real-world velocity estimation. *Nat. Neurosci.* 19, 706–715.
- Li, Y., Dharkar, P., Han, T.H., Serpe, M., Lee, C.H., and Mayer, M.L. (2016). Novel functional properties of *Drosophila* CNS glutamate receptors. *Neuron* 92, 1036–1048.
- Littleton, J.T., and Ganetzky, B. (2000). Ion channels and synaptic organization: analysis of the *Drosophila* genome. *Neuron* 26, 35–43.
- Liu, W.W., and Wilson, R.I. (2013). Glutamate is an inhibitory neurotransmitter in the *Drosophila* olfactory system. *Proc. Natl. Acad. Sci. USA* 110, 10294–10299.
- Mahr, A., and Aberle, H. (2006). The expression pattern of the *Drosophila* vesicular glutamate transporter: a marker protein for motoneurons and glutamatergic centers in the brain. *Gene Expr. Patterns* 6, 299–309.
- Maisak, M.S., Haag, J., Ammer, G., Serpe, E., Meier, M., Leonhardt, A., Schilling, T., Bahl, A., Rubin, G.M., Nern, A., et al. (2013). A directional tuning map of *Drosophila* elementary motion detectors. *Nature* 500, 212–216.
- Marvin, J.S., Borghuis, B.G., Tian, L., Cichon, J., Harnett, M.T., Akerboom, J., Gordus, A., Renninger, S.L., Chen, T.W., Bargmann, C.I., et al. (2013). An optimized fluorescent probe for visualizing glutamate neurotransmission. *Nat. Methods* 10, 162–170.
- Masu, M., Iwakabe, H., Tagawa, Y., Miyoshi, T., Yamashita, M., Fukuda, Y., Sasaki, H., Hiroi, K., Nakamura, Y., Shigemoto, R., et al. (1995). Specific deficit of the ON response in visual transmission by targeted disruption of the mGluR6 gene. *Cell* 80, 757–765.
- Maus, A.S., Meier, M., Serpe, E., and Borst, A. (2014). Optogenetic and pharmacologic dissection of feedforward inhibition in *Drosophila* motion vision. *J. Neurosci.* 34, 2254–2263.
- Maus, A.S., Pankova, K., Arenz, A., Nern, A., Rubin, G.M., and Borst, A. (2015). Neural circuit to integrate opposing motions in the visual field. *Cell* 162, 351–362.
- Meldrum, B.S. (2000). Glutamate as a neurotransmitter in the brain: review of physiology and pathology. *J. Nutr.* 130, 1007S–1015S.
- Mosbacher, J., Schoepfer, R., Monyer, H., Burnashev, N., Seeburg, P., and Ruppertsberg, J. (1994). A molecular determinant for submillisecond desensitization in glutamate receptors. *Science* 266, 1059–1062.
- Raghu, S.V., and Borst, A. (2011). Candidate glutamatergic neurons in the visual system of *Drosophila*. *PLoS One*. <https://doi.org/10.1371/journal.pone.0019472>.
- Ringach, D., and Shapley, R. (2004). Reverse correlation in neurophysiology. *Cognit. Sci.* 28, 147–166.
- Ringach, D.L. (2004). Mapping receptive fields in primary visual cortex. *J. Physiol.* 558, 717–728.
- Rister, J., Pauls, D., Schnell, B., Ting, C.Y., Lee, C.H., Sinakevitch, I., Morante, J., Strausfeld, N.J., Ito, K., and Heisenberg, M. (2007). Dissection of the peripheral motion channel in the visual system of *Drosophila melanogaster*. *Neuron* 56, 155–170.
- Schnell, B., Joesch, M., Forstner, F., Raghu, S.V., Otsuna, H., Ito, K., Borst, A., and Reiff, D.F. (2010). Processing of horizontal optic flow in three visual interneurons of the *Drosophila* brain. *J. Neurophysiol.* 103, 1646–1657.
- Scott, E.K., Raabe, T., and Luo, L. (2002). Structure of the vertical and horizontal system neurons of the lobula plate in *Drosophila*. *J. Comp. Neurol.* 454, 470–481.
- Shapley, R., and Lennie, P. (1985). Spatial frequency analysis in the visual system. *Annu. Rev. Neurosci.* 8, 547–583.
- Shinomiya, K., Karuppururai, T., Lin, T.Y., Lu, Z., Lee, C.H., and Meinertzhagen, I.A. (2014). Candidate neural substrates for OFF edge motion detection in *Drosophila*. *Curr. Biol.* 24, 1062–1070.
- Silies, M., Gohl, D.M., Fisher, Y.E., Freifeld, L., Clark, D.A., and Clandinin, T.R. (2013). Modular use of peripheral input channels tunes motion-detecting circuitry. *Neuron* 79, 111–127.
- Srinivasan, M.V., Laughlin, S.B., and Dubs, A. (1982). Predictive coding: a fresh view of inhibition in the retina. *Proc. R. Soc. Lond. B Biol. Sci.* 216, 1471–2954.
- St-Pierre, F., Marshall, J.D., Yang, Y., Gong, Y., Schnitzer, M.J., and Lin, M.Z. (2014). High-fidelity optical reporting of neuronal electrical activity with an ultrafast fluorescent voltage sensor. *Nat. Neurosci.* 17, 884–889.
- Strother, J.A., Wu, S.T., Wong, A.M., Nern, A., Rogers, E.M., Le, J.Q., Rubin, G.M., and Reiser, M.B. (2017). The emergence of directional selectivity in the visual motion pathway of *Drosophila*. *Neuron* 94, 168–182.
- Takemura, S.Y., Nern, A., Chklovskii, D.B., Scheffer, L.K., Rubin, G.M., and Meinertzhagen, I.A. (2017). The comprehensive connectome of a neural substrate for ‘ON’ motion detection in *Drosophila*. *Elife* 6, 1–16.
- Takemura, S.Y., Karuppururai, T., Ting, C.Y., Lu, Z., Lee, C.H., and Meinertzhagen, I.A. (2011). Cholinergic circuits integrate neighboring visual signals in a *Drosophila* motion detection pathway. *Curr. Biol.* 21, 2077–2084.
- Traynelis, S.F., Wollmuth, L.P., McBain, C.J., Menniti, F.S., Vance, K.M., Ogden, K.K., Hansen, K.B., Yuan, H., Myers, S.J., and Dingledine, R. (2010). Glutamate receptor ion channels: structure, regulation, and function. *Pharmacol. Rev.* 62, 405–496.
- Tsutsui, H., Jinno, Y., Tomita, A., Niino, Y., Yamada, Y., Mikoshiba, K., Miyawaki, A., and Okamura, Y. (2013). Improved detection of electrical activity with a voltage probe based on a voltage-sensing phosphatase. *J. Physiol.* 591, 4427–4437.
- Tuthill, J.C., Nern, A., Holtz, S.L., Rubin, G.M., and Reiser, M.B. (2013). Contributions of the 12 neuron classes in the fly lamina to motion vision. *Neuron* 79, 128–140.
- Von Hassenstein, B., and Reichardt, W. (1956). Systemtheoretische Analyse der Zeit-, Reihenfolgen- und Vorzeichenbewertung bei der Bewegungsperzeption des Rüsselkäfers *Chlorophanus*. *Sech. B J. Chem. Sci.* 11, 513–524.
- Wasserman, S.M., Aptekar, J.W., Lu, P., Nguyen, J., Wang, A.L., Keles, M.F., Grygoruk, A., Krantz, D.E., Larsen, C., and Frye, M.A. (2015). Olfactory neuromodulation of motion vision circuitry in *Drosophila*. *Curr. Biol.* 25, 467–472.
- Yang, H.H., St-Pierre, F., Sun, X., Ding, X., Lin, M.Z., and Clandinin, T.R. (2016). Subcellular imaging of voltage and calcium signals reveals neural processing in vivo. *Cell* 166, 245–257.
- Zucker, R.S. (1993). Calcium and transmitter release. *J. Physiol. Paris* 87, 25–36.

ISCI, Volume 7

Supplemental Information

**Glutamate Signaling
in the Fly Visual System**

Florian G. Richter, Sandra Fendl, Jürgen Haag, Michael S. Drews, and Alexander Borst

Supplemental Information

Supplemental Figures

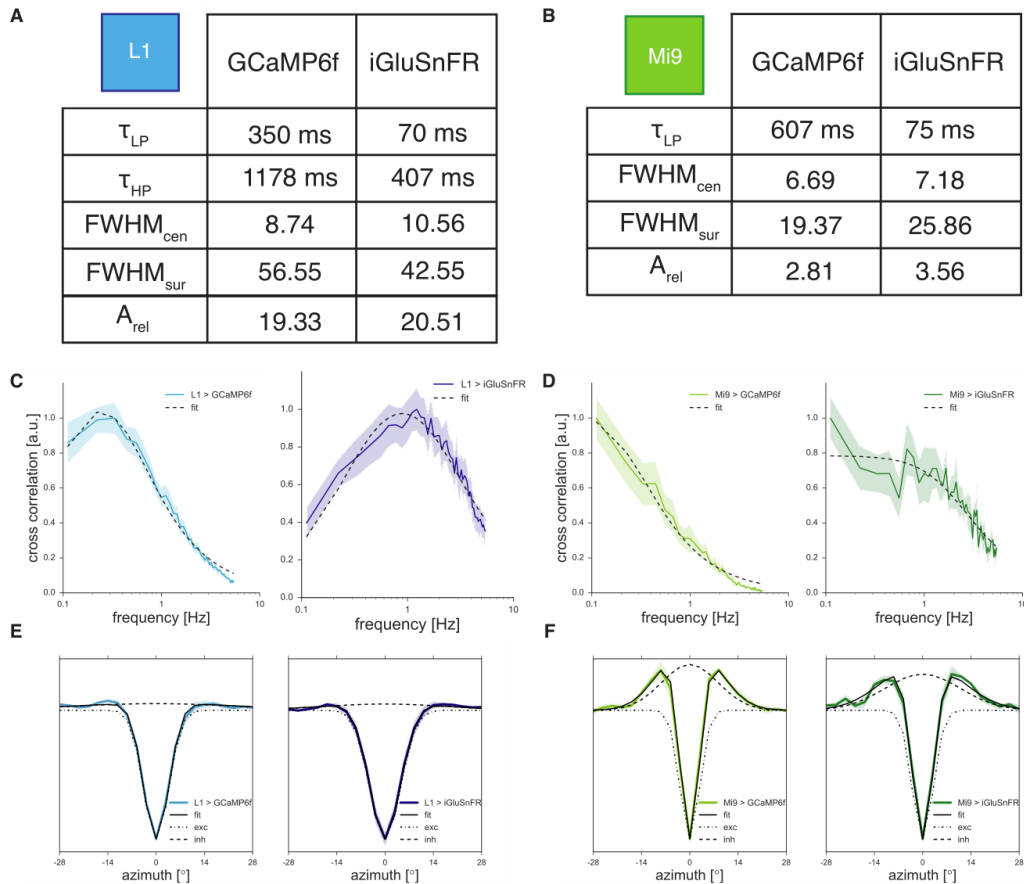


Figure S1. Model fits to L1 and Mig data, related to Fig 3

(A) Parameters to quantitatively describe the receptive field characteristics of L1 recorded either with GCaMP6f (left column) or iGluSnFR (right column). First two parameters describe temporal components of the receptive field, last three parameters describe those of the spatial component. (B) Same as (A) only for Mig. Description of highpass characteristics is missing, since Mig is best described by a pure low-pass.

(C) Impulse responses from Figure 3 D-E plotted in frequency space. Black dashed lines mark the fit of a 1st order band-pass filter (for time constants see table (A)).

(D) Same as (C) only for Mig. Black dashed lines mark the fit of a 1st order low-pass filter.

(E)+(F) Spatial receptive fields from Figure 3 D-E. Data are fitted with a Mexican hat function that captures both, the excitatory center as well as the inhibitory surround of these receptive fields. cen = center, sur = surround, LP = low-pass, HP = high-pass, A = amplitude, τ = time constant, FWHM = full width at half maximum.

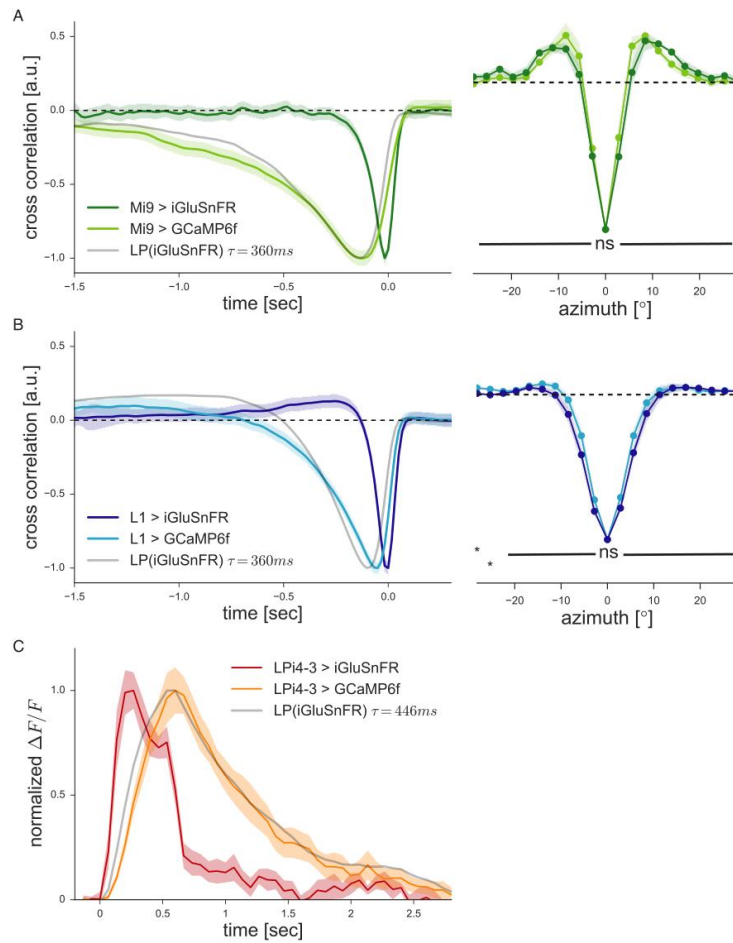


Figure S2. GCaMP data resembles low-pass filtered iGluSnFR data, related to Fig 3 and 4

(A) Low-pass filtering of the Mig impulse response measured with iGluSnFR with a time constant of 360 ms (grey) shows the best fit with the impulse response measured with GCaMP6f (left panel). Spatial receptive fields (right panel) are not significantly different from each other, when measured with the two different sensors.

(B) Same as (A) for L1

(C) Low-pass filtering of the LPi4-3 > iGluSnFR response to local flicker with a time constant of 446 ms (grey) shows the best fit to response measured with GCaMP6f (orange).

Transparent Methods

Flies/preparation

Flies were raised and kept on standard cornmeal-agar medium on a 12 hour light/12 hour dark cycle at 25°C and 60% humidity. For imaging experiments, the genetically-encoded calcium indicators GCaMP6f or the genetically encoded glutamate sensor iGluSnFR (Chen et al., 2013; Marvin et al., 2013) were expressed using the Gal4-UAS system in cell-type specific Gal4 fly lines, resulting in the following genotypes:

Genotypes:

L1>GCa6f:	w+; R48A08-AD/UAS-GCaMP6f; R66A01-DBD/UAS-GCaMP6f
L1>iGluSnFR:	w+; R48A08-AD/+; R66A01-DBD/UAS-iGluSnFR (BL59611, AV184)
Mi9>GCa6f:	w+; R48A07-AD/UAS-GCaMP6f; VT046779-DBD/UAS-GCaMP6f
Mi9>iGluSnFR:	w+; R48A07-AD/+; VT046779-DBD/UAS-iGluSnFR (BL59611, AV184)
LPI>GCa6f:	w+; +/UAS-GCaMP6f; R38G02-Gal4/UAS-GCaMP6f
LPI>iGluSnFR:	w+; +; R38G02-Gal4/UAS-iGluSnFR (BL59611, AV184)

For immunohistochemical stainings in Figure 2:

L1>myr::GFP:	w-; R48A08-AD/UAS-myr::GFP; R66A01-DBD/+
Mi9>myr::GFP:	w-; R48A07-AD/ UAS-myr::GFP; VT046779-DBD/+
LPI4-3>myr::GFP:	w-; UAS-myr::GFP/+; R38G02-Gal4/+

The transgenic fly lines driving split-Gal4 expression in the lamina neuron L1 were generated and described in (Tuthill et al., 2013). Mi9 in (Strother et al., 2017) and the one of LPI's in (Mauss et al., 2015). For calcium and glutamate imaging experiments, flies were prepared as previously described (Maisak et al., 2013; Strother et al., 2017). Briefly, flies were anaesthetized on ice, fixed with their backs, legs and wings to a Plexiglas holder with the back of the head exposed to a recording chamber filled with fly external solution. The cuticle at the back of the head on one side was cut away with a fine hypodermic needle and removed together with muscles and air sacks covering the underlying optic lobe.

Data acquisition and analysis:

Data analysis was performed offline using custom-written routines in Matlab and Python 2.7 (with the SciPy and OpenCV-Python Libraries).

2-photon imaging:

Imaging was performed on custom-built 2-photon microscopes as previously described (Maisak et al., 2013) and controlled with the ScanImage software in Matlab (Pologruto et al., 2003). Acquisition rates were between 15 (for LPI experiments) and 23.67 Hz (for L1 and Mi9 experiments), image resolution between 64x64 and 128x32 pixels (for L1 and Mi9 experiments). Before starting the acquisition, we verified that the receptive fields of the cells were located on the stimulus arena by showing a search stimulus consisting of moving gratings.

Calcium imaging was performed as previously described in (Arenz et al., 2017). In brief: Images were automatically registered using horizontal and vertical translations to correct for the movement of the brain. Fluorescence changes ($\Delta F/F$ values) were then calculated using a standard baseline algorithm (Jia et al., 2011). Regions of interest (ROIs) were drawn on the average raw image by hand in the medulla layer M1 for L1 and in layer M10 for Mi9. For LPi neurons, ROIs were routinely chosen in the lobula plate, encompassing small regions with single to few axon terminals. Averaging the fluorescence change over this ROI in space resulted in a $\Delta F/F$ time course. Glutamate imaging was performed with the same settings as the calcium imaging experiments.

Visual stimulation for L1 and Mi9 experiments

The spatiotemporal response properties of the L1 and Mi9 columnar input elements were determined on a custom-built projector-based arena, as previously described in (Arenz et al., 2017). Stimuli were projected with 2 commercial micro-projectors (TI DLP Lightcrafter 3000) onto the back of an opaque cylindrical screen covering 180 ° in azimuth and 105 ° in elevation of the fly's visual field. The projectors refresh rate is 180 Hz (at 8 bit color depth). For all stimuli used here, we set the medium brightness to a 8-bit grayscale value of 50, which corresponds to a medium luminance of 55 ± 11 cd/m². Stimuli were rendered using a custom written software in Python 2.7.

Visual stimulation for LPi4-3 experiments with telescope

This technique has been previously described in (Haag et al., 2016). In brief: Antidromic illumination of the fly's head visualizes the hexagonal structure of the optical axes of the ommatidia (Franceschini, 1975; Schuling et al., 1989). Visual stimuli are generated on the AMOLED display (800x600 pixels, pixel size 15x15 mm, maximal luminance > 1500 cd/m²; $\lambda = 530$ nm; refresh rate 85 Hz) (SVGA050SG, Olightek). This allows to precisely position the stimuli onto single lamina cartridges. In order to prevent stimulus light from entering the photomultiplier of the two-photon micro-scope, light generated by the AMOLED display was filtered with a long-pass filter (514 LP, T: 529.4– 900 nm, AHF). The AMOLED display was controlled with MATLAB and the psychophysics toolbox (V3.0.11;(Brainard, 1997)).

White noise reverse-correlation

The analysis of spatial receptive fields was previously described in (Arenz et al., 2017). For the input elements, spatiotemporal receptive fields were calculated following standard reverse-correlation methods (Dayan and Abbott, 2013; French, 1976). First, the mean value was subtracted from the raw signals of single ROIs by using a low-pass filtered version of the signal (Gaussian filter with 120 seconds standard deviation) as a baseline for a $\Delta F/F$ -like representation of the signal.

The stimulus-response reverse correlation function was calculated as:

$$K(x, \tau) = \int_0^T dt S(x, t - \tau) \cdot R(t)$$

with S for the stimulus and R for the response of the neuron. The resulting spatiotemporal fields were normalized in z-score. Only receptive fields with peak amplitudes above 10 standard deviations from the mean were taken for further analysis (for Mi9-GCaMP6f the threshold

was lowered to 7). Cross-sections through the receptive fields along the space axis were fit with a Gaussian function to determine the position of the peak (Suppl. Fig. 1 E-F).

Gaussian noise stimulus

The same stimulus was used in (Arenz et al., 2017). In brief: The stimulus consisted of 64 vertical bars covering an angle of 180° in total. The intensity of each bar fluctuated randomly around a mean intensity of 50 on the 8-bit grayscale of the display. The intensities were drawn from a Gaussian distribution with a standard deviation of 25% contrast. In time, the stimulus was low-pass filtered with a Gaussian window with approximately 22ms standard deviation, which restricted the frequency content of the stimulus to frequencies below 10Hz. For Mi9-GCaMP6f imaging, similarly, the time window was 45ms long, covering frequencies until up to 5Hz.

Spatial receptive field

The analysis of spatial receptive fields was previously described in (Arenz et al., 2017). In brief: One-dimensional spatial receptive fields are cross-sections through the peak of the spatiotemporal receptive fields along the space axis and are averaged over the 12 samples (200ms) around the peak. For both L1 and Mi9 we found a small-field, antagonistic center-surround organization of the spatial receptive field using the vertical white noise stimulus. The black dashed lines in Suppl. Fig 1 represents a Mexican hat function (Difference of Gaussian). Mathematically such a function can be described as follows:

$$RF_{1D}(\varphi) = e^{-\frac{1}{2}\frac{\varphi^2}{\sigma_{cen}^2}} - A_{rel} \cdot e^{-\frac{1}{2}\frac{\varphi^2}{\sigma_{sur}^2}}$$

with φ as azimuth, σ_{cen} and σ_{sur} as the standard deviations of center and surround, respectively, and $A_{rel} = A_{sur}/A_{cen}$ the relative strength of the surround in relation to the amplitude of the center Gaussian (which is normalized to 1).

Temporal receptive field

The analysis of temporal receptive fields was previously described in (Arenz et al., 2017). In brief: The time-reversed impulse responses shown in Figure 3 are cross-sections through the center of the spatiotemporal receptive fields along the time axis and are averaged over the three center pixels. For the determination of the time constants (tau), we sought to describe the response characteristic of each cell with a simplified model that catches the main properties. For that, we fitted simple 1st order filters (e.g. 1st order low-pass for Mi9; 1st order bandpass for L1) to the impulse responses of all cells.

The model fit in Suppl. Fig 2 (grey lines) was performed by low-pass filtering the measured iGluSnFR response of each neuron type (L1, Mi9, LPi) with a 1st order low-pass filter and optimizing the time-constant such that the difference between the low-pass filtered signal and the measured calcium response of the neurons was minimal. The fitting procedure was implemented using standard least square algorithms (SciPy 0.19).

Immunohistochemistry

Fly brains were dissected in ice-cold 0.3% PBST and fixed in 4% PFA in 0.3% PBST for 25 min at room temperature. Subsequently, brains were washed 4-5 times in 0.3% PBST and blocked in 10% normal goat serum (NGS) in 0.3% PBST for 1 hour at room temperature. Primary antibodies used were mouse anti-bruchpilot brp (nc82, Developmental Studies

Hybridoma Bank, 1:20) and rabbit anti-VGluT (courtesy of H. Aberle, 1:500). Secondary antibodies used were: goat anti-mouse ATTO 647N (Rockland, 1:300) and goat anti-rabbit Alexa Fluor 568 (Life Technologies, 1:300). Myr::GFP-labeled cells were imaged natively without antibody staining. 5% NGS was added to all antibody solutions and both primary and secondary antibodies were incubated for at least 48 hours at 4°C. Brains were mounted in Vectashield Antifade Mounting Medium (Vector Laboratories) and imaged on a Leica TCS SP8 confocal microscope.

Supplemental References

- Brainard, D.H. (1997). The psychophysics toolbox. *Spat. Vis.* 10, 433–436.
- Franceschini, N. (1975). Sampling of the visual environment by the compound eye of the fly: Fundamentals and applications. *Photoreceptor Opt.* 98–125.
- Jia, H., Rochefort, N.L., Chen, X., Konnerth, A. (2011). In vivo two-photon imaging of sensory-evoked dendritic calcium signals in cortical neurons. *Nat. Protoc.* 6, 28–35.
- Pologruto, T.A., Sabatini, B.L., Svoboda, K. (2003). ScanImage: Flexible software for operating laser scanning microscopes. *Biomed. Eng. Online* 2.
- Schuling, F.H., Mastebroek, H.A.K., Bult, R., Lenting, B.P.M. (1989). Properties of elementary movement detectors in the fly *Calliphora erythrocephala*. *J. Comp. Physiol. A* 165, 179–192.

2.3 DYNAMIC SIGNAL COMPRESSION FOR ROBUST MOTION VISION IN FLIES

SUMMARY Sensory systems need to reliably extract information from highly variable natural signals. Flies, for instance, use optic flow to guide their course and are remarkably adept at estimating image velocity regardless of image statistics. Current circuit models, however, cannot account for this robustness. Here, we demonstrate that the *Drosophila* visual system reduces input variability by rapidly adjusting its sensitivity to local contrast conditions. We exhaustively map functional properties of neurons in the motion detection circuit and find that local responses are compressed by surround contrast. The compressive signal is fast, integrates spatially, and derives from neural feedback. Training convolutional neural networks on estimating the velocity of natural stimuli shows that this dynamic signal compression can close the performance gap between model and organism. Overall, our work represents a comprehensive mechanistic account of how neural systems attain the robustness to carry out survival-critical tasks in challenging real-world environments.

AUTHORS Michael S. Drews, Aljoscha Leonhardt (co-first author), Nadezhda Pirogova, **Florian G. Richter**, Anna Schuetzenberger, Lukas Braun, Etienne Serbe, and Alexander Borst

CONTRIBUTIONS M.S.D., A.L., and A.B. jointly conceived the study. M.S.D. and A.L. designed all experiments. A.L. and L.B. conducted behavioral experiments. E.S. recorded electrophysiological responses. M.S.D., N.P., **F.G.R.**, and A.S. performed calcium imaging. A.L. designed and analyzed the convolutional model. M.S.D. and A.L. analyzed data, performed modelling, and wrote the manuscript. All authors participated in editing the manuscript.

Dynamic Signal Compression for Robust Motion Vision in Flies

Highlights

- *Drosophila* motion processing robustly estimates the velocity of moving natural scenes
- Visual interneurons in the fly visual system dynamically adapt to stimulus contrast
- This adaptation relies on fast spatial integration of neural feedback
- Contrast adaptation accounts for robust motion vision in computational circuit models

Authors

Michael S. Drews, Aljoscha Leonhardt, Nadezhda Pirogova, ..., Lukas Braun, Etienne Serbe, Alexander Borst

Correspondence

drews@neuro.mpg.de (M.S.D.),
leonhardt@neuro.mpg.de (A.L.)

In Brief

Flies reliably estimate the velocity of moving natural scenes regardless of image statistics. Current models of *Drosophila* motion vision fail to explain this robustness. Drews, Leonhardt, et al. show that flies achieve this performance by rapidly adjusting the sensitivity of visual interneurons in the medulla to surround contrast.



Drews et al., 2020, Current Biology 30, 209–221
January 20, 2020 © 2019 The Authors. Published by Elsevier Ltd.
<https://doi.org/10.1016/j.cub.2019.10.035>

CellPress

Dynamic Signal Compression for Robust Motion Vision in Flies

Michael S. Drews,^{1,2,4,*} Aljoscha Leonhardt,^{1,4,5,*} Nadezhda Pirogova,^{1,2} Florian G. Richter,^{1,2} Anna Schuetzenberger,^{1,2} Lukas Braun,³ Etienne Serbe,¹ and Alexander Borst¹

¹Department Circuits-Computation-Models, Max-Planck-Institute of Neurobiology, 82152 Martinsried, Germany

²Graduate School of Systemic Neurosciences, LMU Munich, 82152 Martinsried, Germany

³Bernstein Center for Computational Neuroscience, 10115 Berlin, Germany

⁴These authors contributed equally

⁵Lead Contact

*Correspondence: drews@neuro.mpg.de (M.S.D.), leonhardt@neuro.mpg.de (A.L.)

<https://doi.org/10.1016/j.cub.2019.10.035>

SUMMARY

Sensory systems need to reliably extract information from highly variable natural signals. Flies, for instance, use optic flow to guide their course and are remarkably adept at estimating image velocity regardless of image statistics. Current circuit models, however, cannot account for this robustness. Here, we demonstrate that the *Drosophila* visual system reduces input variability by rapidly adjusting its sensitivity to local contrast conditions. We exhaustively map functional properties of neurons in the motion detection circuit and find that local responses are compressed by surround contrast. The compressive signal is fast, integrates spatially, and derives from neural feedback. Training convolutional neural networks on estimating the velocity of natural stimuli shows that this dynamic signal compression can close the performance gap between model and organism. Overall, our work represents a comprehensive mechanistic account of how neural systems attain the robustness to carry out survival-critical tasks in challenging real-world environments.

INTRODUCTION

Visual motion represents a critical source of sensory feedback for navigation. Self-motion results in particular patterns of local directional cues across the retina. Detection of these optic flow fields allows animals to estimate and control their current heading [1]. Flies, for instance, react to whole-field retinal motion by turning in the same direction as their surroundings. This optomotor response enables them to maintain a straight path under perturbations as well as over long distances [2, 3].

For the reflex to work effectively, biological motion detectors need to respond reliably and independently of the particular visual statistics of the environment. This poses a challenge given the complexity of natural scenes [4, 5]. Motion vision systems therefore need to employ processing strategies that maintain robust performance despite the variability of natural visual input.

Recent circuit mapping efforts have yielded unprecedented insight into the neural substrate of motion detection in *Drosophila* [6, 7]. The fly optic lobe consists of sequential neuropils (retina, lamina, medulla, lobula, and lobula plate) and is arranged in columns that process visual input retinotopically. In various combinations, lamina cells L1–L5 feed into a light-sensitive ON or a dark-sensitive OFF pathway, each comprising at least four cell types in the medulla [8]. Medulla units fall into two classes characterized either by transient temporal filtering and moderate center-surround antagonism in their spatial receptive field (Mi1 and Tm3 for ON; Tm1, Tm2, and Tm4 for OFF) or by tonic responses and strong antagonistic surround (Mi4 and Mi9 for ON; Tm9 for OFF) [9–13]. Postsynaptic T4 and T5 cells then compute local ON and OFF motion, respectively, by comparing medulla signals with different dynamics across neighboring columns [8, 14–19]. Jointly, they are necessary for the optomotor response [20]. By pooling appropriate T4 and T5 signals, lobula plate tangential cells (LPTCs) detect optic flow fields that correspond to rotations around different body axes and ultimately control turning [3, 21–23].

For artificial stimuli, fly motion processing is well explained by correlation-based detector models that rely on multiplication of spatially adjacent, asymmetrically filtered luminance signals [24]. These elementary motion detectors (EMDs) account for subtle features of behavioral and neural responses such as pattern-induced shifts in velocity tuning [25, 26], intrinsic velocity gain control [27], or reverse-phi sensitivity [28, 29]. However, EMD output strongly depends on contrast as defined by the average difference between light and dark [26]. EMDs thus invariably confound image contrast with velocity. Since local contrast varies substantially within natural images [4], output from individual EMDs is sparse and fluctuates heavily under naturalistic conditions (Figures S1A–S1C). Motion responses in flies, however, have been shown to be highly robust, across both time and different natural scenes [30, 31].

Various general mechanisms for adaptation to naturalistic signals have been described in the fly visual system. These include gain control in photoreceptors or LPTCs [32–34], redundancy reduction through lateral inhibition [35], subtractive enhancement of flow field selectivity [36], and tailoring of processing to fundamental natural scene statistics [31, 37, 38]. However, none effectively address the problem of contrast fluctuations.



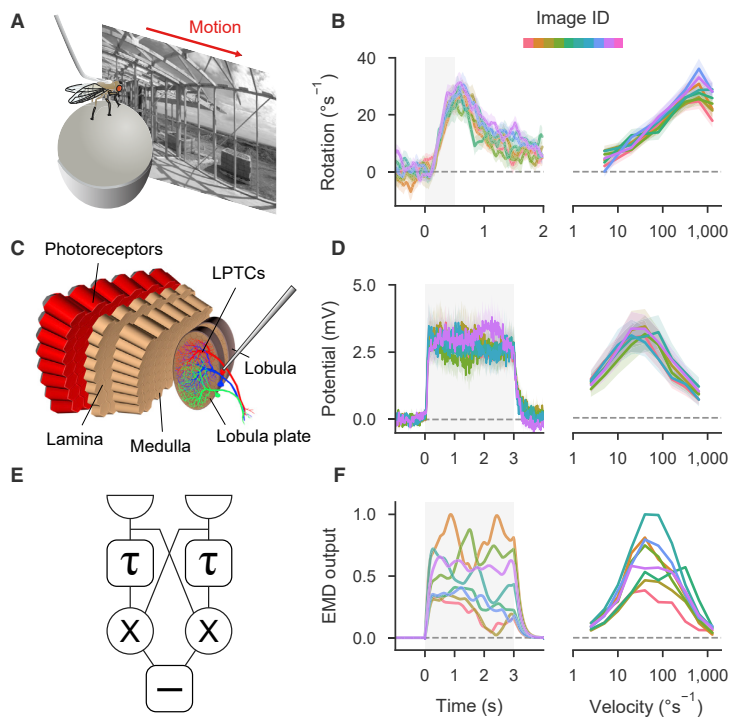


Figure 1. Flies Respond More Robustly to Natural Scene Variability Than Predicted by Correlation-Based Motion Detectors

(A) Illustration of behavioral set-up. Tethered wild-type *Drosophila* were stimulated with translating natural images.

(B) Left: turning responses for images moving at 80°s^{-1} ($n = 16$ flies). Each color indicates a distinct scene. Images moved during gray-shaded period. Right: velocity tuning curves for all measured scenes (averaged between 0 and 1 s after motion onset).

(C) Illustration of fly visual system. Photoreceptor signals are processed in five retinotopically arranged neuropils. Wide-field lobula plate tangential cells (LPTCs) respond to particular optic flow fields.

(D) Left: membrane potential of horizontal system LPTCs in response to images moving at 20°s^{-1} ($n = 11$ cells from 9 flies). Right: velocity tuning curves (averaged between 0 and 3 s after motion onset).

(E) Schematic of an individual correlation-based elementary motion detector (EMD; τ denotes delay line; \times , multiplication; $-$, subtraction).

(F) Left: responses of an array of EMDs to stimulation with natural images moving at 20°s^{-1} . Right: velocity tuning curves of EMD array (evaluated like LPTC output). Note that in contrast to experiments, model responses were averaged across many different starting phases. Shaded areas around curves indicate bootstrapped 68% confidence intervals.

See also Figure S1 and Table S2.

In vertebrate visual systems, contrast sensitivity is continuously regulated through the mechanism of divisive normalization [39–41]. Here, the response of a neuron is effectively divided by local contrast, estimated as the average activity within a population of neighboring neurons. The process compresses signals of varying contrast into a fixed range by dynamically adjusting gain to current conditions [5] and renders the neural representation of stimuli largely invariant with respect to contrast. However, so far, no comparable mechanism has been described for the invertebrate visual system.

Here, we investigate how the fly visual system copes with contrast variability and demonstrate that dynamic signal compression based on divisive contrast normalization renders motion processing robust to the challenges imposed by natural visual environments.

RESULTS

Fly Motion Responses Are Robust to Natural Scene Variability

To rigorously assess the robustness of *Drosophila* motion processing, we measured optomotor responses to a diverse set of moving naturalistic panoramas on a walking treadmill setup (Figure 1A). Fly turning was highly consistent across images and velocity tuning curves showed virtually no variation over different scenes, matching previous findings [31] (Figure 1B; Figure S1). To quantify reliability at the neural level, we recorded the membrane potential of horizontal system LPTCs that detect

optic flow fields corresponding to yaw rotation (Figure 1C). Potential was tuned to scene velocity and again exhibited little image-dependent variation (Figure 1D). Additionally, membrane voltage proved highly stable across time. This was consistent with earlier work in hoverflies [30].

To perform a consistent comparison, we tested the robustness of EMDs on the same set of stimuli as in behavior and electrophysiology (Figure 1E). As anticipated from a multitude of similar studies [31, 37, 42, 43], responses were remarkably unreliable across time and images (Figure 1F). For most images, temporally resolved output fluctuated strongly, average amplitudes differed, and tuning curves exhibited peaks at different velocities. Overall, EMDs provided a poor readout of true image velocity. This stands in stark contrast to the experimentally observed robustness of motion responses and leads to the central question: how does the fly visual system compensate for natural contrast variability?

Sensitivity of Optomotor Response Is Modulated by Surround Contrast

We designed an optomotor stimulus to establish whether *Drosophila* dynamically adapt the sensitivity of motion-induced turning to image contrast, which could serve to normalize variation within natural scenes. The stimulus segregated the visual field into a background and a foreground pattern (Figure 2A). The background contained random luminance fluctuations but no net motion. Pattern movement within the foreground window triggered turning. For both, average contrast could be controlled

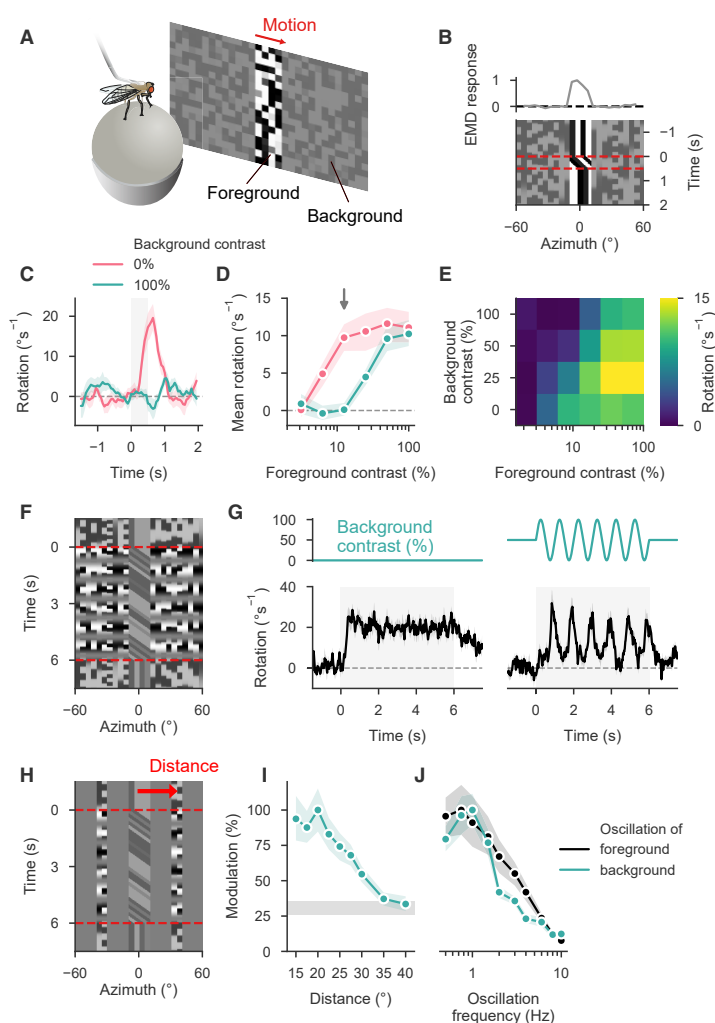


Figure 2. Sensitivity of *Drosophila* Optomotor Response Is Controlled by Surround Contrast

(A) Experimental set-up. Visual display is separated into two areas whose contrast can be set independently.

(B) Bottom: space-time plot of base stimulus. Foreground pattern moved during time span indicated by dashed lines; background is dynamic but contains no coherent motion. Top: time-averaged response of EMD array along azimuth. Only foreground produced net activity.

(C) Turning responses for extreme background contrast conditions ($n = 16$ wild-type flies) at foreground contrast 12.5%. Gray-shaded area indicates motion.

(D) Mean rotation (averaged between 0 and 1 s after stimulus onset) as a function of foreground contrast for two background conditions ($n = 16$; gray arrow indicates foreground contrast depicted in C).

(E) Heatmap of mean rotation for multiple background conditions. With increasing background contrast, optomotor sensitivity shifted rightward ($n = 16$).

(F) Example stimulus for mapping magnitude of sensitivity shift. Background contrast was modulated at 1 Hz.

(G) Left: baseline turning response in the absence of background contrast ($n = 16$, foreground contrast 25%). Right: turning response for sinusoidal change in background contrast (data taken from spatial experiment evaluated in I at distance 15°). During high-contrast phase, optomotor response was suppressed; turning modulation allowed readout of background-induced changes in gain.

(H) Illustration of spatial oscillation experiment. Distance indicates separation between centers of foreground motion and flanking background.

(I) Turning response modulation as a function of distance between motion stimulus and background ($n = 16$). Gray-shaded bar indicates 68% confidence interval around baseline modulation in the absence of background.

(J) Turning response modulation as a function of carrier frequency for either foreground ($n = 13$) or background ($n = 13$). Shaded area around curves indicates bootstrapped 68% confidence interval. See also Figure S2, Table S2, and Videos S1 and S2.

independently. We confirmed that the background by itself produced no net activity in EMDs (Figure 2B).

At zero background contrast, foreground motion induced a reliable optomotor response (Figure 2C). Turning was fully suppressed at maximum background contrast, proving that turning gain is controlled by surround contrast. Average field luminance was constant for all conditions, so linear processing could not account for the phenomenon. A full measurement of contrast tuning curves for foreground motion revealed a smooth shift of the dynamic range of the optomotor response toward the current surround contrast (Figures 2D and 2E).

To efficiently map features of contrast gain control in a single stimulus condition, we sinusoidally modulated background contrast over time, which resulted in oscillations around mean turning (Figures 2F and 2G). Whenever background contrast was high, syndirectional rotation in response to motion was

transiently suppressed. Evaluating oscillation amplitude thus allowed a readout of the level of contrast-induced gain adjustment. We determined the spatial scale of suppression by varying the spacing between foreground and a windowed background, separated by uniform gray (Figure 2H). Modulation fell with distance between motion stimulus and background stripe and dropped to baseline at approximately 35°, so contrast estimation was non-local but spatially limited (Figure 2I; Figures S2A and S2B; full width at half maximum of 43.8° for zero-centered Gaussian least-squares fit to mean tuning curve).

When we varied oscillation frequency in the background, suppression followed contrast changes up to fast timescales beyond 3 Hz (Figure 2J; Figures S2C–S2F). However, modulation decreased at lower frequencies than for equivalent foreground oscillations, which is indicative of temporal integration. We additionally evaluated the lag between contrast oscillation and

turning by means of cross-correlation (Figures S2G and S2H). The maximum suppressive effect of background modulation was delayed with respect to the effect of foreground modulation by approximately 70 ms (bootstrapped 95% CI: 33–114 ms). This supported the previous conclusion that the mechanism for background contrast estimation operates on slower timescales than the primary motion pathway. Silencing T4 and T5 cells abolished all contrast-guided oscillatory turning (Figures S2I–S2K), suggesting that contrast adaptation is not mediated by a system parallel to motion detection [44]. Our experiments thus point to a rapid, spatially distributed gain control mechanism that arises in early visual processing.

Signal Compression Emerges in Transient Medulla Neurons

We next used two-photon calcium imaging to locate the neural origin of contrast adaptation. The calcium indicator GCaMP6f was genetically expressed in particular cell types [45]. We targeted visual stimuli to individual neurons by determining receptive field coordinates through a combination of stochastic stimuli and online reverse correlation (Figures 3A and 3B; STAR Methods). This procedure additionally yielded estimated linear receptive fields for L1–L5, analogously to the ones previously described for medulla neurons [9] (Figures S3A–S3T). Consistent with earlier functional work [29, 46], spatiotemporal filters grouped into tonic (L3) or transient units (L1, L2, L4, and L5) like they did in the medulla. In contrast to all other lamina cells, we found that the polarity of the L5 receptive field center is ON.

To precisely map context-dependent changes in contrast sensitivity for a given cell type, we then presented drifting sine gratings with separately controlled contrast in the foreground (as defined by a 25° circular window centered on the receptive field) and the background (Figure 3C). At a fixed foreground contrast, L1 activity followed local grating luminance and was independent of background contrast (Figure 3D). Responses in downstream synaptic partner Tm3, however, showed the signature of gain control as signal amplitude was increasingly suppressed by growing surround contrast (Figure 3E).

We performed these experiments for all major columnar cell types in the circuit as well as T4 and T5 cells (Figure 3F). To obtain contrast tuning curves, we evaluated calcium modulation at the stimulus frequency. Lamina units tracked foreground contrast but were weakly, if at all, modulated by the surround except for a vertical shift at low levels (Figures 3G–3K). This was likely due to background leaking into the receptive fields since antagonistic surrounds extend beyond 25° for some cell types (Figure S3) [9]. In the medulla (Figures 3L–3U), tonic Mi4, Mi9, and Tm9 showed similar tuning as L1–L5 and again little surround dependency. However, for all transient cells (Mi1 and Tm3 for ON; Tm1, Tm2, and Tm4 for OFF), increasing background contrast had a strongly suppressive effect, which is a hallmark of divisive contrast normalization [41].

As with the corresponding behavioral experiments (Figure 2), linear receptive fields could not explain the effect given that the average luminance was constant for all conditions. Curves were shifted rightward on the logarithmic axis, which corresponds to divisive stretching in linear contrast space. Importantly, preferred direction responses in T4 and T5 were also strongly background dependent (Figures 3P and 3U) even

though not all their medulla inputs are subject to gain control. Finally, sensitivity to foreground contrast was generally higher in ON than OFF units.

Several cell types—particularly medulla transient cells—showed a dependency between fluorescence modulation at the target frequency and average response (Figure S4), possibly due to temporal integration by the calcium indicator [47]. Depending on this average activity, a saturating transformation between calcium signal and GCaMP fluorescence could by itself introduce compression of strong signal amplitudes due to ceiling effects at the far end of the sensor's dynamic range. To rule this out, we directly compared mean activity with oscillation amplitude and found no region in which this correlation was negative (Figures S4Q–S4S).

To quantify tuning curves in detail, we fit a closed-form model resembling common models of divisive normalization to the data (Figure 3V; STAR Methods) [41, 48]. Here, response gain is regulated by a divisive term that depends on background contrast while a linear term represents the combined contribution of foreground contrast and background leakage. The model accurately reproduced tuning curves for each cell type (Figure 3W; Table S1). Critically, it accounted for vertical shifts as well as sigmoidal tuning curves and context-dependent changes in contrast sensitivity.

We computed a normalization index from model parameters that estimates the degree of normalization. Given that different cell types had different baseline sensitivities and that horizontal shifts on a logarithmic scale correspond to multiplication, we quantified the relative factor by which tuning curves would shift when background contrast was increased from 0% to 100% (STAR Methods). This index was substantially higher in transient medulla cells (Mi1, Tm3, Tm1, Tm2, and Tm4) and direction-selective T4 and T5 cells than in L1–L5 or tonic medulla units (Mi4, Mi9, and Tm9; Figure 3X). Interestingly, L2 and L5 exhibited mildly elevated normalization indices. For L2, this may be related to previously described non-linearities in its receptive field structure [49].

Normalization Relies on Fast Integration of a Pool of Transient Units

Overall, fly contrast gain control appeared to be based on divisive normalization that predominantly originates in medulla units with transient response dynamics. We focused on these neurons to investigate the mechanism in detail. Responses in Mi1, Tm1, Tm2, and Tm3 were equally suppressed for all background grating directions relative to a reference stimulus with zero background contrast (Figure 4A). Temporal frequency tunings for suppression resembled band-pass filters with a peak at 2 Hz (Figure 4B). Crucially, static backgrounds did not have a suppressive effect. Suppression steadily increased with the outer diameter of an annulus containing the background pattern, which again indicated an extended integration area (Figure 4C). Spatiotemporal features of neural gain control thus matched our findings from behavior (Figure 2).

To determine the temporal scale of normalization, we designed a contrast-step stimulus in which the foreground was replaced by a single light pulse matching each cell type's polarity (Figure 4D). By varying the time interval between motion onset of the background grating and the onset of the pulse, we scanned

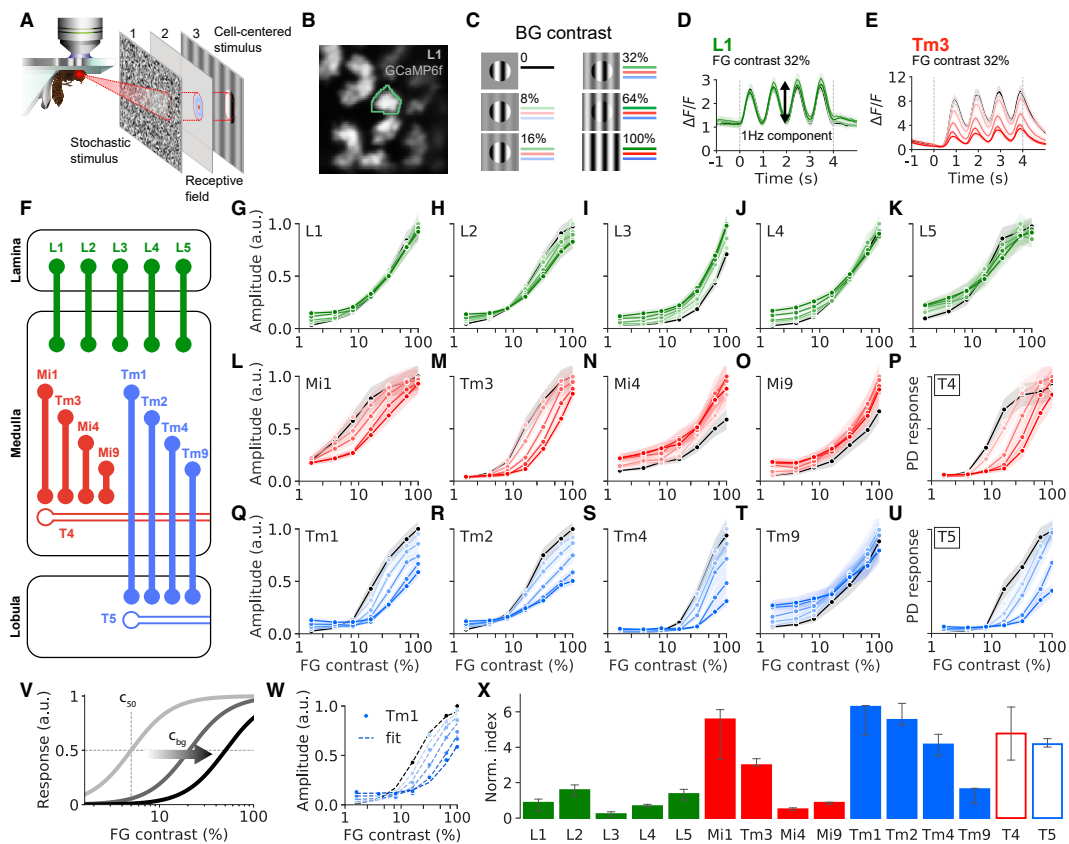


Figure 3. Contrast Normalization Emerges in Transient Medulla Neurons

(A) Schematic of experimental procedure. (1) White noise stimulus. (2) Receptive field reconstruction from single-neuron calcium signals. (3) Drifting grating with different contrasts in foreground and background.

(B) Two-photon image of L1 axon terminals expressing GCaMP6f. Green line indicates example region of interest.

(C) Experimental protocol. Darker color shade corresponds to higher background contrast as used in (G)–(U). Zero background contrast condition is shown in black.

(D and E) Average calcium responses of L1 (D) and Tm3 (E) for fixed foreground and various background contrasts.

(F) Schematic of the motion circuit including all neurons measured.

(G–K) Contrast tuning curves measured as amplitude of calcium signals at stimulus frequency for L1–L5. Shaded areas show bootstrapped 68% confidence intervals around the mean (L1 in G: 21/7 cells/files, L2 in H: 26/8, L3 in I: 23/6, L4 in J: 19/6, L5 in K: 18/9).

(L–P) Contrast tuning curves for ON pathway neurons (Mi1 in L: 20/5, Tm3 in M: 21/8, Mi4 in N: 20/13, Mi9 in O: 21/9, T4 in P: 23/10).

(Q–U) Contrast tuning curves for OFF pathway neurons (Tm1 in Q: 21/7, Tm2 in R: 20/6, Tm4 in S: 20/13, Tm9 in T: 19/6, T5 in U: 21/9).

(V) Illustration of divisive normalization model for tuning curves. Increasing background contrast c_{bg} shifts the sigmoidal tuning curve from baseline sensitivity c_{50} to higher contrasts.

(W) Example fit of model for Tm1.

(X) Normalization index for all neurons shown as median with 68% bootstrapped confidence intervals. Transient medulla neurons Mi1, Tm3, Tm1, Tm2, and Tm4, as well as T4 and T5, exhibited strongest degree of normalization.

See also [Figures S3](#) and [S4](#), [Tables S1](#) and [S2](#), and [Video S3](#).

the temporal profile of the suppressive signal. For the tested neurons Tm3 and Tm2, we found virtually immediate response reduction within a measurement precision of 50 ms given by the smallest tested onset difference. We observed transient ringing of suppression strength at the background temporal frequency. Ringing was stronger when the grating was present

before motion onset compared to when it was masked by uniform gray. A similar effect has been described in LPTCs [26], where it results from neural integration of multiple transient, out-of-phase inputs. In sum, these findings indicated that surround suppression derives from a pool of transient neurons that are not selective for direction. Both isotropy and frequency

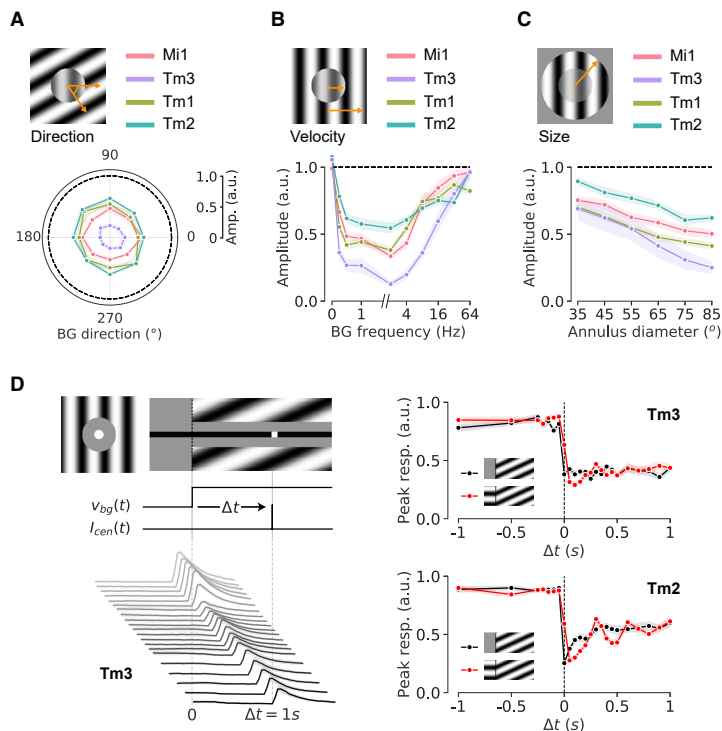


Figure 4. Neural Contrast Normalization Relies on Rapid Integration of a Pool of Transient Units

(A) Polar plot of response amplitude for different directions of background motion. Black dashed line represents response to reference stimulus with background contrast of 0%. For each neuron, foreground contrast was chosen to maximize possible background suppression (Mi1: 16%, Tm3: 32%, Tm1: 64%, Tm2: 100%).

(B) Responses for different background contrast frequencies, revealing band-pass tuning of suppression.

(C) Suppression strength increased with outer diameter of background annulus (Mi1: 21/9 cells/fly, Tm3: 20/6, Tm1: 18/6, Tm2: 21/4 in A–C).

(D) Top left: x-y and x-t plots of contrast-step stimulus for Tm3 (ON center). Background contrast frequency was 3 Hz. Center left: velocity function $v_{bg}(t)$ of background and intensity function $I_{cen}(t)$ of center pulse. Bottom left: mean responses of Tm3 for different time intervals Δt . Right: mean peak amplitude for Tm3 and Tm2 (Tm3: 19/6, Tm2: 20/5). Black line shows condition where the background grating was masked before onset; red where background was visible but static.

Shaded areas around curves indicate bootstrapped 68% confidence intervals. See also modeling in Figure S5, Table S2, and Video S4.

When measuring tuning curves (similar to Figure 3 but only for background contrasts 0% and 100%), baseline contrast sensitivity as measured by the semi-saturation constant of model fits was significantly increased (Figure 5D). This suggests that Tm3 cells were disinhibited due to a reduced pool signal. We observed similar effects for ON-sensitive Mi1 cells (Figures 5E and 5F), but the impact was less pronounced than for Tm3 cells. Absolute signal amplitude was generally not affected by silencing, demonstrating that cells remained visually responsive in the presence of TNT (see Figure 5B).

In the OFF pathway, blocking Tm1 cells did not have any significant effects (Figures 5G and 5H). In contrast, when blocking Tm2, we observed an almost complete loss of background suppression across frequencies (Figure 5I). For this cell type, we did not observe any change in contrast tuning curves for the 0% background condition, and consequently, the fitted semi-saturation constant was not affected (Figure 5J). For full background contrast, however, suppression at high foreground contrasts was strongly reduced. Additionally, background leakage at low foreground contrasts increased substantially compared to control flies. As with Tm3 and Mi1, this is compatible with Tm2 cells being disinhibited due to the silencing of a suppressive signal derived from recurrent output. We therefore conclude that in the fly, contrast normalization is at least partially based on feedback from a combination of medulla neurons.

Neural Feedback Is Critical for Contrast Normalization

Spatial pooling, however, could occur over either feedforward signals from the lamina or feedback from the medulla (Figure 5A). In vertebrate systems, it has proven difficult to distinguish the two [41, 50, 51]. Fly transient units in the lamina or medulla have similar temporal properties (Figures S3U and S3V), and both implementations produce equivalent steady-state output [48], so we used genetic silencing to pinpoint the source. We co-expressed a calcium indicator and the tetanus toxin light chain (TNT; STAR Methods) [52] in different medulla cell types, blocking chemical synaptic output and thus feedback from the entire neuron array but leaving feedforward input and calcium signals intact.

For the ON pathway unit Tm3, we observed significantly reduced suppression across background frequencies when compared to controls with inactive TNT (Figures 5B and 5C).

When measuring tuning curves (similar to Figure 3 but only for background contrasts 0% and 100%), baseline contrast sensitivity as measured by the semi-saturation constant of model fits was significantly increased (Figure 5D). This suggests that Tm3 cells were disinhibited due to a reduced pool signal. We observed similar effects for ON-sensitive Mi1 cells (Figures 5E and 5F), but the impact was less pronounced than for Tm3 cells. Absolute signal amplitude was generally not affected by silencing, demonstrating that cells remained visually responsive in the presence of TNT (see Figure 5B).

In the OFF pathway, blocking Tm1 cells did not have any significant effects (Figures 5G and 5H). In contrast, when blocking Tm2, we observed an almost complete loss of background suppression across frequencies (Figure 5I). For this cell type, we did not observe any change in contrast tuning curves for the 0% background condition, and consequently, the fitted semi-saturation constant was not affected (Figure 5J). For full background contrast, however, suppression at high foreground contrasts was strongly reduced. Additionally, background leakage at low foreground contrasts increased substantially compared to control flies. As with Tm3 and Mi1, this is compatible with Tm2 cells being disinhibited due to the silencing of a suppressive signal derived from recurrent output. We therefore conclude that in the fly, contrast normalization is at least partially based on feedback from a combination of medulla neurons.

Contrast Normalization Improves Robustness to Natural Scene Variability

Could this type of response normalization account for the robustness of fly motion detection? Previous work on EMDs

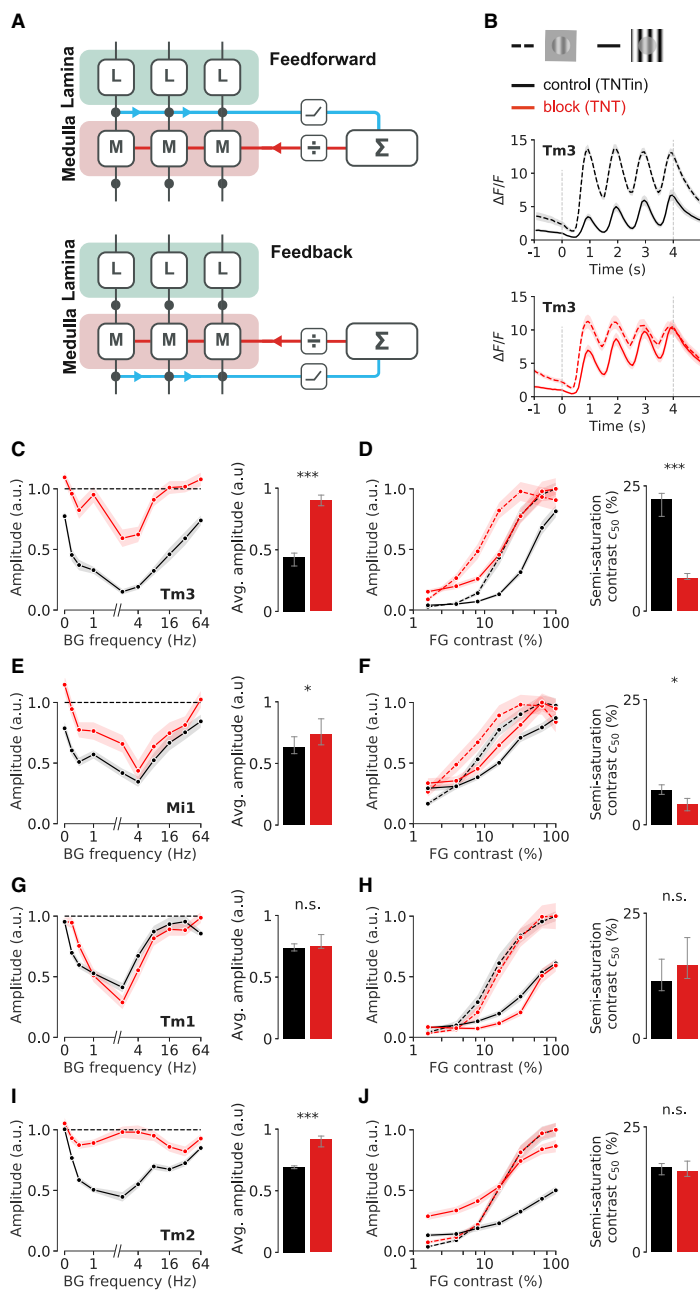


Figure 5. Neural Feedback Underlies Contrast Normalization

(A) Schematic of feedforward and feedback model for surround suppression.

(B) Mean responses of Tm3 for TNT block (red) and TNTin controls (black) at background frequency 16 Hz (dashed line indicates reference response and solid line the response at full background contrast; Tm3 block: 21/5 cells/flyes, Tm3 control: 20/5).

(C) Left: frequency tuning for block experiment. Black dashed line represents response to reference stimulus. Right: average amplitude over all frequencies was higher for Tm3 block flies (Mann-Whitney U: 8, *** $p < 0.001$).

(D) Left: foreground contrast tuning for block experiments at 0% and 100% background contrast. Right: contrast sensitivity was increased for Tm3 block flies as measured by lowered semi-saturation constant c_{50} (Mann-Whitney U: 39, *** $p < 0.001$).

(E) Blocking results for Mi1 (as in C). Average amplitude over all frequencies was reduced for Mi1 block flies (Mi1 block: 20/5, Mi1 control: 21/6; Mann-Whitney U: 143, * $p = 0.04$).

(F) Blocking results for Mi1 (as in D). Contrast sensitivity was increased for Mi1 block flies (Mann-Whitney U: 128, * $p = 0.02$).

(G) Blocking results for Tm1 (as in C). No significant effect was found for Tm1 block flies (Tm1 block: 20/5, Tm1 control: 19/5; Mann-Whitney U: 169, NS $p = 0.28$).

(H) Blocking results for Tm1 (as in D). Sensitivity was not affected (Mann-Whitney U: 158, NS $p = 0.19$).

(I) Blocking results for Tm2 (as in C; Tm2 block: 20/5, Tm2 control: 25/6; Mann-Whitney U: 17, *** $p < 0.001$).

(J) Blocking results for Tm2 (as in D; Mann-Whitney U: 239, NS $p = 0.49$). Semi-saturation constant at 0% background contrast did not change for Tm2 block flies. Shaded areas show bootstrapped 68% confidence intervals around the mean. Error bars show bootstrapped 68% confidence intervals around the median.

See also Table S2.

data-driven LPTC model and found moderate reduction of cross-image variability compared to a model with bypassed normalization (Figures S5L–S5N). However, post hoc ablation may specifically disadvantage the simpler model. To investigate performance limits in a principled way, we pursued a task-driven approach.

Recent progress in deep artificial networks has made it feasible to use image-processing models of neural systems for rigorously assessing performance on real-world problems [54–56]. EMD-like architectures are concisely expressed as multi-layer convolutional networks [54] and fully differentiable, rendering them amenable to optimization methods like gradient descent.

and natural scenes has exploited compressive transforms but did so heuristically or without surround-dependent gain control [42, 43, 53]. We evaluated natural image responses in the

We designed a fly-like neural network and independently trained possible types of contrast processing such that each model class could optimally adapt to a specific, behaviorally relevant task.

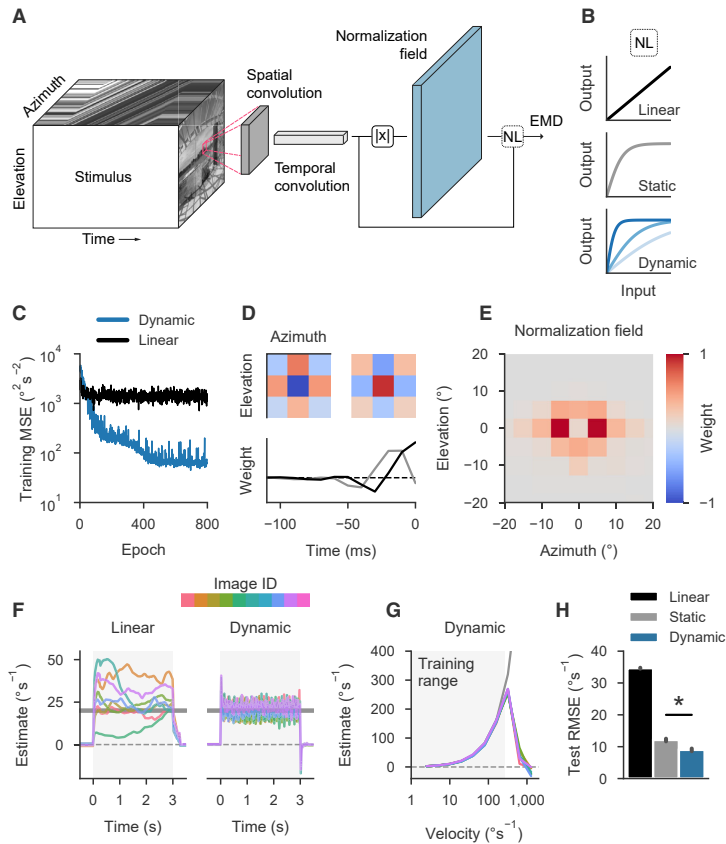


Figure 6. Contrast Normalization Enhances Robustness to Natural Scene Variability

(A) Schematic of single convolutional input filter. Motion stimuli are sequentially processed by a spatial $3 \times 3 \times 1$ (azimuth, elevation, time) and a temporal $1 \times 1 \times 30$ filter. Through a transfer function, the signal is combined with a normalization signal generated by a $11 \times 11 \times 1$ convolution operating on full-wave rectified input signal. The output of two distinct channels is processed analogously to multiplicative EMDs.

(B) Input-output relationships for linear, static, and dynamic models. In the dynamic model, response sensitivity is a function of normalization field activity.

(C) Training mean squared error (MSE) for two example models during stochastic gradient descent.

(D) Spatial and temporal receptive fields for the two channels of a typical dynamic model. Depicted are normalized filter weights.

(E) Spatial receptive field of normalization pool for the model from (D).

(F) Model output for individual images moving at 20°s^{-1} during gray-shaded period. Gray line indicates target velocity. Left: example model without non-linearity. Right: example model with dynamic non-linearity.

(G) Velocity tuning curves of example dynamic model for individual images (averaged between 0 and 3 s after motion onset). Gray line indicates true velocity. Gray-shaded area indicates the 99th percentile of absolute velocities in training set.

(H) Mean performance of trained models on held-out test set, estimated as root mean square error (RMSE; $n = 22/23/16$ for linear/static/dynamic; $*p < 0.001$, $t = 9.01$, Student's t test with assumed equal variance; only difference between static and dynamic was tested). Error bars indicate bootstrapped 68% confidence intervals. See also Figure S6.

All models featured linear, spatiotemporally separable input convolutions (Figure 6A). We evaluated three alternatives for contrast transformation: a linear stage where output was transmitted unchanged, a statically compressive stage that limited signal range independently of context, and a dynamic compression stage with adaptive gain depending on the output of a contrast-sensitive surround filter (Figures 6A and 6B; STAR Methods). Resulting output from two distinct channels was then processed according to a multiplicative EMD scheme. Through backpropagation and stochastic gradient descent, models were trained to estimate the true velocity of natural images translating at random speeds.

All models successfully learned the task on the training set (Figure 6C). We initialized convolutions randomly but after training observed antagonistic spatial filters and transient temporal filters where one channel was phase delayed with respect to the other (Figure 6D; Figures S6A–S6C). Models thus made extensive use of redundancy reduction through center-surround configurations [35] and discovered the EMD strategy of delay and compare [26]. Normalization fields for the dynamic model spanned approximately 30° in azimuth and invariably excluded information from the center of the filter (Figure 6E; Figure S6C). Interestingly, dynamic models exploited normalization in both

channels and switched normalization strategies during training, transitioning from purely static to purely context-dependent compression (Figures S6D and S6E). Overall, normalized networks acquired representations that matched filtering and gain control properties of the fly medulla.

When tested on previous experimental stimuli (Figure 1), linear models exhibited improved velocity tuning curves compared to a standard EMD (Figures 1F and 6F; Figure S6F), but estimates still varied substantially across time. Dynamic models, on the other hand, proved extremely robust at extracting scene motion across time, images, and velocities within the velocity range of the training set (Figures 6F and 6G). Given that all networks were based on a multiplicative EMD scheme, typical phenomena like the velocity optimum were still present. We compared average estimation error on a held-out test set and found both types of non-linear compression to vastly outperform the linear stage (Figure 6H). The performance of static compression indicates that simple response saturation already enhances robustness to contrast fluctuations in natural scenes. However, fly-like context sensitivity consistently decreased test error over the static non-linearity (error reduction 22.0%–29.2%; bootstrapped 95% CI). Finally, we benchmarked generalization on a fully independent image set (Figure S6G), where linear models failed

catastrophically while both compressive stages retained performance. This was particularly pronounced when testing images with high dynamic range (STAR Methods). Critically, on all datasets, dynamic compression resulted in substantial error reduction with respect to both linear transfer and static compression.

DISCUSSION

In summary, our work represents the first demonstration that divisive contrast normalization occurs in the fly visual system and offers a comprehensive look at non-linear response properties in a virtually complete motion vision circuit. We established at multiple levels of motion processing that responses to moving panoramas are substantially more robust than predicted by correlation-based models of the system. Our behavioral experiments indicate that the sensitivity of the optomotor response is regulated by average contrast in a spatially confined part of the visual field. Critically, we traced the emergence of this dynamic signal compression to local elements in the medulla of the fly optic lobe and used targeted circuit manipulation to identify neural feedback as a critical underlying mechanism. Finally, our task-driven approach revealed that the inclusion of spatial contrast normalization drastically improves velocity estimation in correlation-based models of fly motion vision.

Implications for Fly Motion Vision

Previous work on the function of local units in the *Drosophila* optic lobe mostly explored linear properties of light responses, often relying on first-order systems identification techniques like reverse correlation [9–11, 29]. Investigation of non-linear contributions generally focused on computations in direction-selective T4 and T5 cells [13–19, 57, 58].

Here, we describe a powerful non-linearity, adaptive gain control that occurs in a majority of columnar neurons involved in the detection of motion. This casts doubt on the extent to which existing functional descriptions can be generalized. Linear filter estimates are typically based on responses to dynamic noise stimuli of fixed amplitude [9, 10, 29]. Our work suggests that this contrast regime only corresponds to one particular adaptation state for any measured cell type, so filter properties may well differ for stimuli with differing contrast characteristics. Step and edge responses, for instance, are usually measured on backgrounds with uniform luminance [11, 12, 18, 59]. This places cells in a maximally sensitive state due to lack of surround inhibition and is likely to affect both response amplitude and kinetics. Signal compression may reconcile observed discrepancies between studies conducted with different stimuli.

Interestingly, visual interneurons exhibited qualitatively different sensitivity curves even at constant background contrast. In the lamina, for instance, only tonic cell type L3 responded linearly to increasing visual contrast. Sensitivity curves of transiently responding cell types like L1 and L2, on the other hand, proved approximately logarithmic. This is in line with expectations from previous work in other fly species [60] but deviates from predictions based on white noise characterizations [29].

Moreover, we observed a stark discrepancy in baseline sensitivity between ON- and OFF-sensitive neurons, where tuning curves of dark-selective units were shifted toward higher pattern contrast. Notably, due to strong surround suppression, full-field

gratings elicited comparatively weak responses in T5 units whereas T4 cells were driven effectively by the same stimuli. This adds to previous work on ON-OFF asymmetries in the *Drosophila* visual system [31, 38]. We conclude that even at primary processing stages, the fly visual system represents contrast in a multiplexed fashion where individual channels diverge with respect to how they transmit information about luminance differences. The function of these asymmetries remains to be investigated.

The proposed model based on divisive normalization accurately captures most features of the observed contrast tuning curves (see Figure 3; Figure S5; Table S1). Certain discrepancies remain. For instance, the normalization model predicts that responses for different background contrasts eventually plateau at the same level. However, we observed in both behavior (Figure 2E) and T4 responses (Figure 3P) that in the absence of background contrast, saturation occurred at a lower level than for other conditions. To explain such non-monotonic behavior, further investigation of the underlying mechanism is required.

Divisive normalization of local motion signals has previously been suggested to occur at the level of LPTCs, through either isotropic pooling of EMDs in hypothetical secondary cell types [33] or passive membrane properties of LPTCs [61, 62]. Here, we show that gain control already originates upstream of motion-sensitive cell types T4 and T5. However, LPTC-intrinsic gain control mechanisms, including temporal adaptation [32], could well be complementary such that at each processing stage, the fly visual system makes use of compression to optimize the reliability of output signals.

In flies, there is ample evidence for changes in visual coding that depend on the behavioral state of the animal. Various interneurons within the optic lobe, for instance, are affected by the activity of octopaminergic projection units, leading to drastic shifts in response gain or temporal tuning [9, 59, 63–67]. Our calcium imaging experiments were performed in immobilized *Drosophila*. It will be of interest to explore whether the properties of contrast gain control are modulated by locomotion, particularly in highly state-sensitive units like Mi4 [59].

Mechanism of Signal Compression

Our experiments suggest that neural feedback plays a crucial role in gain adjustment. At this point, the cellular origin of feedback is unknown. Present experiments indicate a visual integration field that spans many columns (Figures 2 and 4). Moreover, the observed contrast compression appears to be suppressive. All tested medulla cell types with strong background contrast dependency emit acetylcholine, which, in the *Drosophila* visual system, is generally thought to be excitatory [68, 69]. Inhibitory interneurons could mediate the required synaptic sign reversal. Signal compression could then be implemented through lateral neighbor-to-neighbor interactions between columnar medulla units where suppressive signals spread through a local network. Alternatively, we hypothesize that wide-field interneurons pool local medulla units across multiple columns and provide recurrent inhibitory input to the same cells. In our data-driven model, such a pool cell mechanism accounted for all observed spatiotemporal properties of signal compression including ringing effects (Figure S5). Finally, our TNT-based intervention strategy

should leave coupling via electrical synapses intact [52, 70]. We can therefore not exclude that gap junctions are also involved in shaping contrast response properties.

Silencing feedback from individual medulla cell types had differential effects, ranging from completely abolished suppression in Tm2 to unchanged responses in Tm1 (Figure 5). This suggests either that multiple cell types feed into the pool signal with varying weight or that alternative mechanisms provide the compressive signal, for example, in Tm1. Moreover, it is an open question whether all cell types are suppressed by one or multiple pool cell types. Asymmetries in sensitivity between ON and OFF pathways, for instance, could be an indicator for polarity-specific sources of suppression.

In both distal and proximal layers of the medulla, the class of neuropil-intrinsic Dm and Pm neurons contains approximately 20 cell types and offers a possible substrate for the mechanism [71, 72]. These neurons arborize within the medulla and exhibit diverse stratification and tiling patterns, often spanning dozens of columns and thus approximately matching the observed suppression field of local units. Dm and Pm units release either GABA or glutamate for which receptors in the fly visual system are mostly inhibitory [68], pointing to these cell types as potential candidates for gain control.

Functional Relevance

Normalization has often been described as a generic mechanism for removing higher-order correlations from natural signals [5, 73–75]. Here, we close the loop between neural mechanism and an ecologically critical behavior, the optomotor response, and demonstrate how contrast gain control can render motion detection resilient to challenges imposed by natural scene statistics. Specifically, normalization serves to distinguish between ecologically relevant parameters like retinal image velocity and nuisance factors like image contrast.

Various biomimetic modeling studies have incorporated compressive transforms along the motion processing cascade to improve robustness under naturalistic visual conditions [43, 53, 76]. In contrast to our work, these normalization stages were not based on experimental evidence, required *ad hoc* parameter tuning, and generally operated in the temporal domain. Interestingly, the fly visual system bases gain control on a temporally immediate, spatially extended estimate of contrast. This represents a trade-off where spatial resolution is sacrificed in favor of temporal resolution, which may be advantageous for global optic flow estimation in rapidly moving animals.

To assess the exact causal contribution of contrast compression to the robustness of velocity estimation in *Drosophila*, one would need to disrupt this mechanism specifically while leaving all other visual processing intact. Silencing the synaptic output of medulla neurons (Figure 5) demonstrates the importance of neural feedback for gain control but should additionally affect feedforward processing in downstream units, particularly T4 and T5 [11, 12, 77, 78]. Future mapping of the circuits underlying contrast compression will provide the tools for establishing causality.

The convolutional network (Figure 6) solves the task of estimating velocity across diverse environments and at little computational cost, particularly compared to standard optic flow algorithms like the Lucas-Kanade method [79]. Present findings

may thus aid the design of low-power, low-latency machine vision systems suitable for autonomous vehicles [80, 81].

Comparison with Other Sensory Systems

Gain control in the *Drosophila* optic lobe bears a striking resemblance to normalization in other systems and modalities like fly olfaction [82] or mammalian auditory cortex [83] as well as processing in vertebrate visual areas from retina to V1 [48, 84–86]. Spatial and temporal tuning or isotropy of non-linear surround suppression in the lateral geniculate nucleus, in particular, qualitatively match that of transient units in the fly medulla [40]. The present study suggests differences at the implementation level. For instance, investigations into divisive normalization in mammalian V1 cells point to feedforward mechanisms underlying gain control whereas the fly visual system appears to rely primarily on feedback signals (Figure 5) [50]. Both systems, however, realize a similar algorithm. This provides further proof for evolutionary convergence on canonical solutions in neural sensory processing [41].

Overall, our work establishes the *Drosophila* visual system with its defined cell types, known connectivity patterns, powerful genetic toolkit, and direct correspondence between circuit and task as a novel model for the study of normalization. It thus lays the foundation for future mechanistic inquiries into the functional, cellular, molecular, and biophysical underpinnings of a crucial computation in sensory processing.

STAR★METHODS

Detailed methods are provided in the online version of this paper and include the following:

- KEY RESOURCES TABLE
- LEAD CONTACT AND MATERIALS AVAILABILITY
- EXPERIMENTAL MODEL AND SUBJECT DETAILS
- METHOD DETAILS
 - Natural image sets
 - Behavioral experiments
 - Electrophysiology
 - Calcium imaging
 - Modeling
- QUANTIFICATION AND STATISTICAL ANALYSIS
 - Data evaluation for behavioral experiments
 - Data evaluation for electrophysiological experiments
 - Data evaluation for calcium imaging experiments
 - Statistical tests
- DATA AND CODE AVAILABILITY

SUPPLEMENTAL INFORMATION

Supplemental Information can be found online at <https://doi.org/10.1016/j.cub.2019.10.035>.

ACKNOWLEDGMENTS

We thank S. Prech for technical assistance; J. Kuhl for schematics; A. Nern, G.M. Rubin, and T. Schilling for supplying unpublished Gal4 driver lines; G. Ammer for immunohistochemistry; R. Brinkworth for providing access to natural images; and L. Groschner, A. Mauss, and M. Meier for commenting on drafts of the manuscript. The study was supported by the DFG (SFB 870) and the Max Planck Society.

AUTHOR CONTRIBUTIONS

M.S.D., A.L., and A.B. jointly conceived the study. M.S.D. and A.L. designed all experiments. A.L. and L.B. conducted behavioral experiments. E.S. recorded electrophysiological responses. M.S.D., N.P., F.G.R., and A.S. performed calcium imaging. A.L. designed and analyzed the convolutional model. M.S.D. and A.L. analyzed data, performed modeling, and wrote the manuscript. All authors participated in editing the manuscript.

DECLARATION OF INTERESTS

The authors declare no competing interests.

Received: August 2, 2019

Revised: September 17, 2019

Accepted: October 18, 2019

Published: January 9, 2020

REFERENCES

- Gibson, J.J. (1950). *The Perception of the Visual World* (Houghton Mifflin).
- Dickinson, M.H. (2014). Death Valley, *Drosophila*, and the Devonian toolkit. *Annu. Rev. Entomol.* *59*, 51–72.
- Borst, A. (2014). Fly visual course control: behaviour, algorithms and circuits. *Nat. Rev. Neurosci.* *15*, 590–599.
- Geisler, W.S. (2008). Visual perception and the statistical properties of natural scenes. *Annu. Rev. Psychol.* *59*, 167–192.
- Rieke, F., and Rudd, M.E. (2009). The challenges natural images pose for visual adaptation. *Neuron* *64*, 605–616.
- Mauss, A.S., Vlasits, A., Borst, A., and Feller, M. (2017). Visual circuits for direction selectivity. *Annu. Rev. Neurosci.* *40*, 211–230.
- Yang, H.H., and Clandinin, T.R. (2018). Elementary motion detection in *Drosophila*: Algorithms and mechanisms. *Annu. Rev. Vis. Sci.* *4*, 143–163.
- Shinomiya, K., Huang, G., Lu, Z., Parag, T., Xu, C.S., Aniceto, R., Ansari, N., Cheatham, N., Lauchie, S., Neace, E., et al. (2019). Comparisons between the ON- and OFF-edge motion pathways in the *Drosophila* brain. *eLife* *8*, e40025.
- Arenz, A., Drews, M.S., Richter, F.G., Ammer, G., and Borst, A. (2017). The temporal tuning of the *Drosophila* motion detectors is determined by the dynamics of their input elements. *Curr. Biol.* *27*, 929–944.
- Behnia, R., Clark, D.A., Carter, A.G., Clandinin, T.R., and Desplan, C. (2014). Processing properties of ON and OFF pathways for *Drosophila* motion detection. *Nature* *512*, 427–430.
- Serbe, E., Meier, M., Leonhardt, A., and Borst, A. (2016). Comprehensive characterization of the major presynaptic elements to the *Drosophila* OFF motion detector. *Neuron* *89*, 829–841.
- Strother, J.A., Wu, S.-T., Wong, A.M., Nern, A., Rogers, E.M., Le, J.Q., Rubin, G.M., and Reiser, M.B. (2017). The emergence of directional selectivity in the visual motion pathway of *Drosophila*. *Neuron* *94*, 168–182.e10.
- Salazar-Gatzimas, E., Agrochao, M., Fitzgerald, J.E., and Clark, D.A. (2018). The neuronal basis of an illusory motion percept is explained by decorrelation of parallel motion pathways. *Curr. Biol.* *28*, 3748–3762.e8.
- Maisak, M.S., Haag, J., Ammer, G., Serbe, E., Meier, M., Leonhardt, A., Schilling, T., Bahl, A., Rubin, G.M., Nern, A., et al. (2013). A directional tuning map of *Drosophila* elementary motion detectors. *Nature* *500*, 212–216.
- Gruntman, E., Romani, S., and Reiser, M.B. (2018). Simple integration of fast excitation and offset, delayed inhibition computes directional selectivity in *Drosophila*. *Nat. Neurosci.* *21*, 250–257.
- Salazar-Gatzimas, E., Chen, J., Creamer, M.S., Mano, O., Mandel, H.B., Matulis, C.A., Pottackal, J., and Clark, D.A. (2016). Direct measurement of correlation responses in *Drosophila* elementary motion detectors reveals fast timescale tuning. *Neuron* *92*, 227–239.
- Leong, J.C.S., Esch, J.J., Poole, B., Ganguli, S., and Clandinin, T.R. (2016). Direction selectivity in *Drosophila* emerges from preferred-direction enhancement and null-direction suppression. *J. Neurosci.* *36*, 8078–8092.
- Haag, J., Arenz, A., Serbe, E., Gabbiani, F., and Borst, A. (2016). Complementary mechanisms create direction selectivity in the fly. *eLife* *5*, e17421.
- Fisher, Y.E., Silies, M., and Clandinin, T.R. (2015). Orientation selectivity sharpens motion detection in *Drosophila*. *Neuron* *88*, 390–402.
- Bahl, A., Ammer, G., Schilling, T., and Borst, A. (2013). Object tracking in motion-blind flies. *Nat. Neurosci.* *16*, 730–738.
- Busch, C., Borst, A., and Mauss, A.S. (2018). Bi-directional control of walking behavior by horizontal optic flow sensors. *Curr. Biol.* *28*, 4037–4045.e5.
- Haikala, V., Joesch, M., Borst, A., and Mauss, A.S. (2013). Optogenetic control of fly optomotor responses. *J. Neurosci.* *33*, 13927–13934.
- Krapp, H.G., and Hengstenberg, R. (1996). Estimation of self-motion by optic flow processing in single visual interneurons. *Nature* *384*, 463–466.
- Hassenstein, B., and Reichardt, W. (1956). Systemtheoretische Analyse der Zeit-, Reihenfolgen- und Vorzeichenauswertung bei der Bewegungsperzeption des Rüsselkäfers *Chlorophanus*. *Z. Naturforsch. B* *11*, 513–524.
- Joesch, M., Plett, J., Borst, A., and Reiff, D.F. (2008). Response properties of motion-sensitive visual interneurons in the lobula plate of *Drosophila melanogaster*. *Curr. Biol.* *18*, 368–374.
- Borst, A., Reisenman, C., and Haag, J. (2003). Adaptation of response transients in fly motion vision. II: Model studies. *Vision Res.* *43*, 1309–1322.
- Borst, A., Flanagan, V.L., and Sompolinsky, H. (2005). Adaptation without parameter change: Dynamic gain control in motion detection. *Proc. Natl. Acad. Sci. USA* *102*, 6172–6176.
- Eichner, H., Joesch, M., Schnell, B., Reiff, D.F., and Borst, A. (2011). Internal structure of the fly elementary motion detector. *Neuron* *70*, 1155–1164.
- Clark, D.A., Bursztyn, L., Horowitz, M.A., Schnitzer, M.J., and Clandinin, T.R. (2011). Defining the computational structure of the motion detector in *Drosophila*. *Neuron* *70*, 1165–1177.
- Straw, A.D., Rainsford, T., and O'Carroll, D.C. (2008). Contrast sensitivity of insect motion detectors to natural images. *J. Vis.* *8*, 1–9.
- Leonhardt, A., Ammer, G., Meier, M., Serbe, E., Bahl, A., and Borst, A. (2016). Asymmetry of *Drosophila* ON and OFF motion detectors enhances real-world velocity estimation. *Nat. Neurosci.* *19*, 706–715.
- Harris, R.A., O'Carroll, D.C., and Laughlin, S.B. (2000). Contrast gain reduction in fly motion adaptation. *Neuron* *28*, 595–606.
- Reichardt, W., Poggio, T., and Hausen, K. (1983). Figure-ground discrimination by relative movement in the visual system of the fly. *Biol. Cybern.* *46*, 1–30.
- van Hateren, J.H. (1997). Processing of natural time series of intensities by the visual system of the blowfly. *Vision Res.* *37*, 3407–3416.
- Srinivasan, M.V., Laughlin, S.B., and Dubs, A. (1982). Predictive coding: a fresh view of inhibition in the retina. *Proc. R. Soc. Lond. B Biol. Sci.* *216*, 427–459.
- Mauss, A.S., Pankova, K., Arenz, A., Nern, A., Rubin, G.M., and Borst, A. (2015). Neural circuit to integrate opposing motions in the visual field. *Cell* *162*, 351–362.
- Fitzgerald, J.E., and Clark, D.A. (2015). Nonlinear circuits for naturalistic visual motion estimation. *eLife* *4*, e09123.
- Clark, D.A., Fitzgerald, J.E., Ales, J.M., Gohl, D.M., Silies, M.A., Norcia, A.M., and Clandinin, T.R. (2014). Flies and humans share a motion estimation strategy that exploits natural scene statistics. *Nat. Neurosci.* *17*, 296–303.
- Demb, J.B. (2008). Functional circuitry of visual adaptation in the retina. *J. Physiol.* *586*, 4377–4384.

40. Bonin, V., Mante, V., and Carandini, M. (2005). The suppressive field of neurons in lateral geniculate nucleus. *J. Neurosci.* *25*, 10844–10856.
41. Carandini, M., and Heeger, D.J. (2011). Normalization as a canonical neural computation. *Nat. Rev. Neurosci.* *13*, 51–62.
42. Dror, R.O., O'Carroll, D.C., and Laughlin, S.B. (2001). Accuracy of velocity estimation by Reichardt correlators. *J. Opt. Soc. Am. A Opt. Image Sci. Vis.* *18*, 241–252.
43. Brinkworth, R.S.A., and O'Carroll, D.C. (2009). Robust models for optic flow coding in natural scenes inspired by insect biology. *PLoS Comput. Biol.* *5*, e1000555.
44. Bahl, A., Serbe, E., Meier, M., Ammer, G., and Borst, A. (2015). Neural mechanisms for *Drosophila* contrast vision. *Neuron* *88*, 1240–1252.
45. Chen, T.-W., Wardill, T.J., Sun, Y., Pulver, S.R., Renninger, S.L., Baohan, A., Schreiter, E.R., Kerr, R.A., Orger, M.B., Jayaraman, V., et al. (2013). Ultrasensitive fluorescent proteins for imaging neuronal activity. *Nature* *499*, 295–300.
46. Silies, M., Gohl, D.M., Fisher, Y.E., Freifeld, L., Clark, D.A., and Clandinin, T.R. (2013). Modular use of peripheral input channels tunes motion-detecting circuitry. *Neuron* *79*, 111–127.
47. Strother, J.A., Nern, A., and Reiser, M.B. (2014). Direct observation of ON and OFF pathways in the *Drosophila* visual system. *Curr. Biol.* *24*, 976–983.
48. Heeger, D.J. (1992). Normalization of cell responses in cat striate cortex. *Vis. Neurosci.* *9*, 181–197.
49. Freifeld, L., Clark, D.A., Schnitzer, M.J., Horowitz, M.A., and Clandinin, T.R. (2013). GABAergic lateral interactions tune the early stages of visual processing in *Drosophila*. *Neuron* *78*, 1075–1089.
50. Freeman, T.C.B., Durand, S., Kiper, D.C., and Carandini, M. (2002). Suppression without inhibition in visual cortex. *Neuron* *35*, 759–771.
51. Li, B., Thompson, J.K., Duong, T., Peterson, M.R., and Freeman, R.D. (2006). Origins of cross-orientation suppression in the visual cortex. *J. Neurophysiol.* *96*, 1755–1764.
52. Sweeney, S.T., Broadie, K., Keane, J., Niemann, H., and O'Kane, C.J. (1995). Targeted expression of tetanus toxin light chain in *Drosophila* specifically eliminates synaptic transmission and causes behavioral defects. *Neuron* *14*, 341–351.
53. Shoemaker, P.A., O'Carroll, D.C., and Straw, A.D. (2005). Velocity constancy and models for wide-field visual motion detection in insects. *Biol. Cybern.* *93*, 275–287.
54. LeCun, Y., Bengio, Y., and Hinton, G. (2015). Deep learning. *Nature* *521*, 436–444.
55. Yamins, D.L.K., and DiCarlo, J.J. (2016). Using goal-driven deep learning models to understand sensory cortex. *Nat. Neurosci.* *19*, 356–365.
56. McIntosh, L., Maheswaranathan, N., Nayebi, A., Ganguli, S., and Baccus, S. (2016). Deep learning models of the retinal response to natural scenes. In *Advances in Neural Information Processing Systems 29*, D.D. Lee, M. Sugiyama, U.V. Luxburg, I. Guyon, and R. Garnett, eds., pp. 1369–1377.
57. Haag, J., Mishra, A., and Borst, A. (2017). A common directional tuning mechanism of *Drosophila* motion-sensing neurons in the ON and in the OFF pathway. *eLife* *6*, e29044.
58. Wienecke, C.F.R., Leong, J.C.S., and Clandinin, T.R. (2018). Linear summation underlies direction selectivity in *Drosophila*. *Neuron* *99*, 680–688.e4.
59. Strother, J.A., Wu, S.-T., Rogers, E.M., Eliason, J.L.M., Wong, A.M., Nern, A., and Reiser, M.B. (2018). Behavioral state modulates the ON visual motion pathway of *Drosophila*. *Proc. Natl. Acad. Sci. USA* *115*, E102–E111.
60. Laughlin, S. (1981). A simple coding procedure enhances a neuron's information capacity. *Z. Naturforsch., C, Biosci.* *36*, 910–912.
61. Borst, A., Egelhaaf, M., and Haag, J. (1995). Mechanisms of dendritic integration underlying gain control in fly motion-sensitive interneurons. *J. Comput. Neurosci.* *2*, 5–18.
62. Weber, F., Machens, C.K., and Borst, A. (2010). Spatiotemporal response properties of optic-flow processing neurons. *Neuron* *67*, 629–642.
63. Suver, M.P., Mamiya, A., and Dickinson, M.H. (2012). Octopamine neurons mediate flight-induced modulation of visual processing in *Drosophila*. *Curr. Biol.* *22*, 2294–2302.
64. Tuthill, J.C., Nern, A., Rubin, G.M., and Reiser, M.B. (2014). Wide-field feedback neurons dynamically tune early visual processing. *Neuron* *82*, 887–895.
65. Jung, S.N., Borst, A., and Haag, J. (2011). Flight activity alters velocity tuning of fly motion-sensitive neurons. *J. Neurosci.* *31*, 9231–9237.
66. Maimon, G., Straw, A.D., and Dickinson, M.H. (2010). Active flight increases the gain of visual motion processing in *Drosophila*. *Nat. Neurosci.* *13*, 393–399.
67. Chiappe, M.E., Seelig, J.D., Reiser, M.B., and Jayaraman, V. (2010). Walking modulates speed sensitivity in *Drosophila* motion vision. *Curr. Biol.* *20*, 1470–1475.
68. Davis, F.P., Nern, A., Picard, S., Reiser, M.B., Rubin, G.M., Eddy, S.R., and Henry, G.L. (2018). A genetic, genomic, and computational resource for exploring neural circuit function. *bioRxiv*. <https://doi.org/10.1101/385476v1>.
69. Mauss, A.S., Meier, M., Serbe, E., and Borst, A. (2014). Optogenetic and pharmacologic dissection of feedforward inhibition in *Drosophila* motion vision. *J. Neurosci.* *34*, 2254–2263.
70. Joesch, M., Schnell, B., Raghu, S.V., Reiff, D.F., and Borst, A. (2010). ON and OFF pathways in *Drosophila* motion vision. *Nature* *468*, 300–304.
71. Nern, A., Pfeiffer, B.D., and Rubin, G.M. (2015). Optimized tools for multi-color stochastic labeling reveal diverse stereotyped cell arrangements in the fly visual system. *Proc. Natl. Acad. Sci. USA* *112*, E2967–E2976.
72. Fischbach, K.F., and Dittrich, A.P. (1989). The optic lobe of *Drosophila melanogaster*. I: A Golgi analysis of wild-type structure. *Cell Tissue Res.* *258*, 441–475.
73. Schwartz, O., and Simoncelli, E.P. (2001). Natural signal statistics and sensory gain control. *Nat. Neurosci.* *4*, 819–825.
74. Mante, V., Frazor, R.A., Bonin, V., Geisler, W.S., and Carandini, M. (2005). Independence of luminance and contrast in natural scenes and in the early visual system. *Nat. Neurosci.* *8*, 1690–1697.
75. Mante, V., Bonin, V., and Carandini, M. (2008). Functional mechanisms shaping lateral geniculate responses to artificial and natural stimuli. *Neuron* *58*, 625–638.
76. Shoemaker, P.A., Hyslop, A.M., and Humbert, J.S. (2011). Optic flow estimation on trajectories generated by bio-inspired closed-loop flight. *Biol. Cybern.* *104*, 339–350.
77. Ammer, G., Leonhardt, A., Bahl, A., Dickson, B.J., and Borst, A. (2015). Functional specialization of neural input elements to the *Drosophila* ON motion detector. *Curr. Biol.* *25*, 2247–2253.
78. Meier, M., Serbe, E., Maisak, M.S., Haag, J., Dickson, B.J., and Borst, A. (2014). Neural circuit components of the *Drosophila* OFF motion vision pathway. *Curr. Biol.* *24*, 385–392.
79. Lucas, B.D., and Kanade, T. (1981). An iterative image registration technique with an application to stereo vision. *Proceedings of the International Joint Conference on Artificial Intelligence* *2*, 674–679.
80. Plett, J., Bahl, A., Buss, M., Kühnlenz, K., and Borst, A. (2012). Bio-inspired visual ego-rotation sensor for MAVs. *Biol. Cybern.* *106*, 51–63.
81. Bagheri, Z.M., Cazzolato, B.S., Grainger, S., O'Carroll, D.C., and Wiederman, S.D. (2017). An autonomous robot inspired by insect neurophysiology pursues moving features in natural environments. *J. Neural Eng.* *14*, 046030.
82. Olsen, S.R., Bhandawat, V., and Wilson, R.I. (2010). Divisive normalization in olfactory population codes. *Neuron* *66*, 287–299.
83. Rabinowitz, N.C., Willmore, B.D.B., Schnupp, J.W.H., and King, A.J. (2011). Contrast gain control in auditory cortex. *Neuron* *70*, 1178–1191.
84. Baccus, S.A., and Meister, M. (2002). Fast and slow contrast adaptation in retinal circuitry. *Neuron* *36*, 909–919.
85. Busse, L., Wade, A.R., and Carandini, M. (2009). Representation of concurrent stimuli by population activity in visual cortex. *Neuron* *64*, 931–942.

86. Carandini, M., Heeger, D.J., and Movshon, J.A. (1997). Linearity and normalization in simple cells of the macaque primary visual cortex. *J. Neurosci.* *17*, 8621–8644.
87. Tuthill, J.C., Nern, A., Holtz, S.L., Rubin, G.M., and Reiser, M.B. (2013). Contributions of the 12 neuron classes in the fly lamina to motion vision. *Neuron* *79*, 128–140.
88. Pologruto, T.A., Sabatini, B.L., and Svoboda, K. (2003). ScanImage: flexible software for operating laser scanning microscopes. *Biomed. Eng. Online* *2*, 13. <https://doi.org/10.1186/1475-925X-2-13>.
89. Meyer, H.G., Schwegmann, A., Lindemann, J.P., and Egelhaaf, M. (2014). Panoramic high dynamic range images in diverse environments. <https://doi.org/10.4119/unibi/2689637>.
90. Brand, A.H., and Perrimon, N. (1993). Targeted gene expression as a means of altering cell fates and generating dominant phenotypes. *Development* *118*, 401–415.
91. Kingma, D.P., and Ba, J. (2014). Adam: A method for stochastic optimization. arXiv, arXiv:1412.6980. <https://arxiv.org/abs/1412.6980>.
92. Richter, F.G., Fendl, S., Haag, J., Drews, M.S., and Borst, A. (2018). Glutamate signaling in the fly visual system. *iScience* *7*, 85–95.
93. Jia, H., Rochefort, N.L., Chen, X., and Konnerth, A. (2011). In vivo two-photon imaging of sensory-evoked dendritic calcium signals in cortical neurons. *Nat. Protoc.* *6*, 28–35.

STAR★METHODS

KEY RESOURCES TABLE

REAGENT or RESOURCE	SOURCE	IDENTIFIER
Deposited Data		
Experimental data (behavior, electrophysiology, and calcium imaging)	This study	https://github.com/borstlab/normalization_paper
Experimental Models: Organisms/Strains		
<i>D. melanogaster</i> : WT: Canton S	N/A	N/A
<i>D. melanogaster</i> : L1-AD: w ¹¹¹⁸ ; VT027316-AD; +	Courtesy of A. Nern / Janelia Research Campus	N/A
<i>D. melanogaster</i> : L1-DBD: w ¹¹¹⁸ ; +; R40F12-DBD	Courtesy of A. Nern / Janelia Research Campus	RRID: BDSC_69935
<i>D. melanogaster</i> : L2-AD: w ¹¹¹⁸ ; R53G02-AD; +	[87]	RRID: BDSC_68990
<i>D. melanogaster</i> : L2-DBD: w ¹¹¹⁸ ; +; R29G11-DBD	[87]	RRID: BDSC_70173
<i>D. melanogaster</i> : L3-AD: w ¹¹¹⁸ ; R59A05-AD; +	[87]	RRID: BDSC_70751
<i>D. melanogaster</i> : L3-DBD: w ¹¹¹⁸ ; +; R75H07-DBD	[87]	RRID: BDSC_69459
<i>D. melanogaster</i> : L4-AD: w ¹¹¹⁸ ; R20A03-AD; +	[87]	RRID: BDSC_68957
<i>D. melanogaster</i> : L4-DBD: w ¹¹¹⁸ ; +; R31C06-DBD	[87]	RRID: BDSC_68978
<i>D. melanogaster</i> : L5-AD: w ¹¹¹⁸ ; R21A05-AD; +	[87]	RRID: BDSC_70588
<i>D. melanogaster</i> : L5-DBD: w ¹¹¹⁸ ; +; R31H09-DBD	[87]	RRID: BDSC_68980
<i>D. melanogaster</i> : Mi1-AD: w ¹¹¹⁸ ; R19F01-AD; +	[12]	RRID: BDSC_68955
<i>D. melanogaster</i> : Mi1-DBD: w ¹¹¹⁸ ; +; R71D01-DBD	[12]	RRID: BDSC_69066
<i>D. melanogaster</i> : Tm3-AD: w ¹¹¹⁸ ; R13E12-AD; +	[12]	RRID: BDSC_68830
<i>D. melanogaster</i> : Tm3-DBD: w ¹¹¹⁸ ; +; R59C10-DBD	[12]	RRID: BDSC_69153
<i>D. melanogaster</i> : Mi4-AD: w ¹¹¹⁸ ; R48A07-AD; +	[12]	RRID: BDSC_71070
<i>D. melanogaster</i> : Mi4-DBD: w ¹¹¹⁸ ; +; R13F11-DBD	[12]	RRID: BDSC_69722
<i>D. melanogaster</i> : Mi9-AD: w ¹¹¹⁸ ; R48A07-AD; +	[12]	RRID: BDSC_71070
<i>D. melanogaster</i> : Mi9-DBD: w ¹¹¹⁸ ; +; VT046779-DBD	[12]	RRID: BDSC_74714
<i>D. melanogaster</i> : Tm1-AD: w ¹¹¹⁸ ; R41G07-AD; +	[68]	RRID: BDSC_71049
<i>D. melanogaster</i> : Tm1-DBD: w ¹¹¹⁸ ; +; R74G01-DBD	[68]	RRID: BDSC_69767
<i>D. melanogaster</i> : Tm2: w ¹¹¹⁸ ; +; VT012282	[11]	N/A
<i>D. melanogaster</i> : Tm2split-AD: w ¹¹¹⁸ ; R28D05-AD; +	[68]	RRID: BDSC_68974
<i>D. melanogaster</i> : Tm2split-DBD: w ¹¹¹⁸ ; +; R82F12-DBD	[68]	RRID: BDSC_69250
<i>D. melanogaster</i> : Tm4: w ¹¹¹⁸ ; +; R35H01	[11]	RRID: BDSC_49922
<i>D. melanogaster</i> : Tm9: w ¹¹¹⁸ ; +; VT065303	[11]	N/A
<i>D. melanogaster</i> : T4-AD: w ¹¹¹⁸ ; VT016255-AD; +	Vienna Drosophila Resource Center	N/A
<i>D. melanogaster</i> : T4-DBD: w ¹¹¹⁸ ; +; VT012314-DBD	Vienna Drosophila Resource Center	N/A
<i>D. melanogaster</i> : T5-AD: w ¹¹¹⁸ ; VT013975-AD; +	Vienna Drosophila Resource Center	N/A
<i>D. melanogaster</i> : T5-DBD: w ¹¹¹⁸ ; +; R42H07-DBD	Bloomington Drosophila Stock Center	RRID: BDSC_69609
<i>D. melanogaster</i> : T4/T5-AD: w ¹¹¹⁸ ; R59E08-AD; +	[44]	RRID: BDSC_71101
<i>D. melanogaster</i> : T4/T5-DBD: w ¹¹¹⁸ ; +; R42F06-DBD	[44]	RRID: BDSC_69285
<i>D. melanogaster</i> : w+; P{20XUAS-IVS-GCaMP6f}attP40; +	Bloomington Drosophila Stock Center	RRID: BDSC_42747
<i>D. melanogaster</i> : w+; +; PBac{20XUAS-IVS-GCaMP6f}VK00005	Bloomington Drosophila Stock Center	RRID: BDSC_52869
<i>D. melanogaster</i> : UAS-TNT; +; UAS-TNT; +	[52]	N/A
<i>D. melanogaster</i> : UAS-TNTin; +; UAS-IMPTNT-Q; +	[52]	N/A

(Continued on next page)

Continued		
REAGENT or RESOURCE	SOURCE	IDENTIFIER
Software and Algorithms		
Custom-written software in Python	This study	https://github.com/borstlab/normalization_paper
ScanImage 3.8	[88]	http://scanimage.vidriotechnologies.com/display/SH/ScanImage+Home
Other		
Natural images for experiments and modeling	[43]	N/A
Natural images for modeling	[89]	https://doi.org/10.4119/unibi/2689637

LEAD CONTACT AND MATERIALS AVAILABILITY

Further information and requests for resources and reagents should be directed to and will be fulfilled by the Lead Contact, Aljoscha Leonhardt (leonhardt@neuro.mpg.de). This study did not generate new unique reagents.

EXPERIMENTAL MODEL AND SUBJECT DETAILS

Drosophila melanogaster were kept on a 12 h light/12 h dark cycle at 25°C and 60% humidity on standard cornmeal-agar medium. Genetic expression of effectors was targeted through the Gal4-UAS system [90]. Resulting genotypes and their abbreviations are listed in Table S2.

Unless stated otherwise, locomotion and tangential cell responses were recorded in wild-type Canton S flies 1 to 5 days after eclosion (Figures 1 and 2). We used the genetically encoded calcium indicator GCaMP6f [45] to determine the functional properties of individual cell types (Figures 3, 4, and 5). Throughout silencing experiments (Figure 5; Figure S2), we expressed tetanus toxin light chain (TNT) or an inactive version (TNTin) in the cell type of interest [52]. For calcium imaging experiments involving silencing (Figure 5), one day old flies were collected and put on 29°C for 3 days to boost expression of TNT or TNTin.

METHOD DETAILS

Natural image sets

For electrophysiology, behavioral, and modeling experiments, we used images from a published set of 20 natural panoramic scenes [43] termed dataset A. All images were independently processed as follows: We averaged across color channels and downsampled the scene to a resolution of 1,600 × 320 pixels (covering 360° sampled at 0.225 pixels per degree along the azimuth) using linear interpolation. To be able to render 12 bit images on conventional screens with 8 bits of dynamic range, we first performed standard gamma correction by raising raw pixel values to a power of 0.45 and then clipped the top percent of pixel intensities. The resulting image was scaled to fill the range between 0 and 255.

For optomotor experiments (Figure 1), we selected a subset of 8 images that covered different types of terrain. From this set, we again selected a subset of 6 images to determine tangential cell responses. We used all 20 images to build the convolutional network (Figure 6), randomly assigning 15 scenes to the training and 5 to the test set. Finally, we validated the trained convolutional model with images from an independent panoramic scene collection [89] consisting of 421 images (Figure S6G). These scenes were kept at their native resolution of 927 × 251 pixels (corresponding to an azimuthal sampling rate of 0.39 pixels per degree) and processed as above, yielding dataset B. We then generated two test sets: One had gamma correction applied to limit the images' bit depth ("low dynamic range" or LDR) and the other one was left at 12 bit depth to produce a dataset with high dynamic range (HDR).

Behavioral experiments

Experiments on the treadmill setup were conducted as described before [20, 31, 44]. Briefly, we tethered flies to a thin metal rod and placed them on air-cushioned polyurethane balls whose movement was tracked at 4 kHz, allowing for direct readout of rotational motion along all three axes. Temperature within the vicinity of the fly was 25°C at the start of each experiment. Using a closed-loop thermoregulation system, we linearly increased it to 34°C within 15 min to encourage locomotion.

For visual stimulation, we used three identically calibrated computer screens that were placed in a rectangle surrounding the fly. To simulate a cylindrical display, all stimuli were rendered onto a virtual cylinder and distorted accordingly before projection onto screens. Our setup covered approximately 270° in azimuth and 120° in elevation of the visual field. All stimuli were displayed at 144 Hz and at a spatial resolution greatly exceeding that of the fly eye. Screens had a maximum luminance of approximately 100 cd m⁻² and a luminance depth of 8 bit; for all descriptions below, we assume pixel brightness to range from 0 to a maximum of 1. Patterns were generated in real-time and programmed in Python 2.7 using the game engine Panda3D.

We measured velocity tuning curves (Figure 1) for 8 distinct natural images at 6 logarithmically spaced velocities ranging from 5 to $1,280\text{ s}^{-1}$. Initial image phase was randomized on each trial. Scenes were displayed at their native gamma-corrected mean luminance and contrast (see above). On each trial, images stood still for 1.5 s, then were rotated at the chosen velocity for 0.5 s, and remained fixed for another 1.5 s.

The optomotor contrast stimulus separated the visual field into two areas (see Figure 2A; Figure S2). For the so-called background, we tiled the visual field with pixels of size $5^\circ \times 5^\circ$. At each pixel location we drew a temporal frequency f from a normal distribution ($\mu = 0\text{ Hz}$, $\sigma = 1\text{ Hz}$) and a starting phase λ from a uniform distribution covering 0 to 360° . Instantaneous luminance of each pixel i was then determined by a random sinusoid of the form

$$I_i(t) = 0.5 + 0.5 c_{bg} g(\sin(2\pi f_i t + \lambda_i))$$

where the experimental parameter c_{bg} runs from 0 to 100% and controls the effective contrast of the background. To increase average contrast in the visual field, we applied the compressive transform

$$g(x) = x \sqrt{\frac{1 + \alpha^2}{1 + \alpha^2 x^2}}$$

where $\alpha = 5$ determined the degree of curve flattening. Using this method, we generated stochastic and dynamic visual input at a controllable contrast level without introducing coherent motion (see Figure 2B).

The so-called foreground delivered a coherent motion stimulus driving the optomotor response. It consisted of two vertical stripes that were placed at plus and minus 90° from the frontal axis of the fly, each spanning 20° in azimuth and the full screen elevation. We again tiled each stripe with pixels covering an area of approximately $5^\circ \times 5^\circ$. For each pixel i , luminance was fixed over time and determined by

$$I_i(t) = 0.5 + 0.5 c_{fg} g(\sin(\lambda_i))$$

where the experimental parameter c_{fg} controls the effective motion contrast and λ was independently drawn from a uniform distribution covering 0 to 360° . The pixelated noise pattern smoothly wrapped around the azimuthal borders when moving. Note that for all instantiations of the stimulus, mean luminance across the visual field was 0.5. We verified that at typical scales of visual processing in *Drosophila* (approximated as a Gaussian filter with FWHM = 25° that covers a majority of the receptive fields of visual neurons; see [9]), variation in average luminance around this mean was small (Figure S2L).

For the basic contrast tuning experiment (Figures 2A–2E; see Video S1), we exhaustively measured combinations of logarithmically spaced values for c_{fg} (1.6, 3.1, 6.3, 12.5, 25, 50, and 100%) and c_{bg} (0, 25, 50, and 100%). At the beginning of each trial we simultaneously presented the dynamic background and the static foreground pattern. Between 1.5 and 2.0 s following stimulus onset, the foreground pattern moved at a fixed velocity of 50° s^{-1} . For oscillation experiments (Figures 2F–2J), the motion period was extended to 6 s. While the foreground pattern was moving, we sinusoidally modulated the contrast of either fore- or background between 0 and 100% around a mean value of 50% and at the specified temporal frequency (see Figure 2F; Figures S2A, S2C, and S2E; Video S2). When mapping the spatial extent of the contrast-induced modulation, we set the modulation frequency to 1 Hz and restricted the background pattern to two stripes of 10° width flanking each foreground pattern (see Figure S2A). The distance parameter (15, 17.5, 20, 22.5, 25, 27.5, 30, 35, or 40°) determined the separation between centers of foreground and background. In this experiment, we additionally measured a zero-contrast background condition to obtain an appropriate modulation baseline. Here, the motion stimulus had a contrast of 25% and luminance in the rest of the field was set to a uniform 0.5. Example traces in Figure 2G are taken from this spatial experiment (for distance 15° or no background). For the temporal experiments, we measured oscillation frequencies of 0.5, 0.75, 1, 1.5, 2, 3, 4, 6, 8, and 10 Hz (Figure 2J). Background contrast was zero when measuring foreground tuning; for background tuning, foreground contrast was set to 25%.

All stimulus patterns were displayed twice throughout optomotor experiments, once in clockwise and once in counterclockwise direction of motion. We recorded multiple trials to obtain robust turning responses for each fly (15 trials for natural image stimuli, 20 for contrast tuning, 25 for oscillation stimuli). Presentation order was shuffled across conditions within any trial to mitigate adaptation effects. Individual experiments lasted between 60 and 120 min.

Electrophysiology

Our patch-clamp recordings from tangential cells followed established protocols [11]. Cell bodies of horizontal system (HS) units were targeted visually through a microscope. We confirmed their preferred direction by stimulation with oriented moving sine wave gratings before each experiment.

Visual stimulation was delivered using a cylindrical projector-based arena as previously described [9]. Briefly, the screen of the arena covered a viewing angle of the fly of 180° in azimuth and 105° in elevation. Stimuli were generated at a framerate of 180 Hz using green light spanning approximately 500 nm to 600 nm in wavelength. The maximum luminance this arena achieved was $276 \pm 48\text{ cd m}^{-2}$ (mean \pm SD across devices). All visual stimuli were rendered using custom software written in Python 2.7 and the Panda3D framework. Membrane potential was recorded using custom software written in MATLAB (MathWorks, MA).

We measured tuning curves for 6 distinct natural image panoramas at 9 logarithmically spaced velocities ranging from 2.5 to 640 s^{-1} (Figure 1). On each presentation, the scene was displayed at a fixed phase, stayed still for 1 s, and then rotated horizontally for 3 s at the chosen constant velocity. Image movement was always in the preferred direction of the HS unit. We showed images at

their native gamma-corrected mean luminance and contrast (see above). Each condition was repeated 5 times. Conditions and trials were randomly interleaved to exclude adaptation effects along any stimulus dimension.

Calcium imaging

Calcium imaging experiments were performed using custom-built two-photon microscopes as described before [9]. The imaging acquisition rate was 11.8 Hz for all experiments, or 23.7 Hz for the experiment in Figure 4D, with imaging resolutions ranging from 32×32 to 64×128 pixels. Image acquisition was controlled using the ScanImage software (version 3.8) [88]. We prepared flies as previously described [9, 14]. Briefly, *Drosophila* were anesthetized on ice and glued onto an acrylic glass holder with the back of their head exposed to a perfusion chamber filled with Ringer's solution. Then the cuticula was surgically opened to allow optical access.

Stimuli were presented using the same projector system as in electrophysiological experiments, with additional long-pass filters (cut-off wavelength of 550 nm) in front of the projectors to spectrally separate visual stimulation from GCaMP fluorescence signals.

To identify receptive field (RF) positions of individual neurons, white noise stimuli of 3 min length were used (except for T4 and T5 cells, see below). The stimuli were pre-rendered at 60 Hz and generated as previously described [9]. Briefly, the spatial resolution of all white noise stimuli was 2.8° of visual angle corresponding to 64 pixels across the 180° screen. For all lamina cells, the same stimulus was used in order to provide a systematic description of their spatiotemporal filtering properties (Figure S3). This stimulus had a Gaussian autocorrelation with a standard deviation of approximately 45 ms in time and a contrast of 25% around a mean intensity value of 50 on an 8 bit grayscale. For some medulla cell types, variants of this stimulus with higher contrast or longer time constants were used if necessary to reliably locate their RFs on the arena. Specifically, we mapped RFs for Tm4, Mi4, Mi9 and Tm9 with a binary stimulus at 100% contrast and a temporal cut-off frequency of 1 Hz. For Mi9, we chose a 1D version of this stimulus, consisting of horizontal (1.5 min) and vertical bars (1.5 min) instead of pixels.

For T4 and T5, we relied on a novel stochastic motion noise stimulus to determine RF coordinates. First, we determined the preferred direction of an ROI using drifting gratings. Then we displayed a stimulus consisting of 20 randomly distributed 15° wide circular windows. Inside of each window, a 30° wavelength sine grating drifted at 30°s^{-1} in the preferred direction (Figure S3X). The positions of these 20 windows were changed and randomly chosen every second over 4 min. Reverse correlation of T4 and T5 responses with the area covered by those windows at a given time point yielded motion-sensitive RFs which were fit with a Gaussian to determine center coordinates (Figure S3Y). These were verified by presenting 25° windows containing full contrast drifting gratings at the estimated RF center and 6 hexagonally distributed positions around the center. Cells responded only to the grating in the RF center (Figure S3Z).

For the experiments shown in Figure 3, a 25° circular window around the RF center of a cell defined the foreground whereas the rest of the screen was defined as background. Before stimulus presentation, we verified that RF centers were sufficiently distant from the border of the screen to allow full display of the foreground. A drifting sine grating with 30° wavelength and a velocity of 30°s^{-1} was shown, starting with medium gray at the center of the RF and moving for 4 s after stimulus onset (see Video S3). The contrast of the grating was varied independently between background and foreground. A stimulus matrix of 7 foreground contrasts (1, 6, 4, 8, 16, 32, 64 and 100%) and 6 background contrasts (0, 8, 16, 32, 64 and 100%) at a constant mean luminance of 0.5 was presented.

For the experiments shown in Figures 4A–4C, the foreground contrast was chosen depending on the cell type as the point where the suppression elicited by 100% background contrast (as measured in Figure 3) would be greatest. This was 16% for Mi1, 32% for Tm1, 100% for Tm2 and 64% for Tm3. The background had 100% contrast and 30° wavelength. We varied either its direction, its velocity (0, 0.25, 0.5, 1, 2, 4, 8, 16, 32 or 64°s^{-1}), or restricted its presentation to an annulus with changing outer diameter. A reference condition with 0% background contrast was added to the stimulus protocol.

For the contrast-step stimulus experiments shown in Figure 4D (see Video S4), the background grating had 30° spatial wavelength, drifted with 90°s^{-1} after motion onset and its initial phase was randomized. For Tm2 it had full contrast, for Tm3 44% contrast. The 25° foreground window was 50% gray and we placed a 5° wide dot in the center. For Tm3, the dot was initially black and set to white for a duration of 50 ms at a given time interval after motion onset of the background grating. For Tm2, the dot was initially white and then set to black. The time interval was varied in steps of 50 ms from -250 ms to 500 ms and then in steps of 100 ms. Negative values indicate that the surround grating started to move after the dot changed its intensity. Additional time intervals were -500 ms and -1 s. The block experiments in Figure 5 were performed with the same frequency tuning stimuli as before (Figure 4B). For the contrast tunings, the same stimuli as in Figure 3 were used but with background contrast of either 0 or 100% only.

All stimuli were repeated three times in randomized condition order to prevent adaptation to any stimulus features.

Modeling

Natural motion stimuli

To evaluate the performance of our models under naturalistic conditions, we generated a synthetic set of motion sequences that closely mimicked the experimental stimuli described above. For each sequence we translated 360° images at a fixed horizontal velocity through a virtual window spanning 100° in azimuth. Given their panoramic nature, scenes wrapped around seamlessly at each border. Movies were generated at a time resolution of 100 Hz. To reduce jitter for small velocities, we linearly interpolated non-integer pixel shifts. Fly eye optics were simulated ahead of time. We blurred each frame with a Gaussian filter (full width at half-maximum of 4°) to approximate the acceptance angle of each photoreceptor [26] and then sampled individual signals from a rectangular grid with isotropic spacing of 4° (yielding 23×17 receptor signals per frame for dataset A and 23×23 for dataset B, as described above).

For the comparison in [Figure 1](#), we modeled the exact stimulus parameters of the electrophysiological experiment including an approximation of the image's starting phase on the arena. We generated sequences for our convolutional detector models ([Figure 6](#)) as follows: The set of 20 panoramic images was randomly split into a training group consisting of 15 scenes and a test group consisting of 5 scenes. For each sequence, a random image was drawn from the appropriate set. The stimulus lasted 5 s. Between 1 and 4 s, scene velocity stepped from zero to a fixed value drawn from a Gaussian distribution with $SD = 100^\circ s^{-1}$. The initial window phase followed a uniform distribution spanning 360° . To further augment the dataset, we flipped the underlying image along the horizontal and vertical axes with a probability of 50%. We generated 8,192 such sequences for the training set and 512 for the test set.

Experimental stimuli

For all modeling experiments in [Figure S5](#), we replicated the experimental protocols described above as precisely as feasible. All stimuli were projected onto a field of view that spanned 120° in azimuth and 90° in elevation at a spatial resolution of 1° for calcium imaging experiments and 0.5° for behavioral experiments. Frames were then blurred and sampled as described for natural image stimuli. Brightness values for all stimuli ran from 0 to 1 and we fixed the mean level for contrast stimuli at 0.5. For calcium imaging stimuli, we always placed the foreground disk at the center of the field of view. Patterns were rendered and processed at 100 Hz.

Tuning curves for the basic contrast experiment ([Figures S5B–S5D](#)), the frequency experiment ([Figure S5F](#)), and the background diameter experiment ([Figure S5G](#)) were estimated from a single trial per parameter setting. For the background orientation experiment ([Figure S5E](#)) and the step interval experiment ([Figure S5H](#)) we averaged 100 trials with randomized background pattern phases to approximate the experimental phase stochasticity that results from individual cell receptive fields being located in different parts of the visual field. We averaged 200 trials for the behavioral stimuli ([Figure S5K](#)) to account for the intrinsic stochasticity of the stimulus and to generate reliable model responses. Throughout [Figure S5](#), we calculated point estimates for all tuning curves exactly as described for the behavioral and calcium data.

Tuning curve normalization model

The analytical model for divisive normalization ([Figures 3V–3X](#)) resembles previous formulations in the literature [[48](#), [50](#), [86](#)]. The steady-state response R of a neuron is given by

$$R(c_{fg}, c_{bg}) = \frac{L_{fg}c_{fg}^p + L_{bg}c_{bg}^p}{c_{50}^p + c_{fg}^p + S^p}$$

where c_{fg} and c_{bg} are foreground and background contrast and L_{fg} and L_{bg} are weight factors defining the respective amount of linear contribution of foreground and background to the response. The semi-saturation constant c_{50} determines the contrast at which the cell responds with 50% strength and the parameter p defines the steepness of the saturation curve.

The normalization term

$$S = w_{pool} \cdot c_{bg}^q$$

gives the amount of divisive surround suppression which is proportional to background contrast to a power of q , which accounts for possible non-linear scaling behavior, with a proportionality weight constant w_{pool} . In this model, the normalization index w_{pool}/c_{50} quantifies how much the sigmoidal tuning curve shifts to the right when c_{bg} is increased from 0 to 1 (full contrast), in relation to the semi-saturation constant. It thus describes the fold decrease in contrast sensitivity between no background contrast and full background contrast.

For evaluation of the normalization index ([Figure 3X](#)), this model was fit individually for each cell. Parameter fits to the average tuning curve per cell type are listed in [Table S1](#). Since tuning curves from individual cells are subject to measuring inaccuracies, we cross-validated fit quality. We optimized model parameters for the average tuning curve of 50% of all measured cells per type and evaluated variance explained for the other 50%. This was repeated 100 times with shuffled training and validation sets. For all cell types, cross-validated variance explained was more than 90% (see $R^2_{\text{DivisiveNorm}}$ in [Table S1](#)). When we repeated this procedure with a fully linear model

$$R(c_{fg}, c_{bg}) = L_{fg}c_{fg} + L_{bg}c_{bg}$$

variance explained dropped substantially for all units except L3 (see R^2_{linear} in [Table S1](#)).

This analysis was implemented using Python 2.7 and NumPy 1.11.3. Optimization of model parameters was performed using the L-BFGS-B algorithm in SciPy 0.19.0.

Data-driven detector model

The reference model in [Figure 1](#) was based on a standard implementation of the Reichardt-type correlational motion detector [[26](#)]. Briefly, all receptor signals of the two-dimensional input grid (see above) were filtered with a first-order high-pass ($\tau = 150$ ms). We then multiplied each local signal with the delayed horizontal neighbor (first-order low-pass, $\tau = 50$ ms). This was done twice in a mirror-symmetrical fashion and resulting output was subtracted. Finally, we summed across all local detectors to derive a model of tangential cell output. For the illustration in [Figure S1C](#), we simulated the receptor array at the full image resolution without blurring. These models were implemented in Python 3.6 using PyTorch 0.4.1.

We simulated time-resolved cell models for three basic response types: a purely linear low-pass unit (modeled after L3; [Figure S5B](#)), a strongly normalized band-pass unit (modeled after Mi1; [Figure S5C](#)), and a weakly normalized low-pass unit (modeled after Mi9; [Figure S5D](#)). We hand-tuned parameters based on our and previous work [[9](#)] to qualitatively match response properties

of the corresponding cell. Models were implemented as signal processing cascades (see Figure S5A). First, signals at each location in the field of view were filtered with a spatial difference of Gaussians kernel that had a central full-width at half-maximum (FWHM) of 6° and a FWHM of 20° in the surround. In accordance with results from receptive field mapping (Figure S3), the weight ratio between surround and center was 100% for low-pass units and 50% for the band-pass model. Full-field flashes would thus produce no activation in low-pass units. This was followed by first-order temporal filters: a single low-pass filter for low-pass units ($\tau = 80$ ms) or serial low- ($\tau = 50$ ms) and high-pass filters ($\tau = 150$ ms) for band-pass units. We then left the signal as is for ON cells or sign-inverted it for OFF cells and half-wave rectified the output by setting all negative values to zero.

For normalized cell models, we calculated local input P_i from the normalization field by pooling across rectified signals x_i with a Gaussian kernel (FWHM = 30°). Final output was then calculated using the divisive normalization equation

$$f(x_i) = \frac{x_i^p}{c_{50}^p + x_i^p + (w_{pool}P_i)^p}$$

where i indexes across points in space and time, c_{50} determines baseline sensitivity, exponent p regulates the static response non-linearity, and w_{pool} adjusts sensitivity to the normalization field signal. We manually tuned normalization parameters for the band-pass ($c_{50} = 0.012$, $p = 1.3$, $w_{pool} = 1.5$) and the low-pass cell ($c_{50} = 0.12$, $p = 1.1$, $w_{pool} = 3.0$) to match critical features of the empirical contrast tuning curves (Figures S5C and S5D).

To generate simulated T4 responses (Figures S5I and S5J), we multiplied the output of spatially adjacent low- and band-pass units. For the linear reference model we bypassed the final normalization step in both arms of the detector. We built the LPTC model (Figure S5K) as a spatial array of T4 and T5 cells covering the full field of view, analogously to the previously described two-quadrant detector [28]. For the T5 model, we used two OFF-sensitive input units with identical parameters as for ON cells. Output from syndirectionally tuned T4 and T5 motion detectors was summed and subtracted from a mirror-symmetric, oppositely tuned array to produce LPTC model output. The same model was used to simulate natural scene responses (Figures S5L–S5N). All models in Figure S5 were implemented using Python 3.6 and NumPy 1.15.

To quantify the robustness of velocity tuning for models and LPTCs (Figure S5N), we calculated per-velocity coefficients of variation as the ratio between response standard deviation across images and response mean across images. For neural data, we used cell-averaged mean potential to estimate these parameters.

Task-driven detector model

We implemented the trained detector model as a four-layer convolutional neural network consisting of linear input filters, a normalization stage, local multiplication, and linear spatial summation. In contrast to typical deep architectures used for object recognition, this network processed three-dimensional inputs spanning two dimensions of space as well as time.

First, receptor signals of shape $23 \times 17 \times 500$ or $23 \times 23 \times 500$ (azimuth, elevation, time), depending on the dataset, were processed in two independent convolutional channels. The convolutions were temporally causal and spatiotemporally separable. Each of the channels was composed of a $3 \times 3 \times 1$ spatial filter (covering 3 simulated receptors in azimuth and elevation) followed by a temporal filter of shape $1 \times 1 \times 30$ (corresponding to 300 ms at the chosen time resolution of 100 Hz). Convolutions had no bias parameter. In contrast to standard Reichardt detectors, each filter weight was allowed to vary freely during optimization.

Second, we passed local output signals x_i (where i indexes points in space and time) through one of three types of local normalization: a simple pass-through (termed “linear”)

$$f(x_i) = x_i$$

a static and contrast-independent compression stage (termed “static”)

$$f(x_i) = \tanh\left(\frac{x_i}{c}\right)$$

where the trained parameter c determines the sensitivity of the saturating function, or an adaptive saturation stage (termed “dynamic”)

$$f(x_i) = \tanh\left(\frac{x_i}{c + P_i}\right)$$

where c again determines the baseline sensitivity and P_i is the instantaneous output of a $11 \times 11 \times 1$ spatial filter (centered on the location of x_i and operating on full-wave rectified output signals $|x_i|$; see Figure 6A). This models the fast and spatially distributed normalization we observed during experiments. We chose the hyperbolic tangent because it generalizes to positive and negative input values, the transformation closely resembles the normalization model described above, and it is more commonly used in the field of deep learning. Spatiotemporal filters were optimized independently for each of the two channels while the sensitivity parameter c was shared.

Third, we then combined signals from both channels in a EMD-type scheme where adjacent signals were multiplied and output from two mirror-symmetric pairs was subtracted. This stage was parameter-free. Finally, resulting signals were summed across space and multiplied by a trained scalar amplification factor to generate the final time-resolved output of the model. The base model without normalization had 79 trainable parameters; static normalization added one parameter and dynamic normalization another 242.

We trained each model architecture to estimate the true velocity of translation stimuli using automatic differentiation, backpropagation, and stochastic gradient descent. The loss function we applied was the mean squared error (MSE) between model output and current velocity of the scene. Weights were updated using the Adam optimizer [91], with parameters set to standard values ($\beta_1 = 0.9$, $\beta_2 = 0.999$, $\epsilon = 10^{-8}$). Models were trained over 800 epochs with a batch size of 128; no early stopping was used. We set the initial learning rate to 0.025 and divided it by a factor of 4 after 400, 500, and 600 steps. Input convolutional layers were initialized to random values drawn from a uniform distribution. For the pooling receptive field, we initialized each weight with 0.0001 and the sensitivity factor c with 1.0. Static sensitivity as well as pooling weights were constrained to be positive. In the dynamic normalization model, we applied a L_2 penalty of 400.0 to the spatial weights of the pooling stage. Hyperparameters were determined in preliminary experiments with an independent image set. We optimized each architecture 16 to 23 times with different random number generator seeds to assess reliability and did not select models post hoc.

We implemented all architectures in Python 3.6 using PyTorch 0.4.1 for automatic differentiation. Depending on model type, a single optimization run took between 6 and 14 hs on an NVIDIA Titan Xp GPU.

QUANTIFICATION AND STATISTICAL ANALYSIS

Data evaluation for behavioral experiments

To ensure data quality, we excluded all flies whose average forward velocity during the experiment was below 0.25 cm s^{-1} and whose average turning tendency was either slowly drifting or far from 0° s^{-1} . Fewer than 20% of all experiments failed these criteria. Measurements of ball movement were downsampled via linear interpolation for further processing (to 50 Hz for natural image stimuli, Figure 1; 20 Hz for contrast tuning, Figure 2; 100 Hz for oscillation stimuli, Figure 2). Trials were averaged.

Responses for clockwise and counterclockwise motion were subtracted and divided by two to minimize residual deviations from straight forward walking. Traces for natural image and contrast tuning stimuli were filtered using a first-order low-pass with a time constant of 100 ms. For the contrast oscillation experiments, we evaluated modulation at the relevant carrier frequency by calculating the zero-padded Fourier Transform of the turning trace and averaging the amplitude spectrum in a window of width 0.2 Hz centered on the target frequency. These values were normalized per experiment such that the modulation peak after averaging was 100%. We applied a Savitzky-Golay filter (window length 11 samples, 5th order polynomial) before plotting traces from oscillation experiments; this did not affect the analysis.

All analysis for behavioral experiments was performed in custom-written software using Python 3.6, NumPy 1.15, and SciPy 1.1.

Data evaluation for electrophysiological experiments

Voltage data were digitized at 1,000 Hz. To account for slow drift in potential, we subtracted the average voltage in a 1 s window before stimulus onset from each trace per stimulus condition and trial. Signals were then low-pass filtered (8th order Chebyshev Type 1) and resampled at 100 Hz. Finally, we averaged cell responses across trials. Cells whose mean depolarization during full-contrast sine grating presentation in preferred direction remained below 5 mV were discarded before further analysis. All analysis for electrophysiological experiments was performed in custom-written software using Python 3.6, NumPy 1.15, and SciPy 1.1.

Data evaluation for calcium imaging experiments

Calcium imaging stacks were registered in order to correct for translational movement artifacts of brain tissue using custom-written software. Responses of individual neurons were extracted by manually selecting small regions of interest (ROI) encompassing individual anatomical structures. For T4 and T5 these corresponded to single or few axon terminals; for Mi and Tm cells, individual axon terminals could be identified clearly through visual inspection. For ON pathway medulla cells, signals were measured in layer 10 of the medulla, for OFF pathway medulla cells in layer 1 of the lobula. For lamina cells L1–5, signals were measured at axon terminals in corresponding layers 1–5 in the medulla. For T4 and T5, signals were recorded in the lobula plate.

To reconstruct RFs, calcium signals were mean subtracted and reverse-correlated with the stimulus as previously described [9]. 1D Gaussians were fit to horizontal and vertical cross-sections of spatial receptive fields to obtain precise RF coordinates. For lamina cells (Figure S3), all reconstructed RFs were peak-aligned and analyzed as previously [9]. For 1D projections of spatial RFs (Figures S3F–S3J), an average of 1D projections of 2D RFs along 3600 evenly distributed projection angles between 0° and 360° was calculated. This enhanced the visibility of the center-surround structure but neglected possible anisotropies in the spatial structure of RFs [49]. For impulse responses (Figures S3K–S3O) the temporal receptive field of the 9 center pixels was averaged; frequency responses (Figures S3P–S3T) are the Fourier-transformed impulse responses. Deconvolution (Figures S3U and S3V) was performed by dividing the frequency spectra with the frequency response of a 1st order low-pass filter with time-constant 350 ms as a proxy for calcium indicator dynamics [9, 92].

Relative fluorescence changes ($\Delta F/F$) from raw calcium traces were obtained by adapting an automatic baseline detection algorithm [93]. Briefly, raw data were first smoothed with a Gaussian window (full-width at half maximum, FWHM = 1 s). Then, minima within a 90 s long sliding window were extracted and the resulting trace smoothed with a Gaussian window (FWHM = 4 min). The result was used as a dynamic baseline F_0 and $\Delta F/F$ values were computed as $\Delta F/F = (F - F_0)/F_0$.

For further evaluation, only recordings with good signal-to-noise ratio (SNR) were taken. The criterion was that the standard deviation of the mean signal averaged over trials had to be at least 120% of the mean standard deviation over trials. This criterion filtered out cells with an inter-trial variance larger than the typical cell response (caused by movement artifacts or photobleaching).

In addition, the standard deviation of the mean signal had to be larger than 25% $\Delta F/F$. On average, 90% of all cells measured passed these criteria with slight variations due to different levels of GCaMP expression depending on the genotype.

For experiments with drifting gratings, the driving foreground contrast frequency was 1 Hz. For these experiments, we evaluated the amplitude of the 1 Hz component of the signal. This was achieved by computing the Fourier coefficient at that frequency, using the equation

$$F = \left| \frac{1}{T} \int_0^T dt s(t) e^{-2\pi i \cdot 1\text{Hz} \cdot t} \right|$$

where $s(t)$ denotes the signal and T the stimulation time. For experiments in Figure 4D, we evaluated the peak response of the calcium signal. For Figure S4, we additionally evaluated the average calcium signal (F_0) during stimulus presentation and normalized it to the maximum amplitude of the 1 Hz component (F_1).

Amplitudes were averaged over trials and normalized to the maximum, then averaged over cells and normalized to the maximum. For Figures 4 and 5, amplitudes were normalized to the response amplitude for the reference stimulus.

Statistical tests

Unless indicated otherwise, error bars show bootstrapped 68% confidence intervals around the mean (estimated as corresponding distribution percentiles after resampling the data 1,000 times). All statistical tests were two-tailed and performed at a 5% significance level. Normality of data distributions was assessed visually but not tested formally. Sample sizes are given in each figure legend and were not based on power analysis but predetermined in line with standards in the field. We did not blind experimenters to genotypes or conditions during data gathering and analysis.

DATA AND CODE AVAILABILITY

Code and experimental data are available on GitHub (https://github.com/borstlab/normalization_paper).

Current Biology, Volume 30

Supplemental Information

**Dynamic Signal Compression
for Robust Motion Vision in Flies**

Michael S. Drews, Aljoscha Leonhardt, Nadezhda Pirogova, Florian G. Richter, Anna Schuetzenberger, Lukas Braun, Etienne Serbe, and Alexander Borst

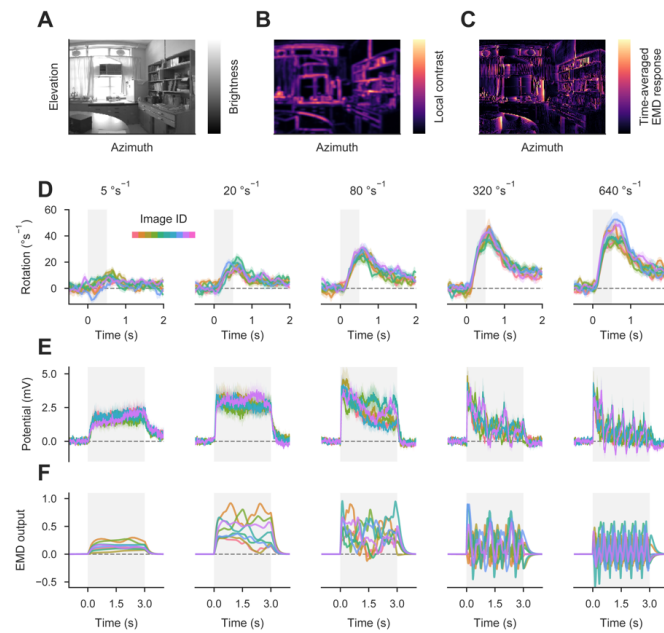


Figure S1 | Behavioral, neural, and model responses to natural scenes. Related to Figure 1.

(A) Natural image patch as seen through the field of view of model LPTC. (B) Estimate of local contrast in natural image patch. RMS contrast was estimated by filtering the image with a Gaussian ($\sigma = 0.5^\circ$), subtracting the filtered image from the original, squaring the mean-subtracted image, filtering it with a Gaussian ($\sigma = 0.5^\circ$), and taking the square root. (C) Spatially reconstructed output of simulated LPTC for same image patch as before, plotted as the square root of the time-averaged response. A horizontally motion-sensitive LPTC was constructed using the same parameters as in Figure 1F (STAR Methods) with the exception of more fine-grained sampling at exactly the image resolution. The depicted panorama was moved for 16 s at a velocity of 22.5°s^{-1} , resulting in a single complete rotation. Responses at each pixel location were then averaged across the full stimulus period. This demonstrates that the response of the EMD array depends strongly on squared local image contrast. (D) Turning responses for 8 images (indicated by trace color) and 5 velocities (indicated by panel title; $N=16$ wild-type flies; data as in Figure 1B). Gray shaded area indicates duration of motion stimulus. (E) Membrane potential for 6 images and 5 velocities ($N=11$ HS cells from 9 flies; data as in Figure 1D). (F) Output of model LPTC for same images and velocities as E (data as in Figure 1F). See Table S2.

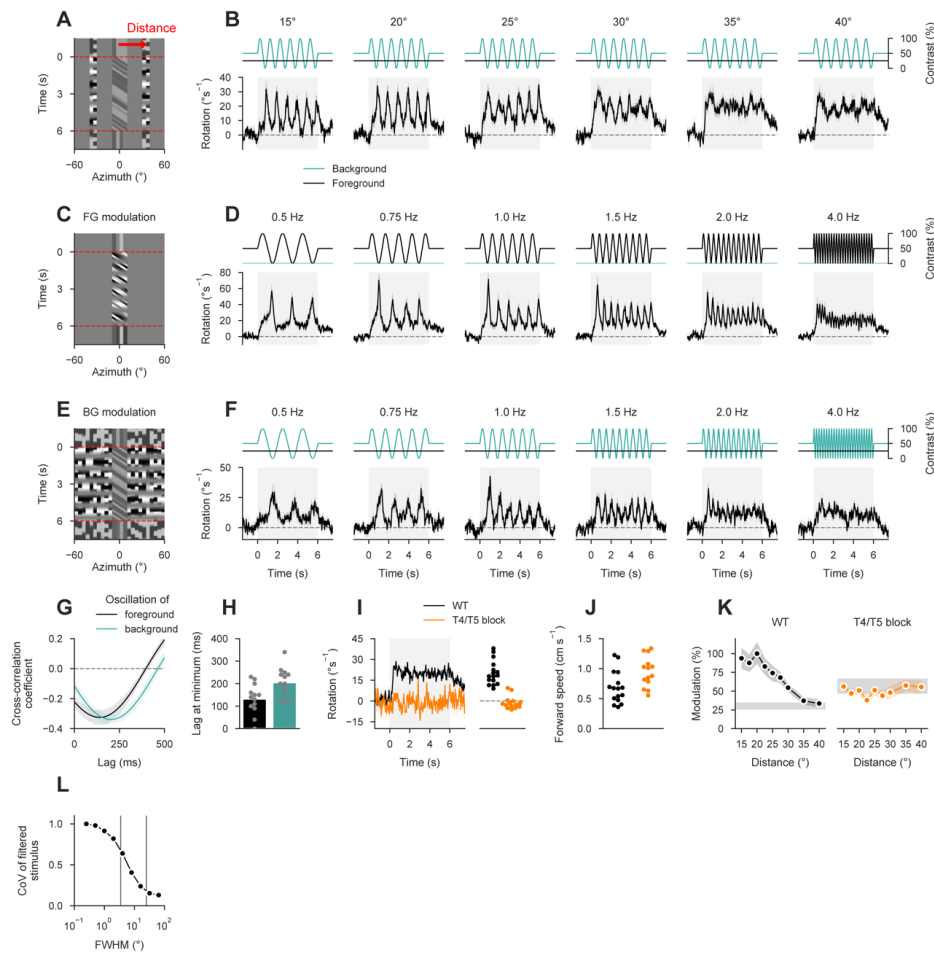


Figure S2 | Detailed behavioral responses to contrast stimuli. Related to Figure 2.

(A) Illustration of spatial oscillation experiment. Background was restricted to 10 ° wide stripes flanking the foreground motion stimulus at the center distance indicated by the red arrow. Dashed lines indicate period during which foreground pattern moved at 50 °s⁻¹. This arrangement was repeated at plus and minus 90 ° from the frontal axis of the fly; 0 ° in this plot indicates the center of the foreground. (B) Contrast traces and turning responses for five distance conditions (indicated above each panel). Top, instantaneous contrast (25 % in foreground, oscillating at 1 Hz in background). Bottom, turning response of the fly (N=16 wild-type flies). Modulation was reduced as spacing between foreground and background increased. (C) Illustration of temporal foreground modulation stimulus at 1 Hz frequency. (D) Contrast traces and turning responses for five foreground oscillation frequencies (N=13; background contrast was 0 %). Modulation decreased as frequency increased. (E) Illustration of temporal background modulation stimulus at 1 Hz frequency. (F) Contrast traces and turning responses for five background oscillation frequencies (N=13; foreground contrast was 25 %). Modulation again decreased with frequency. (G) Normalized cross-correlation between contrast oscillation and turning behavior for 1 Hz data from D and F. (H) Lag between stimulus oscillation and turning, evaluated as per-fly lag at first minimum within 500 ms for cross-correlations from G. (I) Left, comparison of turning responses between wild-type flies and flies in which T4/T5 cells were silenced using TNT (STAR Methods; N=16/14 for WT/block flies). Right, turning responses averaged between 0 and 6 s following motion onset. Syndirectional turning was abolished in T4/T5-silenced flies. (J) Average forward speed throughout full experiment. T4/T5 block flies did not exhibit

locomotion deficiencies. **(K)** Comparison of spatial oscillation tuning. T4/T5 block flies did not show modulation at the contrast oscillation frequency of 1 Hz and a generally increased level of baseline fluctuation. **(L)** Evaluation of luminance properties at different spatial scales for the behavioral stimulus. Normalized coefficient of variation across visual field was calculated after applying a Gaussian filter with different full-widths at half-maximum (FWHM). Gray lines indicate typical FWHM of ommatidium (left) and full receptive field of medulla cells (right). See Table S2.

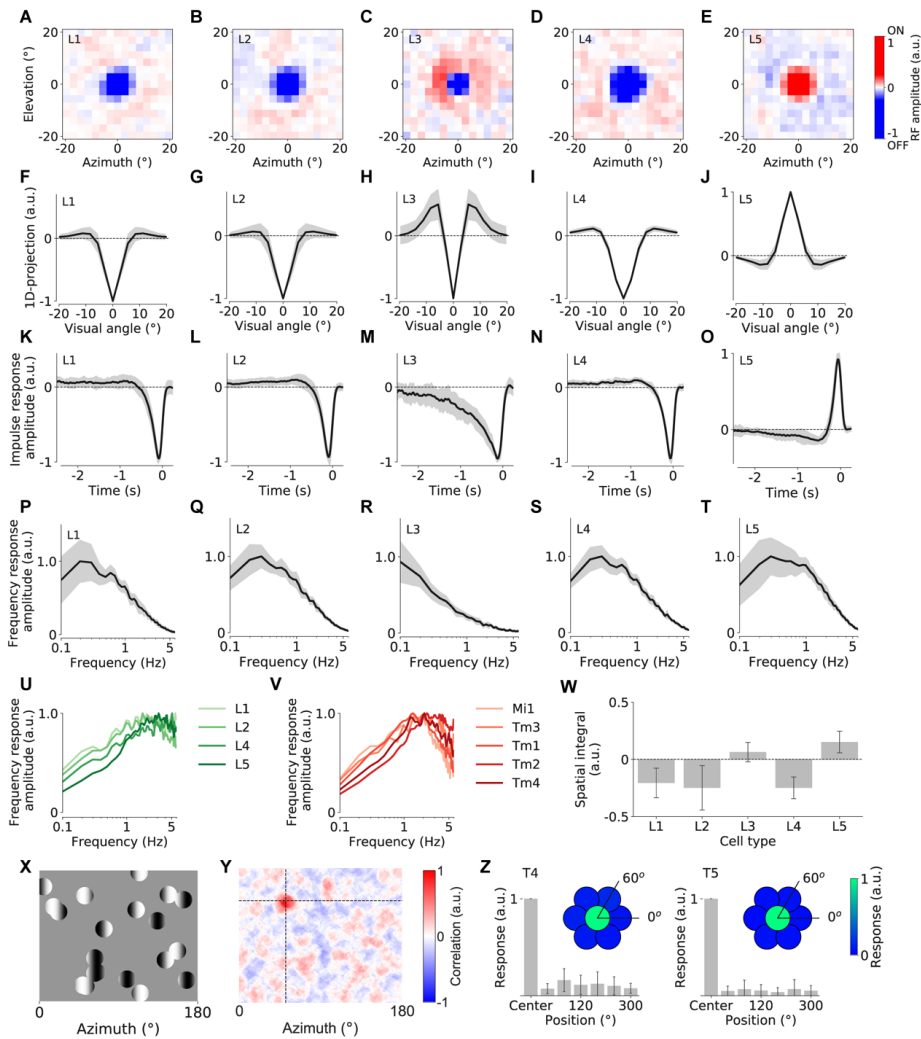


Figure S3 | Lamina and T4/T5 receptive field mapping. Related to Figure 3.

(A–E) Averaged 2D spatial receptive fields (RF) of L1–L5 from reverse correlation using white noise stimulation (L1: 21/7 cells/flies, L2: 34/5, L3: 34/5, L4: 17/6, L5: 18/9). (F–J) 1D projection (averaged over all orientations) of the RFs in A–E. All cell types possessed linear RFs with antagonistic center-surround structure. (K–O) Temporal RFs measured in the center of the spatial RFs. (P–T) Frequency-space representations of temporal RFs. (U) Frequency representations of lamina transient cells (all lamina cells except for L3) after deconvolution with a putative linear GCaMP6f low-pass filter with time constant 350 ms as performed previously [S1]. (V) Deconvolved frequency responses of medulla bandpass filter cells (replotted from previous work [S1]). (W) Spatial integral of the 2D RFs in A–E. For L3, the strong antagonistic ON surround exactly counterbalanced the OFF-center contribution. (X) x-y plot of the stochastic motion noise stimulus used for localizing T4/T5 RFs. (Y) Example RF of a T4 cell from reverse correlation with the motion noise stimulus. (Z) Average responses of T4/T5 to 25° windowed drifting gratings probing different positions around the estimated RF center. This validated the RF coordinates obtained from the stochastic motion noise stimulus. All data are shown as mean \pm s.d. See Table S2.

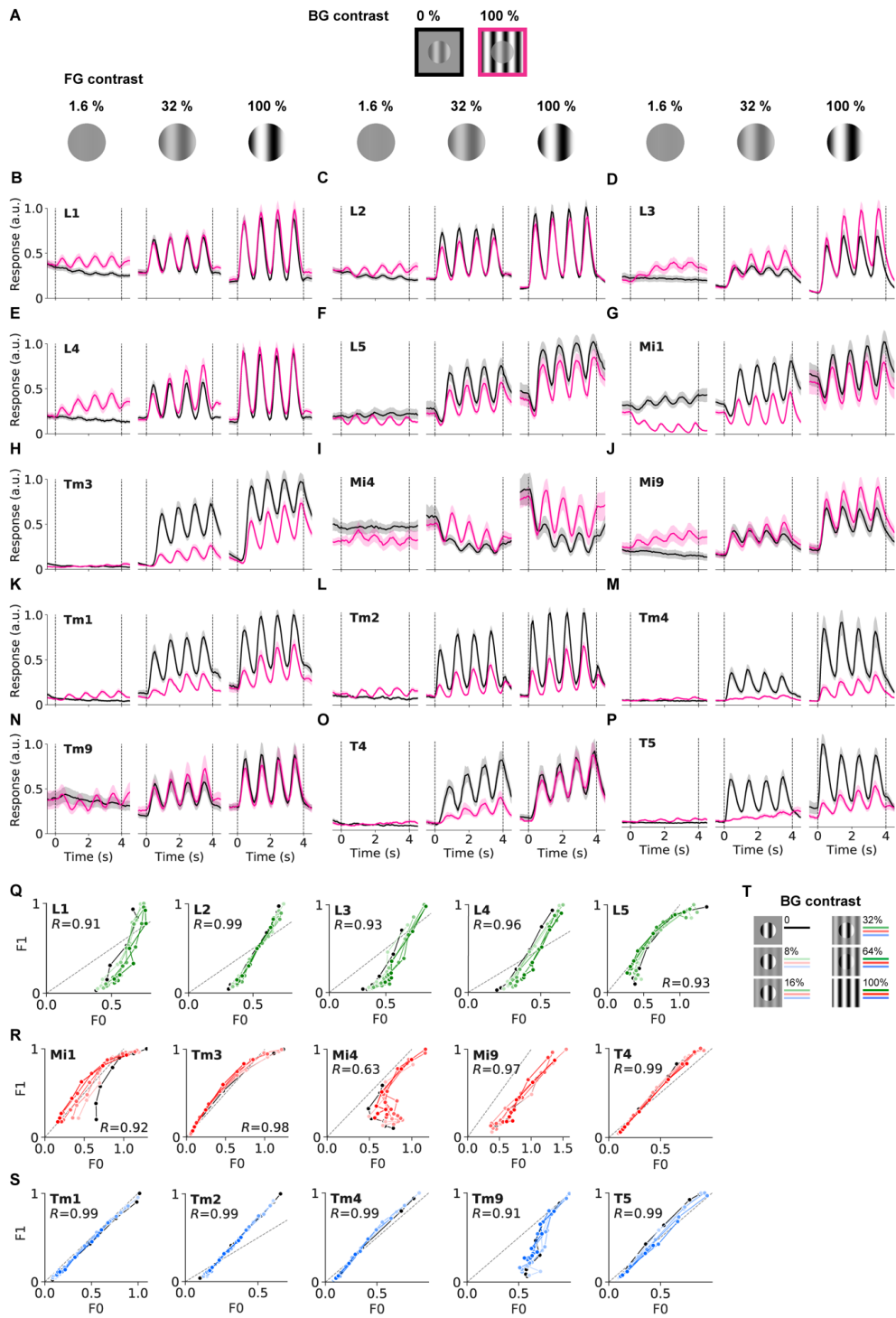


Figure S4 | Raw calcium responses for basic contrast stimuli. Related to Figure 3.

(A) Shown is only a subset of the data evaluated in Figure 3. Background contrast of 0 % is indicated by black lines, background contrast of 100 % is depicted in magenta. Responses are shown only for 3 out of 7 foreground contrasts. (B–P) Average calcium responses of all neurons to combinations of different foreground and background contrasts. (Q) Shown is a correlation analysis of the same dataset as in Figure 3 for the lamina cells L1–L5. On the y-axis is the F1-component of the calcium response (as evaluated in Figure 3) while the x-axis indicates the F0-component of the signal, i.e. the average calcium response during the stimulus. Data points corresponding to the same BG contrast are connected by lines and color-coded analogously to Figure 3. All data points are normalized to the maximum F1 response for each cell type. The gray dashed line marks the diagonal of the coordinate system. Correlation coefficient R is indicated in each panel. (R) Same as in Q but for ON-pathway medulla cells Mi1–Mi9 and for T4 cells. (S) Same as in Q but for OFF-pathway medulla cells Tm1–Tm9 and for T5 cells. (T) Color legend for panels Q–S. Darker color shade corresponds to higher background contrast, similarly to Figure 3. Zero background contrast condition is shown in black. See Table S2.

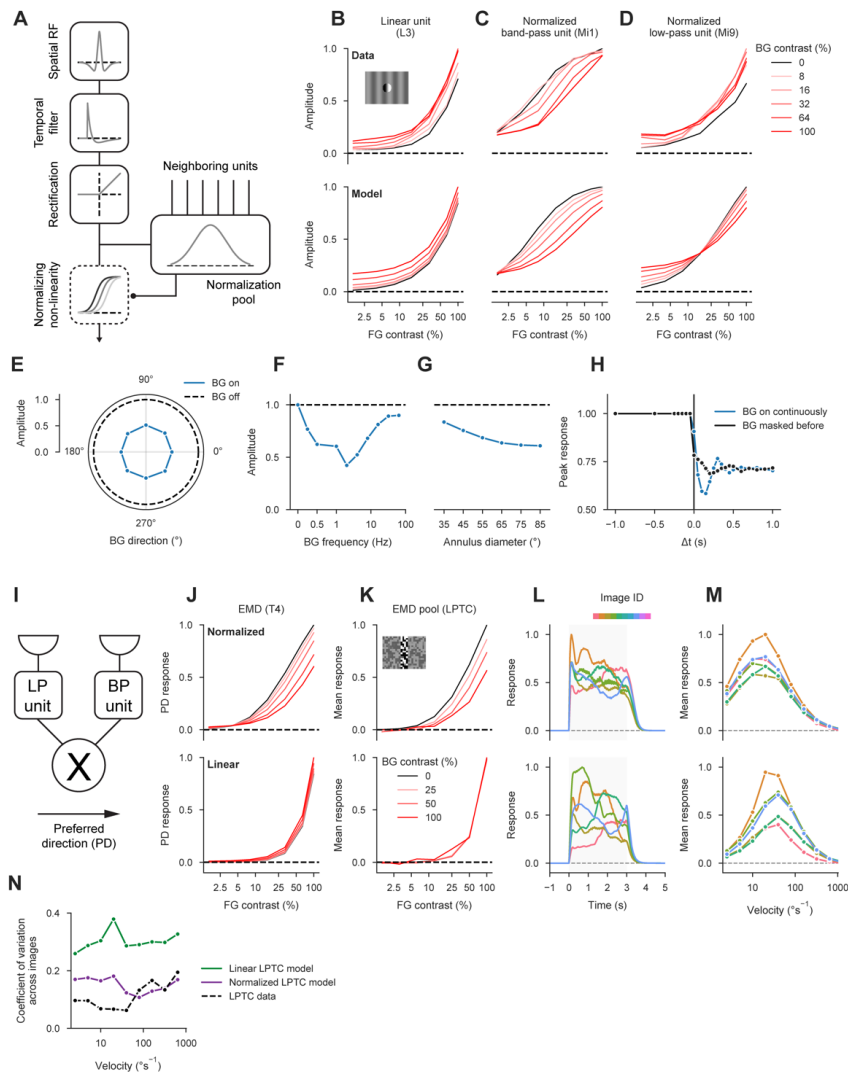


Figure S5 | Data-driven functional model of normalization circuit. Related to Figure 4.

(A) Illustration of signal cascade for data-driven cell model (STAR Methods). Filter elements are sketched for an ON band-pass cell with normalization. (B–D) Contrast tuning curves for three model cells, estimated using the same protocol as during calcium imaging (FG = foreground, BG = background). Top, empirical data for L3, Mi1, and Mi9 (see Figure 3). Inset depicts a single frame from stimulus centered on recorded cell with background contrast 25 % and foreground contrast 100 %. Bottom, tuning curves from models manually tuned to resemble their empirical counterparts (see STAR Methods for parameters). (E) Responses of normalized ON band-pass cell model to orientation tuning stimulus (see Figure 4A; dashed line marks reference stimulus without background). Stimuli and evaluation were exactly matched to the experiment. (F) Responses of the same model to background frequency tuning experiment (see Figure 4B; dashed line marks reference stimulus without background). (G) Responses of the same model to background size stimulus (see Figure 4C;

dashed line marks reference stimulus without background). **(H)** Responses of the same model to contrast-step protocol (see Figure 4D). **(I)** Illustration of T4 or T5 model. Signals from a strongly normalized band-pass and a weakly normalized low-pass unit covering adjacent areas of the visual field are multiplied, yielding a direction-selective signal. **(J–M)** Top, responses from motion detector models with normalization. Bottom, responses from motion detector models in which normalization was switched off for both input arms. **(J)** Foreground contrast tuning for simulated T4 cell (see Figure 3). **(K)** Responses to behavioral contrast stimulus for a LPTC model composed of T4 and T5 models (STAR Methods). **(L)** Responses to various natural scenes moving at 20°s^{-1} (modelled and evaluated as in Figure 1). **(M)** Velocity tuning curves for natural scenes (modelled and evaluated as in Figure 1). **(N)** Coefficient of variation across images for individual image velocities (derived from velocity tuning curves in M and Figure 1F; STAR Methods). A model including input normalization outperformed the linear model and approximated the variability of LPTC responses.

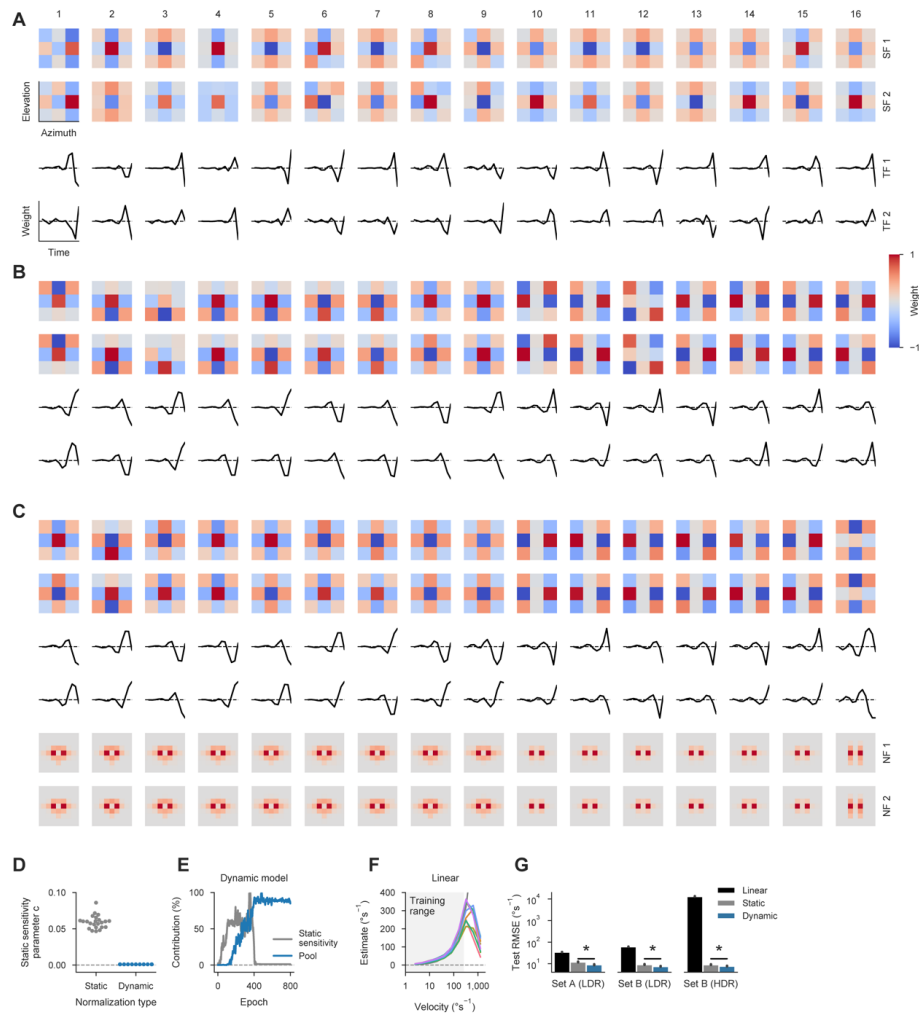


Figure S6 | Detailed receptive fields and performance data for task-driven model. Related to Figure 6.

(A–C) Receptive fields and temporal filters for 16 models of each non-linearity configuration (A, linear; B, static; C, dynamic). Models were sorted by test set error (increasing from left to right). Each pair of spatial and temporal filters was normalized to the maximum absolute weight across both channels (SF = spatial filter, TF = temporal filter, NF = normalization filter). Axis limits are the same as in Figure 6. (D) Values of sensitivity parameter c for all static (N=23) and dynamic (N=16) normalization models. (E) Evolution of weights for a single dynamic model. Both curves were independently normalized to their maximum across epochs. Pool contribution was quantified as the sum of weights across both $11 \times 11 \times 1$ normalization filters. (F) Velocity tuning curves of best-performing linear model for various images (analogously to Figure 6G). Gray curve indicates true scene velocity on logarithmic axis. (G) Quantification of average model performance for all tested data sets (analogously to Figure 6H; LDR = low dynamic range, HDR = high dynamic range). See STAR Methods for details on how data sets were generated. Note that performance is plotted on a logarithmic axis. N=22/23/16 for linear/static/dynamic; * $P < 0.001$; $t = 9.01/7.51/7.72$ for set A/set B (LDR)/set B (HDR); Student's t-test with assumed equal variance; only difference between static and dynamic was tested.

Cell type	L _{fg}	L _{bg}	p	c ₅₀	w _{pool}	q	Norm. index	R ² _{DivisiveNorm}	R ² _{linear}
L1	1.47	0.07	1.10	0.53	0.22	0.97	0.42	98.39 ± 0.10	92.55 ± 0.14
L2	1.10	0.05	1.37	0.23	0.36	0.77	1.58	99.29 ± 0.03	85.17 ± 0.13
L3	1.68	0.16	1.46	1.00	0.00	1.27	0.00	95.90 ± 0.08	97.17 ± 0.07
L4	1.41	0.12	1.23	0.53	0.32	1.09	0.61	98.94 ± 0.04	93.71 ± 0.07
L5	1.04	0.05	1.29	0.14	0.19	1.10	1.36	94.51 ± 0.23	69.34 ± 0.24
Mi1	1.03	0.03	1.21	0.06	0.25	1.05	4.33	97.37 ± 0.14	56.26 ± 0.41
Mi4	1.61	0.33	0.90	1.00	0.31	5.92	0.31	90.08 ± 0.26	87.50 ± 0.35
Mi9	1.69	0.23	0.99	1.00	0.40	2.87	0.40	92.40 ± 0.24	89.61 ± 0.32
T4	0.96	0.01	2.47	0.11	0.49	0.74	4.45	96.78 ± 0.15	74.17 ± 0.35
T5	1.08	0.07	1.97	0.26	1.17	0.92	4.55	97.02 ± 0.13	77.27 ± 0.27
Tm1	0.98	0.09	1.87	0.18	0.86	0.71	4.75	97.53 ± 0.11	78.67 ± 0.29
Tm2	1.08	0.17	1.36	0.20	1.14	0.91	5.76	97.58 ± 0.08	73.09 ± 0.32
Tm3	1.02	0.01	1.97	0.16	0.53	0.72	3.39	97.97 ± 0.12	82.33 ± 0.20
Tm4	1.06	0.11	2.33	0.40	1.44	0.81	3.61	96.77 ± 0.16	76.96 ± 0.37
Tm9	1.83	0.50	0.92	0.98	1.01	1.65	1.03	96.37 ± 0.14	87.42 ± 0.25

Table S1 | Fits for divisive normalization model. Related to Figure 3.

Short name	Full genotype	Used in
WT	w ⁺ /w ⁺ ; +/+; +/+	Figure 1, Figure 2
T4/T5 block	w ⁺ /w ⁺ ; R59E08-AD/UAS-TNT; R42F06-DBD/+	Figure S2
L1-GCaMP6f	w ⁺ /w ⁺ ; VT027316-AD/UAS-GCaMP6f; R40F12-DBD/UAS-GCaMP6f	Figure 3, Figure S3–S4
L2-GCaMP6f	w ⁺ /w ⁺ ; R53G02-AD/UAS-GCaMP6f; R29G11-DBD/UAS-GCaMP6f	Figure 3, Figure S3–S4
L3-GCaMP6f	w ⁺ /w ⁺ ; R59A05-AD/UAS-GCaMP6f; R75H07-DBD/UAS-GCaMP6f	Figure 3, Figure S3–S4
L4-GCaMP6f	w ⁺ /w ⁺ ; R20A03-AD/UAS-GCaMP6f; R31C06-DBD/UAS-GCaMP6f	Figure 3, Figure S3–S4
L5-GCaMP6f	w ⁺ /w ⁺ ; R21A05-AD/UAS-GCaMP6f; R31H09-DBD/UAS-GCaMP6f	Figure 3, Figure S3–S4
Mi1-GCaMP6f	w ⁺ /w ⁺ ; R19F01-AD/UAS-GCaMP6f; R71D01-DBD/UAS-GCaMP6f	Figure 3, Figure 4, Figure S4
Tm3-GCaMP6f	w ⁺ /w ⁺ ; R13E12-AD/UAS-GCaMP6f; R59C10-DBD/UAS-GCaMP6f	Figure 3, Figure 4, Figure S4
Mi4-GCaMP6f	w ⁺ /w ⁺ ; R48A07-AD/UAS-GCaMP6f; R13F11-DBD/UAS-GCaMP6f	Figure 3, Figure S4
Mi9-GCaMP6f	w ⁺ /w ⁺ ; R48A07-AD/UAS-GCaMP6f; VT046779-DBD/UAS-GCaMP6f	Figure 3, Figure S4
Tm1-GCaMP6f	w ⁺ /w ⁺ ; R41G07-AD/UAS-GCaMP6f; R74G01-DBD/UAS-GCaMP6f	Figure 3, Figure 4, Figure S4
Tm2-GCaMP6f	w ⁺ /w ⁺ ; +/UAS-GCaMP6f; VT012282/UAS-GCaMP6f	Figure 3, Figure 4a-c, Figure S4
Tm2split-GCaMP6f	w ⁺ /w ⁺ ; R28D05-AD/UAS-GCaMP6f; R82F12-DBD/UAS-GCaMP6f	Figure 4
Tm4-GCaMP6f	w ⁺ /w ⁺ ; +/UAS-GCaMP6f; R35H01/UAS-GCaMP6f	Figure 3, Figure S4
Tm9-GCaMP6f	w ⁺ /w ⁺ ; +/UAS-GCaMP6f; VT065303/UAS-GCaMP6f	Figure 3, Figure S4
T4-GCaMP6f	w ⁺ /w ⁺ ; VT016255-AD/UAS-GCaMP6f; VT012314-DBD/UAS-GCaMP6f	Figure 3, Figure S3, Figure S4
T5-GCaMP6f	w ⁺ /w ⁺ ; VT013975-AD/UAS-GCaMP6f; R42H07-DBD/UAS-GCaMP6f	Figure 3, Figure S3, Figure S4
Mi1-GCaMP6f, TNT-E	w ⁺ /w ⁺ ; R19F01-AD/UAS-TNT-E; R71D01-DBD/UAS-GCaMP6f	Figure 5
Mi1-GCaMP6f, TNTin	w ⁺ /w ⁺ ; R19F01-AD/UAS-TNTin; R71D01-DBD/UAS-GCaMP6f	Figure 5

Tm3-GCaMP6f, TNT-E	w ⁺ /w ⁻ ; R13E12-AD/UAS-TNT-E; R59C10- DBD/UAS-GCaMP6f	Figure 5
Tm3-GCaMP6f, TNTin	w ⁺ /w ⁻ ; R13E12-AD/UAS-TNTin; R59C10- DBD/UAS-GCaMP6f	Figure 5
Tm1-GCaMP6f, TNT-E	w ⁺ /w ⁻ ; R41G07-AD/UAS-TNT-E; R74G01- DBD/UAS-GCaMP6f	Figure 5
Tm1-GCaMP6f, TNTin	w ⁺ /w ⁻ ; R41G07-AD/UAS-TNTin; R74G01- DBD/UAS-GCaMP6f	Figure 5
Tm2split-GCaMP6f, TNT-E	w ⁺ /w ⁻ ; R28D05-AD/UAS-TNT-E; R82F12- DBD/UAS-GCaMP6f	Figure 5
Tm2split-GCaMP6f, TNTin	w ⁺ /w ⁻ ; R28D05-AD/UAS-TNTin; R82F12- DBD/UAS-GCaMP6f	Figure 5

Table S2 | Genotypes and abbreviations. Related to Figures 1–5.

Supplemental Reference

- S1. Arenz, A., Drews, M.S., Richter, F.G., Ammer, G., and Borst, A. (2017). The temporal tuning of the *Drosophila* motion detectors is determined by the dynamics of their input elements. *Curr. Biol.* 27, 929–944.

3

DISCUSSION

Studying the visual system of *Drosophila melanogaster* in general and the motion vision circuit in particular is an appealing topic. Arthropods are by far the largest and diverse group of animal species on this planet, which conquered almost every corner on land during their long path of evolution. The general building blocks of the visual system are conserved despite the enormous diversity (Strausfeld, 2012). Therefore understanding general circuit motifs and basic computations in flies may be generalizable and transferrable to other species. The fruit fly's neurogenetic toolbox, a connectome of the whole circuitry from photoreceptors to dendrites of the motion-sensitive T4 and T5 cells, and the much smaller number of neurons are critical advantages on the path towards a detailed understanding of elementary motion detection.

For decades researchers have derived hypotheses on how the direction of visual motion might be detected from computational models. Three essential criteria were formulated. First, inputs must be spatially separated. Second, inputs must be differentially filtered in time. Third, inputs signals must be non-linearly integrated.

In Manuscript 2.1 we systematically characterized the response properties of all putative input elements to T4 and T5 cells that were known at the time when I started my Ph.D. Two out of four neurons in the ON-pathway (Mi4 & Mi9) have previously not been characterized. For the other inputs, different studies had measured either the membrane potential or the calcium signal of these cells with stimuli varying from study to study. As we will see in the following discussion, using different stimuli, such as gratings, moving or extending bars, may yield different outcomes. Therefore we systematically characterized all input cells to T4 and T5 cells using a stochastic white-noise stimulus while simultaneously monitoring the calcium levels. This allowed a direct comparison of the dynamics and extent of the spatial receptive fields. Through the use of computer simulations we were able to show that by placing the slow low-pass neurons Mi4 and Mi9 at the outer sides of a three-arm hybrid detector, while the fast band-pass elements Mi1 or Tm3 reside in the center, the ON pathway model achieved peak direction selectivity and matched experimental results best.

In Manuscript 2.2 my colleagues and I confirmed the glutamatergic transmitter phenotype of Mi9. Using a newly developed glutamate sensor (iGluSnFR) we again measured the temporal properties of Mi9, but used transmitter release instead of calcium signals as a proxy for neural activity. Since iGluSnFR possesses significantly faster kinetics compared to the calcium sensor (GCaMP), the transmitter release could be defined with much greater precision. Convolution of the glutamatergic signal with the determined calcium kernel revealed a good match between the two data sets.

Lastly, in Manuscript 2.3 we were able to demonstrate that the responses of some of the neurons in the circuit are modulated by background contrast far outside the linear receptive field that we had determined in the previous manuscripts. Dynamically adapting to global contrast changes had previously been investigated in mammalian systems. We showed that models for the *Drosophila* motion vision circuit which implement such a divisive contrast normalization step are superior to ones without when confronted with naturalistic stimuli.

In the first part of this chapter, I will discuss anatomical and functional similarities between the visual system in mammals and flies. In a second part, I will further elaborate on how the field of *Drosophila* motion vision has progressed towards a biophysically plausible model of T4 cells.

3.1 THE VISUAL SYSTEM OF FLIES AND MAMMALS – COMMONALITIES AND DIFFERENCES

Despite the division of the two phyla over 600 million years ago (De Robertis and Sasai, 1996) and the fundamentally different outward appearances of the mammalian and the fly visual systems, convergent evolution brought forward striking parallels in terms of structure, development, and function (reviewed in Sanes and Zipursky (2010)). Conserved principles between species could hint at computational algorithms and strategies that are close to optimal in fulfilling the challenges faced by an animal using vision to behave in the physical world. Moreover, we can use our knowledge of the mammalian system to generate hypotheses wherever we have gaps in our understanding of the insect visual system. In the following section, I will therefore discuss similarities in anatomy and structure of the circuit as well as commonalities in the physiology.

3.1.1 Anatomy and functional structure

An anatomical resemblance was already pointed out by Ramón y Cajal and Sánchez (1915), as seen in Figure 11. One can easily appreciate some key aspects which are conserved between the two phyla. Cells are arranged in orderly layers. Instances of specific cell types are repeated in a regular tiling principle (Wässle and Riemann, 1978; Devries and Baylor, 1997; Rockhill et al., 2000). Finally, cell types run either perpendicularly or in parallel (e.g. horizontal cells in mammals, see Figure 13 a; amacrine cells like Lat in invertebrates, see Figure 3 b) to the aforementioned layers.

In Section 1.2 I laid out the basic anatomical structure of the fly optic lobe. The mammalian retina consists of five distinct layers: the outer and inner nuclear layer, which contain cell bodies but no synapses; the outer and inner plexiform layer, which contain synapses but no cell bodies; and lastly the ganglion cell layer. Six cell types dominate the mammalian retina: Photoreceptors, bipolar cells, horizontal cells, amacrine cells, retinal ganglion cells, and glial cells (Masland, 2001; Wässle, 2004). Based on anatomical and

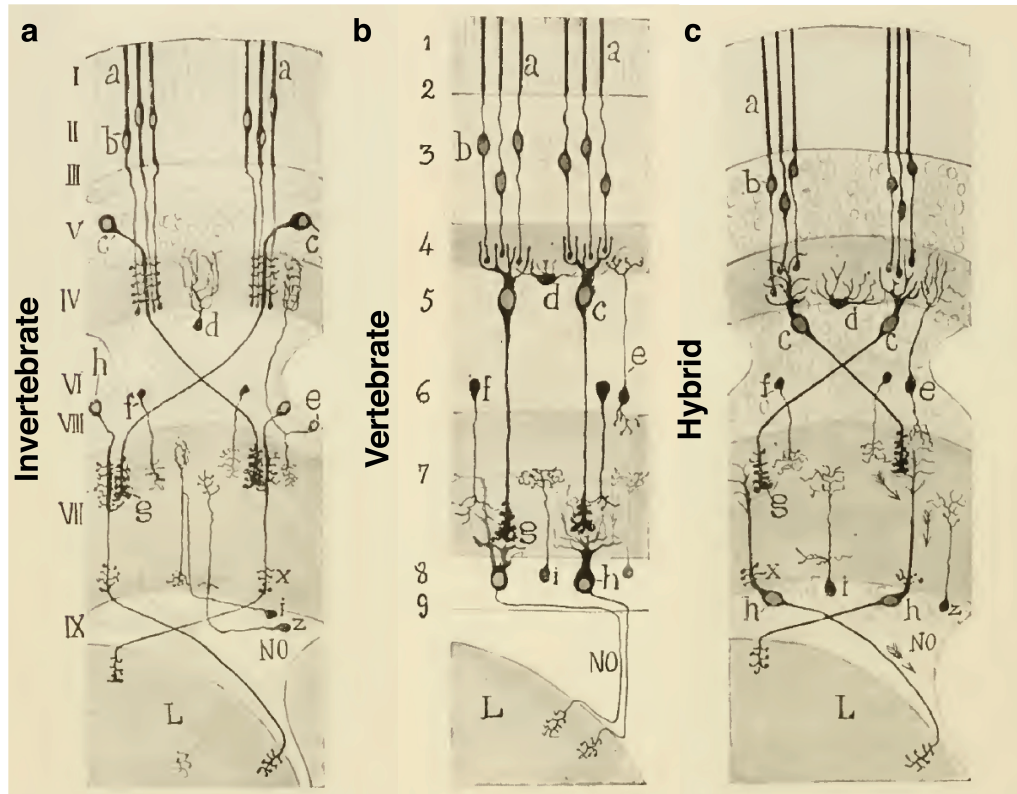


Figure 11: Comparison of vertebrate and invertebrate anatomy. **a** The insect retina (I - III), Lamina (IV + V), Medulla (V - VIII) and Lobula (L). **a** and **b** in the original drawings depict photoreceptors, **c** shows lamina monopolar cells and **h** denotes transmedullary neurons. **b** Schematic of major cell types in the vertebrate retina and their connections. Arabic numerals denote regions that correspond to the Roman numbers in (a) which [Ramón y Cajal and Sánchez \(1915\)](#) believed to be similar. **c** Ramon y Cajal drew a combination of the two retina organizations. For this, he displaced the cell bodies of the invertebrate retina such that the similarity to the vertebrate one would become more apparent. As a result lamina monopolar cells appear as bipolar cells (c) invertebrate amacrine cells resemble now horizontal cells (d) and transmedulla cells become more similar to vertebrate retinal ganglion cells (h). NO = *nervio optico*, optic nerve. Pictures were taken and modified from [Ramón y Cajal and Sánchez \(1915\)](#).

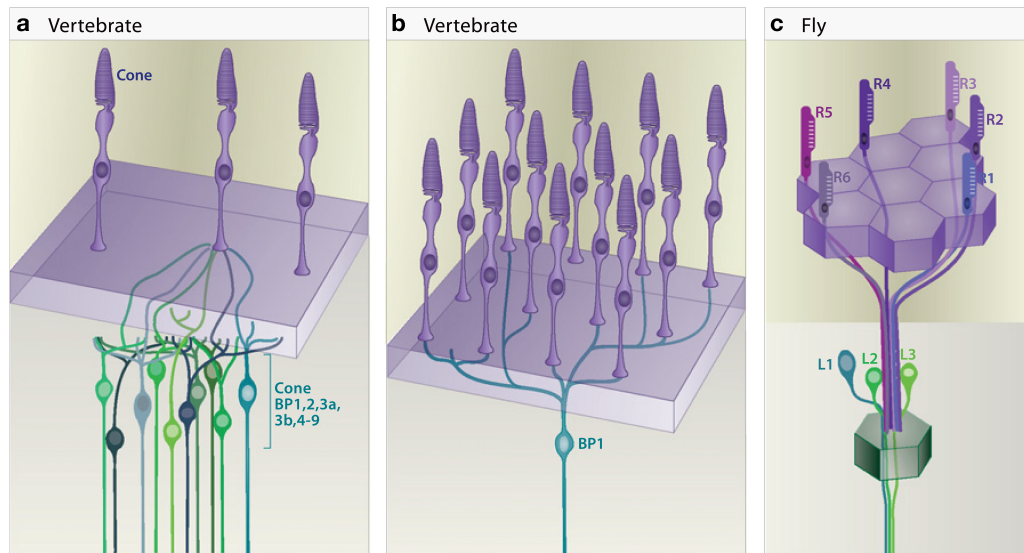


Figure 12: Convergence and divergence in the visual system. **a** An individual mouse cone photoreceptor synapses onto at least 10 different bipolar cell types. **b** A single mouse bipolar cell receives input from at least 10 cone photoreceptors. **c** Neurons in one lamina cartridge receive input from 6 different photoreceptor subtypes. Each subtype input comes from a different ommatidium. This concept is called neural superposition and serves to improve sensitivity while simultaneously preserving visual acuity. The figure is taken and modified with permission from (Sanes and Zipursky, 2010).

functional characteristics or based on molecular expression profiles each cell type can be split up into several sub-types.

OUTER RETINA Rods and cones are the two types of mammalian photoreceptors, with rods being 20-30 times more numerous depending on the species (Carter-Dawson and Lavail, 1979). There is only one type of rod but cones can be subdivided into separate classes based on the light-sensitive pigments (opsins) they express. Rods are highly sensitive and therefore mainly, but not exclusively, active during dim light conditions (Szikra et al., 2014). Cones are less sensitive and mainly active during bright daylight where they provide the animal with color vision (Dacey, 2000). In the inner plexiform layer photoreceptors are connected to 1-3 horizontal cell types and to at least 13 bipolar cell types via electrical and chemical synapses (Masland, 2012b; Connaughton, 2011). Bipolar cell types in the mouse retina can be grouped according to their molecular profiles, the polarity of changes in incoming light to which they respond preferentially (ON or OFF), whether they receive rod or cone photoreceptor input or both, from which sub-type of cone photoreceptor (medium wavelength sensitivity (M) or short-wavelength sensitivity (S)) they receive input, or according to their transiency and if they generate spikes (see Figure 13 b, (Behrens et al., 2016; Euler et al., 2014)).

INNER RETINA Despite enormous diversity and complexity, cells in the inner plexiform layer are arranged in a layer-specific manner (Sanes and Zipursky, 2010). Here, 13 bipolar cell types, at least 40 types of amacrine

cells, and a minimum of 20 types of RGCs form an intricate web of synaptic connections (Masland, 2012a; Euler et al., 2014; Völgyi et al., 2009; MacNeil et al., 1999). The axons of RGCs in turn collectively form the optic nerve and project to at least ten different brain areas (Van Essen et al., 1992).

On a structural basis, there are multiple similarities to the fly visual system that stand out. First, a small number of major neuronal classes defines the whole circuitry. Diversity is hence achieved by dividing neuronal classes into multiple sub-types. Second, the visual systems are arranged in a layered structure with repetitive units across the layer (e.g., columnar cells in the fly and bipolar cells in the mammalian retina). A third anatomical similarity concerns multi-contact synapses that are formed between the photoreceptors and their subsequent partners. Mammalian ON bipolar cells, for instance, intrude on the photoreceptor axon terminal, thereby getting closer to a specialized active zone of transmitter release called *ribbon*. Synapses to OFF bipolar cells in contrast are located further away from the active zone (DeVries et al., 2006; Haverkamp et al., 2000). The time until the transmitter released by the presynaptic photoreceptors diffuses towards the postsynaptic receptors in OFF bipolar cells is therefore thought to impose a delay on the signal (Haverkamp et al., 2001). Similar to the pedicle synapse in mammals, *Drosophila* photoreceptors form a multi-contact tetrad synapse with amacrine, L1, and L2 cells. As in mammalian photoreceptors, the ones in *Drosophila* contain an unusually large presynaptic specialization called *T-bar* (Sanes and Zipursky, 2010).

Taken together, despite having fundamentally different optical apparatuses in compound versus lens eyes, the general principles downstream of photoreceptors seem to be conserved across the two phyla. The similarities are so remarkable that they led Ramón y Cajal and Sánchez (1915) to form a hypothetical hybrid of the two systems as depicted in Figure 11 c.

3.1.2 Parallel pathways

The very first connection between photoreceptors and bipolar cells yields commonalities not only in anatomy but also in function. Multiplexing, for example, is a technique that is frequently used in signal processing and telecommunications (Schwartz and Batchelor, 2008). In resource-constrained systems, it is typically beneficial to transmit multiple logically distinct signals via shared pathways. Arthropods and mammals seem to make use of this concept in the early visual system, where different aspects of the incoming visual signal are processed in separate, parallel channels, fed forward, and integrated later on. I present three examples for such splits that are present in early visual circuits of mouse and fly:

1. **ON-OFF split:** During darkness mammalian photoreceptors are depolarized and release glutamate, creating a so-called *dark current*. Conversely, upon illumination photoreceptors hyperpolarize (in contrast to invertebrate photoreceptors which depolarize, see Chapter 1.2) and less glutamate is released, therefore producing an OFF signal. The photoreceptor signal is then split into two parallel processing channels. It is either conveyed without sign inversion via ionotropic glutamate

receptors to OFF bipolar cells (Euler et al., 2014) or via metabotropic glutamate receptors (mGluR6) onto ON bipolar cells (Masu et al., 1995; Slaughter and Miller, 1981), effectively hyperpolarizing the cell and therefore inverting the sign of the initial signal.

As introduced in chapter 1.2.1, in *Drosophila* achromatic visual information is split into two distinct channels at the synapse between the lamina monopolar cells L1 and L2 and the medulla cells (Joesch et al., 2010). In contrast to the mammalian visual system, where this split occurs right at the first synapse, in the fly visual system visual information is split one synapse further downstream. The lamina appears to be a neuropil that is additionally "inserted" with no obvious correspondence in the mammalian system (Borst and Helmstaedter, 2015). However, it is striking that L1 and L2 hyperpolarize upon illumination, similarly to mammalian photoreceptors. Positive change in luminance is therefore represented in the same way, namely by hyperpolarization. For cell types in the downstream layers, we observe a clear separation between ON and OFF cells just as with bipolar cells in the mammalian retina, with ON cells becoming more active whenever luminance increases (e.g., Mi1) and OFF cells becoming more active whenever luminance decreases (e.g., Tm2).

2. **Chromatic versus achromatic split:** Rods and cones in the mammalian retina provide specialized input to subsequent bipolar cells, thereby splitting color and non-color vision (so-called *scotopic* vision) into parallel pathways (Yoshimatsu et al., 2021). In the fly, color and non-color vision first arise at the level of photoreceptors, with R1-R6 processing achromatic and R7 and R8 providing color vision (Schnaitmann et al., 2018). Additionally, both streams are processed in parallel like in the mammalian retina.
3. **Spatial multiplexing:** A single cone photoreceptor in the mouse retina forms synapses with at least 10 different bipolar cell types (as seen in Figure 12 a). A single bipolar cell, in turn, samples signals from ≈ 10 cone photoreceptors (Wässle et al., 2009) (see Figure 12 b).

In the fly, the convergence of multiple photoreceptor signals onto one cell type downstream is called *neural superposition*. To increase sensitivity without losing visual acuity, evolution came up with an intricate wiring system depicted in Figure 12 c. Due to the circular arrangement within one facet, each of the photoreceptors R1-R6 collects light from a slightly offset point in space. The curvature of the fly's eye, however, means that photoreceptors from neighboring ommatidia have the same optical axes. The six receptor cells from six different ommatidia then converge in the same lamina cartridge (Vigier, 1909; Braitenberg, 1967; Kirschfeld, 1967; Trujillo-Cenóz, 1965). Therefore lamina cartridges are a good example for multiplexing in the visual system, since they converge signals from multiple photoreceptors and then diverge them onto subsequent medullary neurons (≈ 60 , see Section 1.2).

3.1.3 Motion vision circuitry

In the section above, I described the high-level layout of the mammalian retina and showed examples of multiplexing in the early visual system as a general circuit motif in two phyla. For my doctoral work, motion vision is of particular interest. Therefore, I will specifically describe the wiring of the mammalian motion vision circuit and how some functional aspects relate to the work included in this thesis.

First, photoreceptors relay signals onto bipolar cells. Here, the achromatic visual information is split into an ON and an OFF channel. In the inner plexiform layer (IPL) ON and OFF bipolar cells synapse onto the direction-selective cells SACs of the same polarity preference (ON-SAC, OFF-SAC) and direction-selective retinal ganglion cells (DSRGCs) [Vlasits and Baden \(2019\)](#); [Helmstaedter et al. \(2013\)](#); [Yonehara and Roska \(2013\)](#); [Euler et al. \(2002\)](#).

Classically, direction selectivity in the mammalian retina was studied in DSRGCs of rabbits and mice ([Vlasits and Baden, 2019](#); [Barlow and Levick, 1965](#)). Out of at least 20 different types of RGCs ([Völgyi et al., 2009](#)), only a subset exhibits direction-selective responses: OFF-JAM-B cells, which prefer upward motion ([Kim et al., 2008](#)); ON ganglion cells, with three subtypes and 120 degrees of separation in their preferred directions ([Oyster and Barlow, 1967](#); [Sun et al., 2006](#)); and ON-OFF ganglion cells, with one subtype for each of the four cardinal directions (front-to-back, back-to-front, upward and downward) ([Elstrott et al., 2008](#)).

Direction selectivity, however, first arises on the radially symmetric dendrites of SACs (see Figure 13 e). Each dendritic branch responds maximally (preferred direction response) when stimulated centrifugally (from the soma towards the distal tips, green arrow) and minimally (null direction response) when stimulated centripetally (from the distal tip inwards towards the soma, red arrow) ([Euler et al., 2002](#)). SAC dendrites and the dendrites of T₄ and T₅ cells are thus the primary direction-selective neurons in each circuit ([Maisak et al., 2013](#); [Euler et al., 2002](#)).

But how does direction-selectivity arise in the first place?

Having spatially offset inputs, with one delayed in time with respect to the other, represents two out of three essential criteria for the *Hassenstein-Reichardt correlator* and the *Barlow-Lewick correlator* as described in Section 1.3 ([Hassenstein and Reichardt, 1956](#); [Barlow et al., 1964](#)). Given the overwhelming success these models had in predicting biological responses and properties, it stands to reason that spatial and temporal asymmetries are indeed implemented at a cellular level. It is therefore critical for the understanding of motion vision to know how synapses on the dendrites of motion-sensitive neurons are spatially distributed and which temporal properties the presynaptic partners possess. I will discuss these offsets comparatively:

SPATIAL OFFSET When looking at the distribution of bipolar cell synaptic connections with their postsynaptic direction-selective SAC, it becomes apparent that at least two subgroups are wired differentially (see Figure 13 d). Whereas the slower CBC₂ (orange curve) mainly contacts the SAC dendrite close to the soma, the faster CBC₃ (blue curve) forms most synapses

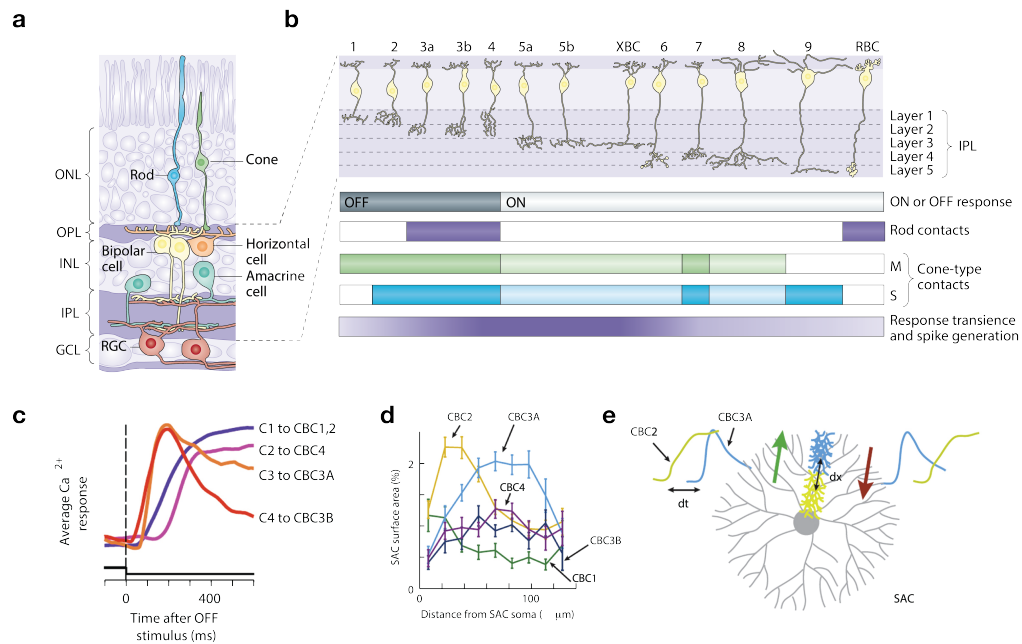


Figure 13: Space and time in retinal bipolar cells. **a** Schematic of the three nuclear and two plexiform layers and the main cell types in the mouse retina: light travels through the entire tissue where rod and cone photoreceptors transduce light into electrochemical signals. The signal is then shaped by horizontal cells and transferred onto at least 13 types of bipolar cells, which in turn synapse onto either starburst amacrine cells (SAC) or retinal ganglion cells (RGC). RGCs then collectively form the optic nerve and project to higher brain areas. **b** Morphology of 13 distinct types of bipolar cells (12 cone bipolar cells and one rod bipolar cell) in the mouse retina lined up according to the inner plexiform layer to which they project. Bipolar cells can be grouped according to their polarity preference (ON or OFF), whether they transmit signals from rods (second row in purple), whether they receive inputs from cones that process light of shorter (S, blue, fourth row) or medium (M, green, third row) wavelengths or how transiently they respond (purple gradient at the bottom). **c** Differential calcium response dynamics of four different OFF cone bipolar cell clusters. Functional clusters were determined based on the location of their projections. Clusters fall into slow sustained (violet and blue) and transient (orange and red) response. **d** Lines show contacts of bipolar cell subtypes to starburst amacrine cells (SAC) as a function of distance from the SAC soma. Data is based on electron microscopic data. Note that distribution is not homogeneous. **e** Spatial offset dx between two types of cone bipolar cell synapses onto the SAC dendrite (yellow for CBC2 and blue for CBC3A). Temporal offset dt between the two cone bipolar cell types is depicted for stimulation along the preferred (green arrow, upper left traces) and null direction (red arrow, upper right traces). Figure taken and modified with permission from (Euler et al., 2014) for panels a+b and (Borst and Helmstaedter, 2015) for panels c-e.

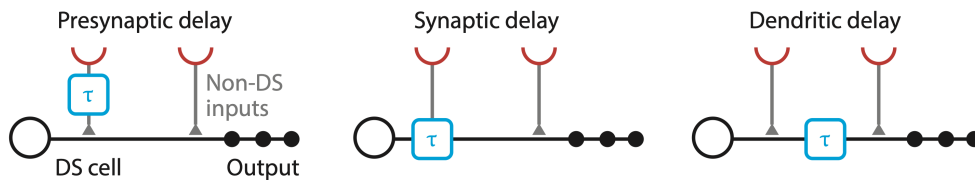


Figure 14: Temporal delay mechanisms. Two spatially offset inputs (red half circles) are delayed by different temporal dynamics in the presynaptic inputs (left), by synaptic delays on the postsynaptic membrane (middle), e.g. through receptors with different kinetics, or by intrinsic properties of the dendritic membrane of direction-selective cells (right). Figure taken with permission from (Vlasits and Baden, 2019).

further distally (Kim et al., 2014a; Ding et al., 2016). The arrangement of input synapses to T4 & T5 dendrites in flies is shown in Figure 15 c+d. The distribution of input synapses found in EM reconstructions (Takemura et al., 2017; Shinomiya et al., 2019) as well as the distribution of transmitter receptors (Fendl et al., 2020) follow a clear pattern. Faster cell types like Mi1 & Tm3 in the ON pathway and Tm1, Tm2 & Tm4 in the OFF pathway synapse onto the central part of the dendritic tree, whereas the slower Mi9, Mi4 (ON pathway), and Tm9 (OFF pathway) cells flank the central inputs distally or proximally. In both organisms, we therefore find that motion-sensitive neurons have laterally extended connection fields, with different input cell types making connections at different sites. Given the retinotopic spatial organisation of these input cell types, this pattern is ideally suited to receiving differently tuned inputs that are offset in visual space.

TEMPORAL OFFSET In principle, there are three mechanisms by which two spatially offset signals can be asymmetrically delayed: (1) The relative delay already exists in the membrane signals of the input cells; (2) the delay arises due to different kinetics of receptors on the postsynaptic membrane; or (3) intrinsic filtering of the dendritic membrane separates the inputs in time (see Figure 14 Vlasits and Baden (2019)). The three options are not mutually exclusive. There is some evidence for these mechanisms in the mammalian retina:

(1) Looking at OFF bipolar cell types, we find that they exhibit distinguishable temporal dynamics which fall into two distinct classes: slow, sustained, and low-pass filter-like (blue and violet curve, see Figure 13 c) on the one hand, and a fast transient band-pass filter (orange and red, see Figure 13 c) like responses on the other hand (Kim et al., 2014b; Greene et al., 2016; Baden et al., 2013; Borghuis et al., 2013). (2) The exact receptor types expressed and their distribution on SAC dendrites is currently unknown (Vlasits and Baden, 2019), so we can currently not draw firm conclusions on the role of receptor kinetics in generating such delays. (3) Another hypothesis, which is based on computer simulations, suggests an electrotonic delay in the dendritic membrane of SACs. The SAC presynaptic transmitter release sites are located at the distal part of the thin ($\approx 200\text{-}300\text{ nm}$) dendrite and are thought to represent a compartment with a high input resistance (≈ 1

$G\Omega$) (Vlasits et al., 2016; Hausselet et al., 2007). Sequentially stimulating the spatially offset excitatory inputs are therefore summed up optimally when stimulated centripedally compared to centrifugal stimulation.

In starburst amacrine cells, it is thus plausible that a combination of intrinsic dendritic filtering and different input dynamics together create the required offset for elementary motion detection. Conversely, in *Drosophila* we have made some progress toward understanding the mechanisms behind the required temporal delay:

(1) In Manuscript 2.1 we used white-noise stimuli and reverse correlation to identify the spatial and temporal characteristics of all putative input elements to the elementary motion detectors, T₄ for the ON pathway and T₅ for the OFF pathway respectively. In the temporal domain, we found that inputs generally fall into two classes: transient band-pass filters and slow sustained low-pass filters. In the ON pathway, Mi₉ & Mi₄ appear as pure low-pass filters, whereas Mi₁ & Tm₃ show band-pass filter characteristics. This bears a clear resemblance to the dynamics of the bipolar cell depicted in Figure 13 c. (2) In theory, a temporal delay can also be implemented through metabotropic receptors. Although the data set of Fendl et al. (2020) is not yet complete, the dendritic receptors labelled so far are all fast and ionotropic. (3) Because the dendrite of T₄ and T₅ cells are inaccessible to classical electrophysiology, only estimations about the electrotonic properties of the dendritic membrane are currently possible (Borst, 2018). Recently developed tools for labelling the endogenous receptor distribution (Fendl et al., 2020) will maybe inspire computational approaches in finding out if there is an additional delay in the dendritic membrane of T₄ and T₅ cells.

Taken together, it seems likely that the different dynamics in the presynaptic input elements are sufficient to create the necessary temporal delay in the fly elementary motion detector (Arenz et al., 2017).

3.1.4 Biophysical implementation of filtering

Investigating the dynamics of neurons in the fly medulla has been a major task of my thesis. We were able to show differential response kinetics of the neurons, how they are influenced by neuromodulators, and how the responses of some neurons are suppressed by background contrast. However, as the previous section has already shown, we still don't know how response kinetics are generated and modulated at the physiological and biophysical levels. In the following, I will compare our findings to mammalian bipolar cells and how the signals of both bipolar and medulla cells are shaped. Discussing the extensive body of literature from mammalian bipolar cells (Euler et al., 2014) might give answers to questions that are largely untouched in the fly: Due to which mechanisms do the dynamics of these cells arise? Which receptors are involved? How is contrast adaptation implemented at the biophysical level? I will follow the path of a signal passing through retina bipolar cells and highlight commonalities or differences along the way.

DENDRITIC MECHANISMS The bipolar cell's dendritic signal is initially determined by the composition of glutamatergic photoreceptor input (i.e. how

many connections and of which photoreceptor subtype) and GABAergic input from horizontal cells (see schematic in Figure 13 a). Horizontal cells provide the bipolar cells' spatial receptive field with an antagonistic surround that enhances contrast discrimination (Miller and Dacheux, 1983; Duebel et al., 2006; Thoreson and Mangel, 2012; Vardi et al., 2000).

Additionally to interactions at the cellular level, cell-intrinsic mechanisms shape the dendritic response properties. OFF bipolar cells for instance express different combinations of ionotropic glutamate receptors, such as AMPA or kainate or both, thereby creating unique kinetics (Regus-Leidig and Brandstätter, 2012; DeVries, 2000; Lindstrom et al., 2014). ON bipolar cells, however, all express the same metabotropic glutamate receptor (mGluR6) but still possess different dendritic kinetics (Masu et al., 1995; Ichinose et al., 2014). These different response kinetics are achieved by either different components in the second-messenger component of the receptor (Cao et al., 2012; Pearrin et al., 2011), differentially expressed voltage-gated calcium channels (De Sevilla Müller et al., 2013) or inward-rectifying potassium channels (Sulaiman et al., 2013).

In Manuscript 2.1, we used 2-photon calcium imaging in combination with white-noise stimuli and reverse correlation to identify the spatio-temporal receptive fields of all putative input elements to the elementary motion detectors. Except for Tm3, all spatial receptive fields show a center-surround structure. In the temporal domain, we found that inputs generally fall into two classes: transient band-pass filters and slow and sustained low-pass filters. In the ON pathway, Mi9 & Mi4 appear as pure low-pass filters, whereas Mi1 & Tm3 show band-pass filter characteristics.

Whereas bipolar cells receive direct photoreceptor input, medulla cells in the motion vision pathway receive their major dendritic input from the lamina. Hence medulla cells could inherit their spatial and temporal receptive field structures to large extent from lamina neurons. Mi9, for instance, receives the majority of its synapses from the lamina monopolar cell L3 (Takemura et al., 2017). L3 shares major features with Mi9 such as extent, polarity, and center-surround structure of the spatial receptive as well as slow-sustained filter characteristics in the temporal domain (Silies et al., 2013; Fisher et al., 2015a) (see also manuscript 2.3). This however pushes the initial question just one synapse further upstream. Mi4 receives transient band-pass-like input from L5. Therefore it can't simply inherit its dynamics from upstream lamina neurons. Two options seem plausible: Mi4 receives its low-pass filter characteristics from another synaptic partner or the signal it receives from the lamina is filtered intrinsically. Mi4 and Mi9 are reciprocally connected (Takemura et al., 2017). It seems therefore also feasible that Mi9 is the dominant input to Mi4 that defines its response characteristics.

The faster cells Mi1 & Tm3 receive their major input from L1 (Takemura et al., 2017). L1 already possesses faster band-pass-like characteristics (Clark et al., 2011; Reiff et al., 2010; Drews et al., 2020). Therefore, key features of the filter could already be implemented one synapse further upstream in the lamina. While for *Drosophila* L1 there is no evidence of how they achieve their temporal high-pass component, recent studies argued that L2 acquires transiency by the expression of the rapidly inactivating potassium channels called *Shaker* and *Shal* (Gür et al., 2019). Since L1 and L2 responses

are indistinguishable, the results from L2 might be transferrable to L1. This however awaits further investigations.

With large high-resolution transcriptomes (Davis et al., 2020) and connectomes (Rivera-Alba et al., 2011; Takemura et al., 2013; Meinertzhagen and O'Neil, 1991) of lamina and medulla circuits, future experimental data should be able decipher the responsible components that contribute to the broadly different filter time constants in lamina and medulla cells (Arenz et al., 2017; Drews et al., 2020; Richter et al., 2018).

THE NEURITE After the complementary mechanisms mentioned before have played in concert in the bipolar cell dendrite, their combined contribution is reflected in the dendritic voltage which is passed down a largely passive axon cable to the axon terminal. Along its way, the signal is low-pass filtered because of the axial resistance and the membrane capacitance leading to an attenuation of fast voltage transients (Euler et al., 2014). Following that logic, there is a trend in mammalian retinal bipolar cells that neurons with shorter cables are responsible for processing fast changes in the visual scene and vice versa (Connaughton, 2011).

Neurites in fly medulla cells too could be subject to passive filtering. The length and diameter of the neurite and its membrane resistance determine the conduction velocity of electrical signals. The low-pass filtering properties of a neuron are defined by the time constant, which depends linearly on its input resistance (Koch, 2004). It could therefore be that slower medulla neurons like Mi4 and Mi9 simply have a higher specific membrane resistance.

AXONAL MECHANISMS The voltage signal arrives at the axon terminal of bipolar cells where it is subject to local non-linear signal transformations that are carried out in every chemical synapse (from voltage to calcium to transmitter, see section 1.1.1 and Figure 1).

The first transformation is defined by the dynamics of the calcium channels that open when the axonal membrane becomes depolarized. In bipolar cells calcium mainly enters through L-type calcium channels that are clustered around a specialized structure in the presynapse called *ribbon* (Zenisek et al., 2003; Llobet et al., 2003). Within the cell, the calcium undergoes a variety of time-consuming processes (in the order of hundreds of milliseconds) like diffusion, buffering, and extrusion from the cytoplasm (Euler et al., 2014). Transmitter release is influenced by various adaptive processes. The process is initiated by a small pool of primed vesicles that are close to the active zone. Second, an intermediate pool of vesicles that are tethered to the ribbon but not primed releases the transmitter. After hundreds of milliseconds, this pool undergoes depletion. The depletion of these two pools underlies short and long-term contrast adaptations (Ozuysal and Baccus, 2012; Nikolaev et al., 2013; Manookin and Demb, 2006).

In manuscript 2.3 we showed that responses of medullary neurons are dynamically suppressed by dividing local contrast changes through the average contrast of the visual scene background. Such a mechanism, therefore, normalizes the neuronal responses to the current contrast of the visual environment. Importantly, this effect was pronounced in the band-pass filter cells (i.e. Mi1, Tm3 in the ON pathway, Tm1, Tm2, Tm4 in the OFF pathway)

and less so in low-pass filter cells (i.e. Mi9, Mi4 in the ON pathway, Tm9 in the OFF pathway). Furthermore, we showed that medulla cells are the first in the motion vision circuit to perform this operation (the effect is absent in lamina cells L1-L5) and that T4 and T5 cells most likely inherit compressed signals from the upstream circuitry. We suggested that this mechanism derives at least in part from feedback rather than feedforward input. Which cell type is providing this feedback or how the signals are integrated in biophysical terms at the synapse remained unsolved.

NEUROMODULATION Bipolar cell axon terminals receive local GABAergic or glycinergic inhibitory input from amacrine cells (Euler and Masland, 2000; Masland, 2012b; Euler and Wässle, 1998; Eggers et al., 2007; Ivanova et al., 2006). With more than 42 identified cell types, amacrine cells are the most diverse and at the same time understudied group of interneurons in the retina (Lin and Masland, 2006; MacNeil and Masland, 1998; MacNeil et al., 1999; Masland, 2012a). Most GABAergic amacrine cells additionally release neuromodulatory substances, suggesting that they play a role in regulating the behavioral state of the circuit (Yang et al., 2013; Tooker et al., 2013) as well as integrating information from other sensory modalities like olfaction (Esposti et al., 2013). Amacrine cells therefore could act as gates for visual information flow in a context and stimulus-dependent manner.

Neuromodulation is a prominent example how a cell's activity and tuning properties can be shifted. It has been shown in monkeys, mice, and flies that visual circuits alter their tuning properties according to their behavioral demands (Maimon, 2011). One way to change the gain of a cell towards a desired value, is adapting the membrane resistance by the opening and closing of ion channels. By Ohm's law, increasing the input resistance of a cell leads to an increased voltage response induced by a fixed input current. Therefore closing the ion channels of a cell can act as a way to boost the gain of the cell.

In the fly's lobula plate, tangential cells shift their temporal frequency tuning optimum towards higher frequencies during tethered flight or walking (Chiappe et al., 2010; Maimon et al., 2010; Jung et al., 2011). The membrane resistance however drops, making it electrically leakier (Rosner et al., 2010). To still boost sensory responses, LPTCs most likely receive increased input from the upstream visual circuit. This state-dependent modulation of visual responses in the fly's LPTCs is realized by large octopaminergic neurons that innervate large parts of the optic lobe (Sinakevitch and Strausfeld, 2006; Longden and Krapp, 2009; Long et al., 2010; Suver et al., 2012; Busch et al., 2009). Strother et al. (2018) showed that already the medulla neurons in the ON motion vision pathway modulate their baseline calcium level according to their behavioral state and that octopaminergic neurons are necessary for walking flies to adequately process fast moving visual stimuli. In summary, in both the mammalian and the fly's visual system, the general state of the animal influences visual processing early in the circuit and only a few synapses away from photoreceptor input.

In manuscript 2.1 we made use of this modulatory effect. We applied the octopamine agonist *Chlordimeform* (CDM) and measured the temporal filtering properties of T4 and T5 cells and all their respective inputs *in vivo*.

Temporal tuning optima shifted towards higher frequencies for T4 and T5 cells and all the input elements. Notably, the effect was stronger on input neurons with band-pass characteristics than on neurons that are low-pass filters. The resulting filter bank allowed us to make a biologically plausible suggestion on where to place the neural correlates of the input lines in the three-arm detector model (Figure 10).

CONCLUSIONS The voltage in bipolar cell axon terminals reflects a complex combination of dendritic inputs, cell-intrinsic voltage transformations, and additional modulatory input from amacrine cells. Intriguingly, these response characteristics are well captured, across many stimulus conditions, by the classic linear-nonlinear-Poisson cascade model. In this model, input signals are first transformed by a set of spatio-temporal linear filters (e.g., spatial center-surround receptive fields and first-order band-pass filters), then fed through a non-linearity (e.g., rectification), and finally used to drive a Poisson spiking model (Euler et al., 2014). This resembles the models we used to model medulla cell responses in Arenz et al. (2017). However, such abstractions often miss out on specific biophysical details of the signal-generating process as well as more complex circuit interactions like feedback. Future approaches should implement neuromodulation, feedback, biophysical plausible properties of receptors, and their distribution.

3.2 FLY MOTION VISION

Where are we in understanding how direction selectivity arises in *Drosophila* motion detectors? A complete connectome of the motion vision circuitry has been assembled over the course of decades (Takemura et al., 2008, 2013; Takemura, 2015; Takemura et al., 2017; Shinomiya et al., 2019, 2014). Functional response properties (Ammer et al., 2015; Drews et al., 2020; Arenz et al., 2017; Strother et al., 2017; Fisher et al., 2015a; Serbe et al., 2016; Meier et al., 2014; Meier and Borst, 2019; Richter et al., 2018) and the transmitter phenotypes (Takemura et al., 2017; Richter et al., 2018; Davis et al., 2020; Shinomiya et al., 2019) of the inputs to T4/T5 cells have been described in great detail. Models evolved from classical Hassenstein-Reichardt (Behnia et al., 2014; Behnia and Desplan, 2015) and Barlow-Levick (Fisher et al., 2015b; Takemura, 2015) to a combination of both models, resulting in a high degree of direction selectivity, closely matching the experimental data (Haag et al., 2016, 2017; Borst, 2018).

Additionally, several studies investigated the RNA profiles of almost all cell types in the fly optic lobe, including T4 and T5 cells (Davis et al., 2020; Pankova and Borst, 2016; Hoermann et al., 2020; Konstantinides et al., 2018).

Although this is a valuable repertoire that can complement anatomical and physiological data, it is problematic to infer the protein level from mRNA levels. Both mRNA and protein levels are subject to complex regulatory post-transcriptional, translational, and protein degradation mechanisms (Vogel and Marcotte, 2012). With a recently developed genetic labeling method, it is possible to visualize the endogenous expression of receptor proteins in *Drosophila* neurons. For T4 and T5 cells, the subcellular distribution of the

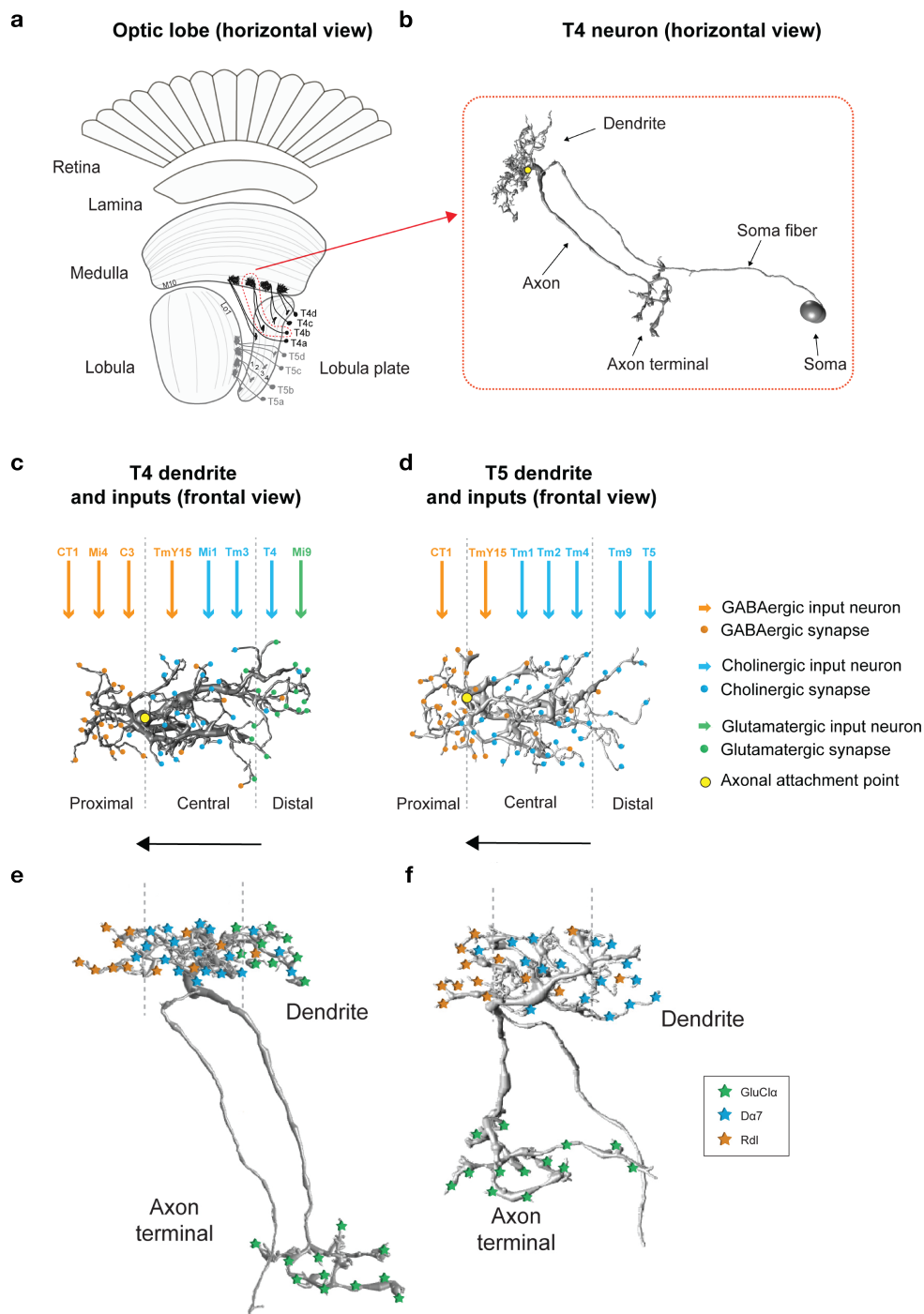


Figure 15: Distribution of input synapses and receptors on T4 and T5 cells. **a** Schematic of the optic lobe of the fly and one cell of each T4 (darker grey) and T5 (lighter grey) cell subtype projecting from medulla and lobula respectively to one of the layers of the lobula plate. **b** Morphology of one exemplary EM-reconstructed T4 neuron showing the location of the dendrite, axon and cell body in relation to each other. **c** Input synapses on the dendrite are arranged in a particular order dependent on the transmitter released by the input cell. Dendrites are elongated on the direction contrary to the preference of visual motion. In this example, a T4b cell dendrite is elongated towards the right whereas its preferred direction is to the left (Arrows). **d** Same as in **c** but for T5 cells. Note that a glutamatergic input is absent compared to T5 cells. **e** Distribution of the glutamate-gated chloride channel $\text{GluCl}\alpha$, the acetylcholine receptor subunit $D\alpha 7$ and the GABA receptor subunit Rdl . **f** Same as in **e** for T5 cells. The figure is used and modified with permission from (Fendl et al., 2020).

Acetylcholine (ACh) receptor subunit $D\alpha 7$, the GABA receptor subunit Rdl and the glutamate-gated chloride channel $GluCl\alpha$ (among others) have been shown (Fendl et al., 2020). The following picture emerges: in T4 dendrites $GluCl\alpha$ is located at the very distal end, $D\alpha 7$ is distributed in the center and Rdl is expressed mainly on the proximal end. At the membrane of T5 cells, a similar arrangement for $D\alpha 7$ and Rdl is applicable, however, $GluCl\alpha$ is not expressed (see Figure 15 e+f). This compartmentalized expression of receptors at the dendrite matches the location of input synapses intriguingly well (Figure 15 c-f). The glutamatergic input Mi9 synapses onto T4 cells on the distal part of the dendrite where $GluCl\alpha$ is expressed. $D\alpha 7$ in the center of the dendrites conveys the cholinergic signal from Mi1 & Tm3 for T4 cells and from Tm1, Tm2 & Tm4 for T5 cells. Lastly, Rdl is located at the proximal sides of the dendrite where CT1, Mi4, C3 & TmY15 synapse onto T4 dendrites and CT1 & TmY15 synapse onto T5 dendrites (see Figure 15).

Although the picture of receptor distribution is far from complete (Davis et al., 2020) it gives rise to tempting speculations. All the receptors that are described so far are ionotropic and fast. This suggests that the differential input dynamics proposed by the current algorithmic model (See Figure 9) are already created in the inputs themselves and that the synapse does not add any additional delay.

So what is there still to learn?

The above-mentioned findings open the door to look one level deeper into how direction selectivity arises at the dendritic membrane. Recently, a biophysical model has been brought forward for how a purely passive piece of membrane can accomplish a non-linear operation such as multiplication in terms of ionic conductances and membrane potential (Borst, 2018). The author suggests, that on the T4 cell's dendrite can achieve the required signal amplification derived for the 3-arm detector (see Chapter 1.3 and Figure 9) by multiplying the inhibitory glutamate input Mi9 on the distal arm of the dendrite together with an excitatory inhibitory input in the center (putatively the cholinergic inputs Mi1 & Tm3). At first glance a combination of a negative inhibitory with a positive excitatory input is counter-intuitive. It is owed to peculiarities of the glutamatergic input Mi9 however, that this becomes plausible. In the presence of glutamate-gated chloride channel $GluCl\alpha$ glutamate acts as an inhibitory transmitter (Liu and Wilson, 2013; Mauss et al., 2015). Mi9 has an OFF receptive field center, despite being attributed to the ON pathway (Arenz et al., 2017; Richter et al., 2018; Salazar-Gatzimas et al., 2018). Assuming a constant tonic release of neurotransmitters from Mi9 in darkness, an ON edge moving along T4's preferred direction would result in a release from inhibition on the preferred side of the receptive field. As a consequence the input resistance of the T4 cell rises, which acts as an amplifier to a subsequent excitatory input. In this way, the preferred direction response would become supra-linear and therefore enhanced. Stimulation in the null direction would produce sub-linearity, because the excitatory input would arrive at the dendrite before the inhibition is released. Whether the model represents the physiological reality awaits further experimental proof.

How preferred direction enhancement is implemented in the OFF pathway is less clear. As depicted in Figure 15 d, the columnar input (Tm9)

on the distal side of the T5 cell's dendrite releases acetylcholine as a transmitter (Davis et al., 2020; Shinomiya et al., 2019) and has an OFF receptive field center (Serbe et al., 2016; Arenz et al., 2017; Fisher et al., 2015a). Therefore a mechanism as proposed for the T4 cell seems unlikely for T5 cells. The excitatory receptor $D\alpha 7$ is distributed in the central and the distal part of the dendrite (Fendl et al., 2020). It is thus plausible that Tm9 on the distal side of the dendrite provides excitatory input. Based on mRNA levels, however, other receptors types are expressed in T4 and T5 cells (Davis et al., 2020). It has therefore been speculated that muscarinic acetylcholine receptors ensure inhibitory input that would be in line with a Barlow-Levick model (Shinomiya et al., 2014).

The second non-linear component of the three-arm detector, a division (null direction suppression), could be implemented for instance by opening an inhibitory conductance (i.e. chloride) that is larger than the leak conductance (Torre and Poggio, 1978). This type of inhibition is called "shunting inhibition" because an excitatory input is suppressed by division rather than linear subtraction (Carandini and Heeger, 1994). On the proximal side of T4 and T5 dendrites, such a type of inhibition could be implemented by the integration of inhibitory GABAergic input (Mi4, C3, and CT1 for T4 and CT1 for T5) via the *Rdl* receptors (Fendl et al., 2020). Another possibility is the integration of a modest inhibitory conductance, followed by a rectification (i.e. a voltage-gated calcium channel) (Koch, 2004). Definite answers will only follow after ionic currents can be measured and manipulated by pharmacological or genetic means.

VOLTAGE-GATED SODIUM CHANNELS The aforementioned model does not require any active conductances (Borst, 2018). However, according to mRNA levels quantified in Davis et al. (2020) and protein levels quantified in Fendl et al. (2020), the voltage-gated sodium channel *Paralytic* or *Para* is highly expressed in T4 and T5 cells and limited to the fiber connecting dendrites and axon terminal. Importantly, there is no expression in the fiber connecting the dendrite and the cell body or dendrites and axon terminals. Voltage-gated sodium channels are classically involved in generating the rising phase of an action potential and are essential for the excitability of the membrane (Catterall, 2000). Rapidly depolarizing synaptic inputs open Na^+ channels, Na^+ enters the cell along its concentration gradient (outside ≈ 10 times higher than inside), resulting in an even larger depolarization. When the equilibrium potential of Na^+ is reached, the inactivation of Na^+ channels and efflux of K^+ ions bring the cell's membrane potential back to rest (Kandel et al., 2000). Despite being the sole voltage-gated sodium channel gene in insects the exact kinetics remain unclear because dozens of alternative splice variants of the gene can alter biophysical characteristics of the channel (Lin et al., 2009).

Experiments in the lobula giant movement detector of locusts (LGMD) showed a multiplication-like mechanism. Here, a multiplication is approximated by feeding input signals through a logarithmic non-linearity, summing them linearly on the target dendrite, and transforming this sum via an exponential non-linearity.

Mathematically, this can be defined as:

$$e^{\log_x + \log_y} = e^{\log_x} \cdot e^{\log_y} = x \cdot y \quad (3)$$

The resulting signal therefore is the product of the two input signals. By locally blocking voltage-gated sodium channels with tetrodotoxin (TTX) the authors showed that voltage-gated sodium channels are essential for mapping the membrane potential to firing rate in an exponential manner (Gabbiani et al., 2002). Whether voltage-gated sodium channels like *Para* also contribute to non-linearities in T4 and T5 cells is not yet understood.

Patch-clamp electrophysiology experiments have reported that T4 and T5 cells exclusively convey graded potentials instead of action potentials (Gruntman et al., 2018, 2019). So how do these two findings fit with the presence of voltage-gated sodium channels? In the following, I want to discuss two possibilities. First, the *Para* channel could have a different role than contributing to an action potential. In direction-sensitive and opponent mechanosensory neurons in *Drosophila*, Na⁺ channels do not act as amplifiers of depolarization but rather as buffers that stabilize the cell's resting membrane potential by counteracting any change in the cell's voltage (Azevedo and Wilson, 2017). This is due to the depolarized membrane potential of the cell at around -50 mV. In this way additional depolarization causes Na⁺ channel to inactivate and hyperpolarization results in an opening of the channels. T4 and T5 cells however are much more hyperpolarized at rest (≈ -60 mV) (Gruntman et al., 2018, 2019), therefore a similar role seems less likely.

Other explanations are derived from the general morphology of invertebrate neurons. In contrast to vertebrate neurons, where the cell body of any given neuron is located between the dendrite and axon of the cell, invertebrates "outsourced" the cell body such that from the dendrite one cable runs towards the axon terminal whereas another one ramifies to a cell body (Figure 15 b). In the case of T4 cells the latter is extremely thin (≈ 2 nm) and dependent on the location on the distal-proximal axis ≈ 40 -120 μ m long. It could therefore be that high frequency components are attenuated (Euler et al., 2014) and action potentials arrive at a reduced amplitude at the cell body where voltage signals were measured so far (Gruntman et al., 2018, 2019).

Furthermore, it could be that due to compartmentalization action potentials do not propagate along the cable from the dendrite to the cell body. A recent study links connectomic to physiology data between second-order projection neurons (PNs) to third-order lateral horn neurons (LHNs) in the olfactory network of *Drosophila*, which appear to be remarkably similar to T4 and T5 neurons concerning their morphology. Generating one single action potential (AP) via optogenetic stimulation in the presynaptic PN neurons and measuring the postsynaptic potential (EPSP) in LHN cells, they report three major findings. First, the amplitude of EPSPs increases linearly with the density of synapses across a diverse set of connection types. Second, connection weight decreases with synaptic distance along the cable that connects dendritic and axonal arbors. Third, multi-compartment models predict EPSPs much more accurately than single-compartment models (Liu et al., 2021).

To test whether such mechanisms actually take place in T4 and T5 cells, one would optimally perform patch-clamp recordings at the dendrite and the axon terminal. This is however impossible to the minuscule size of these arborizations.

VOLTAGE IMAGING To overcome these problems researchers have made efforts to create genetically encoded fluorescent voltage indicators (GEVI) that allow non-invasive, all-optical monitoring of the membrane potential (reviewed in (Knöpfel and Song, 2019; Madhusoodanan, 2019)) and have been successfully demonstrated for studying brain function in various model organisms, including mice, fish, and flies (Chamberland et al., 2017; Miyazawa et al., 2018; Aimon et al., 2019; Abdelfattah et al., 2019).

In the fly motion vision circuit voltage indicators have been used to measure subcellular voltage responses of the lamina monopolar cells L1 & L2 and a selection of the presynaptic inputs of T4 cells (Mi1 & Tm3) and T5 cells (Tm1&Tm2), as well as the responses of T5 cells (Yang et al., 2016; Wiennecke et al., 2018). The indicators used in these studies have slow kinetic properties and are therefore unable to show action potentials. Nowadays indicators that are fast enough to detect spikes, exhibit an acceptable signal-to-noise and are compatible with 2-photon imaging (Villette et al., 2019). Combined with genetic targeting of single cells this will enhance the understanding of signal processing in T4 and T5 cells and beyond.

3.3 CONCLUDING REMARKS

In summary, the work in this cumulative thesis has contributed to the accelerating progress the field of *Drosophila* motion vision has seen over the past decades. First, we comprehensively characterized all the input elements to the elementary motion detectors in the fly with a standardized stimulus set that allowed comparisons of the spatial and temporal response properties between cell types. This was hard to infer from previous data because of varying stimulus conditions or physiological techniques and paved the way for mapping individual cell types onto plausible roles in the algorithmic model. The result was largely confirmed by anatomical data from EM reconstructions. Additionally, we showed that response properties in the early visual system are not fixed but instead are influenced by neuromodulatory transmitters that most likely encode the behavioral state of the animal. Second, we determined the dynamics of transmitter release of one particularly interesting glutamatergic cell type in the circuit with newly available indicators. Lastly, we showed that neurons in the early visual system are subject to non-linear processing of surround contrast outside their linear receptive field that we had determined in the previous manuscripts. Despite being well studied in the mammalian visual circuitry and other sensory modalities, it was the first time that a mechanism for divisive contrast normalization has been shown in the fly visual system. Our findings lay the groundwork for interesting, but so far unresolved, questions. What is the cellular or biophysical implementation of contrast normalization in medulla cells? Do active conductances shape direction-selectivity in T4 and T5 cells? How do circuits

downstream of T₄ and T₅ cells filter motion information such that behaviorally relevant information can be optimally extracted? Finding answers to these questions will be the next step in understanding visual computation at a fundamental level.

BIBLIOGRAPHY

- Abdelfattah, A. S., Kawashima, T., Singh, A., Novak, O., Liu, H., Shuai, Y., Huang, Y.-C., Campagnola, L., Seeman, S. C., Yu, J. et al. (2019) Bright and photostable chemigenetic indicators for extended in vivo voltage imaging. *Science*, **365**, 699–704.
- Ache, J. M., Polsky, J., Alghailani, S., Parekh, R., Breads, P., Peek, M. Y., Bock, D. D., von Reyn, C. R. and Card, G. M. (2019) Neural basis for looming size and velocity encoding in the *Drosophila* giant fiber escape pathway. *Current Biology*, **29**, 1073–1081.
- Aimon, S., Katsuki, T., Jia, T., Grosenick, L., Broxton, M., Deisseroth, K., Sejnowski, T. J. and Greenspan, R. J. (2019) Fast near-whole-brain imaging in adult *Drosophila* during responses to stimuli and behavior. *PLoS biology*, **17**, e2006732.
- Allen, M. J. and Murphey, R. (2007) The chemical component of the mixed gf-ttmn synapse in *Drosophila melanogaster* uses acetylcholine as its neurotransmitter. *European Journal of Neuroscience*, **26**, 439–445.
- Ammer, G., Leonhardt, A., Bahl, A., Dickson, B. J. and Borst, A. (2015) Functional specialization of neural input elements to the *Drosophila* ON motion detector. *Current Biology*, **25**, 2247–2253.
- Arenz, A., Drews, M., Richter, F., Ammer, G. and Borst, A. (2017) The temporal tuning of the *Drosophila* motion detectors is determined by the dynamics of their input elements. *Current Biology*, **27(7):929–944**.
- Azevedo, A. W. and Wilson, R. I. (2017) Active mechanisms of vibration encoding and frequency filtering in central mechanosensory neurons. *Neuron*, **96**, 446–460.
- Baden, T., Berens, P., Bethge, M. and Euler, T. (2013) Spikes in mammalian bipolar cells support temporal layering of the inner retina. *Current Biology*, **23**, 48–52.
- Bahl, A., Ammer, G., Schilling, T. and Borst, A. (2013) Object tracking in motion-blind flies. *Nature Neuroscience*, **16**, 730–738.
- Baines, R. A., Uhler, J. P., Thompson, A., Sweeney, S. T. and Bate, M. (2001) Altered electrical properties in *Drosophila* neurons developing without synaptic transmission. *Journal of Neuroscience*, **21**, 1523–1531.
- Bando, Y., Sakamoto, M., Kim, S., Ayzenshtat, I. and Yuste, R. (2019) Comparative evaluation of genetically encoded voltage indicators. *Cell reports*, **26**, 802–813.
- Barlow, H. and Levick, W. R. (1965) The mechanism of directionally selective units in rabbit's retina. *Journal of Physiology*, **178**, 477.

- Barlow, H. B., Hill, R. M. and Levick, W. R. (1964) Retinal Ganglion Cells Responding Selectively to Direction and Speed of Image Motion in the Rabbit. *Journal of Physiology*, **173**:377–407.
- Bausenwein, B., Dittrich, A. P. and Fischbach, K. F. (1992) The optic lobe of *Drosophila melanogaster*. II. Sorting of retinotopic pathways in the medulla. *Cell and Tissue Research*, **267**, 17–28.
- Bausenwein, B. and Fischbach, K. F. (1992) Activity labeling patterns in the medulla of *Drosophila melanogaster* caused by motion stimuli. *Cell and Tissue Research*, **270**, 25–35.
- Baylor, D. A., Lamb, T. D. and Yau, K.-W. (1979) Responses of retinal rods to single photons. *J. Physiol*, **288**.
- Behnia, R., Clark, D. A., Carter, A. G., Clandinin, T. R. and Desplan, C. (2014) Processing properties of ON and OFF pathways for *Drosophila* motion detection. *Nature*, **512**, 427–430.
- Behnia, R. and Desplan, C. (2015) Visual circuits in flies: beginning to see the whole picture. *Current opinion in neurobiology*, **34**, 125–132.
- Behrens, C., Schubert, T., Haverkamp, S., Euler, T. and Berens, P. (2016) Connectivity map of bipolar cells and photoreceptors in the mouse retina. *Elife*, **5**, e20041.
- Bellen, H. J., Tong, C. and Tsuda, H. (2010) 100 years of *Drosophila* research and its impact on vertebrate neuroscience: a history lesson for the future. *Nature Reviews Neuroscience*, **11**, 514–522.
- Boergens, K. M., Kapfer, C., Helmstaedter, M., Denk, W. and Borst, A. (2018) Full reconstruction of large lobula plate tangential cells in *Drosophila* from a 3D EM dataset. *PLoS ONE*, **13**, e0207828.
- Bonin, V., Mante, V. and Carandini, M. (2005) The suppressive field of neurons in lateral geniculate nucleus. *Journal of Neuroscience*, **25**, 10844–10856.
- Borghuis, B. G., Marvin, J. S., Looger, L. L. and Demb, J. B. (2013) Two-photon imaging of nonlinear glutamate release dynamics at bipolar cell synapses in the mouse retina. *Journal of Neuroscience*, **33**, 10972–10985.
- Borst, A. (2014) Fly visual course control: behaviour, algorithms and circuits. *Nature Reviews Neuroscience*, **15**, 590–599.
- Borst, A. (2018) A biophysical mechanism for preferred direction enhancement in fly motion vision. *PLoS Computational Biology*, **14**, e1006240.
- Borst, A., Drews, M. and Meier, M. (2020a) The neural network behind the eyes of a fly. *Current Opinion in Physiology*, **16**, 33–42.
- Borst, A. and Egelhaaf, M. (1989) Principles of visual motion detection. *Trends in Neurosciences*, **12**, 297–306.
- Borst, A. and Haag, J. (2002) Neural networks in the cockpit of the fly. *Journal of Comparative Physiology. A, Neuroethology, Sensory, Neural, and Behavioral Physiology*, **188**, 419–437.

- Borst, A., Haag, J. and Mauss, A. S. (2020b) How fly neurons compute the direction of visual motion. *Journal of Comparative Physiology A*, **206**, 109–124.
- Borst, A., Haag, J. and Reiff, D. F. (2010) Fly motion vision. *Annual Review of Neuroscience*, **33**, 49–70.
- Borst, A. and Helmstaedter, M. (2015) Common circuit design in fly and mammalian motion vision. *Nature Neuroscience*, **18**, 1067–1076.
- Boyden, E. S., Zhang, F., Bamberg, E., Nagel, G. and Deisseroth, K. (2005) Millisecond-timescale, genetically targeted optical control of neural activity. *Nature Neuroscience*, **8**, 1263–1268.
- Braitenberg, V. (1967) Patterns of projection in the visual system of the fly. I. Retina-lamina projections. *Experimental Brain Research*, **3**, 271–298.
- Brand, A. H. and Perrimon, N. (1993) Targeted gene expression as a means of altering cell fates and generating dominant phenotypes. *Development*, **118**, 401–415.
- Buchner, E. (1976) Elementary movement detectors in an insect visual system. *Biological Cybernetics*, **24**, 85–101.
- Buchner, E., Buchner, S. and Bülthoff, I. (1984) Deoxyglucose mapping of nervous activity induced in *Drosophila* brain by visual movement. *Journal of Comparative Physiology. A, Neuroethology, Sensory, Neural, and Behavioral Physiology*, **155**, 471–483.
- Busch, S., Selcho, M., Ito, K. and Tanimoto, H. (2009) A map of octopaminergic neurons in the *Drosophila* brain. *Journal of Comparative Neurology*, **513**, 643–667.
- Ramón y Cajal, S. and Sánchez, D. (1915) *Contribución al conocimiento de los centros nerviosos de los insectos*.
- Cao, Y., Pahlberg, J., Sarria, I., Kamasawa, N., Sampath, A. P. and Martemyanov, K. A. (2012) Regulators of G protein signaling RGS7 and RGS11 determine the onset of the light response in ON bipolar neurons. *Proceedings of the National Academy of Sciences*, **109**, 7905–7910.
- Carandini, M. and Heeger, D. J. (1994) Summation and division by neurons in primate visual cortex. *Science*, **264**, 1333–1336.
- Carandini, M. and Heeger, D. J. (2012) Normalization as a canonical neural computation. *Nature Reviews Neuroscience*, **13**, 51–62.
- Carter-Dawson, L. D. and Lavail, M. M. (1979) Rods and cones in the mouse retina. i. Structural analysis using light and electron microscopy. *Journal of Comparative Neurology*, **188**, 245–262.
- Catterall, W. A. (2000) From ionic currents to molecular mechanisms: the structure and function of voltage-gated sodium channels. *Neuron*, **26**, 13–25.

- Chamberland, S., Yang, H. H., Pan, M. M., Evans, S. W., Guan, S., Chavarha, M., Yang, Y., Salesse, C., Wu, H., Wu, J. C. et al. (2017) Fast two-photon imaging of subcellular voltage dynamics in neuronal tissue with genetically encoded indicators. *Elife*, **6**, e25690.
- Chen, T.-W., Wardill, T. J., Sun, Y., Pulver, S. R., Renninger, S. L., Baohan, A., Schreiter, E. R., Kerr, R. A., Orger, M. B., Jayaraman, V., Looger, L. L., Svoboda, K. and Kim, D. S. (2013) Ultrasensitive fluorescent proteins for imaging neuronal activity. *Nature*, **499**, 295–300.
- Chiappe, M. E., Seelig, J. D., Reiser, M. B. and Jayaraman, V. (2010) Walking modulates speed sensitivity in *Drosophila* motion vision. *Current Biology*, **20**, 1470–1475.
- Clark, D. A., Bursztyn, L., Horowitz, M. A., Schnitzer, M. J. and Clandinin, T. R. (2011) Defining the computational structure of the motion detector in *Drosophila*. *Neuron*, **70**, 1165–1177.
- Connaughton, V. (2011) Bipolar cells in the zebrafish retina. *Visual neuroscience*, **28**, 77–93.
- Cottaris, N. P. and De Valois, R. L. (1998) Temporal dynamics of chromatic tuning in macaque primary visual cortex. *Nature*, **395**, 896–900.
- Cowan, W. M. and Kandel, E. R. (2001) A brief history of synapses and synaptic transmission. *Synapses*, 1–87.
- Cruse, H. (1996) *Neural networks as cybernetic systems*. Thieme Stuttgart.
- Cully, D. F., Pareiss, P. S., Liu, K. K., Schaeffer, J. M. and Arena, J. P. (1996) Identification of a *Drosophila melanogaster* glutamate-gated chloride channel sensitive to the antiparasitic agent avermectin. *Journal of Biological Chemistry*, **271**, 20187–20191.
- Dacey, D. M. (2000) Parallel pathways for spectral coding in primate retina. *Annual review of neuroscience*, **23**, 743–775.
- Davis, F. P., Nern, A., Picard, S., Reiser, M. B., Rubin, G. M., Eddy, S. R. and Henry, G. L. (2020) A genetic, genomic, and computational resource for exploring neural circuit function. *Elife*, **9**, e50901.
- De Robertis, E. and Sasai, Y. (1996) A common plan for dorsoventral patterning in bilateria. *Nature*, **380**, 37–40.
- De Sevilla Müller, L. P., Liu, J., Solomon, A., Rodriguez, A. and Brecha, N. C. (2013) Expression of voltage-gated calcium channel $\alpha 2\delta 4$ subunits in the mouse and rat retina. *Journal of Comparative Neurology*, **521**, 2486–2501.
- DeAngelis, G. C., Ohzawa, I. and Freeman, R. D. (1995) Receptive-field dynamics in the central visual pathways. *Trends in neurosciences*, **18**, 451–458.
- Deisseroth, K. (2015) Optogenetics: 10 years of microbial opsins in neuroscience. *Nature neuroscience*, **18**, 1213–1225.

- Denk, W., Strickler, J. H. and Webb, W. W. (1990) Two-photon laser scanning fluorescence microscopy. *Science*, **248**, 73–76.
- DeVries, S. H. (2000) Bipolar cells use kainate and ampa receptors to filter visual information into separate channels. *Neuron*, **28**, 847–856.
- Devries, S. H. and Baylor, D. A. (1997) Mosaic arrangement of ganglion cell receptive fields in rabbit retina. *Journal of neurophysiology*, **78**, 2048–2060.
- DeVries, S. H., Li, W. and Saszik, S. (2006) Parallel processing in two transmitter microenvironments at the cone photoreceptor synapse. *Neuron*, **50**, 735–748.
- Dietzl, G., Chen, D., Schnorrer, F., Su, K.-C., Barinova, Y., Fellner, M., Gasser, B., Kinsey, K., Oppel, S., Scheiblauer, S. et al. (2007) A genome-wide transgenic RNAi library for conditional gene inactivation in *Drosophila*. *Nature*, **448**, 151–156.
- Ding, H., Smith, R. G., Poleg-Polsky, A., Diamond, J. S. and Briggman, K. L. (2016) Species-specific wiring for direction selectivity in the mammalian retina. *Nature*, **535**, 105–110.
- Drews, M. S., Leonhardt, A., Pirogova, N., Richter, F. G., Schuetzenberger, A., Braun, L., Serbe, E. and Borst, A. (2020) Dynamic signal compression for robust motion vision in flies. *Current Biology*, **30**, 209–221.
- Duebel, J., Haverkamp, S., Schleich, W., Feng, G., Augustine, G. J., Kuner, T. and Euler, T. (2006) Two-photon imaging reveals somatodendritic chloride gradient in retinal on-type bipolar cells expressing the biosensor clomeleon. *Neuron*, **49**, 81–94.
- Eaton, R. C., Lavender, W. A. and Wieland, C. M. (1981) Identification of mauthner-initiated response patterns in goldfish: evidence from simultaneous cinematography and electrophysiology. *Journal of Comparative Physiology*, **144**, 521–531.
- Eccles, J. C. (1976) From electrical to chemical transmission in the central nervous system. *Notes and records of the Royal Society of London*, **30**, 219–230.
- Egelhaaf, M., Borst, A. and Warzecha, A.-K. (1992) Photo-ablation of single neurons in the fly visual system reveals neural circuit for the detection of small moving objects. **141**, 119–122.
- Eggermont, J., Johannesma, P. and Aertsen, A. (1983) Reverse-correlation methods in auditory research. *Quarterly reviews of biophysics*, **16**, 341–414.
- Eggers, E. D., McCall, M. A. and Lukasiewicz, P. D. (2007) Presynaptic inhibition differentially shapes transmission in distinct circuits in the mouse retina. *The Journal of physiology*, **582**, 569–582.
- Eichner, H., Joesch, M., Schnell, B., Reiff, D. F. and Borst, A. (2011) Internal structure of the fly elementary motion detector. *Neuron*, **70**, 1155–1164.

- Elstrott, J., Anishchenko, A., Greschner, M., Sher, A., Litke, A. M., Chichilnisky, E. and Feller, M. B. (2008) Direction selectivity in the retina is established independent of visual experience and cholinergic retinal waves. *Neuron*, **58**, 499–506.
- Esposti, F., Johnston, J., Rosa, J. M., Leung, K.-M. and Lagnado, L. (2013) Olfactory stimulation selectively modulates the off pathway in the retina of zebrafish. *Neuron*, **79**, 97–110.
- Euler, T., Detwiler, P. B. and Denk, W. (2002) Directionally selective calcium signals in dendrites of starburst amacrine cells. *Nature*, **418**, 845–852.
- Euler, T., Haverkamp, S., Schubert, T. and Baden, T. (2014) Retinal bipolar cells: elementary building blocks of vision. *Nature Reviews Neuroscience*, **15**, 507–519.
- Euler, T. and Masland, R. H. (2000) Light-evoked responses of bipolar cells in a mammalian retina. *Journal of neurophysiology*, **83**, 1817–1829.
- Euler, T. and Wässle, H. (1998) Different contributions of GABA_a and GABA_c receptors to rod and cone bipolar cells in a rat retinal slice preparation. *Journal of Neurophysiology*, **79**, 1384–1395.
- Exner, S. (1891) *Die Physiologie der facettirten Augen von Krebsen und Insecten: eine Studie*. Franz Deuticke.
- Exner, S. (1894) *Entwurf zu einer physiologischen Erklärung der psychischen Erscheinungen*. F. Deuticke.
- Fayyazuddin, A., Zaheer, M. A., Hiesinger, P. R. and Bellen, H. J. (2006) The nicotinic acetylcholine receptor $\alpha 7$ is required for an escape behavior in *Drosophila*. *PLoS biology*, **4**, e63.
- Fendl, S., Vieira, R. M. and Borst, A. (2020) Conditional protein tagging methods reveal highly specific subcellular distribution of ion channels in motion-sensing neurons. *Elife*, **9**, e62953.
- Fenno, L., Yizhar, O. and Deisseroth, K. (2011) The development and application of optogenetics. *Annual review of neuroscience*, **34**, 389–412.
- Fermi, G. and Reichardt, W. (1963) Optomotorische Reaktionen der Fliege *Musca domestica*. *Kybernetik*, **2**, 15–28.
- Fischbach, K.-F. and Dittrich, A. (1989) The optic lobe of *Drosophila melanogaster*. I. A Golgi analysis of wild-type structure. *Cell and Tissue Research*, **258**, 441–475.
- Fisher, Y. E., Leong, J. C., Sporar, K., Ketkar, M. D., Gohl, D. M., Clandinin, T. R. and Silies, M. (2015a) A class of visual neurons with wide-field properties is required for local motion detection. *Current Biology*, **25**, 3178–3189.
- Fisher, Y. E., Silies, M. and Clandinin, T. R. (2015b) Orientation selectivity sharpens motion detection in *Drosophila*. *Neuron*, **88**, 390–402.

- Freifeld, L., Clark, D. A., Schnitzer, M. J., Horowitz, M. A. and Clandinin, T. R. (2013) GABAergic lateral interactions tune the early stages of visual processing in *Drosophila*. *Neuron*, **78**, 1075–1089.
- Fujiwara, T., Cruz, T. L., Bohoslav, J. P. and Chiappe, M. E. (2017) A faithful internal representation of walking movements in the *Drosophila* visual system. *Nature Neuroscience*, **20**, 72–81.
- Gabbiani, F., Krapp, H. G., Koch, C. and Laurent, G. (2002) Multiplicative computation in a visual neuron sensitive to looming. *Nature*, **420**, 320–324.
- Gibson, J. J. (1950) The perception of the visual world.
- Golgi, C. (1873) Sulla struttura della sostanza grigia dell cervello', *gazz. Med Lombarda*, **33**, 224–46.
- Göppert-Mayer, M. (1931) Über elementarakte mit zwei quantensprüngen. *Annalen der Physik*, **401**, 273–294.
- Götz, K. G. (1964) Optomotorische Untersuchung des visuellen Systems einiger Augenmutanten der Fruchtfliege *Drosophila*. *Kybernetik*, **2**, 77–92.
- Götz, K. G. (1965) Die optischen Übertragungseigenschaften der Komplexaugen von *Drosophila*. *Biological Cybernetics*, **2**, 215–221.
- Götz, K. G. (1987) Course-control, metabolism and wing interference during ultralong tethered flight in *Drosophila melanogaster*. *Journal of Experimental Biology*, **128**, 35–46.
- Govorunova, E. G., Sineshchekov, O. A., Janz, R., Liu, X. and Spudich, J. L. (2015) Natural light-gated anion channels: A family of microbial rhodopsins for advanced optogenetics. *Science*, **349**, 647–650.
- Greene, M. J., Kim, J. S., Seung, H. S. et al. (2016) Analogous convergence of sustained and transient inputs in parallel on and off pathways for retinal motion computation. *Cell reports*, **14**, 1892–1900.
- Gruntman, E., Romani, S. and Reiser, M. B. (2018) Simple integration of fast excitation and offset, delayed inhibition computes directional selectivity in *Drosophila*. *Nature Neuroscience*, **21**, 250–257.
- Gruntman, E., Romani, S. and Reiser, M. B. (2019) The computation of directional selectivity in the *Drosophila* OFF motion pathway. *Elife*, **8**, e50706.
- Gür, B., Sporar, K., Lopez-Behling, A. and Silies, M. (2019) Distinct expression of potassium channels regulates visual response properties of lamina neurons in *Drosophila melanogaster*. *Journal of Comparative Physiology A*, **206**, 273–287.
- Haag, J., Arenz, A., Serbe, E., Gabbiani, F. and Borst, A. (2016) Complementary mechanisms create direction selectivity in the fly. *eLife*, **5**.
- Haag, J. and Borst, A. (1998) Active membrane properties and signal encoding in graded potential neurons. *Journal of Neuroscience*, **18**, 7972–7986.

- Haag, J., Denk, W. and Borst, A. (2004) Fly motion vision is based on Reichardt detectors regardless of the signal-to-noise ratio. *Proceedings of the National Academy of Sciences of the United States of America*, **101**, 16333–16338.
- Haag, J., Mishra, A. and Borst, A. (2017) A common directional tuning mechanism of drosophila motion-sensing neurons in the on and in the off pathway. *Elife*, **6**, e29044.
- Haikala, V., Joesch, M., Borst, A. and Mauss, A. S. (2013) Optogenetic control of fly optomotor responses. *Journal of Neuroscience*, **33**, 13927–13934.
- Hamill, O. P., Marty, A., Neher, E., Sakmann, B. and Sigworth, F. J. (1981) Improved patch-clamp techniques for high-resolution current recording from cells and cell-free membrane patches. *Pflügers Archiv*, **391**, 85–100.
- Hardie, R. C. (1989) A histamine-activated chloride channel involved in neurotransmission at a photoreceptor synapse. *Nature*, **339**, 704–706.
- Hardie, R. C. and Juusola, M. (2015) Phototransduction in *Drosophila*. *Current opinion in neurobiology*, **34**, 37–45.
- Hardie, R. C. and Raghu, P. (2001) Visual transduction in *Drosophila*. *Nature*, **413**, 186–193.
- Hartline, H. K. (1938) The response of single optic nerve fibers of the vertebrate eye to illumination of the retina. *American Journal of Physiology-Legacy Content*, **121**, 400–415.
- Harz, H. and Hegemann, P. (1991) Rhodopsin-regulated calcium currents in *Chlamydomonas*. *Nature*, **351**, 489–491.
- Hassenstein, B. (1951) Ommatidienraster und afferente Bewegungsintegration. *Journal of Comparative Physiology. A, Neuroethology, Sensory, Neural, and Behavioral Physiology*, **33**, 301–326.
- Hassenstein, B. and Reichardt, W. (1956) Systemtheoretische Analyse der Zeit-, Reihenfolgen- und Vorzeichenauswertung bei der Bewegungsperzeption des Rüsselkäfers *Chlorophanus*. *Zeitschrift für Naturforschung B*, **11**, 513–524.
- Hausen, K. (1976) Functional characterization and anatomical identification of motion sensitive neurons in the lobula plate of the blowfly *Calliphora erythrocephala*. *Zeitschrift für Naturforschung C*, **31**, 629–634.
- Hausen, K. (1982a) Motion sensitive interneurons in the optomotor system of the fly: I. The horizontal cells: Structure and signals. *Biological Cybernetics*, **45**, 143–156.
- Hausen, K. (1982b) Motion sensitive interneurons in the optomotor system of the fly: II. The horizontal cells: Receptive field organization and response characteristics. *Biological Cybernetics*, **46**, 67–79.

- Hausselet, S. E., Euler, T., Detwiler, P. B. and Denk, W. (2007) A dendrite-autonomous mechanism for direction selectivity in retinal starburst amacrine cells. *PLoS Biology*, **5**, e185.
- Haverkamp, S., Grünert, U. and Wässle, H. (2000) The cone pedicle, a complex synapse in the retina. *Neuron*, **27**, 85–95.
- Haverkamp, S., Grünert, U. and Wässle, H. (2001) Localization of kainate receptors at the cone pedicles of the primate retina. *Journal of Comparative Neurology*, **436**, 471–486.
- Hayashi, S., Ito, K., Sado, Y., Taniguchi, M., Akimoto, A., Takeuchi, H., Aigaki, T., Matsuzaki, F., Nakagoshi, H., Tanimura, T. et al. (2002) Getdb, a database compiling expression patterns and molecular locations of a collection of gal4 enhancer traps. *genesis*, **34**, 58–61.
- Hecht, S. and Wald, G. (1934) The visual acuity and intensity discrimination of *Drosophila*. *The Journal of General Physiology*, **17**, 517–547.
- Heidenreich, M. and Zhang, F. (2016) Applications of CRISPR–Cas systems in neuroscience. *Nature Reviews Neuroscience*, **17**, 36–44.
- Heisenberg, M. and Buchner, E. (1977) The role of retinula cell types in visual behavior of *Drosophila melanogaster*. *Journal of comparative physiology*, **117**, 127–162.
- Heisenberg, M. and Wolf, R. (1984) *Vision in Drosophila: Genetics of Microbehavior*. Experimental Brain Research Supplementum. Berlin Heidelberg: Springer.
- Helmchen, F. and Denk, W. (2005) Deep tissue two-photon microscopy. *Nature methods*, **2**, 932–940.
- Helmstaedter, M., Briggman, K. L., Turaga, S. C., Jain, V., Seung, H. S. and Denk, W. (2013) Connectomic reconstruction of the inner plexiform layer in the mouse retina. *Nature*, **500**, 168–174.
- Hengstenberg, R. (1982) Common visual response properties of giant vertical cells in the lobula plate of the blowfly *Calliphora*. *Journal of Comparative Physiology. A, Neuroethology, Sensory, Neural, and Behavioral Physiology*, **149**, 179–193.
- Henley, J. R., Cao, H. and McNiven, M. A. (1999) Participation of dynamin in the biogenesis of cytoplasmic vesicles. *The FASEB Journal*, **13**, S243–S247.
- Hoermann, N., Schilling, T., Ali, A. H., Serbe, E., Mayer, C., Borst, A. and Pujol-Martí, J. (2020) A combinatorial code of transcription factors specifies subtypes of visual motion-sensing neurons in *Drosophila*. *Development*, **147**, dev186296.
- Hopp, E., Borst, A. and Haag, J. (2014) Subcellular mapping of dendritic activity in optic flow processing neurons. *Journal of Comparative Physiology A: Neuroethology, Sensory, Neural, and Behavioral Physiology*, **200**, 359–370.

- Ichinose, T., Fyk-Kolodziej, B. and Cohn, J. (2014) Roles of on cone bipolar cell subtypes in temporal coding in the mouse retina. *Journal of Neuroscience*, **34**, 8761–8771.
- Ivanova, E., Müller, U. and Wässle, H. (2006) Characterization of the glycinergic input to bipolar cells of the mouse retina. *European Journal of Neuroscience*, **23**, 350–364.
- Jansonius, N. and Van Hateren, J. (1991) Fast temporal adaptation of ON-OFF units in the first optic chiasm of the blowfly. *Journal of Comparative Physiology A*, **168**, 631–637.
- Jansonius, N. and Van Hateren, J. (1993a) ON-OFF units in the first optic chiasm of the blowfly ii. spatial properties. *Journal of Comparative Physiology A*, **172**, 467–471.
- Jansonius, N. and Van Hateren, J. (1993b) ON spiking units in the first optic chiasm of the blowfly. *Journal of Comparative Physiology A*, **173**, 187–192.
- Jenett, A., Rubin, G. M., Ngo, T. T., Shepherd, D., Murphy, C., Dionne, H., Pfeiffer, B. D., Cavallaro, A., Hall, D., Jeter, J., Iyer, N., Fetter, D., Hausenfluck, J. H., Peng, H., Trautman, E. T., Svirskas, R. R., Myers, E. W., Iwinski, Z. R., Aso, Y., DePasquale, G. M., Enos, A., Hulamm, P., Lam, S. C., Li, H. H., Laverty, T. R., Long, F., Qu, L., Murphy, S. D., Rokicki, K., Safford, T., Shaw, K., Simpson, J. H., Sowell, A., Tae, S., Yu, Y. and Zugates, C. T. (2012) A GAL4-driver line resource for *Drosophila* neurobiology. *Cell Reports*, **2**, 991–1001.
- Joesch, M., Plett, J., Borst, A. and Reiff, D. F. (2008) Response properties of motion-sensitive visual interneurons in the lobula plate of *Drosophila melanogaster*. *Current Biology*, **18**, 368–374.
- Joesch, M., Schnell, B., Raghu, S. V., Reiff, D. F. and Borst, A. (2010) ON and OFF pathways in *Drosophila* motion vision. *Nature*, **468**, 300–304.
- Johns, D. C., Marx, R., Mains, R. E., O'Rourke, B. and Marbán, E. (1999) Inducible genetic suppression of neuronal excitability. *Journal of Neuroscience*, **19**, 1691–1697.
- Jung, S. N., Borst, A. and Haag, J. (2011) Flight activity alters velocity tuning of fly motion-sensitive neurons. *Journal of Neuroscience*, **31**, 9231–9237.
- Kandel, E. R., Schwartz, J. H., Jessell, T. M., Siegelbaum, S., Hudspeth, A. J. and Mack, S. (2000) *Principles of neural science*, vol. 4. McGraw-hill New York.
- Kim, I.-J., Zhang, Y., Yamagata, M., Meister, M. and Sanes, J. R. (2008) Molecular identification of a retinal cell type that responds to upward motion. *Nature*, **452**, 478–482.
- Kim, J. S., Greene, M. J., Zlateski, A., Lee, K., Richardson, M., Turaga, S. C., Purcaro, M., Balkam, M., Robinson, A., Behabadi, B. F., Campos, M., Denk, W. and Seung, H. S. (2014a) Space-time wiring specificity supports direction selectivity in the retina. *Nature*, **509**, 331–336.

- Kim, J. S., Greene, M. J., Zlateski, A., Lee, K., Richardson, M., Turaga, S. C., Purcaro, M., Balkam, M., Robinson, A., Behabadi, B. F., Campos, M., Denk, W., Seung, H. S. and EyeWriters, t. (2014b) Space-time wiring specificity supports direction selectivity in the retina. *Nature*, 1–17.
- Kirschfeld, K. (1967) Die Projektion der optischen Umwelt auf das Raster der Rhabdomere im Komplexauge von *Musca*. *Experimental Brain Research*, **3**, 248–270.
- Kitamoto, T. (2001) Conditional modification of behavior in *Drosophila* by targeted expression of a temperature-sensitive *shibire* allele in defined neurons. *Journal of Neurobiology*, **47**, 81–92.
- Knöpfel, T. and Song, C. (2019) Optical voltage imaging in neurons: moving from technology development to practical tool. *Nature Reviews Neuroscience*, **20**, 719–727.
- Koch, C. (2004) *Biophysics of computation: information processing in single neurons*. Oxford university press.
- Konstantinides, N., Kapuralin, K., Fadil, C., Barboza, L., Satija, R. and Desplan, C. (2018) Phenotypic convergence: distinct transcription factors regulate common terminal features. *Cell*, **174**, 622–635.
- Kosaka, T. and Ikeda, K. (1983) Possible temperature-dependent blockage of synaptic vesicle recycling induced by a single gene mutation in *Drosophila*. *Journal of neurobiology*, **14**, 207–225.
- Krapp, H. G., Hengstenberg, B. and Hengstenberg, R. (1998) Dendritic structure and receptive-field organization of optic flow processing interneurons in the fly. *Journal of Neurophysiology*, **79**, 1902–1917.
- Krapp, H. G. and Hengstenberg, R. (1996) Estimation of self-motion by optic flow processing in single visual interneurons. *Nature*, **384**, 463–466.
- Krapp, H. G., Hengstenberg, R. and Egelhaaf, M. (2001) Binocular contributions to optic flow processing in the fly visual system. *Journal of neurophysiology*, **85**, 724–734.
- Lai, S. L. and Lee, T. (2006) Genetic mosaic with dual binary transcriptional systems in *Drosophila*. *Nature Neuroscience*, **9**, 703–709.
- Land, M. F. (1997) Visual acuity in insects. *Annual review of entomology*, **42**, 147–177.
- Land, M. F. and Collett, T. S. (1974) Chasing behaviour of houseflies (*Fannia canicularis*). *Journal of Comparative Physiology. A, Neuroethology, Sensory, Neural, and Behavioral Physiology*, **89**, 331–357.
- Laughlin, S. B. (1981) A simple coding procedure enhances a neuron's information capacity. *Zeitschrift für Naturforschung. Section C: Biosciences*, **36**, 910–912.

- Laughlin, S. B. and Hardie, R. C. (1978) Common strategies for light adaptation in the peripheral visual systems of fly and dragonfly. *Journal of Comparative Physiology. A, Neuroethology, Sensory, Neural, and Behavioral Physiology*, **128**, 319–340.
- Laughlin, S. B. and Osorio, D. (1989) Mechanisms for neural signal enhancement in the blowfly compound eye. *Journal of Experimental Biology*, **144**, 113–146.
- Leong, J. C., Esch, J. J., Poole, B., Ganguli, S. and Clandinin, T. R. (2016) Direction selectivity in *Drosophila* emerges from preferred-direction enhancement and null-direction suppression. *Journal of Neuroscience*, **36**, 8078–8092.
- Leonte, M.-B., Leonhardt, A., Borst, A. and Mauss, A. S. (2021) Aerial course stabilization is impaired in motion-blind flies. *Journal of Experimental Biology*, **224**, jeb242219.
- Lin, B. and Masland, R. H. (2006) Populations of wide-field amacrine cells in the mouse retina. *Journal of Comparative Neurology*, **499**, 797–809.
- Lin, W.-H., Wright, D. E., Muraro, N. I. and Baines, R. A. (2009) Alternative splicing in the voltage-gated sodium channel DmNav regulates activation, inactivation, and persistent current. *Journal of neurophysiology*, **102**, 1994–2006.
- Lindstrom, S. H., Ryan, D. G., Shi, J. and DeVries, S. H. (2014) Kainate receptor subunit diversity underlying response diversity in retinal OFF bipolar cells. *The Journal of physiology*, **592**, 1457–1477.
- Liu, T. X., Davoudian, P. A., Lizbinski, K. M. and Jeanne, J. M. (2021) Connectomic features underlying diverse synaptic connection strengths and subcellular computation. *bioRxiv*.
- Liu, W. W. and Wilson, R. I. (2013) Glutamate is an inhibitory neurotransmitter in the *Drosophila* olfactory system. *Proceedings of the National Academy of Sciences*, **110**, 10294–10299.
- Llobet, A., Cooke, A. and Lagnado, L. (2003) Exocytosis at the ribbon synapse of retinal bipolar cells studied in patches of presynaptic membrane. *Journal of Neuroscience*, **23**, 2706–2714.
- Long, M. A., Jin, D. Z. and Fee, M. S. (2010) Support for a synaptic chain model of neuronal sequence generation. *Nature*, **468**, 394–399.
- Longden, K. D. and Krapp, H. G. (2009) State-dependent performance of optic-flow processing interneurons. *Journal of neurophysiology*, **102**, 3606–3618.
- Luan, H., Peabody, N. C., Vinson, C. R. and White, B. H. (2006) Refined spatial manipulation of neuronal function by combinatorial restriction of transgene expression. *Neuron*, **52**, 425–436.
- MacNeil, M. A., Heussy, J. K., Dacheux, R. F., Raviola, E. and Masland, R. H. (1999) The shapes and numbers of amacrine cells: matching of photofilled

- with golgi-stained cells in the rabbit retina and comparison with other mammalian species. *Journal of Comparative Neurology*, **413**, 305–326.
- MacNeil, M. A. and Masland, R. H. (1998) Extreme diversity among amacrine cells: implications for function. *Neuron*, **20**, 971–982.
- Madhusoodanan, J. (2019) Genetic light bulbs illuminate the brain. *Nature*, **574**, 437–440.
- Maimon, G. (2011) Modulation of visual physiology by behavioral state in monkeys, mice, and flies. *Current opinion in neurobiology*, **21**, 559–564.
- Maimon, G., Straw, A. D. and Dickinson, M. (2010) Active flight increases the gain of visual motion processing in *Drosophila*. *Nature Neuroscience*, **13**, 393–399.
- Maisak, M. S., Haag, J., Ammer, G., Serbe, E., Meier, M., Leonhardt, A., Schilling, T., Bahl, A., Rubin, G. M., Nern, A., Dickson, B. J., Reiff, D. F., Hopp, E. and Borst, A. (2013) A directional tuning map of *Drosophila* elementary motion detectors. *Nature*, **500**, 212–216.
- Manookin, M. B. and Demb, J. B. (2006) Presynaptic mechanism for slow contrast adaptation in mammalian retinal ganglion cells. *Neuron*, **50**, 453–464.
- Masland, R. H. (2001) The fundamental plan of the retina. *Nature neuroscience*, **4**, 877–886.
- Masland, R. H. (2012a) The tasks of amacrine cells. *Visual neuroscience*, **29**, 3–9.
- Masland, R. H. (2012b) The neuronal organization of the retina. *Neuron*, **76**, 266–280.
- Masu, M., Iwakabe, H., Tagawa, Y., Miyoshi, T., Yamashita, M., Fukuda, Y., Sasaki, H., Hiroi, K., Nakamura, Y., Shigemoto, R. et al. (1995) Specific deficit of the ON response in visual transmission by targeted disruption of the mGluR6 gene. *Cell*, **80**, 757–765.
- Mauss, A. S., Meier, M., Serbe, E. and Borst, A. (2014) Optogenetic and pharmacologic dissection of feedforward inhibition in *Drosophila* motion vision. *Journal of Neuroscience*, **34**, 2254–2263.
- Mauss, A. S., Pankova, K., Arenz, A., Nern, A., Rubin, G. M. and Borst, A. (2015) Neural circuit to integrate opposing motions in the visual field. *Cell*, **162**, 351–362.
- Meier, M. and Borst, A. (2019) Extreme compartmentalization in a *Drosophila* amacrine cell. *Current Biology*, **29**, 1545–1550.
- Meier, M., Serbe, E., Maisak, M. S., Haag, J., Dickson, B. J. and Borst, A. (2014) Neural circuit components of the *Drosophila* OFF motion vision pathway. *Current Biology*, **24**, 385–392.

- Meinertzhagen, I. A. and O'Neil, S. (1991) Synaptic organization of columnar elements in the lamina of the wild type in *Drosophila melanogaster*. *Journal of Comparative Neurology*, **305**, 232–263.
- Miller, R. F. and Dacheux, R. F. (1983) Intracellular chloride in retinal neurons: measurement and meaning. *Vision research*, **23**, 399–411.
- Miyazawa, H., Okumura, K., Hiyoshi, K., Maruyama, K., Kakinuma, H., Amo, R., Okamoto, H., Yamasu, K. and Tsuda, S. (2018) Optical interrogation of neuronal circuitry in zebrafish using genetically encoded voltage indicators. *Scientific reports*, **8**, 1–10.
- Morgan, T. H. (1910) Sex limited inheritance in *Drosophila*. *Science*, **32**, 120–122.
- Mronz, M. and Lehmann, F.-O. (2008) The free-flight response of *Drosophila* to motion of the visual environment. *Journal of Experimental Biology*, **211**, 2026–2045.
- Muijres, F. T., Elzinga, M. J., Melis, J. M. and Dickinson, M. H. (2014) Flies evade looming targets by executing rapid visually directed banked turns. *Science*, **344**, 172–177.
- Nagel, G., Brauner, M., Liewald, J. F., Adeishvili, N., Bamberg, E. and Gottschalk, A. (2005) Light activation of channelrhodopsin-2 in excitable cells of *Caenorhabditis elegans* triggers rapid behavioral responses. *Current Biology*, **15**, 2279–2284.
- Nagel, G., Szellas, T., Huhn, W., Kateriya, S., Adeishvili, N., Berthold, P., Ollig, D., Hegemann, P. and Bamberg, E. (2003) Channelrhodopsin-2, a directly light-gated cation-selective membrane channel. *Proceedings of the National Academy of Sciences of the United States of America*, **100**, 13940–13945.
- Newman, E. A., Araque, A. and Dubinsky, J. M. (2017) *The beautiful brain*.
- Nikolaev, A., Leung, K.-M., Odermatt, B. and Lagnado, L. (2013) Synaptic mechanisms of adaptation and sensitization in the retina. *Nature neuroscience*, **16**, 934–941.
- Oyster, C. W. and Barlow, H. B. (1967) Direction-selective units in rabbit retina: distribution of preferred directions. *Science*, **155**, 841–842.
- Ozuysal, Y. and Baccus, S. A. (2012) Linking the computational structure of variance adaptation to biophysical mechanisms. *Neuron*, **73**, 1002–1015.
- Pankova, K. and Borst, A. (2016) RNA-Seq Transcriptome Analysis of Direction-Selective T4/T5 Neurons in *Drosophila*. *PLoS ONE*, **11**, e0163986.
- Parisky, K. M., Agosto, J., Pulver, S. R., Shang, Y., Kuklin, E., Hodge, J. J., Kang, K., Kang, K., Liu, X., Garrity, P. A., Rosbash, M. and Griffith, L. C. (2008) PDF cells are a GABA-responsive wake-promoting component of the *Drosophila* sleep circuit. *Neuron*, **60**, 672–682.

- Pearring, J. N., Bojang, P., Shen, Y., Koike, C., Furukawa, T., Nawy, S. and Gregg, R. G. (2011) A role for nyctalopin, a small leucine-rich repeat protein, in localizing the TRP melastatin 1 channel to retinal depolarizing bipolar cell dendrites. *Journal of Neuroscience*, **31**, 10060–10066.
- Perkins, L. A., Holderbaum, L., Tao, R., Hu, Y., Sopko, R., McCall, K., Yang-Zhou, D., Flockhart, I., Binari, R., Shim, H.-S. et al. (2015) The transgenic RNAi project at harvard medical school: resources and validation. *Genetics*, **201**, 843–852.
- Pfeiffer, B. D., Jenett, A., Hammonds, A. S., Ngo, T.-T. B., Misra, S., Murphy, C., Scully, A., Carlson, J. W., Wan, K. H., Lavery, T. R. et al. (2008) Tools for neuroanatomy and neurogenetics in *Drosophila*. *Proceedings of the National Academy of Sciences of the United States of America*, **105**, 9715–9720.
- Pfeiffer, B. D., Ngo, T. T., Hibbard, K. L., Murphy, C., Jenett, A., Truman, J. W. and Rubin, G. M. (2010) Refinement of tools for targeted gene expression in *Drosophila*. *Genetics*, **186**, 735–755.
- Port, F., Chen, H.-M., Lee, T. and Bullock, S. L. (2014) Optimized CRISPR/Cas tools for efficient germline and somatic genome engineering in *Drosophila*. *Proceedings of the National Academy of Sciences*, **111**, E2967–E2976.
- Port, F., Strein, C., Stricker, M., Rauscher, B., Heigwer, F., Zhou, J., Beyersdörffer, C., Frei, J., Hess, A., Kern, K. et al. (2020) A large-scale resource for tissue-specific CRISPR mutagenesis in *Drosophila*. *Elife*, **9**, e53865.
- Raji, J. I. and Potter, C. J. (2021) The number of neurons in *Drosophila* and mosquito brains. *PLoS ONE*, **16**, e0250381.
- Regus-Leidig, H. and Brandstätter, J. (2012) Structure and function of a complex sensory synapse. *Acta physiologica*, **204**, 479–486.
- Reiff, D. F., Plett, J., Mank, M., Griesbeck, O. and Borst, A. (2010) Visualizing retinotopic half-wave rectified input to the motion detection circuitry of *Drosophila*. *Nature Neuroscience*, **13**, 973–978.
- Richter, F. G., Fendl, S., Drews, M. S. and Borst, A. (2018) Glutamate signaling in the fly visual system. *iScience*, **7**, 85–95.
- Ringach, D. L. (2002) Spatial structure and symmetry of simple-cell receptive fields in macaque primary visual cortex. *Journal of neurophysiology*.
- Ringach, D. L., Hawken, M. J. and Shapley, R. (1997) Dynamics of orientation tuning in macaque primary visual cortex. *Nature*, **387**, 281–284.
- Rister, J., Pauls, D., Schnell, B., Ting, C., C.-H., L., Sinakevitch, N., Morante, J., Strausfeld, N. J., Ito, K. and Heisenberg, M. (2007) Dissection of the peripheral motion channel in the visual system of *Drosophila melanogaster*. *Neuron*, **56**, 155–170.
- Rivera-Alba, M., Vitaladevuni, S. N., Mischenko, Y., Lu, Z., Takemura, S., Scheffer, L. J., Meinertzhagen, I. A., Chklovskii, D. B. and de Polavieja, G. G. (2011) Wiring economy and volume exclusion determine neuronal placement in the *Drosophila* brain. *Current Biology*, **21**, 2000–2005.

- Rockhill, R. L., Euler, T. and Masland, R. H. (2000) Spatial order within but not between types of retinal neurons. *Proceedings of the National Academy of Sciences*, **97**, 2303–2307.
- Rosenzweig, M., Brennan, K. M., Tayler, T. D., Phelps, P. O., Patapoutian, A. and Garrity, P. A. (2005) The *Drosophila* ortholog of vertebrate TRPA1 regulates thermotaxis. *Genes & Development*, **19**, 419–424.
- Rosner, R., Egelhaaf, M. and Warzecha, A.-K. (2010) Behavioural state affects motion-sensitive neurones in the fly visual system. *Journal of Experimental Biology*, **213**, 331–338.
- Röth, S., Fulcher, L. J. and Sapkota, G. P. (2019) Advances in targeted degradation of endogenous proteins. *Cellular and Molecular Life Sciences*, **76**, 2761–2777.
- Sabatini, B. L. and Tian, L. (2020) Imaging neurotransmitter and neuromodulator dynamics *in vivo* with genetically encoded indicators. *Neuron*, **108**, 17–32.
- Sahel, J.-A., Boulanger-Scemama, E., Pagot, C., Arleo, A., Galluppi, F., Martel, J. N., Degli Esposti, S., Delaux, A., de Saint Aubert, J.-B., de Montleau, C. et al. (2021) Partial recovery of visual function in a blind patient after optogenetic therapy. *Nature Medicine*, 1–7.
- Salazar-Gatzimas, E., Agrochao, M., Fitzgerald, J. E. and Clark, D. A. (2018) The neuronal basis of an illusory motion percept is explained by decorrelation of parallel motion pathways. *Current Biology*, **28**, 3748–3762.
- Sanes, J. R. and Zipursky, S. L. (2010) Design principles of insect and vertebrate visual systems. *Neuron*, **66**, 15–36.
- Schilling, T. and Borst, A. (2015) Local motion detectors are required for the computation of expansion flow-fields. *Biology Open*, **4**, 1105–1108.
- Schnaitmann, C., Haikala, V., Abraham, E., Oberhauser, V., Thestrup, T., Griesbeck, O. and Reiff, D. F. (2018) Color processing in the early visual system of *Drosophila*. *Cell*, **172**, 318–330.
- Schnell, B., Joesch, M., Forstner, F., Raghu, S. V., Otsuna, H., Ito, K., Borst, A. and Reiff, D. F. (2010) Processing of horizontal optic flow in three visual interneurons of the *Drosophila* brain. *Journal of Neurophysiology*, **103**, 1646–1657.
- Schnell, B., Raghu, S. V., Nern, A. and Borst, A. (2012) Columnar cells necessary for motion responses of wide-field visual interneurons in *Drosophila*. *Journal of Comparative Physiology. A, Neuroethology, Sensory, Neural, and Behavioral Physiology*, **198**, 389–395.
- Schuling, F., Mastebroek, H., Bult, R. and Lenting, B. (1989) Properties of elementary movement detectors in the fly *Calliphora erythrocephala*. *Journal of Comparative Physiology A*, **165**, 179–192.

- Schwartz, M. and Batchelor, C. (2008) The origins of carrier multiplexing: Major George Owen Squier and AT&T. *IEEE Communications Magazine*, **46**, 20–24.
- Serbe, E., Meier, M., Leonhardt, A. and Borst, A. (2016) Comprehensive characterization of the major presynaptic elements to the *Drosophila* OFF motion detector. *Neuron*, **89**, 829–841.
- Sherrington, S. C. S. (1906) *The Integrative Action of the Nervous System... With Illustrations*.
- Shinomiya, K., Huang, G., Lu, Z., Parag, T., Xu, C. S., Aniceto, R., Ansari, N., Cheatham, N., Lauchie, S., Neace, E. et al. (2019) Comparisons between the ON- and OFF-edge motion pathways in the *Drosophila* brain. *Elife*, **8**, e40025.
- Shinomiya, K., Karuppururai, T., Lin, T.-Y., Lu, Z., Lee, C.-H. and Meinertzhagen, I. A. (2014) Candidate neural substrates for OFF-edge motion detection in *Drosophila*. *Current Biology*, **24**, 1062–1070.
- Silies, M., Gohl, D. M., Fisher, Y. E., Freifeld, L., Clark, D. A. and Clan-dinin, T. R. (2013) Modular use of peripheral input channels tunes motion-detecting circuitry. *Neuron*, **79**, 111–127.
- Sinakevitch, I. and Strausfeld, N. J. (2006) Comparison of octopamine-like immunoreactivity in the brains of the fruit fly and blow fly. *Journal of Comparative Neurology*, **494**, 460–475.
- Slaughter, M. M. and Miller, R. F. (1981) 2-amino-4-phosphonobutyric acid: a new pharmacological tool for retina research. *Science*, **211**, 182–185.
- Straka, H. and Ammermüller, J. (1991) Temporal resolving power of blowfly visual system: effects of decamethonium and hyperpolarization on responses of laminar monopolar neurons. *J Comp Physiol A*, **168**.
- Strausfeld, N. J. (ed.) (1976) *Atlas of an Insect Brain*. Berlin Heidelberg: Springer.
- Strausfeld, N. J. (2012) *Arthropod brains: evolution, functional elegance, and historical significance*. Belknap Press.
- Strauss, R., Schuster, S. and Götz, K. G. (1997) Processing of artificial visual feedback in the walking fruit fly *Drosophila melanogaster*. *Journal of Experimental Biology*, **200**, 1281–1296.
- Strother, J., Wu, S., Wong, A., Nern, A., Rogers, E., Le, J., Rubin, G. and Reiser, M. (2017) The emergence of directional selectivity in the visual motion pathway of *Drosophila*. *Neuron*, **94**, 168–183.
- Strother, J. A., Nern, A. and Reiser, M. B. (2014) Direct observation of ON and OFF pathways in the *Drosophila* visual system. *Current Biology*, **24**, 976–983.

- Strother, J. A., Wu, S.-T., Rogers, E. M., Eliason, J. L., Wong, A. M., Nern, A. and Reiser, M. B. (2018) Behavioral state modulates the on visual motion pathway of *Drosophila*. *Proceedings of the National Academy of Sciences*, **115**, E102–E111.
- Sulaiman, P., Xu, Y., Fina, M. E., Tummala, S. R., Ramakrishnan, H., Dhingra, A. and Vardi, N. (2013) Kir2.4 surface expression and basal current are affected by heterotrimeric G-proteins. *Journal of Biological Chemistry*, **288**, 7420–7429.
- Sun, W., Deng, Q., Levick, W. R. and He, S. (2006) On direction-selective ganglion cells in the mouse retina. *The Journal of Physiology*, **576**, 197–202.
- Suver, M. P., Mamiya, A. and Dickinson, M. (2012) Octopamine neurons mediate flight-induced modulation of visual processing in *Drosophila*. *Current Biology*, **22**, 2294–2302.
- Svoboda, K. and Yasuda, R. (2006) Principles of two-photon excitation microscopy and its applications to neuroscience. *Neuron*, **50**, 823–839.
- Sweeney, S. T., Broadie, K., Keane, J., Niemann, H. and O’Kane, C. J. (1995) Targeted expression of tetanus toxin light chain in *Drosophila* specifically eliminates synaptic transmission and causes behavioral defects. *Neuron*, **14**, 341–351.
- Szikra, T., Trenholm, S., Drinnenberg, A., Jüttner, J., Raics, Z., Farrow, K., Biel, M., Awatramani, G., Clark, D. A., Sahel, J.-A. et al. (2014) Rods in daylight act as relay cells for cone-driven horizontal cell-mediated surround inhibition. *Nature neuroscience*, **17**, 1728–1735.
- Takemura, S. (2015) Connectome of the fly visual circuitry. *Microscopy*, **64**, 37–44.
- Takemura, S., Bharioke, A., Lu, Z., Nern, A., Vitaladevuni, S. N., Rivlin, P. K., Katz, W. T., Olbris, D. J., Plaza, S. M., Winston, P., Zhao, T., Horne, J. A., Fetter, R. D., Takemura, S., Blazek, K., Chang, L.-A., Ogundeyi, O., Saunders, M. A., Shapiro, V., Sigmund, C., Rubin, G. M., Scheffer, L. J., Meinertzhagen, I. A. and Chklovskii, D. B. (2013) A visual motion detection circuit suggested by *Drosophila* connectomics. *Nature*, **500**, 175–181.
- Takemura, S., Karuppururai, T., Ting, C.-Y., Lu, Z., Lee, C.-H. and Meinertzhagen, I. A. (2011) Cholinergic circuits integrate neighboring visual signals in a *Drosophila* motion detection pathway. *Current Biology*, **21**, 2077–2084.
- Takemura, S., Lu, Z. and Meinertzhagen, I. A. (2008) Synaptic circuits of the *Drosophila* optic lobe: the input terminals to the medulla. *Journal of Comparative Neurology*, **509**, 493–513.
- Takemura, S., Nern, A., Chklovskii, D. B., Scheffer, L. K., Rubin, G. M. and Meinertzhagen, I. A. (2017) The comprehensive connectome of a neural substrate for ‘ON’ motion detection in *Drosophila*. *eLife*, **6**.

- Tammero, L. F. and Dickinson, M. H. (2002) Collision-avoidance and landing responses are mediated by separate pathways in the fruit fly, *Drosophila melanogaster*. *Journal of Experimental Biology*, **205**, 2785–2798.
- Thomas, J. and Wyman, R. (1984) Mutations altering synaptic connectivity between identified neurons in *Drosophila*. *Journal of Neuroscience*, **4**, 530–538.
- Thoreson, W. B. and Mangel, S. C. (2012) Lateral interactions in the outer retina. *Progress in retinal and eye research*, **31**, 407–441.
- Tooker, R. E., Lipin, M. Y., Leuranguer, V., Rozsa, E., Bramley, J. R., Harding, J. L., Reynolds, M. M. and Vigh, J. (2013) Nitric oxide mediates activity-dependent plasticity of retinal bipolar cell output via S-nitrosylation. *Journal of Neuroscience*, **33**, 19176–19193.
- Torre, V. and Poggio, T. (1978) A synaptic mechanism possibly underlying directional selectivity to motion. *Proceedings of the Royal Society B: Biological Sciences*, **202**, 409–416.
- Trevor, A. J., Katzung, B. G., Masters, S. B. and Kruidering-Hall, M. (2010) *Pharmacology examination & board review*. McGraw-Hill Medical New York, NY, USA:.
- Trujillo-Cenóz, O. (1965) Some aspects of the structural organization of the intermediate retina of dipterans. *Journal of ultrastructure research*, **13**, 1–33.
- Tuthill, J. C., Nern, A., Holtz, S. L., Rubin, G. M. and Reiser, M. B. (2013) Contributions of the 12 neuron classes in the fly lamina to motion vision. *Neuron*, **79**, 128–140.
- Tuthill, J. C., Nern, A., Rubin, G. M. and Reiser, M. B. (2014) Wide-field feedback neurons dynamically tune early visual processing. *Neuron*, **82**, 887–895.
- Van Essen, D. C., Anderson, C. H. and Felleman, D. J. (1992) Information processing in the primate visual system: an integrated systems perspective. *Science*, **255**, 419–423.
- Vardi, N., Zhang, L.-L., Payne, J. A. and Sterling, P. (2000) Evidence that different cation chloride cotransporters in retinal neurons allow opposite responses to GABA. *Journal of Neuroscience*, **20**, 7657–7663.
- Venken, K. J. T., Simpson, J. H. and Bellen, H. J. (2011) Genetic manipulation of genes and cells in the nervous system of the fruit fly. *Neuron*, **72**, 202–230.
- Vigier, P. (1909) Mécanisme de la synthèse des impressions lumineuses recueillies par les yeux composés des diptères. *CR Acad Sci*, **148**, 1221–1223.
- Villette, V., Chavarha, M., Dimov, I. K., Bradley, J., Pradhan, L., Mathieu, B., Evans, S. W., Chamberland, S., Shi, D., Yang, R. et al. (2019) Ultrafast two-photon imaging of a high-gain voltage indicator in awake behaving mice. *Cell*, **179**, 1590–1608.

- Vlasits, A. and Baden, T. (2019) Motion vision: a new mechanism in the mammalian retina. *Current Biology*, **29**, R933–R935.
- Vlasits, A. L., Morrie, R. D., Tran-Van-Minh, A., Bleckert, A., Gainer, C. F., DiGregorio, D. A. and Feller, M. B. (2016) A role for synaptic input distribution in a dendritic computation of motion direction in the retina. *Neuron*, **89**, 1317–1330.
- Vogel, C. and Marcotte, E. M. (2012) Insights into the regulation of protein abundance from proteomic and transcriptomic analyses. *Nature reviews genetics*, **13**, 227–232.
- Völgyi, B., Chheda, S. and Bloomfield, S. A. (2009) Tracer coupling patterns of the ganglion cell subtypes in the mouse retina. *Journal of Comparative Neurology*, **512**, 664–687.
- Von Reyn, C. R., Breads, P., Peek, M. Y., Zheng, G. Z., Williamson, W. R., Yee, A. L., Leonardo, A. and Card, G. M. (2014) A spike-timing mechanism for action selection. *Nature neuroscience*, **17**, 962–970.
- Wässle, H. (2004) Parallel processing in the mammalian retina. *Nature Reviews Neuroscience*, **5**, 747–757.
- Wässle, H., Puller, C., Müller, F. and Haverkamp, S. (2009) Cone contacts, mosaics, and territories of bipolar cells in the mouse retina. *Journal of Neuroscience*, **29**, 106–117.
- Wässle, H. and Riemann, H. (1978) The mosaic of nerve cells in the mammalian retina. *Proceedings of the Royal Society of London. Series B. Biological Sciences*, **200**, 441–461.
- Wei, H., Kyung, H. Y., Kim, P. J. and Desplan, C. (2020) The diversity of lobula plate tangential cells (LPTCs) in the *Drosophila* motion vision system. *Journal of Comparative Physiology A*, **206**, 139–148.
- Wernet, M. F. and Desplan, C. (2004) Building a retinal mosaic: cell-fate decision in the fly eye. *Trends in cell biology*, **14**, 576–584.
- Wernet, M. F., Labhart, T., Baumann, F., Mazzoni, E. O., Pichaud, F. and Desplan, C. (2003) Homothorax switches function of *Drosophila* photoreceptors from color to polarized light sensors. *Cell*, **115**, 267–279.
- Wienecke, C. F., Leong, J. C. and Clandinin, T. R. (2018) Linear summation underlies direction selectivity in *Drosophila*. *Neuron*, **99**, 680–688.
- Wilson, R. I., Turner, G. C. and Laurent, G. (2004) Transformation of olfactory representations in the *Drosophila* antennal lobe. *Science*, **303**, 366–370.
- Yamaguchi, S., Wolf, R., Desplan, C. and Heisenberg, M. (2008) Motion vision is independent of color in *Drosophila*. *Proceedings of the National Academy of Sciences of the United States of America*, **105**, 4910–4915.
- Yang, H. H., St-Pierre, F., Sun, X., Ding, X., Lin, M. Z. and Clandinin, T. R. (2016) Subcellular imaging of voltage and calcium signals reveals neural processing *in vivo*. *Cell*, **166**, 245–257.

- Yang, J., Pahng, J. and Wang, G.-Y. (2013) Dopamine modulates the OFF pathway in light-adapted mouse retina. *Journal of neuroscience research*, **91**, 138–150.
- Yeandle, S. and Spiegler, J. B. (1973) Light-evoked and spontaneous discrete waves in the ventral nerve photoreceptor of *Limulus*. *The Journal of General Physiology*, **61**, 552–571.
- Yonehara, K. and Roska, B. (2013) Motion detection: neuronal circuit meets theory. *Cell*, **154**, 1188–1189.
- Yoshimatsu, T., Bartel, P., Schröder, C., Janiak, F. K., St-Pierre, F., Berens, P. and Baden, T. (2021) Ancestral circuits for vertebrate colour vision emerge at the first retinal synapse. *bioRxiv*, 2020–10.
- Zenisek, D., Davila, V., Wan, L. and Almers, W. (2003) Imaging calcium entry sites and ribbon structures in two presynaptic cells. *Journal of Neuroscience*, **23**, 2538–2548.

ACKNOWLEDGEMENTS

First I want to thank Axel for being the supervisor I needed in order to achieve my PhD. He supported me in times of scientific and personal desperation alike and at the same time accompanied the overwhelming majority of good days with splendid happy hours, sunny days in the Würmbad or in the Biergarten. He always found the right balance of giving me enough freedom to develop my scientific ideas and projects but then also gave me pushes in the right direction whenever I needed them. Without him I most likely would have given up at some point and would not have completed my PhD. I thank the whole GSN (graduate school) for organizing many scientific and non-scientific events and meetings. I also want to thank the rest of my TAC, Ruben Portugues and Laura Busse for helpful advice and stimulating discussions concerning my projects.

No less important were the colleagues in the lab who especially in the early phase taught my invaluable lessons about science and included me in fruitful projects. Although the whole lab contributed to an atmosphere that was and still is highly motivating and collaborative, I need to highlight some of my fellow colleagues. I want to thank all post and current members of the P7 office, especially Aljoscha Leonhardt, Michael Drews, Anna Schützenberger, Nadya Pirogova, Birte Zuidinga. I am in deep gratitude for correcting the most bluntly stupid programming errors I made, last-minute correcting abstracts or posters that were close to submission deadline or helping me trouble-shoot the stimulus arena or my 2-photon setup. But above all I want to thank them for being amazing colleagues and friends that made me actually enjoy a great deal of my work and leisure in the past 5 years or so.

Furthermore I want to thank Georg Ammer who really is a walking science dictionary. No matter how complex the question is he is able to shoot out reliable facts about almost every scientific topic regardless of how far away it is from motion vision at speeds Google can only dream of. Topics of his expert knowledge include birds, cephalopodes and the history of shipping just to name a few dubious ones. I also need to thank him for dozens of moutaineering tours where we hiked, scrambled, climbed, skied and snowboarded up and down probably more meters than there are neurons in a fruit fly's brain.

I thank Matthias Meier and Étienne Serbe for countless good hours inside and outside the lab, summers long of trying to break the world record in the art of "danteln". They kindly integrated me already into the group when others were still hesitant and wanted to wait if the guy from Franconia is trust-worthy. I also want to thank É.T. especially for letting me move in with him when I fell victim to the notorious housing market in Munich. But also special thanks to MM for numerous climbing trips, hundreds of table tennis games and even more beers we had together. Needless to say both of course are also brilliant scientists who's opinion I value a lot.

I thank Matthias Gumbert (Gumbi) for sharing my pain during the whole process of writing this thesis. I also thank him for rappeling me down to safety when I got myself in a precarious situation during our first and last mountain tour.

I thank Niko Hörmann for countless espressi, cakes and interesting discussions about many topics, including scientific ones. He always has a different view on things, which, after rejecting his hypothesis, makes you actually reflect your own opinion.

I thank Amalia Braun, for being the engine of good will to make pandemic times as social as possible and always motivating the people in the lab to not go straight home, but rather sit together and have an after work beer, which usually reduces the grumpiness immensely.

I thank Jürgen Haag alias Bulle for helping me build my 2-photon microscope and trouble shooting the reoccurring problems with the sometimes moody setup.

I also thank Sandra Fendl for great and uncomplicated collaboration in the glutamate imaging project, unlimited patience during the PDE project and fun times at the Oktober or Starkbierfest.

Last but by no means least I want to thank my girlfriend Eva Luca Hetzel and my family. Eva supported me through all phases. She shared my excitement when I came home with interesting data, solaced me when the data turned out to be in fact not so interesting or gave me space whenever I needed quiescence. I'd like to thank my mother for supporting me as long as she could, especially in school times, paying hours and hours of math tutoring lessons despite living herself on a low budget. She supported me when teachers, friends, and sometimes even myself gave up on me. She got me through gymnasium and made me the first in the family ever receiving the Abitur, studying and now finally finishing my PhD. I will never forget the sacrifices she made for me and I will be thankful until the rest of my life.

CURRICULUM VITAE

EDUCATION

- 2016–present: PhD student at Graduate School for Systemic Neurosciences (LMU Munich)/Max-Planck-Institute for Neurobiology, Germany; supervised by Alexander Borst
- 2015–2016: B.Sc in Biology at the Ludwigs-Maximilians Universität Munich, Germany
- 2011–2014: B.Sc in Biology at the Julius-Maximilians Universität in Würzburg, Germany
- 2011: Abitur at Gymnasium Marktbreit, Germany

CONFERENCES & MEETINGS

- 2018: Poster presentation at SFN Conference (San Diego, US)
- 2018: Poster presentation at FENS Conference (Berlin, Germany)
- 2017: Poster presentation at École de neuroscience (Paris, France)
- 2016: Poster presentation at FENS Conference (Copenhagen, Denmark)

TEACHING

- Teaching assistant for *Neurobiology Course* in 2014 (JMU Würzburg)
- Teaching assistant for *Introduction to 2-photon imaging* in 2017 (MPI of Neurobiology)

PERSONAL INFORMATION

- Birthday: 15th May 1990
- Nationality: German
- Languages: German (native), English (fluent), French (intermediate)
- Programming languages: Python (experienced), LaTeX (intermediate)

PUBLICATIONS

- Drews MS., Leonhardt A., Pirogova N., **Richter FG.**, [...] Borst, A. (2020). Dynamic Signal Compression for Robust Motion Vision in Flies. *Current Biology* 30, 209-221.
- **Richter FG.**, Fendl S., Haag J., Drews MS., Borst A. (2018). Glutamate Signaling in the Fly Visual System. *iScience* 7, 85-95.
- Arenz A., Drews MS., **Richter FG.**, Ammer G., Borst A. (2017). The Temporal Tuning of the *Drosophila* Motion Detectors Is Determined by the Dynamics of Their Input Elements. *Current Biology* 27, 929-944.
- Martelli C., Pech U., [...], **Richter FG.**, Wegener C., Fiala A., Riemensperger T. (2017). SIFamide Translates Hunger Signals into Appetitive and Feeding Behavior in *Drosophila*. *Cell reports* 20, 464-478.

AFFIDAVIT

Hiermit versichere ich an Eides statt, dass ich die vorliegende Dissertation **Spatiotemporal filtering of the input elements to the *Drosophila* motion detector** selbstständig angefertigt habe, mich außer der angegebenen keiner weiteren Hilfsmittel bedient und alle Erkenntnisse, die aus dem Schrifttum ganz oder annähernd übernommen sind, als solche kenntlich gemacht und nach ihrer Herkunft unter Bezeichnung der Fundstelle einzeln nachgewiesen habe.

I hereby confirm that the dissertation **Spatiotemporal filtering of the input elements to the *Drosophila* motion detector** is the result of my own work and that I have only used sources or materials listed and specified in the dissertation.

.....
München, 30.11.2021
Munich, 30.11.2021

.....
Florian Richter
Unterschrift
Signature

CONTRIBUTIONS

- Drews MS., Leonhardt A., Pirogova N., **Richter FG.**, Schuetzenberger A., Braun L., Serbe E., Borst, A. (2020). Dynamic Signal Compression for Robust Motion Vision in Flies. *Current Biology* 30, 209-221.
 - M.S.D., A.L., and A.B. jointly conceived the study. M.S.D. and A.L. designed all experiments. A.L. and L.B. conducted behavioral experiments. E.S. recorded electrophysiological responses. M.S.D., N.P., **F.G.R.**, and A.S. performed calcium imaging. A.L. designed and analyzed the convolutional model. M.S.D. and A.L. analyzed data, performed modelling, and wrote the manuscript. All authors participated in editing the manuscript.
- **Richter FG.**, Fendl S., Haag J., Drews MS., Borst A. (2018). Glutamate Signaling in the Fly Visual System. *iScience* 7, 85-95.
 - **F.G.R.**, S.F., and A.B. conceived the study and designed the experiments. **F.G.R.** conducted and analyzed the imaging experiments for Mi9 and L1. S.F. performed and analyzed all stainings. J.H. performed and analyzed the LPi experiments. M.S.D. performed data analysis and model fitting of the receptive fields. **F.G.R.** wrote the manuscript with the help of all authors.
- Arenz A., Drews MS., **Richter FG.**, Ammer G., Borst A. (2017). The Temporal Tuning of the *Drosophila* Motion Detectors Is Determined by the Dynamics of Their Input Elements. *Current Biology* 27, 929-944.
 - A.A., M.S.D., and A.B. conceived the study and designed the experiments. A.A. conducted and analyzed the measurements of T4/T5 cell responses. M.S.D. designed the projector-based stimulation arena and performed and analyzed the measurements of the OFF-pathway elements. **F.G.R.** performed and analyzed the experiments describing the ON-pathway neurons. G.A. performed and analyzed the patch-clamp recordings from lobula plate tangential cells. M.S.D. performed the computer simulations. A.A. wrote the manuscript with the help of all authors.

.....
Florian Richter

.....
Sandra Fendl
Co-author

.....
Prof. Dr. Alexander Borst
Supervisor